ADDITIVE MANUFACTURING OF STIFFNESS OPTIMISED AUXETIC BONE SCAFFOLD USING COBALT-CHROMIUM-MOLYBDENUM SUPERALLOY

Chameekara Tharumal Wanniarachchi

A thesis submitted in partial fulfilment of the requirements of the University of Wolverhampton for the degree of Doctor of Philosophy

March 2022

This work or any part thereof has not previously been presented in any form to the University or to any other body whether for the purposes of assessment, publication or for any other purpose (unless otherwise indicated). Save for any express acknowledgments, references and/or bibliographies cited in the work, I confirm that the intellectual content of the work is the result of my own efforts and of no other person.

The right of Chameekara Tharumal Wanniarachchi to be identified as author of this work is asserted in accordance with ss.77 and 78 of the Copyright, Designs and Patents Act 1988. At this date copyright is owned by the author.

Signature……..

Date……26th September 2022……

Abstract

Auxetic materials offer unconventional strain behaviour owing to their negative Poisson's ratio ($-\upsilon$) leading to deformation modes and mechanical characteristics different to traditional porous architecture. This can lead to favourable outcomes for load-bearing tissue engineering constructs, such as bone scaffolds for critical-size defects. Emerging early-stage studies have shown the potential of auxetic architecture in increasing cell proliferation and tissue reintegration due to their $-\upsilon$. However, research on the development of stiffness optimised auxetic architecture for biomedical applications including bone scaffolds or implants is yet to be reported. In this regard, the thesis puts forward an open innovation framework for the selective laser melting (SLM) of auxetic bone scaffolds that offer the strength and porosity requirements while offering stiffness matching to a tibia host section. CoCrMo has been chosen as the biomaterial of choice due to its high elastic modulus and density which offered the potential for conceiving highly porous architectures. CoCrMo stiffness matched auxetic bone scaffolds optimised under two scenarios for their potential to offer near-zero and high negative Poisson's ratio are demonstrated in this thesis. Overall, the investigations carried out in this thesis suggest that CoCrMo auxetic bone scaffolds can be additively manufactured with targeted Poisson's ratio, mechanical performance and porosity characteristics by algorithmically modifying the design parameters. The surrogate model developed in this thesis can be used for user-defined scenarios to generate scaffolds with near-zero and high $-\upsilon$, respectively while offering stiffness matching to host bone. Manufacturers and research institutions can use the validated methodology proposed in this thesis to further refine and generate alternate prototypes to inform further developments in the field of meta-biomaterials.

Acknowledgements

My supervisor, Dr Arun Arjunan, deserves my heartfelt gratitude for his steadfast support throughout this project. This project would not have been possible without the supervision and support of Dr Arun Arjunan. Special thanks go out to Dr Ahmad Baroutaji for his enormous support and guidance. Their support and experience in biomaterials, metamaterials and additive manufacturing were vital to the success of this thesis.

I am also extremely grateful to Mr John Robinson and Mr Neil Basini for arranging to manufacture and test the relevant samples that were essential for the completion of this project. I am also thanking Mr Paul Bates for his assistance in realising the physical tests.

I would like to thank the University of Wolverhampton's Faculty of Science and Engineering for their financial support and for giving me the opportunity to carry out my PhD research.

I am also taking this opportunity to express my heartfelt gratitude to my family, particularly my mother, father, and two sisters, for being my backbone and sticking by me at one of the most difficult and stressful moments in my life. Without their unwavering emotive support and encouragement, this project would have been impossible to complete.

Lastly, I would like to dedicate this thesis to my daughter Shenaya Wanniarachchi, whom I hope to make proud of by studying for this award.

Table of Contents

ABSTRACT I

ACKNOWLEDGEMENTS II

TABLE OF CONTENTS III

LIST OF FIGURES X

LIST OF TABLES XVIII

NOMENCLATURE XXIII

CHAPTER 1 1

INTRODUCTION 1

1.1. Background 1

1.2. Auxetic architecture as a candidate for tibial bone scaffolds 4

1.3. Problem statement 6

1.4. Research aim and objectives 8

1.5. Structure of the thesis 9

1.6. Original contribution to knowledge 11

CHAPTER 2 14

BONE SCAFFOLDS AND THE EMERGENCE OF AUXETIC BIOMATERIALS FOR TISSUE ENGINEERING 14

2.1. Introduction 14

2.2. Bone 14

2.2.1. Tissue composition 14

2.2.2. Bone Structure 17

2.2.3. Mechanical properties of bone 18

2.2.4. Bone remodelling theory 19
2.2.5. Fracture and healing process of a bone 20
2.3. Biomaterials 22
2.3.1. Biomaterial types 23
2.3.1.1. Polymers 24
2.3.1.2. Ceramics 25
2.3.1.3. Metals and its alloys 26
2.3.2. Biomaterials for scaffolds 27
2.4. Scaffold characteristics for bone tissue engineering 30
2.4.1. Porosity and pore size 30
2.4.2. Biocompatibility 31
2.4.3. Mechanical Properties 32
2.4.4. Biodegradability 34
2.4.5. Upcoming trends in bone scaffolds 34
2.5. Failure and wear of bone scaffolds 35
2.5.1. Wear debris 35
2.5.2. Stress shielding 36
2.6. Stiffness and strength in bone scaffold design 37
2.7. Auxetic materials 38
2.7.1. Introduction to auxetic materials 38
2.7.2. Auxetic structures 39
2.7.2.1. Re-entrant structure 39
2.7.2.2. Chiral structures 41
2.7.2.3. Rotating units 42
2.7.2.4. Nodule and fibril structures 43

2.7.3. Properties of auxetic structures 44
2.7.3.1. Elastic and shears modulus 44
2.7.3.2. Indentation behaviour 46
2.7.3.3. Synclastic behaviour 46
2.7.3.4. Variable Permeability 47
2.7.4. Auxetic materials and tissue engineering 48
2.7.5. Application of auxetic structures for bone tissue engineering 50
2.8. Summary and gaps in the literature 54
CHAPTER 3 56
ADDITIVE MANUFACTURING OF BIOMATERIALS 56
3.1. Introduction 56
3.2. Additive manufacturing (AM) 56
3.2.1. Selective Laser Sintering (SLS) 59
3.2.2. Electron Beam Melting (EBM) 61
3.2.3. Selective Laser Melting (SLM) 63
3.2.3.1. Process parameter optimisation 65
3.3. Materials used in AM 67
3.4. Limitations of AM 70
3.4.1. Overhangs and supports 71
3.4.2. Thermal stresses and warping 73
3.4.3. Surface Roughness (Stair Step) 75
3.5 AM for auxetic materials 76
3.6 AM for bone tissue engineering 77
3.7. Mechanical properties of AM lattice materials 81
3.8 AM challenges for biomedical applications 84

CHAPTER 4 86

DESIGN AND ADDITIVE MANUFACTURE OF AUXETIC SCAFFOLDS 86

4.1. Introduction 86

4.2. Methodology 87

4.2.1. Auxetic scaffold design 87

4.2.1.1. Unit cells considered for initial selection 87

4.2.2. Finite element analysis of unit cell assemblies 90

4.2.3. Additive manufacturing 92

4.2.3.1. CoCrMo superalloy feedstock 92

4.2.3.2. CoCrMo Powder characterisation 95

4.2.3.3. Selective laser melting 95

4.2.4. Scanning Electron Microscopy (SEM) 96

4.3. Results and discussion 97

4.3.1. Unit cell properties 97

4.3.2. Selection of auxetic unit cells for scaffold design 99

4.3.3. Design of auxetic bone scaffolds 101

4.3.4. Additive manufacturing 102

4.3.4.1. Powder characteristics 102

4.3.4.2. Selective laser melted samples 104

4.3.4.3. Morphology of the printed scaffolds 106

4.4. Conclusion 109

CHAPTER 5 111

MECHANICAL PERFORMANCE OF SELECTIVE LASER MELTED COCRMO 111

5.1. Introduction 111

5.2. Methodology 112

5.2.1. Theoretical prediction....112
5.2.2. Experimental mechanical testing....113
5.3. Results and discussion....115
5.3.1. Mechanical properties of selective laser melted CoCrMo....115
5.3.2. Ashby's criterion and the performance of CoCrMo auxetic scaffolds....117
5.3.3. Elastic-plastic performance of CoCrMo auxetic scaffolds....118
5.3.4. Failure mode analysis....123
5.4. Conclusion....127
CHAPTER 6....129
FINITE ELEMENT MODELLING OF COCRMO AUXETIC BONE SCAFFOLDS....129
6.1. Introduction....129
6.2. Finite Element Modelling....130
6.2.1. Model geometry....130
6.2.2. Material model and boundary conditions....130
6.2.3. Mesh generation and convergence studies....132
6.2.4. Post-processing for Poisson's ratio evaluation....135
6.3. Results and discussion....136
6.3.1. Finite element model validation....136
6.3.2. Stress distribution within the scaffolds....139
6.4. Conclusion....143
CHAPTER 7....144
IDENTIFYING BEST DESIGNS USING COMBINED TOPSIS AND AHP....144
7.1. Introduction....144
7.2. Multi-criteria decision-making methodology (MCDM)....145
7.2.1. TOPSIS....145

7.2.2. Analytic hierarchy process 148

7.2.3. Scenarios for the selection of auxetic bone scaffolds 150

7.2.3.1. Scenario 1: Auxetic bone scaffold with near-zero $-\boldsymbol{\nu}$ 151

7.2.3.2. Scenario 2: Auxetic bone scaffold with highest $-\boldsymbol{\nu}$ 151

7.3. Results and discussion 152

7.3.1. Scenario 1: Selection of auxetic bone scaffold with near-zero $-\boldsymbol{\nu}$ 153

7.3.2. Scenario 2: Auxetic bone scaffold with highest $-\boldsymbol{\nu}$ 157

7.4. Conclusion 159

CHAPTER 8 161

PARAMETRIC ANALYSIS OF BEST AUXETIC DESIGN 161

8.1. Introduction 161

8.2. Response surface methodology 162

8.3. Results and discussion 166

8.3.1. Scenario 1: Influence of design parameters on the performance of AX4 167

8.3.1.1. Generation of the response surface model for AX4 167

8.3.1.2. Influence of AX4 design parameters on porosity 171

8.3.1.3. Influence of AX4 design parameters on the elastic modulus 172

8.3.1.4. Influence of AX4 design parameters on negative Poisson's ratio 173

8.3.1.5. Influence of AX4 design parameters on yield strength 174

8.3.2. Scenario 2: Influence of design parameters on the performance of AX1 175

8.3.2.1. Generation of the response surface model for AX1 175

8.3.2.2. Influence of AX1 design parameters on porosity 179

8.3.2.3. Influence of AX1 design parameters on elastic modulus 181

8.3.2.4 Influence of AX1 design parameters on Poisson's ratio 182

8.3.2.5 Influence of AX1 design parameters on yield strength 183

8.4. Conclusion..... 184

CHAPTER 9 186

OPTIMISATION AND VALIDATION OF THE BEST AUXETIC SCAFFOLD 186

9.1. Introduction..... 186

9.2. Multi-objective optimisation methodology..... 187

9.3. Results and discussion..... 189

9.3.1 Optimum auxetic bone scaffold for Scenario 1 189

9.3.2 Optimum auxetic bone scaffold for Scenario 2 193

9.4. Conclusion..... 196

CHAPTER 10 198

CONCLUSION AND FUTURE WORK 198

10.1. Main findings of the research 198

10.2. Implications of the research..... 202

10.3. Limitations of the research 204

10.4. Recommendations for future work..... 205

REFERENCES 208

List of figures

Figure 1.1. Scaffold based tissue reconstruction for bone fractures [16] 3

Figure 2.1. Anatomy of a tibial bone section showing outer and inner bone section [40] 15

Figure 2.2. Hierarchical architecture of bone tissue ranging from macro, micro, and nanoscale. Bone has a comparatively dense cortical bone that contributes significantly to load-bearing and an inner trabecular or spongy bone composed of hierarchical Haversian systems or osteons that feature a complex nanoarchitecture of collagen fibrils [48–50] 17

Figure 2.3. Sequences of Secondary Healing Fracture [9] 22

Figure 2.4. Examples of emerging biomaterials [69] showing (a) additively manufactured microporous titanium tissue engineering scaffolds [70], (b) hybrid meta-biomaterial for functional hip implants [71] and (c) cylindrical-shaped meniscus-derived injectable hydrogel [72] 23

Figure 2.5. Deformation of materials showing (a) behaviour of a conventional material resulting in positive Poisson's ratio and (b) showing auxetic materials resulting in negative Poisson's ratio. Adapted from [132] 38

Figure 2.6. 2D re-entrant auxetic structures [138] where (a) refers to double arrow-headed, (b) 2D re-entrant honeycomb, (c) structurally hexagonal re-entrant

honeycomb, (d-f) interconnected stars, (g) sinusoidal lattice, (h) lozenge and (i) square grids.....40

Figure 2.7. 2D re-entrant honeycombs with undeformed and deformed (response to applied horizontal stretching) [141].....41

Figure 2.8. Chiral structures (a) Chiral honeycomb (b) Chiral honeycomb with symmetrical units [3].....42

Figure 2.9. Rotating unit models (a) Triangular units (b) Square units (c) Rectangular units [3].....43

Figure 2.10. Nodule and Fibril structure [132] 44

Figure 2.11. Indentation behaviour of (a) non-auxetic (b) Auxetic [166] 46

Figure 2.12. (a) auxetic synclastic curvature (b) conventional material anticlastic curvature [169] 47

Figure 2.13. Variable permeability application in Smart filters [173] 47

Figure 2.14. Poisson's ratio estimation of PLGA auxetic scaffold where (a) shows the strain monitoring points and (b) the compressed specimen [8] 52

Figure 2.15. Meta-implant (a) CAD model (b) meshed finite element (FE) model of meta-implant based on 3D re-entrant structure (c) Meshed assembly of the implant and femur bone model and (d) Applied load and boundary conditions on the implant and femur bone model [193].....53

Figure 3.1. Steps leading to additive manufacturing from digital model to the final part 58

Figure 3.2. Schematic Selective laser melting process (SLM) [216] 64

Figure 3.3. Support structures on SLM manufactured part [231] 72

Figure 3.4. Part delamination due to the effect of residual stresses in SLM [235] 73

Figure 3.5. X-ray CT image of a 45° orientated additive manufactured part showing a higher surface roughness for the downward-facing side relative to the upward-facing side [238] 76

Figure 3.6. Covid-19 sample swab heads [241] 77

Figure 3.7. Acetabular cup produced by Additive manufacturing [246] 78

Figure 3.8. Built components with different pore sizes [36] 80

Figure 3.9. (a) Schwartz diamond FGPS model (b) the X-Z plane view. Increase in volume fraction indicated by arrow [128] 81

Figure 3.10. Stainless steel cellular structures manufactured by SLM [256] 84

Figure 4.1. All unit cell (UC) variants considered for initial analysis to be qualified for their auxeticity inspired from literature 88

Figure 4.2. Unit cell assemblies designed for finite element qualification 89

Figure 4.3. Finite element model and associated boundary conditions used to simulate the lateral deformation of unit cell assemblies 90

Figure 4.4. Auxeticity of UC assemblies by FEA 100

Figure 4.5. Scaffold designs featuring auxetic unit cells UC1 to UC5 considered in this thesis 101

Figure 4.6. SEM micrograph of CoCrMo superalloy used for scaffold fabrication .. 103

Figure 4.7. Characteristics of the CoCrMo feedstock used for the additive manufacturing of auxetic bone scaffolds showing (a) volume-size distribution and (b) the particle size distribution (PSD) 104

Figure 4.8. Selective laser melted CoCrMo samples showing (a) printed samples on the base plate before post-processing, (b) post-processed scaffold samples and (c) tensile test coupon 105

Figure 4.9. Comparison of porosity between ideal and actual scaffolds 106

Figure 4.10. Scanning electron micrograph showing (a) scaffold as manufactured before shot blasting, (b) after shot blasting and (c) variation of joints from ideal after shot blasting 107

Figure 4.11. SEM data showing the influence of selective laser melting on strut dimension 108

Figure 5.1. Mechanical test setup showing (a) tensile test for the evaluation of CoCrMo bulk material properties and (b) compression test for mechanical properties of the auxetic scaffold 114

Figure 5.2. Mechanical performance of the selective laser melted CoCrMo material showing (a) the stress-strain relationship and (b) the failed tensile test coupons ... 116

Figure 5.3. Theoretically predicted (a) elastic modulus (E_{thr}) (b) yield strength (σ_{thr}) for all respective scaffolds 117

Figure 5.4. Typical compression test stress-strain curve for cellular materials [339] 119

Figure 5.5. The experimental stress-strain relationship for selective laser melted CoCrMo auxetic bone scaffolds showing (a) AX1, (b) AX2, (c) AX3, (d) AX4 and (e) AX5 120

Figure 5.6. Typical compressive stress-strain behaviour for each structure 122

Figure 5.7. Step by step deformation associated with the five scaffolds (a) AX1, (b) AX2, (c) AX3, (d) AX4 and (e) AX5 124

Figure 5.8. SEM data of the failed samples showing (a) AX1, (b) AX2, (d) AX3, (d) AX4 and (e) AX5 126

Figure 6.1. Finite element model showing the (a) element type and (b) boundary conditions 131

Figure 6.2. Finite element force-displacement curves using different element sizes for (a) AX1, (b) AX2, (c) AX3, (d) AX4 and (e) AX5 134

Figure 6.3. Comparison of stress-strain curves obtained from the finite element model and physical tests for (a) AX1, (b) AX2, (c) AX3, (d)AX4 and (e) AX5 137

Figure 6.4. Finite element simulation of the stress distribution in the auxetic scaffold showing (a) AX1, (b) AX2, (c) AX3, (d) AX4 and (e) AX5 142

Figure 7.1. Hierarchical model..... 153

Figure 8.1. Flow chart of the optimisation process using the desirability approach 165

Figure 8.2. Comparison between RS model and finite element predictions for AX4 showing (a) Porosity (φ), (b) elastic modulus (E), (c) Negative Poisson's ratio ($-\upsilon$) and (d) Yield strength (σ_y) 170

Figure 8.3. Influence of the design parameters on AX4 structure showing (a) the influence of strut thickness on porosity, (b) the influence of auxetic angle on porosity and (c) the interdependence of thickness and auxetic angle on porosity 171

Figure 8.4. Influence of the design parameters on AX4 structure showing (a) the influence of strut thickness on elastic modulus, (b) the influence of auxetic angle on elastic modulus and (c) the interdependence of thickness and auxetic angle on elastic modulus..... 172

Figure 8.5. Influence of the design parameters on AX4 structure showing (a) the influence of strut thickness on Poisson's ratio, (b) the influence of auxetic angle on Poisson's ratio and (c) the interdependence of thickness and auxetic angle on Poisson's ratio 174

Figure 8.6. Influence of the design parameters on AX4 structure showing (a) the influence of strut thickness on yield strength, (b) the influence of auxetic angle on yield strength and (c) the interdependence of thickness and auxetic angle on yield strength 175

Figure 8.7. Comparison between RS model and finite element predictions for AX1 showing (a) Porosity (φ), (b) elastic modulus (E), (c) Negative Poisson's ratio ($-\upsilon$) and (d) yield strength (σ_y) 178

Figure 8.8. Influence of the design parameters on AX1 structure showing (a) the influence of strut thickness on porosity, (b) the influence of auxetic angle on porosity and (c) the interdependence of thickness and auxetic angle on porosity 180

Figure 8.9. Influence of the design parameters on AX1 structure showing (a) the influence of strut thickness on elastic modulus, (b) the influence of auxetic angle on elastic modulus and (c) the interdependence of thickness and auxetic angle on elastic modulus 181

Figure 8.10. Influence of the design parameters on AX1 structure showing (a) the influence of strut thickness on Poisson's ratio, (b) the influence of auxetic angle on Poisson's ratio and (c) the interdependence of thickness and auxetic angle on Poisson's ratio 182

Figure 8.11. Influence of the design parameters on AX1 structure showing (a) the influence of strut thickness on yield strength, (b) the influence of auxetic angle on yield strength and (c) the interdependence of thickness and auxetic angle on yield strength 183

Figure 9.1. The desirability of the optimum solution against design variables for AX4 under Scenario 1 191

Figure 9.2. Optimised AX4 scaffold satisfying scenario 1 showing (a) optimum design generated and (b) finite element informed von-mises stress distribution 193

Figure 9.3. The desirability of the optimum solution against design variables for AX1 under Scenario 2 194

Figure 9.4. Optimised AX1 scaffold satisfying scenario 1 showing (a) optimum design generated and (b) finite element informed von-mises stress distribution 195

List of tables

Table 1.1. Examples of biological tissue that feature partial or full auxetic properties are reported in the literature 5

Table 2.1. Mechanical characteristics of cortical and cancellous bone [9]..... 19

Table 2.2. Mechanical properties of metallic biomaterials used for load-bearing implants [9] 26

Table 2.3. Biocompatibility requirement for scaffolds used for bone tissue engineering 32

Table 2.4. Parameters suitable to characterise the mechanical performance of a biomaterial 33

Table 2.5. Auxetic structures as a tissue engineering scaffold 48

Table 3.1. SLM Specifications [194] 64

Table 3.2. AM processes categorisation [227]..... 68

Table 3.3. Print resolution and scalability can be achieved by various AM techniques [226] 69

Table 4.1. Bulk material properties used for the numerical model 91

Table 4.2. Elemental and nodal distribution associated with the converged structural FE model 92

Table 4.3. Chemical composition of the CoCrMo alloy used 93

Table 4.4. Properties of all the nine-unit cell designs where m_{UC}, V_{UC}, ρ_r, E_{thr} and σ_y are mass, volume, relative density, theoretical elastic modulus and yield strength of the unit cells respectively 98

Table 4.6. Properties of the lattice candidates evaluated for scaffold design 99

Table 4.6. Properties of the auxetic bone scaffold designs 102

Table 4.7. Physical parameters and porosity of the additively manufactured scaffolds 105

Table 5.1. Material properties of CoCrMo obtained from tensile test data showing E, σ_y, and σ_{ult} are the Young's modulus, yield strength and ultimate strength, respectively 116

Table 5.2. Experimental mechanical properties of scaffolds 122

Table 6.1. Elements, nodes and solution time associated with the converged finite element model 135

Table 6.2. Comparison between the finite element predicted and actual test data on parameters of interest where E referes to the elastic modulus, σ_y yield strength and υ the Poisson's ratio 138

Table 6.3. Comparison of elastic modulus (E) and yield strength (σ_y) between the different scaffolds evaluated using theoretical, experimental and numerical methods 139

Table 7.1. Saaty rating scale for analytical hierarchy process (AHP) [369] 149

Table 7.2. Decisional matrix and the parametric values used for multi-criteria decision making 152

Table 7.3. Pair-wise comparison matrix to determine the relative importance of the five selected parameters contributing to the selection of a near-zero Poisson's ratio auxetic bone scaffold 154

Table 7.4. Normalised pair-wise comparison matrix to determine the relative importance of the five selected parameters 154

Table 7.5. Criteria relative weights showing the importance of the selected parameters in the selection of a near-zero Poisson's ratio auxetic bone scaffold 154

Table 7.6. The normalised values related to the criteria 155

Table 7.7. Weighted normalised matrix 155

Table 7.8. Positive and negative ideal solution 156

Table 7.9. Ranking matrix identifying the best auxetic scaffolds meeting all the decision criteria while offering a near zero Poisson's ratio 156

Table 7.10. Pair-wise comparison matrix 157

Table 7.11. Normalised pair-wise comparison matrix 157

Table 7.12. Criteria relative weights 157

Table 7.13. Weighted normalised matrix 158

Table 7.14. Positive and negative ideal solutions 158

Table 7.15. Ranking of alternatives for Scenario 2 159

Table 8.1. Design variables selected for the auxetic scaffold to be optimised under Scenario 1 163

Table 8.2. Design variables selected for the auxetic scaffold to be optimised under Scenario 2 163

Table 8.3. CCD matrix showing the design variables and responses for AX4 in Scenario 1 167

Table 8.4. Summary of ANOVA for the developed RS model for AX4 169

Table 8.5. Residual values for the RS models showing deviation of the sampling point responses with respect to ideal 170

Table 8.6. CCD matrix showing the design variables and responses for AX1 in Scenario 2 176

Table 8.7. Summary of ANOVA for the developed RS model for AX1 177

Table 8.8. Residual values for the RS models showing deviation of the sampling point responses with respect to ideal for scaffold AX1 179

Table 9.1. Summarising optimisation criteria used for the designs to generate optimum auxetic bone scaffold to satisfy multiple scenarios 188

Table 9.2. Predicted optimal solution for AX4 under Scenario 1 criteria 191

Table 9.3. Comparison between predicted and FEM values of the optimum AX4 scaffold design 192

Table 9.4. Predicted optimal solution for AX1 under Scenario 2 194

Table 9.5. Comparison between predicted and FEM values of the optimum AX1 scaffold design 195

Nomenclature

AHP	Analytical Hierarchy Process
AM	Additive Manufacturing
ANOVA	Analysis Of Variance
BISO	Bilinear Isotropic Strain Hardening
BMU	Basic Multicellular Unit
CAD	Computer-Aided Design
CCD	Central Composite Design
CoCrMo	Cobalt-Chromium-Molybdenum
CSBD	Critical Size Bone Defects
DMD	Direct Metal Deposition
DoE	Design of Experiment
EBM	Electron Beam Melting
EDM	Electro Discharge Machining
EoD	Ease of Design
FDM	Fused Deposition Modelling
FEA	Finite Element Analysis
FEM	Finite Element Method
FGA	Functionally Graded Auxetic
FGPS	Functionally Graded Porous Scaffold
HA	Hydroxyapatite
LOM	Laminated Object Manufacturing
LPBF	Laser Powder Bed Fusion
MCDM	Multi-Criteria Decision-Making Methodology
PEG	Polyethylene Glycol

PLGA	Poly Lactic-co-Glycolic Acid
PPR	Positive Poisson’s Ratio
PSZ	Partially Stabilised Zirconia
PVCT	Permanent Volumetric Compression with Heat Treatment
PVD	Particle Volume Distribution
RP	Rapid Prototyping
RS	Response Surface
RSM	Response Surface Methodology
S1	Scenario 1
S2	Scenario 2
SEM	Scanning Electron Microscopy
SL	Stereolithography
SLM	Selective Laser Melting
SLS	Selective Laser Sintering
STL	Standard Tessellation Language
THA	Total Hip Arthroplasty
TOPSIS	Technique for Order of Preference by Similarity to Ideal Solution
UCA	Unit Cell Assembly
UC	Unit Cell
UHMWPE	Ultra-High Molecular Weight Polyethylene
X-ray CT	X-ray Computed Tomography
ZPR	Zero Poisson’s Ratio

Chapter 1

Introduction

1.1. Background

Auxetic materials are signified by a negative Poisson's ratio ($-\upsilon$), meaning they shrink in the lateral direction when compressed axially. A number of biological tissues have been reported in the literature [1–3] as featuring $-\upsilon$ demonstrating auxetic behaviour. The auxetic behaviour of biological tissues affects the loading behaviour at the interface of biomaterial and porous structures involved in tissue engineering. Attachment of host tissue to a biomaterial is related to the functional interface that exists between the biomaterial and the tissue. As such tissue engineering constructs such as bone scaffolds featuring auxetic behaviour may offer enhanced opportunities for large load-bearing tissue reconstruction such as in the case of critical size bone defects (CSBD). The rise in digital manufacturing [4,5] techniques such as additive manufacturing offer significant potential for engineering bone scaffolds featuring complex porous architecture leading to auxetic behaviour.

Numerous approaches are found in the literature [5,6] experimenting with the use of tissue engineering scaffolds featuring $-\upsilon$. One of the most critical findings in this regard was reported by Choi *et al*. [7] demonstrating and increased cell proliferation using MG-63 osteoblasts responsible for human bone tissue using the auxetic scaffold. This thesis further extends to the investigations on the potential of auxetic bone scaffolds through conceiving, additively manufacturing and characterising

cobalt-chromium-molybdenum (CoCrMo) auxetic bone scaffolds featuring porosity similar to that of the tibia bone. The overall dimensions of the scaffolds being investigated are targeted toward load bearing large tissue reconstruction such as CSBD. A defect or fracture in bone tissue can be characterised depending on its size. [8] When the size of the defect is larger than 2 cm, normal healing leading to the union without significant external intervention is often not observed [9,10]. These types of bone defects can be characterised as critical size bone defects (CSBD) signified by a large hard tissue void that prevents the bone from healing naturally. Bone defects can be caused through a range of conditions, including high-energy trauma, soft tissue and periosteal stripping (especially in high-grade open tibial fractures), blast injuries, infection, and tumour excision. Generally, a bone defect size of more than 2 cm and a circumferential loss of more than 50% is characterised in the literature as CSBD [11].

Bone tissue is primarily made up of two layers: an exterior and interior layer referred to as cortical and cancellous bone, respectively. The difference between the cortical and cancellous bone tissue is characterised through their difference in porosity. Generally, the porosity of cortical bone ranges from 5-15% and that of cancellous bone ranges from 40-95% [12]. Cortical bone is extremely dense and has a high yield strength of around 130-190 MPa; however, cancellous bone only features 10% of the yield strength of cortical bone [13].

Synthetic bone replacements are increasingly being experimented to alleviate current challenges that exist with autografts and allografts, such as limited availability, donor site difficulties, and the danger of disease transmission and immunological rejection. Damaged bone reconstruction and regeneration is a significant health problem as well as an economic strain. Although autologous or allograft bone transplantations are

available [13], the restricted supply and the risk of disease transmission demand alternative routes for bone tissue reconstruction. Tissue engineering is emerging as an alternative method to heal and rebuild bone defects through the use of porous biomaterials [14]. The technique relies on the use of porous scaffolds that are engineered to mimic the structural integrity and mechanical properties of the host tissue, which allows for tissue ingrowth as shown in Figure 1.1.

Figure 1.1. Scaffold based tissue reconstruction for bone fractures [15]

Three-dimensional (3D) biomaterials that provide a favourable environment for cells to repair tissues and organs are referred to as scaffolds. Biocompatibility, porous structure, and controlled degradation with physiologically acceptable degradation products are all required for a scaffold for bone regeneration. However, the material, structure, and mechanical properties of the scaffold is the most significant factor for load-bearing tissue reconstruction. The scaffold facilitates cell attachment through the interconnected pores, which subsequently integrate the scaffold to form a union [16]. As such, an optimal bone scaffold should mimic the stiffness and porosity of the host bone to allow for effective tissue reintegration while limiting stress shielding effects.

As such, the thesis focuses on the development of biocompatible CoCrMo porous auxetic architecture while mimicking the stiffness and porosity of a tibial host section.

1.2. Auxetic architecture as a candidate for tibial bone scaffolds

A traditional material experiencing tensile load will stretch along the direction of load resulting in progressive shrinking of the cross-section. In this regard, the ratio of the lateral to longitudinal strain is called Poisson's ratio (υ) [6,16]. Most conventional materials have a positive Poisson's ratio ($+\upsilon$) [17]. However, if the material exhibits an alternative behaviour by becoming thicker along the lateral direction when being stretched, the materials will exhibit a negative Poisson's ratio ($-\upsilon$). Such materials that do not exhibit a positive Poisson's ratio are referred to as auxetic material [4,18]. The auxetic behaviour of a material is often informed by the cellular lattice that it is made of or by carefully conceived porous architecture at the sub-micron scale [18,19].

The rapid growth in auxetic materials is due to their unique properties such as high shear modulus, enhanced indentation resistance, variable permeability along with high energy absorption and complex strain distribution [20]. These properties lend auxetic to a variety of complex applications in the automotive, marine, aerospace, nuclear, and biomedical fields due to their peculiar properties. As such, auxetic architectures are being increasingly experimented for the development of optimum products and designs that go beyond the current state of the art with traditional materials. Literature [20–22] in this field particularly shows efforts in the development of new auxetic architecture, associated prediction models and fabrication processes. Furthermore, the rise in digital fabrication techniques such as additive manufacturing is another aspect that is fuelling the auxetic materials research.

Table 1.1. Examples of biological tissue that feature partial or full auxetic properties are reported in the literature

Biological tissue	Type	Species	Reference
Skin	Skin	Cat	[23]
Bone	Tibia	Human	[2]
Skin	Teat	Cow	[24]
Embryonic epithelia	Neuro-epithelium	Axolotl	[25]
Artery	Carotid Artery	Cow	[26]
	Achilles	Cadaveric human	
	Peroneus brevis	Cadaveric human	
Tendon	Deep flexor	Pig	[27]
	Achilles	Human	
	Deep flexor	Sheep	
Intervertebral disc	Annulus fibrosus	Cow	[28]
Intervertebral disc	Annulus fibrosus	Pig	[29]

In addition to artificial materials, numerous biological tissues (Table 1.1) including cancellous tibial bone has demonstrated auxetic behaviour [2]. The auxetic behaviour of cancellous bone has implications when it comes to the recreation of strain distribution in tissue interfacing scaffolds. For a bone scaffold to be optimal, it should recreate the natural mechanical properties of the host tissue, which is particularly critical for the reconstruction of critical size bone defects [11,30]. Furthermore, the investigation into the effect of auxetic scaffolds on cellular behaviour has also been shown to increase cell proliferation and enhance differentiation [1,5,7]. Informed from previous literature, this thesis further explores this direction of research through the development and optimisation of auxetic bone scaffolds that may be used for tissue reconstruction. As such, the aim is to contribute to knowledge creation regarding the potential use of auxetic materials in tissue engineering applications and biomedical devices.

While traditional manufacturing is restricted in its capacity to create cellular structures at the sub-micron scale, this can be achieved through additive manufacturing such as selective laser melting (SLM). SLM uses a layer upon layer method of fusing metal powders with the help of an overhead laser informed by the 3D CAD data in the form of a standard tessellation language (STL) [31]. This offers designers and engineers increased freedom in creating complex porous architecture. When the enhanced design freedom in generation porous materials is combined with advanced visualisation techniques like X-ray computed tomography (X-ray CT), personalised bone scaffolds suitable for tissue engineering can be conceived, which is otherwise challenging with traditional manufacturing techniques. This research exploits the potential of SLM in creating highly complex porous architecture that offers $-\upsilon$ while matching the stiffness of the tibial bone to avoid stress shielding. The powder feedstock for SLM was cobalt-chromium-molybdenum (CoCrMo) superalloy due to its high strength, stiffness and biocompatibility as a bulk material.

1.3. Problem statement

The primary concern when developing scaffolds for load-bearing tissue engineering is to closely replicate the structural performance of natural tissue. A multitude of design and fabrication challenges are required to be considered for the development of a successful tissue engineering scaffold. From a mechanical property standpoint, the strain behaviour of the porous architecture and the bulk stiffness of the scaffold should be a close match to the host tissue. Therefore, if the target tissue is auxetic in parts, an auxetic scaffold would most closely match the properties of this tissue. The matching of this characteristic would be beneficial in recreating the mechanical loading environment that cells would naturally experience. Although studies on the

development of auxetic scaffolds from a tissue engineering perspective are being increasingly documented, these are limited to non-load-bearing tissues where a stiffness match is often not required. In any case, studies on stiffness matched auxetic scaffolds suitable for critical size bone defects are yet to be reported. As such, this thesis explores the development of cobalt-chromium-molybdenum (CoCrMo) porous auxetic scaffolds that can mimic the stiffness of a host tibial section.

Additive manufacturing (AM) is widely considered the targeted technology that will enable the mass customisation of tissue engineering scaffolds and implants. In this regard, the thesis further explores the suitability of selective laser melting (SLM) additive manufacturing as a key enabling technology for the on-demand creation of stiffness matched auxetic scaffolds. Although not auxetic structures, previous studies by Hazlehurst *et al.* [32] have demonstrated that CoCrMo porous cellular structures manufactured using SLM as having comparable mechanical properties to that of bone reducing stress shielding. The thesis builds on these previous studies through conceiving porous architecture that can offer $-\upsilon$ while offering elastic modulus (E) close to bone which is direction yet to be explored.

The thesis explores the use of auxetic cellular architecture for the design and additive manufacturing of bone scaffolds with targeted mechanical characteristics. Numerical techniques are further employed to evaluate the customisability of porous CoCrMo auxetic scaffolds informed by a multi-criteria decision-making algorithm. The optimisation algorithms are used to explore (i) whether stiffness tailoring of auxetic scaffolds is feasible through manipulation of geometrical parameters? (ii) whether the performance of optimum scaffold architecture can be predicted using FE models? and whether CoCrMo auxetic scaffolds fabricated using SLM show stiffness matching the

host bone?. The mechanical performance and characteristics of CoCrMo auxetic cellular structures manufactured by SLM are not fully recognized. Overall, the design and analysis philosophy conceived in this thesis shows how to alter the mechanical properties of auxetic porous bone scaffolds to achieve targeted mechanical properties, enhancing its potential to be used for the reconstruction of critical size bone defects.

1.4. Research aim and objectives

The overall aim of this research was to propose an auxetic porous architecture for Cobalt-Chromium-Molybdenum (CoCrMo) bone scaffolds that can be manufactured using selective laser melting (SLM). The bone scaffolds should exhibit clinically suitable porosity and offer stiffness configurations that will mimic the host bone section. The bone scaffold designs were justified by the results that were observed when adopting a combination of physical testing and numerical analysis. The final design selection was informed by multi-criteria decision making and design optimisation algorithms.

The thesis aims to develop porous auxetic Cobalt-Chromium-Molybdenum (CoCrMo) bone scaffolds that are optimised to reduce stress shielding manufactured using selective laser melting (SLM).

The following objectives collectively contribute to addressing the aim of this thesis:

1. Evaluate a range of state-of-the-art auxetic porous architectures to identify the most promising auxetic that offer suitable, stiffness, strength and -υ range for bone scaffold application.

2. Characterise the mechanical properties of the range of auxetic scaffold designs to include Poisson's ratio, porosity, stiffness, and strength to inform decision-making based on TOPSIS and AHP algorithms.
3. Demonstrate the use of SLM for the on-demand fabrication of CoCrMo auxetic materials featuring porosity ranges suitable for bone scaffolds.
4. Development and validation of a suitable numerical model using the finite element method to parametrically analyse the influence of design variables on the mechanical performance of the scaffolds.
5. Develop a methodology to identify the most suitable porous auxetic architecture for bone scaffolds by using a multi-criteria decision-making method.
6. Generation of the optimum auxetic bone scaffold that offers targeted porosity, mechanical performance, and criteria-based Poisson's ratio (i) maximum negative Poisson's ratio (ii) Poisson's ratio close to zero.

1.5. Structure of the thesis

This thesis is presented in ten chapters with standalone results, discussion, and conclusion each achieving the respective objectives laid out as follows:

Chapter 1 presents the background; problem statement and research aim and objectives.

Chapter 2 presents the literature review on bone structure, its mechanical properties and other fundamental topics relevant to the research. This is complemented by the latest developments in the field of biomaterials used for load-bearing tissue engineering. All of this is presented within the context of auxetic materials, their characteristic properties and applications within the field of bone reconstruction.

Chapter 3 presents a comprehensive literature review on additive manufacturing, in particular selective laser melting (SLM) of relevant materials and their mechanical properties. This chapter goes on to discuss the limitations and the potential of additive manufacturing within the context of biomedical engineering.

Chapter 4 presents the design and manufacture of the auxetic structures using SLM. The quality of the fabricated samples is evaluated through microstructural analysis informed by Scanning electron microscopy (SEM) data.

Chapter 5 investigates the compressive properties of SLM CoCrMo auxetic cellular structures to inform decision making as to the best auxetic porous architecture suitable. The analysis involves both characterisations of the elastic and plastic performance of the respective cellular structures using Gibbons and Ashby criteria and physical experimental tests.

Chapter 6 evaluates the use of the finite element method (FEM) to predict the mechanical properties of the auxetic porous architecture. The numerical data is compared with physical experimental data for model validation and FEM model optimisation.

Chapter 7 uses the combined TOPSIS and AHP multi-criteria decision-making methods to identify the best auxetic design suitable for load-bearing tissue engineering. Subsequent to these two scenarios are presented for optimisation: (i) for stiffness matching while maximising $-\upsilon$ and (ii) stiffness matching while minimising lateral strain.

Chapter 8 conducts a parametric analysis of the best auxetic design identified for multiple scenarios. Response surface (RS) methodology was used to create the model

by using the Central composite design (CCD) method. The results are used to characterise the influence of the design parameters on the targeted responses of interest.

Chapter 9 uses a multi-objective optimisation method for the prediction of the optimum design under selected scenarios. The corresponding response surface model is used to predict the resulting mechanical properties. The accuracy of these predicts was confirmed through developing a numerical model following a validated finite element approach.

Chapter 10 summarises the key findings of this research and indicates the limitations and future prospects of the thesis.

1.6. Original contribution to knowledge

The original contributions to the knowledge of this thesis are as follows:

This research work pioneered the development of a CoCrMo load-bearing auxetic bone scaffold that can be fabricated on-demand using laser powder bed fusion additive manufacturing. This is the first time an auxetic porous framework in CoCrMo is revealed to achieve stiffness matching to a host bone. The use of numerical decision-making and optimisation tools to generate scenario-based auxetic bone scaffolds for targeted porosity, mechanical performance and negative Poisson's ratio is also demonstrated. Ultimately, this thesis offers a new direction in the development and optimisation of load-bearing auxetic bone scaffolds for tissue engineering applications supported by the following eight specific original contributions to knowledge.

I. The thesis reveals the mechanical properties of a range of auxetic CoCrMo porous architecture featuring suitable porosity that can be additively manufactured on-demand are presented.

II. The thesis exposes the limits of theoretical criteria and finite element modelling in predicting the mechanical properties of SLM CoCrMo auxetic bone scaffolds.

III. A validated finite element modelling approach that can predict the mechanical performance of SLM CoCrMo auxetic bone scaffolds is presented. It is demonstrated that the model offers a good agreement with experimental test data.

IV. The combined use of TOPSIS and AHP multi-criteria decision-making tools to identify optimum auxetic bone scaffolds under targeted physical scenarios is demonstrated.

V. The parametric influence of strut thickness and auxetic angle on the mechanical performance of -υ CoCrMo bone scaffolds are revealed.

VI. A response surface model suitable to predict the mechanical performance of SLM CoCrMo auxetic bone scaffolds informed by a central composite training algorithm is described.

VII. An optimum auxetic CoCrMo bone scaffold that can achieve targeted mechanical properties while offering similar stiffness characteristics to human tibia bone is developed and validated.

VIII. The thesis demonstrates the use of laser powder bed fusion to conceive and manufacture auxetic bone scaffolds with targeted stiffness and porosity in a CoCrMo superalloy.

The above statements collectively contribute to the body of knowledge on the performance, characterisation, and fabrication of auxetic bone scaffolds that can achieve targeted mechanical performance.

Chapter 2

Bone scaffolds and the emergence of auxetic biomaterials for tissue engineering

2.1. Introduction

This chapter provides an in-depth literature review regarding human bone tissue, bone scaffolds for tissue engineering, implantable biomaterials and auxetic materials. The chapter starts by introducing the anatomy and mechanical properties of the bone, followed by the bone remodelling and healing process. This is followed by a critical review on the requirement of biomaterial characteristics required for bone scaffolds. The chapter is concluded with a review on bone failures, the role of bone scaffolds in their repair and the significance of auxetic materials in bone tissue engineering.

2.2. Bone

2.2.1. Tissue composition

Bone tissue is primarily made up of collagen and calcium phosphate. Collagen is a smooth protein, and calcium phosphate is the component that hardens the structure [33–35]. The collagen and calcium mix keeps the bone sturdy and resilient enough to survive loading. There are over two hundred bones with a wide variety of geometric configurations in the human skeletal system. These rely on variables, such as skeletal location, physiological activity, age, and gender.

The bones and teeth comprise more than 99% of the body's calcium, and the remaining 1% is contained in semen [34]. The overall structure of the bone can be primarily characterised by two parts referred to as the cortical and trabecular bone, as shown in Figure 2.1. The cortical bone is strong and robust and shapes the bone's exterior layer. The internal framework of the bone is made up of trabecular bone and has a spongy, honeycomb-like composition.

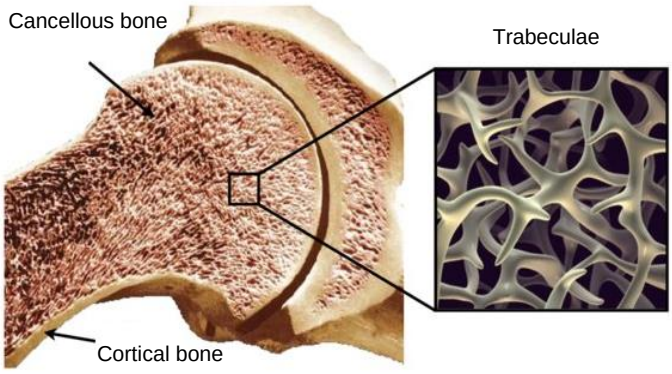

Figure 2.1. Anatomy of a tibial bone section showing outer and inner bone section [36]

Besides water, bone comprises inorganic and organic phases as a matrix. The percentages of these materials range from 40, 35 and 25%, individually. The inorganic process accounts for 60 to 70% of the weight of the bone, consisting predominantly of a crystalline mineral referred to as non-stoichiometric hydroxyapatite ($Ca_{10}(PO_4)_6(OH)_2$) [37]. The scale of apatite crystals differs in thickness from 2-10 nm and width over 15-30 nm by a rod-like (or else, in the shape of a plate) shape relying on the position of crystals within collagen fibrils (larger) or inside the trimmings of collagen fibrils (smaller).

Different diseases and treatments often influence the scale of the particle and the crystalline nature of the bone mineral regarding the degree of structural order [37]. In the case of diabetes and Paget's disease, crystal size was observed to be reduced

but enhanced in osteoporotic entities. Bone strength is influenced by shifts in the form and scale of the Hydroxyapatite (HA) crystals [38]. The HA present in the bone is non-stoichiometric as the apatite crystals produce replacements for calcium ions such as potassium, magnesium, strontium and sodium, chloride and fluoride for the hydroxyl groups and carbonate for the depleted groups [39].

The particle sizes and non-stoichiometry of the apatite crystals provide the mineral stage with the bioavailability desired for osteoplastic bone restoration. Woodard (1962) [40] assessed the human cortical bone concentration of focuses aged between 5-72 years old and discovered that the Ca/P molar ratio varies from 1.37 to 1.71 based on age, with infants and the elderly having the lowermost values [8]. However, there was no connection between the Ca/P molar concentration in the mineral process of the bone in addition to the age or gender of humans in other researches performed [33].

The organic portion accounts for 25-30% of the bone mass and consists of around 90% in collagen, a natural polymer. Type I collagen is formed by osteoblasts and accumulated to create mature (lamellar) bone-in perpendicular or transverse concentrations [41]. The mineral particles add hardness to the composite framework, while ductility and resilience are given by the collagen. Non-collagenous proteins govern the production of collagen and the volume of fibrils, mineralisation, and attachment of cells. Water is found in particles of cells, oils, collagen and bone mineral-apatite, comprising a residual 10% of bone weight [35]. It leads to the attachment of collagen to the mineral phase. Eventually, in the bone matrix, although in limited concentrations, growth factors and neurotransmitters are also present. They play an effective function in controlling the development, stimulation, and segregation of bone cells, as well as connecting bone formation and periodontal ligament mechanisms [35].

2.2.2. Bone Structure

Bone tissue is arranged in an ordered way, referring to its mechanical position in the body's protection and movement, as well as to its other functions [42]. Over multiple stages of hierarchy, the tissue's material properties shift [43]. To recognise its behaviour, bone tissue must also be analysed on different scales, which is critical for deciding the required design criteria for material replacement [8]. The hierarchical structure of bone may be separated into separate groups depending on the size, as shown in Figure 2.2.

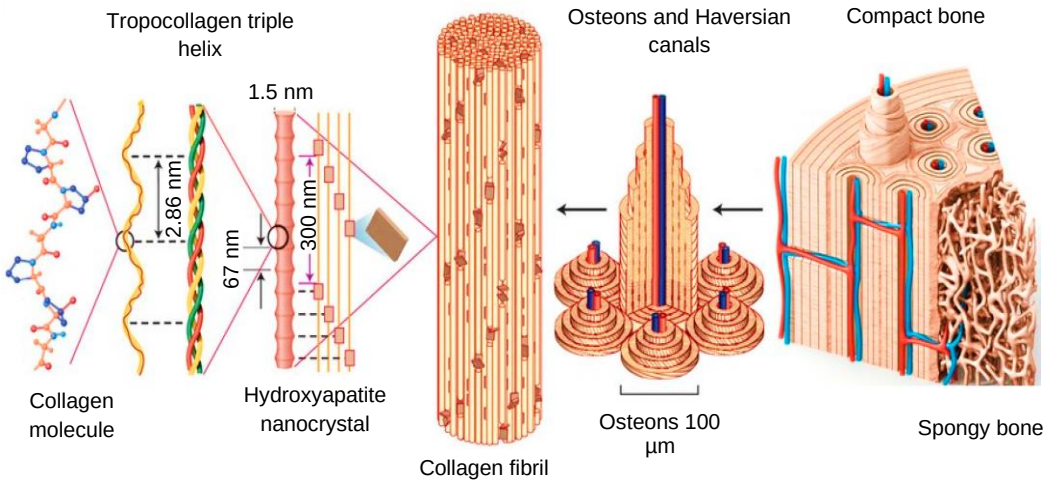

Figure 2.2. Hierarchical architecture of bone tissue ranging from macro, micro, and nanoscale. Bone has a comparatively dense cortical bone that contributes significantly to load-bearing and an inner trabecular or spongy bone composed of hierarchical Haversian systems or osteons that feature a complex nanoarchitecture of collagen fibrils [44–46]

At the macroscopic stage, appropriate to the specific functional or physiological requirements and its position, the bone is categorised into cortical (compact) bone or cancellous (trabecular or spongy) bone. The cortical bone defines as a thick substance made up of Harversian structures that are proven to survive mechanical shocks, thereby supplying the skeleton with both support and protection [8]. In the shape of canaliculi, osteocytes, and connective tissue, it has a medium porosity of over 3-5%,

but it rises with age and osteoporotic modifications to the skeleton. The cortical bone accounts for 80% (wt.) of the overall skeletal mass in humans. The rivets of the positive and negative frames (diaphysis) across the cancellous bone of the intervertebral disc is at the edges (metaphysis) of the long bones along the circumference of the iliac and in the skulls [8]. The density of the cortical bone shell on the outermost layer differs from tenths of a millimetre (in the vertebrae) to a number of millimetres or even centimetres (in the mid-shaft of the vertebral bodies). In comparison, the thickness of the flaps in the bone tissue varies from 100-300 µm.

2.2.3. Mechanical properties of bone

Bone can be classified as a natural material, which has a basic stress-strain relationship, but its strength varies with the sex, age, location, and the orientation of the load. The mechanical and physical properties of bone establish the essential parameters for the creation of scaffolds with acceptable properties for load-bearing. The capacity of the bone to resist fracture (or the general strength of the bone) is calculated by a variety of variables, including density, mass concentrations and other structural properties of the bone matrix. Regulated factors, such as the type of load (tension, compression and shear), pressure frequency and molecular structure of the bone, also influence the characteristics of a scaffold [8]. The compressive test, three-point bending test and the uniaxial tensile test have been conventionally used to measure the properties of bone. But now, different techniques such as nano-indentation and ultrasound are being used due to less material requirements and can measure directional effects [47].

Cortical bone is shown in Figure 2.1. has a dense structure leading to high compressive and tensile strength, as shown in Table 2.1. However, the bending and

shear strength along the longitudinal direction of a bone are comparatively lower. Cortical bone can resist higher ultimate stresses in comparison to cancellous bone. However, due to the high stiffness of the cortical bone, it tends to be more frangible than cancellous bone [12]. Although lower than cortical, the strength of cancellous bone is higher in compression than tension and lowest in shear, and these elastic and strength properties vary with apparent density [48].

Table 2.1. Mechanical characteristics of cortical and cancellous bone [8]

Properties	**Cortical bone longitudinal direction**	**Cortical bone transversal direction**	**Cancellous bone**
Compressive elastic modulus (GPa)	17-20	6-13	0.1-5
Tensile strength (MPa)	79-151	51-56	10-20
Compressive strength (MPa)	170-193	133	7-10
Yield strength in compression (MPa)	131-224	106-131	21.3
Fracture toughness (MPa$\sqrt{\boldsymbol{m}}$)	2-12	2-12	0.1

2.2.4. Bone remodelling theory

The complex mechanism where old bone renewed is called bone remodelling. Bone remodelling is a major factor to consider while developing load-bearing bone scaffolds. Due to the vascular structure of the bone, it reacts to hormonal and mechanical signals, allowing it to adjust to the environment it is in, and as a result, it modifies its mass and structure to withstand the mechanical loading it is being subjected to [49].

According to Wolf's law (1986) [50], bone is designed to adjust to various mechanical loading that causes stress in its arrangement. As such, these mechanical forces are of utmost importance in bone formation and resorption. It happens due to the action of osteoclasts and osteoblasts, which are responsible for aged bone resorption and

new bone formation, respectively. The full period of bone remodelling comprises activation-formation sequences, all directly connected and coordinated at the basic multicellular unit (BMU) [51].

Resorption, reversal, and formation are the three steps that make up the remodelling cycle. In the resorption phase, osteoclasts begin eroding the bone matrix and forming Howship's lacunae on the surface of the bone [50,52]. Osteoclasts are large, multicellular organisms that are typically located as a consequence of their own resorptive behaviour in interaction with a calcified bone surface and inside pits known as Howship's lacunae [8]. New osteoclasts are continually recruited to the remodelling site to switch the dead osteoclasts or to sustain the prevailing cells during this process. There is a reversal period after osteoclastic resorption is complete when mononuclear cells emerge on the bone surface. Those cells offer signals for osteoblast differentiation and migration, as well as formulating the surface for fresh osteoblasts to initiate bone formation. Osteoblasts lay down bone till the resorbed bone is entirely substituted by a different bone in the formation stage [50].

2.2.5. Fracture and healing process of a bone

A bone fracture is a partial or complete break in the continuity of bone tissue as a result of high impact force or stress or medical conditions such as osteoporosis, osteopenia, bone cancer [8]. They are classified as either open or closed fractures. An open fracture is, also known as compound or complex fracture, is one in which the skin is ruptured or has an open wound near the shattered bone. And closed fracture, also known as a simple fracture, is a broken bone without penetrating the skin. There is a high risk of infection in open fractures due to the open wound [53].

The most often broken long bones in the human body are the femur, tibia, and humerus [54]. High energy trauma is the most common cause of long bone fractures, which is known as comminuted fractures. A comminuted fracture means the bone is broken into two or more pieces. This type of fracture is more difficult to heal and might result in permanent deformity of the wounded part [8].

The healing of a fracture is one of the most amazing of all the body's repair processes since it results in the physical reconstruction of the wounded tissue is, something extremely similar to its original shape rather than a scar. Fracture healing usually takes 6-8 weeks and results in complete restoration of the function and architecture of the shattered bone [8].

Long-bone fracture repair can be split into two categories: primary (direct) healing and secondary (indirect) healing. Primary bone healing occurs when the ends of the bones are compressed close together, and there is no mobility between them. It generally only happens after surgery, and the fracture ends have been repaired tightly with plates and screws [55]. The action of osteoclasts and osteoblasts joins and heals the bone ends [56]. Secondary bone healing occurs when the body responds to an injury by ejecting fibrous or scar tissue between the ends of the bones. Fibrous tissue forms and grows with time, making the bone ends stiffer and limiting mobility. Scar tissue is transformed into bone when it is stimulated by a small amount of movement. It usually arises when there are micro-motions between the fracture ends, which is frequent following intramedullary nailing and external fixation procedures. Motion enhances this form of fracture healing, whereas stiff fixation inhibits it [55].

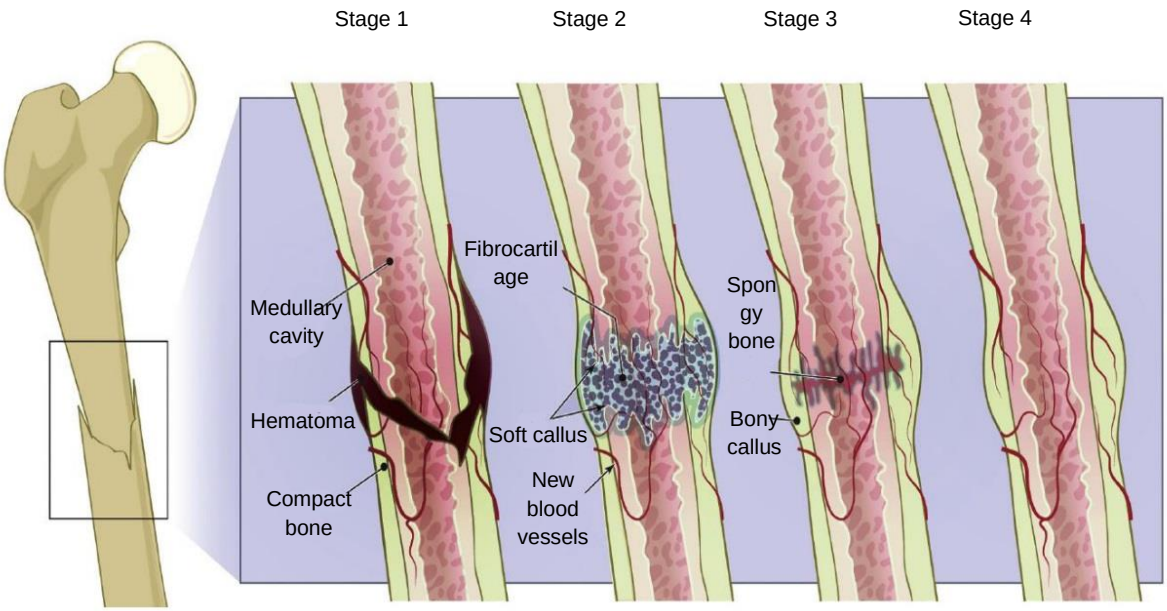

Figure 2.3. Sequences of Secondary Healing Fracture [8]

2.3. Biomaterials

Over the years, the term ‘biomaterial’ has been interpreted in many ways based on the context in which they are clinically applied [57–60]. Traditionally biomaterials were distinguished as a base material other than drugs used to treat, augment, replace or support organs, tissues, or bodily functions [61,62]. However, the newer definition of biomaterials calls for the requirement to have ‘adequate functionality’ for a material to be qualified as a biomaterial [63]. In generic terms, any material that augments or supports living tissues while performing a certain function can be classified as a biomaterial. These biomaterial functionalities may include:

i. Partial substitution or full replacement of tissues and organs.

ii. Enhancement of tissue functions, aesthetics, or biomechanics.

iii. Facilitate tissue integration, provide infection resistance, accelerate healing or diagnosis of tissue damage or disease.

Biomaterials are expected to act as substrates for host tissue integration rather than standalone devices [64,65]. These roles of biomaterial are not only important to facilitate the host tissue functions but also to repair them predetermined interactions. Biomaterial scaffolds for tissue engineering (Figure 2.4a), hybrid meta-biomaterials (Figure 2.4b), and injectable hydrogels (Figure 2.4c) are all examples of new biomaterials that challenges the boundaries of the traditional biomaterials requiring functional classification.

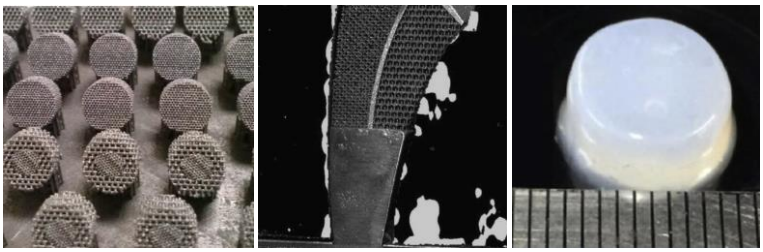

(a) **(b)** **(c)**

Figure 2.4. Examples of emerging biomaterials [66] showing (a) additively manufactured microporous titanium tissue engineering scaffolds [67], (b) hybrid meta-biomaterial for functional hip implants [68] and (c) cylindrical-shaped meniscus-derived injectable hydrogel [69]

2.3.1. Biomaterial types

Biomaterials may be categorised into bioinert, bioactive, and biodegradable based on tissue reaction. Although embedded in the human body, a bioinert substance has limited contact with the underlying tissue [70]. Stainless steel, alumina, titanium, partially stabilised zirconia (PSZ), and ultra-high molecular weight polyethylene (UHMWPE) are examples of bioinert biomaterials. By forming a thin fibrous capsule around the implant, the body communicates with bioinert materials to differentiate it from the host cells, so its bio-functionality depends on tissue incorporation via the implant. Contrastingly, when a biologically active substance is inserted into the body, it allows the achievement of a biological interface that allows

communicating with the tissue at the cellular level, resulting in direct chemical reactions to the bone tissue [70]. Synthetic hydroxyapatite, glass ceramics and bioactive glasses are examples of bioactive biomaterials. In comparison, a biodegradable biomaterial degrades with time, allowing it to be replaced by growing tissue. Biomaterials immediately available for the manufacturing of orthopaedic implants can be broken down into metals and alloys, ceramics, polymers, and composites [8].

2.3.1.1. Polymers

Polymers are materials made of long, repeating chains of molecules. The materials have unique properties, depending on the type of molecules being bonded and how they are bonded. Some polymers bend and stretch, like rubber and polyester. [71]. Polymers show poor electronic and magnetic properties because of the covalent magnetic properties inside the molecules. A variety of influences, including the nature of the base, chemical side groups, chain configurations and molecular weight, affect the thermo-mechanical behaviour of polymers [72].

In biological applications such as contact lenses, medication guidance systems, dental implants, and bone tissue engineering, polymers are an emerging category of biomaterials. Nevertheless, polymers are regularly used in the fabrication of common medical and surgical devices [73]. Polymers are inexpensive to manufacture in comparison to metals and ceramic biomaterials. They still have strong biocompatibility and versatility, offering a range of mechanical strength and structural characteristics [74]. Biodegradable polymers that can degrade within the body either chemically or hydrolytically in a non-toxic manner have also been developed [75]. Protein-based (such as elastin, collagen, gelatine, fibrin, albumin, silk and keratin) and

polysaccharide-based polymers are the main biodegradable materials currently in use [76].

2.3.1.2. Ceramics

Ceramic materials are non-metallic solids that contain complexes of crystalline ceramic and amorphous glass. Ceramics used for the restoration and rehabilitation of diseased or injured sections of the musculoskeletal system are defined by the word 'bio-ceramics.' In biomedical implants such as polymers for orthopaedic, dental implants, and bone fillings, maxillofacial prosthetics, bone scaffolds and alveolar ridge augmentation, bio-ceramics, either thick or translucent, have been commonly utilised [70]. Bio-ceramics are strong, stiff, and biocompatible materials in general but can offer low tensile strength and demonstrate brittle failure modes. Bio-ceramics may be divided into three groups as per their physiological reaction: essentially bioinert, such as pyrolytic carbon, alumina, and zirconia; bioactive, such as HA and bioactive glasses; and environmentally friendly, such as TCP [77].

Bioinert ceramics exhibit both high *in vivo* molecular reliability and low mechanical power. They integrated into the bone tissue when inserted into living bone in conjunction with the 'touch osteogenesis' sequence, thereby creating fresh tissue on the implant surface, enclosed by a non-adhesive envelope of fibrous tissue, without chemically interfering with the implant [78]. They have high fracture toughness and offer excellent corrosion resistance. Due to its strong fracture resilience, zirconia is widely used in the vertebral bodies of complete hip joints, while alumina is being used for orthodontic treatment and hip prostheses for its excellent biocompatibility, reliability and elevated strength and stiffness tolerance.

2.3.1.3. Metals and its alloys

For load-bearing implants such as complete joint prostheses (artificial joints) for elbows, shoulders, knees and ankles, metals and alloys have been commonly used, as well as for prosthetic devices, such as frames, pins, and screws [79]. Examples of titanium used for load-bearing scaffolds are shown in Figure 2.4a and 2.4b. In maxillo-facial treatment, cardiovascular surgery and dental materials, synthetic replacements are most often used.

Table 2.2. Mechanical properties of metallic biomaterials used for load-bearing implants [8]

Material	**Modulus of elasticity (GPa)**	**Yield strength (MPa)**	**Tensile strength(MPa)**
Cortical bone	15-30	30-70	70-150
Stainless steel	190	221-1213	586-1351
Co-Cr alloy	210-253	448-1606	655-1896
Titanium (Ti)	110	485	760
Ti alloy	116	896-1034	965-1103

Metals have tight inter-atomic bonds that, in response to standard compressive strength, offer those decent mechanical properties and impact resistance, so they bend without cracking under high loads. However, under the complex physiological and metabolic characteristics of biological cells, they have poor resistance to corrosion [80]. With the exception of commonly pure titanium, owing to its superior mechanical properties, such as hardness and corrosion tolerance, alloys are more widely used than metallic materials. Common biomaterials used for metallic orthopaedic implants are alloys of titanium, cobalt-chromium and stainless steel of 316 and 316L [81], with the mechanical properties as summarised in Table 2.2.

2.3.2. Biomaterials for scaffolds

To ensure an effective establishment of new tissue, bone tissue scaffolds must comply with different macro and microstructural properties. In tissue engineering applications, there are many other characteristics that are extremely important for scaffolds, such as corrosion resistance and bioactivity [82]. The material characteristics for bone scaffolds without causing any immunological respondents should be well assimilated with the tissue of the host. Biocompatibility gives dominance to tissue engineering over allograft and auto-graft methods, where host disapproval is commonly observed due to inflammatory processes. In order to satisfy as a biomaterial for scaffold fabrication, biomaterial, as well as to help avoid tissue inflammation, any dissolved organic materials or deterioration goods from the scaffold should be biocompatible as well.

The only striking observation of biomaterials from the earlier era was their biocompatibility, while biomaterials of the new class were targeted at bio interactivity. Although the first generation was neutral, the second generation aided in promoting tissue repair. Biomaterials can also be bio-responsive, meaning they may trigger genes to affect all facets of cell growth and differentiation [82]. Inorganic materials and naturally derived or synthetically modified polymers are materials experimented with for bone scaffolds. Composite materials of polymers and ceramics have also been formulated to modify the mechanical characteristic of polymers to exploit their superior potential and maximise tissue interaction.

Metals are one of the oldest biomaterials used mostly for implants [83]. The first documented usage of implantable devices includes aluminium, zinc, gold and silver [83]. Currently, titanium and its alloys are the most commonly used metallic biomaterial for orthopaedic and dental implants due to its biocompatibility, non-toxicity and

strength properties. There is exceptional biocompatibility of commercially pure titanium but comparatively low strength. Thanks to their strong biocompatibility, corrosion tolerance and resilience, metal alloys are introduced as chronic conditions and fracture-fixation implants [83]. Regrettably, metals come with implantable lift, so metallic implants typically need to be extracted, particularly in the case of kids.

The bone scaffold should have qualifying characteristics such as mechanical properties similar to host bone, biocompatibility, blood supply and porosity suited for ingrowth [84]. Additionally, literature saying that the porosity greater than 50% is necessary for complete the bone ingrowth [11]. According to the literature all the previous work has done to achieve those characteristics failed to match the stiffness of the scaffold with the host bone [85,86]. Therefore, high strength (200 GPa) CoCrMo material has been chosen in this research.

Composite scaffolds featuring hybrids of ceramics and polymers, or synthetic polymers with organic polymers, are one of the most promising options [87]. Composite products have a hardness and compressive endurance polymer phase and a bioactivity inorganic phase, which increases functional properties and the frequency of degradation. Sol-gel synthesis is a method that can build a polymeric network with chemical compositions. Their mechanical and physical properties are not quite as strong as the material characteristics of the bone [88]. Every process has various structures, and the best attributes of all kinds should be interconnected by tissue-engineering templates [89].

The three-dimensional biomaterial architecture that promotes the association and differentiation of osteo-inducible cells on their surfaces can be defined as a bone

scaffold. The first experiment on tissue scaffolding was the seeding of cartilage cells on bone spicules by Green at the beginning of 1970 [90]. Seeding cells from functionalised biomaterials on carefully constructed scaffolds have since been proposed for new tissue formation [91]. Both osteoinductive activities and osteoconductive are appropriately predicted from bone scaffolds. Osteoconduction is the mechanism through which scaffolds allow for the longitudinal displacement of osteoinducible cellular materials, such as osteoblasts, mesenchymal cells and osteoclasts, as well as supporting vasculature. However, osteoinductivity relates to the division of cells into osteogenic cells from various lineages [92]. Multiple inorganics and organic, biodegradable, and non-biodegradable materials are being used in the manufacture of bone scaffolds [92]. Each has its own corrosion resistance, resorption and biocompatibility characteristics that influence osteoconduction and osteoinduction.

Tissue researchers are seeking to engineer nearly any human tissue today. Cartilage, bone, heart valves, nerves, intestine, bowel, liver [93] are possible tissue-engineered materials. In general, tissue engineering strategies include the use of a porous scaffold, which acts both *in vitro* and *in vivo* as a three-dimensional framework for initial cellular uptake and eventual tissue creation. The scaffold provides cells with the requisite resources for binding, proliferating, and maintaining their differentiated function. The ultimate form of the freshly grown soft or hard tissue [94] is determined by its design. In the initial periods of regenerative medicine, the product of choice for scaffolds was mostly assumed to be scientifically proven materials such as collagen and polyglycolide. For more sophisticated scaffold systems, the task is to assemble cells/tissue in a suitable 3D arrangement and address structural triggers in a suitable

spatial and temporal manner such that the individual cells expand and shape the appropriate cellular processes and do so in a manner that can be carried out on a wide scale, efficiently and adequately.

2.4. Scaffold characteristics for bone tissue engineering

Tissue-engineered biomaterials for bone either compliments or replace the need for allogeneic/autologous grafts, where the size of repair has significant limitations. The constructs that are currently being experimented with in this regard feature bioactive properties within a metallic [95–97], ceramic [98], polymer [99,100], composites [101,102], or hybrid [103,104] scaffold. However, future bone biomaterials are also expected to decompose sacrificially partly or fully, allowing for replacement by growing tissue throughout the repair. Many examples of this are being experimented [105–108] with Li *et al.* [109] demonstrating AM porous zinc biodegradable scaffolds for tissue reconstruction. For bone tissue engineering using engineered scaffolds, they must meet various macro and microstructural properties to allow tissue ingrowth. As the following characteristics are essential features for a scaffold to suitable for bone tissue engineering.

2.4.1. Porosity and pore size

Porosity, along with pore formation and porous volume, plays an important role throughout the development of bone scaffolds since they influence the distribution of cells within the highly porous and are often essential for the provision of nutrients to grafted and replenished cells [110]. In order to enable bone tissue to expand, scaffolds must be permeable, with accessible and completely intertwined pores and porous sizes varying between 100-400 μm. Porous scaffolds encourage cellular proliferation,

enable considerable growth rates within the framework of nutrients, oxygen and dissolved substances, and facilitate improved vascularisation [110]. Rising porosity, though, will mitigate the dimensional integrity of the scaffold, so it is crucial that the equilibrium between permeability, porosity, pore size and shape are carefully designed.

2.4.2. Biocompatibility

When a material possesses acceptable biocompatibility to meet the requirement of a biomedical application, it can be defined as a biomaterial [111]. Therefore, the qualification of a material as a 'biomaterial' depends on it meeting the biological and chemical comparability required for the targeted application. However, the question then arises; "How can one quantify the biocompatibility of biomaterials for designing medical devices?" In its simplest form, a biomaterial must satisfy biocompatibility, which may be interpreted as an acceptable material functionality without any unwarranted reaction at the tissue level or to the immune systems. If a material satisfies all these requirements, then it can be classified as biocompatible [112–114].

According to Ramakrishna *et al*. [115], tissue engineering biomaterials requires the highest biocompatibility as they are in direct contact with biological tissues and are expected to initiate bio integration processes. Nevertheless, for any material to be deemed biocompatible, it should satisfy the acceptable performance requirements under all categories, as shown in Table 2.3. Based on these assessments, acceptable biocompatibility can be defined as the effect to which the biomaterial does not induce any measurable harm. Put simply, no harm to the host body as a result of the biomaterial defines biocompatibility [61,116].

Table 2.3. Biocompatibility requirement for scaffolds used for bone tissue engineering

Biocompatibility assessments	**Short definition**
Cytotoxicity	Capacity to induce cell or tissue death
Carcinogenicity	Capacity to induce cancer formation
Mutagenicity	Capacity to damage genes
Pyrogenicity	Capacity to induce adverse immune responses such as fever
Allergenicity	Capacity to cause sensitisation and allergic reactions
Thrombogenicity	Capacity to induce blood clotting

2.4.3. Mechanical Properties

Dynamic stresses are needed to grow bone *in vivo*; thus, bone scaffolds must have adequate strength and rigidity to maintain the functional stability and safety of the growing tissues. Biodegradable polymeric scaffolds will show dynamics and tuneable absorption coefficients consistent with cancellous bone [117]. Dense ceramics such as HA and TCP, on the other side, show strength development and elastic modules comparable to human cortical bone, but they are fragile, and deterioration levels are low. The compressive strength of bone differs widely from cancellous to cortical bone, as described above [117], as shown in Table 2.1. Therefore, it becomes important to develop a porous architecture that mimics the stiffness (elastic modulus E) of the tissue the scaffold replaces. Studies have shown that the mechanical characteristics of a scaffold can be customised by manipulating the structure, size and shape of the porous architecture.

Table 2.4. Parameters suitable to characterise the mechanical performance of a biomaterial

Material properties	**Equivalent meaning**	**Units**
Young's modulus ($\boldsymbol{E}$)	Stiffness Elastic modulus	$\boldsymbol{N/m^2 \ \ or \ Pa}$
Yield strength ($\boldsymbol{\sigma_y}$)	Elastic limit	$\boldsymbol{Pa}$
Ultimate strength ($\boldsymbol{\sigma_{ult}}$)	Strength Failure stress Stress at fracture	$\boldsymbol{Pa}$
Strain at rupture ($\boldsymbol{\varepsilon_{max}}$)	Extensibility Failure strain	-
Poisson's ratio ($\boldsymbol{v}$)	The ratio of transverse contraction strain to longitudinal extension strain	-
Hardness	Resistance to wear	Rockwell hardness (HR) Brinell hardness (BR) Vickers hardness (HV) Knoop hardness (HK)
Toughness ($\boldsymbol{U_T}$)	Energy to break per unit volume Energy to break per unit area	$\boldsymbol{J/m^3}$ $\boldsymbol{J/m^2}$
Modulus of resilience ($\boldsymbol{U_r}$)	Energy to yield per unit volume	$\boldsymbol{J/m^3}$
Fracture toughness ($\boldsymbol{K_{IC}}$)	Capacity to resist crack growth	$\boldsymbol{Pa\sqrt{m}}$
Fatigue life ($\boldsymbol{N_f}$)	Durability	Number of cycles to failure

The opportunities that emerging biomaterials offer for structural optimisation asks the question: "what are the best mechanical properties that a biomaterial can offer? Generally, an ideal biomaterial mimics the mechanical behaviour of the biological tissue that is being replaced [118]. Researchers commonly use a wide variety of terms when it comes to describing the mechanical performance of tissues, biomolecules, and biomaterials. These terms fall within the domain of mechanics of materials and materials engineering in general [119]. However, the methodology cannot be broadly

applied to select the biomaterial that offers the highest strength and biocompatibility. It is important to first determine the required parameters that constitute all the relevant parameters for each of the requirements and how to control them. This is because what may seem like a suitable material under quasi-static loading may fail in other areas post-implantation. In this regard, it may turn out that for the loading scenario, a slightly weaker material with superior hardness may be the most suitable [120]. Since these terms may not be easily understood by researchers or practitioners in other fields, Table 2.4 summarises a simpler set of meanings for the mechanical parameters for importance.

2.4.4. Biodegradability

Another essential element for scaffolds in the recovery of bone tissue is biodegradability. In order to allow room for new tissue to expand, an optimal scaffold should dissolve *in vivo* at a regulated irradiation dose so that the rate of degradation is close to new bone formation [121]. The scaffold's deterioration behaviour can differ as per their applications. Scaffolds used in spinal fusion, for instance, should take 9 months or more to crumble, whereas scaffolds used in craniomaxillofacial implementations should take 3 to 6 months to degrade [121]. The rate of deterioration may typically be adjusted by adjusting either the structure of the monomer or the method of producing the scaffold.

2.4.5. Upcoming trends in bone scaffolds

Conceptually solid scaffolds have been identified as binary configurations of polymer/ceramic, metal/ceramic composite materials or polymer/metal, but they have not yet fit the initial bone tissue [92]. Given the poor molecular structure of polymeric,

ceramic, and composite biomaterials, as well as the absence of metal corrosion resistance, only a well-orchestrated particle acceleration build consisting of all biodegradable polymers can be an ideal scaffold for biomedical applications. In designed to account for material characteristics, the centre of such an ideal system should be composed of a ceramic-coated biocompatible alloy. An osteoinductive composite filled with proper growth factors could be the next step. Biomolecules such as collagen and/or gelatine may be used to render secondary structures. It is also important to recognise matched porosity with modified pore sizes that allow angiogenesis [92]. The next wave of scaffold/prosthesis combinations would be the ones featuring metallic centres with bioactive and biodegradable coatings. These scaffolds will be load-bearing while decaying in a timely manner, while the metallic component will survive in the body for longer without inconveniencing the functional integrity of the bone.

2.5. Failure and wear of bone scaffolds

The failure of a bone scaffold can be initiated by mechanical failure of implanted components or through the failure of fixation, and surgical problems such as blood clots, infections and nerve damage can be involved. But mechanically reason for failure can be the loosening of the implant. It can be caused by implant wear debris and through the stress shielding effect.

2.5.1. Wear debris

Osteoblasts are the main cellular component of the bone which responsible for bone tissue formation, and they perform a substantial part in aseptic loosening. The formulating movement of the implant causes wear debris to be generated via fretting

and fragmentation [49]. Zhang *et al.* [122] concluded that the wear particle exposure from *in vitro* models to osteoblasts results in the obstruction of multiple cellular functions. Due to this reaction indirectly contribute to osteoclastic bone resorption and release chemical and enzymes into the human body. These chemicals and enzymes can affect the failure of the bone and result in the loosening of the implant [122].

2.5.2. Stress shielding

Stress shielding is a condition common with all types of joint arthroplasty and is extremely prominent in the repair of hip and knee load-bearing joints [123]. The load shift to the proximal femur is decreased following Total hip arthroplasty (THA) when femoral stems are implanted with a marginally greater density than the bone. Thus, half of the load that was historically entirely borne by the bone is carried by the femoral stem [124]. This allows the tension distributed in the residual host bone to reduce, which means that the peri-prosthetic bone is insufficiently filled and does not remodel. In this case, stress shielding will eventually impact THA's survival and thus encourage any requirement for surgical intervention. Stress protection can also lead to THA's premature loss by stem mobility and peri-prosthetic bone fractures [49].

The mismatch of elastic modulus between scaffold implants and bone tissues is critical in managing stress shielding. The current implants and scaffolds clinically used do not provide stiffness matching leading to nonhomogeneous stress transmission between the implants and surrounding bone tissue [125]. This causes the bone tissue to deteriorate and lose its load-bearing capacity, leading to osteoporosis and fractures surrounding the implants [126]. Apart from bio-inspired morphologies, the effective design of load-bearing scaffolds is required to match the mechanical characteristics of the host bone tissues to avoid stress shielding. Although gradient geometric design

can reduce the stress shielding phenomena by lowering the relative density and stiffness at the scaffold-tissue interface, this can only solve the problem partially [127].

2.6. Stiffness and strength in bone scaffold design

For bulk material, the stiffness and strength correspond to material properties such as Young's modulus (E) (also known as elastic modulus) and the yield strength (σ_y). However, for a porous material at the microscopic scale, this is influenced both by the properties of the bulk material and the porous architecture. In general, the relative density of a porous structure can control its mechanical properties. Gibson and Ashby's [128] models are the most common estimation tool for the mechanical properties of a porous material that is made up of repeating unit cells. This has been demonstrated by earlier works by Gibson and Ashby (1997) [129] have provided simple foam structure to demonstrate the relationship between elastic modulus, yield strength and relative density, as shown in Equations (2.1) and (2.2), respectively [130]:

$$\frac{E_S}{E_B} = C\left(\frac{\rho_S}{\rho_B}\right)^2 \tag{2.1}$$

$$\frac{\sigma_S}{\sigma_B} = C\left(\frac{\rho_S}{\rho_B}\right)^{\frac{3}{2}} \tag{2.2}$$

where E_S, ρ_S is the elastic modulus and density of the cellular structure, E_B , ρ_B elastic modulus and density of the fully dense solid material. C is a constant depending on the material and the cell geometry [49]. When it comes to the strength of the porous architecture, σ_S, σ_B are the yield strength of the cellular structure and the fully dense solid material respectively [49]. The Equations (2.1) and (2.2) are useful in analytically predicting the stiffness and the strength of the cellular structures at the design stage [131].

2.7. Auxetic materials

2.7.1. Introduction to auxetic materials

Auxetic materials have unique architecture that results in distinct deformation characteristics [17]. Although materials deform differently, the vast majority of materials behave conventionally, meaning they expand axially under tension while contracting in the transverse direction, as shown in Figure 2.5a. The ratio of transverse strain to axial strain gives a measure of how a material deforms under load, which is known as Poisson's ratio. A material that expands axially but contracts transversely in response to a tensile force (Figure 2.5a) or expands transversely while contracting axially under compressive force has a positive Poisson's ratio (PPR). Material that displays auxetic behaviour, on the other hand, expands in the axial and one or more orthogonal directions under tension and has a negative Poisson's ratio, as shown in Figure 2.5b. Under compressive forces, auxetic materials contract both axially and transversely.

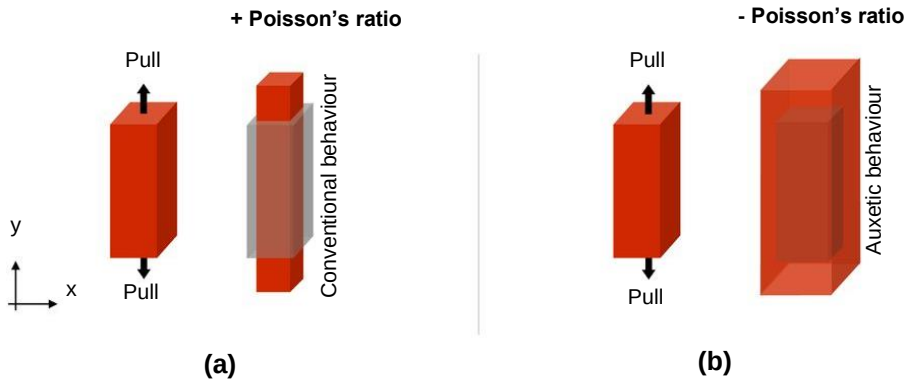

Figure 2.5. Deformation of materials showing (a) behaviour of a conventional material resulting in positive Poisson's ratio and (b) showing auxetic materials resulting in negative Poisson's ratio. Adapted from [132]

The Poisson's ratio of a material can be calculated by using the equations below:

$$\varepsilon_y = \frac{\Delta y}{y_0} \tag{2.3}$$

$$\varepsilon_x = \frac{\Delta x}{x_0} \tag{2.4}$$

$$\upsilon_{yx} = -\left(\frac{\varepsilon_x}{\varepsilon_y}\right) \tag{2.5}$$

where ε_y, ε_x are the longitudinal and lateral strain of the cellular structure, respectively, Δy , Δx change in length and width of the cellular structure, respectively. $y_{0,}x_0$ are the original length and width of the cellular structure, respectively. υ_{yx} is the Poisson's ratio of the cellular structure.

2.7.2. Auxetic structures

The growth of auxetic materials has been largely centred around foams and materials featuring repeating unit cells, such as honeycombs [133]. Cellular materials have been used for the creation of advanced materials in a wide range of applications, spanning from re-entrants to maladjusted 3D structural foam networks [8]. Some major auxetic architecture includes the ones featuring re-entrant 2D and 3D cellular elements, chiral frameworks and revolving units [77,134].

2.7.2.1. Re-entrant structure

Due to its effectiveness, understandability, and capacity to generate high $-\upsilon$, the re-entrant honeycomb framework has been extensively studied among other structural architectures, which demonstrate improved mechanical properties and options for many implementations [77,135]. Under uniaxial pressure, the structure can enlarge in all directions and diminish in all positions under uniaxial tension when sufficient cell

measurements and re-entrant angles in the auxetic structure are selected [136,137]. The re-entrant frameworks will be the simplistic honeycomb system, as seen in Figure 2.7, indicating auxetic characteristics among other frameworks.

Figure 2.6(a) shows the double arrow-headed structure [138], which shows auxetic behaviour while opening and closing the arrowheads. The arrangements in Figure 2.6(d, e, f) show the auxetic effect due to hinging under uniaxial load or/and strut flexure. Due to the structural symmetry of hexagonal honeycomb Figure 2.6(c), it shows better planar isotropic properties than the standard 2D re-entrant structure.

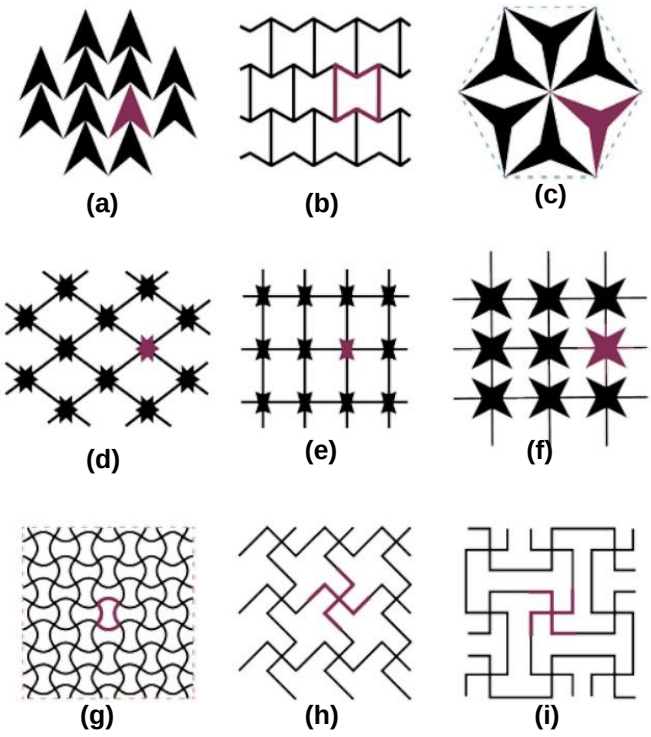

Figure 2.6. 2D re-entrant auxetic structures [139] where (a) refers to double arrow-headed, (b) 2D re-entrant honeycomb, (c) structurally hexagonal re-entrant honeycomb, (d-f) interconnected stars, (g) sinusoidal lattice, (h) lozenge and (i) square grids

Figure 2.6(g) sinusoidal ligament shows its auxetic behaviour by the opening of re-entrant cells into almost rectangular cells. Because of the extension and rotation of each side in the unit cells, the structure shows the auxetic effects. The structure of

square grids, as shown in Figure 2.6(i), exhibit a higher auxetic effect than the structure Lozenge in Figure 2.6(h) under the same strain according to the analysis by Smith *et al.* [133].

Figure 2.7 shows the honeycomb deforming by hinging of the diagonal struts in response to an applied uniaxial load. The orientation of the diagonal struts along the horizontal direction of applied stretch causes the struts aligned along the vertical direction to move apart, thereby reporting the auxetic effect [140]. But the, most honeycombs of this type deform mainly by flexure of the diagonal struts, with hinging and axial stretching of the struts also occurring at the same time [141].

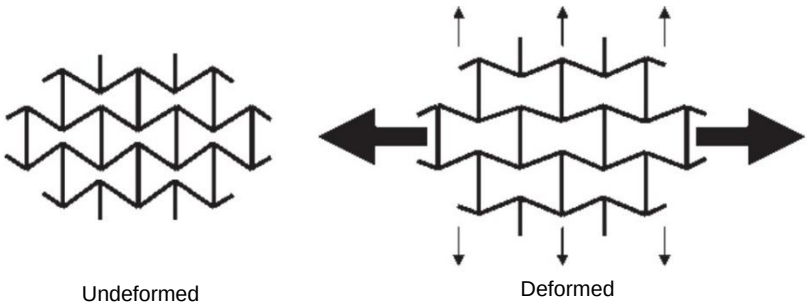

Figure 2.7. 2D re-entrant honeycombs with undeformed and deformed (response to applied horizontal stretching) [141]

2.7.2.2. Chiral structures

A substance that is not superimposed over its mirror reflection or a molecule accompanied by special groups bound to it is the definition of a chiral [142,143]. Chiral honeycomb has in-plane rigidity sharply out of plane bearing ability and rule than conventional honeycombs [144,145]. One of the auxetic systems containing nodes and ribs that are proportional to the nodes is the chiral system. A rectangle, circle or some other geometrical shape can be the node [146]. The latest study has shown that

the auxetic influence of the chiral system has increased substantially by incorporating soft hinges and stronger cores [128,147].

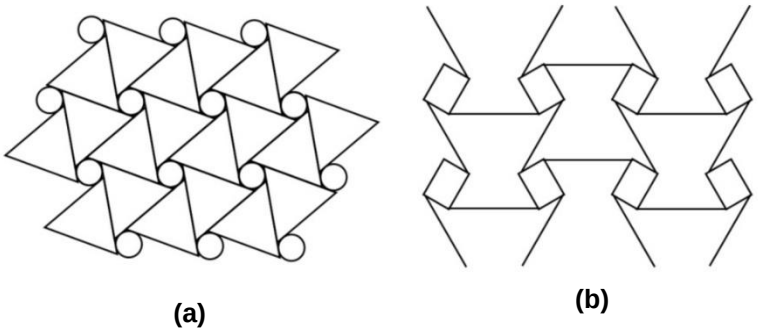

Figure 2.8. Chiral structures (a) Chiral honeycomb (b) Chiral honeycomb with symmetrical units [3]

Figure 2.8 shows the chiral honeycomb structures by connecting straight ribs to central nodes [148,149]. The rotation of the nodes provides the deformation mechanism of the structure. If all the nodes rotate in the same direction, these structures are referred to as chiral, and if the nodes rotate in both clockwise and anti-clockwise directions, it is called anti-chiral [144]. The auxetic effects are achieved through wrapping or unwrapping of the ribs around the nodes in response to an applied force, as shown in the above figure [139].

2.7.2.3. Rotating units

Rotating unit systems are formed by the configuration of uniform, shape or varying sizes units joined at the vertices, and the vertices may be hinged or bound by springs [150,151]. Furthermore, these constructs have been formed by connecting the rigid or semi-rigid squares, triangles, rectangles and tetrahedrons, as seen in Figure 2.9. These configurations were first established by Grima and Evans [152] in synthetic crystalline solids and then suggested alternating triangles, rectangles, and squares

[151]. Units can rotate to expand to accomplish auxetic behaviour when the structure is extended and reveals the $-\upsilon$ influence [153].

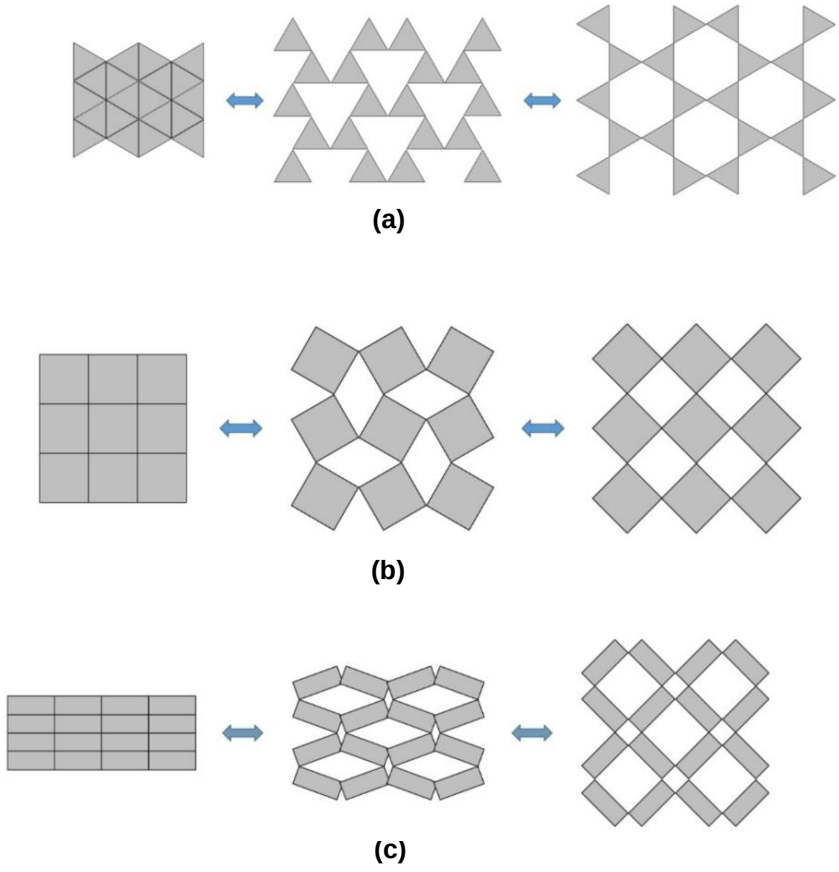

Figure 2.9. Rotating unit models (a) Triangular units (b) Square units (c) Rectangular units [3]

The perfect model of rotating squares with rigid units was found to be independent of the initial geometry and the loading directions, with Poisson's ratio shown to be -1. So, it was too simplistic to characterise the deformation of uniaxial extension [154].

2.7.2.4. Nodule and fibril structures

As shown in Figure 2.10, a simple 2D model will explain the different types of microstructure and the auxetic microporous polymer first generated by Caddock and Evans [155]. This framework comprises nodules and fibrils that are entangled. The

fibrils induce lateral nodule translation when a tensile load is applied, contributing to a strain-dependent negative Poisson's ratio [156].

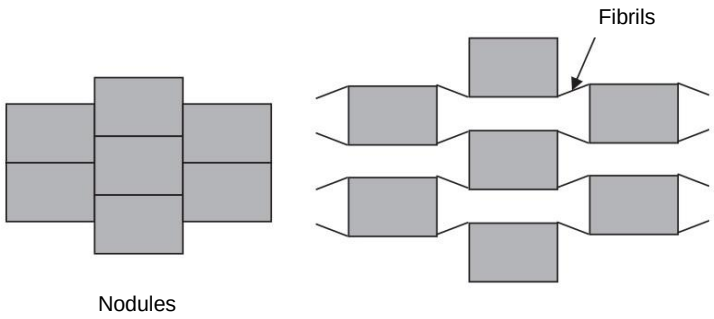

Figure 2.10. Nodule and Fibril structure [132]

In a 3D model, there are not just the 2D nodule and fibril recommendations based, and according to the previous innovative studies, these 3D hexagonal models display higher $-\upsilon$ impact than the 2D models. In addition, it is necessary to extend these 3D nodules and fibril frameworks to materials such as body-centred cubic metals and foams and extended micro-porous polymers through off effects [156,157].

2.7.3. Properties of auxetic structures

2.7.3.1. Elastic and shears modulus

Auxetic materials show excellent mechanical properties due to the negative Poisson's ratio effect. These properties include plane stress fatigue resistance, shear modulus, and indentation resistance [158]. Hypothetically, the Poisson's ratio assumes values between -1 and 0.5 for the isotropic 3D materials and -1 to 1 for the isotropic conjugated polymers, but the Poisson ratio varies from $-\infty$ to 0 for anisotropic materials [47]. It can be argued that the elastic behaviour of a structure regulates the magnitude of Poisson's ratio. Relatively high bending tolerance, fracture ability and

shear modulus can be expected from a well-designed negative auxetics architecture [159].

There are four parameters influencing the elastic behaviour of any material, and they are the elastic modulus (E), shear modulus (G), bulk modulus (K) and the Poisson's ratio (υ). The relationship that describes the elastic performance of a material is as shown in Equations 2.6 and 2.7 [160]:

$$G = \frac{E}{2(1+\upsilon)} \tag{2.6}$$

$$K = \frac{E}{3(1-2\upsilon)} \tag{2.7}$$

Most structural materials are required to have a higher shear modulus than the bulk modulus [161]. The performance of an auxetic structure can be credited to a change in cell geometry controlled by the volumetric compression ratio. Increasing the volumetric compression ratio gives an increase to a relative minimum in Poisson's ratio and decreases the elastic modulus, and show the rise in shear modulus and toughness [162]. That means the material becomes easy to deform volumetrically but difficult to shear due to the increase in shear modulus.

In comparison to traditional materials, Auxetic materials exhibit improved fracture resilience. Auxetic substance stretches and covers the gap as the component is pulled where there is a crack. As a consequence of the persistent volumetric power density of re-entrant fully accessible copper foams, Li *et al.* [163] performed tensile strength tests and observed that the tensile strength of re-entrant foam is greater than that of traditional foams.

2.7.3.2. Indentation behaviour

Hardness is the tolerance of a material to incision, wear, or scratch to irreversible deformation. According to Anurag and Harsha [164], the influence of $-\upsilon$ can lead to increased toughness auxetic structures at the macroscopic level. Generally, auxetic materials show lower stiffness and better indentation tolerance than traditional materials [165], which can be advantageous to reduce stress shielding in tissue engineering.

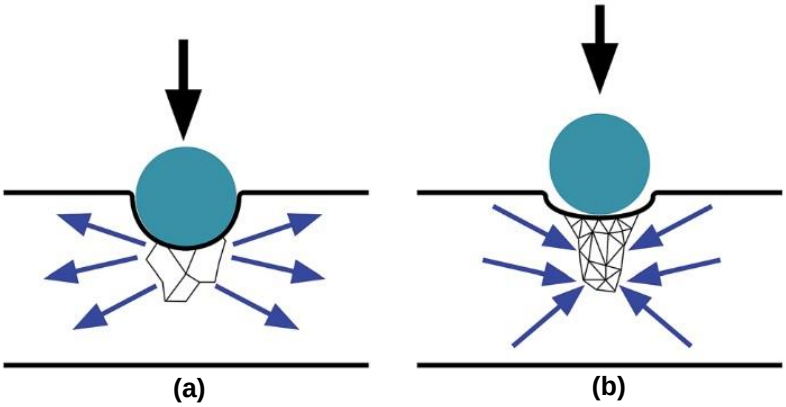

Figure 2.11. Indentation behaviour of (a) non-auxetic (b) Auxetic [166]

As shown in Figure 2.11, as opposed to non-auxetic materials, the auxetic content continues to flow to the stage where the load is added, which produces a region of denser medium and its improved indentation resistance [47,157].

2.7.3.3. Synclastic behaviour

Another interesting characteristic called synclastic activity can be a peculiar behaviour of auxetic materials. This suggests that it has a normal propensity not to form dome-shaped (synclastic) surfaces like traditional materials that appear to exhibit anticlastic activity (saddle shape) when exposed to an out-of-plane maximum deflection

[19,167,168], as shown in Figure 2.12. The material may be brought to the ideal form without a special guide as a result of inherent synclastic behaviour [132].

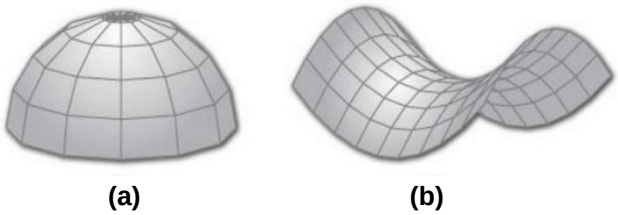

Figure 2.12. (a) auxetic synclastic curvature (b) conventional material anticlastic curvature [169]

2.7.3.4. Variable Permeability

Auxetic materials have unique property, which is able to open pores when stretched, and this feature is considered to have a considerable capability for the various types of filter applications [170]. The unique pore opening characteristic of auxetic material was demonstrated by Alderson *et al.* [171], which offered enhanced filter performance from macro to the nanoscale, as shown in Figure 2.13. Auxetic polymers and structures can improve pore size and shape when increasing pressure or uniaxial stretching. Alderson *et al.* [172], in another study, carried out a glass bead transmission test on auxetic polyurethane foams where the advantages of auxetic materials in mass transportation applications was confirmed.

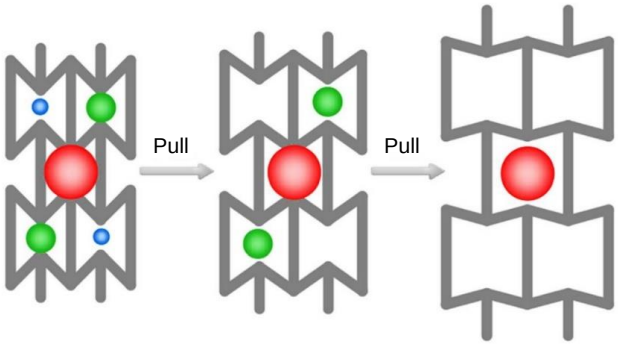

Figure 2.13. Variable permeability application in Smart filters [173]

2.7.4. Auxetic materials and tissue engineering

Tissue engineering is based on the creation of artificial tissue that mimics natural tissue and can be used to enhance or replace biological tissues during the surgical treatment. For tissue engineering to be effective, a variety of aspects and challenges must be considered.

When creating auxetic tissue engineering scaffolds, one of the factors to consider is material selection. There are a variety of auxetic materials that have been developed, including microporous or nanocrystalline metallic, polymer, ceramic, and composites. Auxetic materials that are developed through repeating unit cells that offer targeted functionalities are also referred to as metamaterials [174]. Metamaterials have enhanced and peculiar mechanical properties compared to conventional materials. Auxetic metamaterials are increasingly being investigated for optical, acoustic, energy harvesting and biomedical applications [175]. There are specific microstructures in every auxetic material that leads to creating a -Poisson's ratio ($-\upsilon$). This, in turn, affects the deformation mechanism such as bending, stretching and torsion [17].

Table 2.5. Auxetic structures as a tissue engineering scaffold

Fabrication Technology	**Specific fabrication method**	**Material**	**Cell type**	**Biological effect**	**Ref**
Additive manufacturing	Dynamic optical projection stereolithography	PEGDA	HMSC (Human bone marrow)	Grew on scaffold	[176]
	Dynamic optical	PEGDA	HMSC (Human bone marrow)	Grew on scaffold	[177]

	projection stereolithography				
	Two-photon stereolithography	PEGDA	10T1/2 (mouse embryonic fibroblast)	Unable to divide	[178]
	Dynamic optical projection stereolithography	Polyurethane	10T1/2 (mouse embryonic fibroblast) C2C12 (mouse myoblast)	Grew on scaffold	[4]
	Micro-stereolithography	PEGDA	HTMSC (human turbinate mesenchymal stromal cell)	Proliferation increased on $-\boldsymbol{v}$	[179]
	Fused deposition modelling	Poly($\boldsymbol{\varepsilon}$ –caprolactone)	HUVEC (human umbilical vein endothelial cell) BMSC (bone marrow stem cell)	Adhered and grew on scaffold	[5]
	Fused deposition modelling + electrospinning	Thermoplastic Polyurethane	HTMSC (human turbinate mesenchymal stromal cell)	Grew on scaffold	[180]
Additive manufacturing + electrospinning	Fused deposition modelling	Poly($\boldsymbol{\varepsilon}$ –caprolactone)	HUVEC (human umbilical vein endothelial cell) VSMC (Vascular smooth muscle cell)	Made multilayers	[181]
	Fused deposition modelling + electrospinning	Poly($\boldsymbol{\varepsilon}$ –caprolactone)	-	Attached with the printed scaffold and hydrogel	[182]

Soft lithography	Deep reactive ion etching	Silicon	-	-	[183]
	Deep reactive ion etching	Silicon	HMSC (human mesenchymal stem cell)	Interacted at a sub-cellular level	[136]
Machining	Micro-ablation	Chitosan (polyaniline coating)	Neonatal rat ventricular myocytes and fibroblasts	Grew on scaffold (cytocompatibility)	[184]
Foaming	Compressed foams	Polyurethane	Chondrocytes (primary from cartilage)	Proliferation increased	[185]
	Solvent casting/ salt leaching	HA/PLGA	MG-63 (human osteoblast)	Proliferation increased	[186]
	Solvent casting/ salt leaching	PLGA	MG-63 (human osteoblast)	Proliferation increased	[7]
	Heated foams	Polyurethane and polyester	ES-D3 (mouse embryonic stem cell) iPSK3 (human induced pluripotent stem cell)	Vascular differentiation increased	[187]
	Compressed and heated foams	Polyurethane	ES-D3 (mouse embryonic stem cell) iPSK3 (human induced pluripotent stem cell)	Neural differentiation increased	[188]
Textile	Fabric knitting	Poly(ε –caprolactone)	Human dermal fibroblasts	Cell metabolic activity increased	[189]

2.7.5. Application of auxetic structures for bone tissue engineering

Auxetic structures have potential in the biomedical industry due to their negative Poisson's ratio [190]. Auxetic bone scaffolds, dental implants, neck braces, dilators, cage spacers for spine surgery and the femoral component of the total hip implant are some of the auxetic structural applications that use in the biomedical industry.

Baker [6] showed the potential application of auxetic materials for the reconstruction of intervertebral discs. The work was based on finite element analysis carried out mimicking the L4-L5 motion segment to investigate stress on the intervertebral disc. This study concluded that the use of intervertebral disc with a negative Poisson's ratio would be helpful to prevent disc degeneration disease. The principle is that the decrease in horizontal motion would prevent the impact of nerves by the intervertebral disc. The degeneration of the intervertebral disc [47] is one of the major reasons for causes of low back pain, and most of these cases are related to ageing. Total disc replacement is one of the treatments for lower back pain, and it completely removes the damaged intervertebral disc and replaces it with an artificial disc [77].

Choi *et al.* [7] investigated the use of auxetic PLGA (Poly Lactic-co-Glycolic Acid) scaffolds and their effectiveness in increasing the number of bone cells under compressive stimulation. It was shown that a negative Poisson's ratio architecture would conduct high compressibility in all directions and that scaffold was expected to undergo a rapid increase in the number of bone cells effectively [7]. The scaffold was manufactured using the casting method [191], and a permanent volumetric compression with heat treatment (PVCT) method was used to create an auxetic response from the scaffolds. The resulting $-\upsilon$ was calculated through strain images from the compressed test, as shown in Figure 2.14. The results demonstrated an auxetic response of the PLGA scaffold resulting in an accelerated bone cells response due to the compressive stimulation.

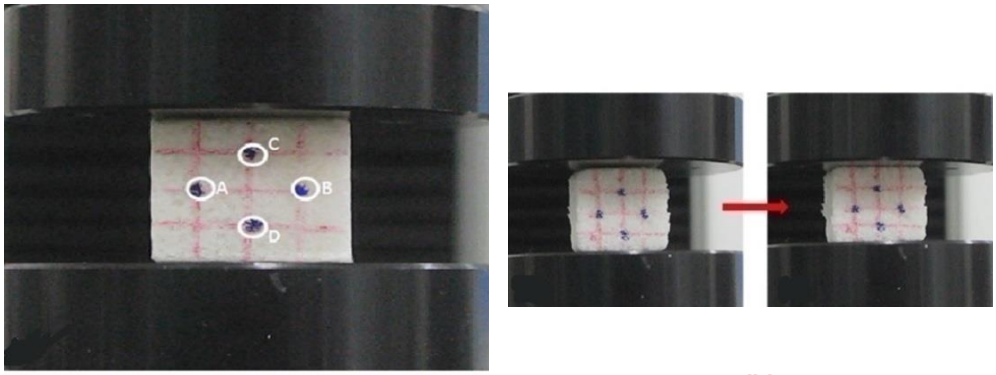

(a) **(b)**

Figure 2.14. Poisson's ratio estimation of PLGA auxetic scaffold where (a) shows the strain monitoring points and (b) the compressed specimen [7]

Abdelaal *et al.* [192] explored the fabrication of auxetic cellular structures for biomedical applications within the context of femoral hip replacement. Due to the mismatching of the stiffness between bone and the implant, the stress shielding phenomenon is common in traditional hip implants resulting in implant loosening. To avoid stress mismatching, it is better to replace an implant that has similar mechanical properties as the host bone. The study showed the potential of a functionally graded auxetic (FGA) polymer structure that shows a negative Poisson's ratio. The study also found that an increase in structure porosity using auxetic architecture leads to an increase in $-\upsilon$ of the structure [192]. This study demonstrates the use of auxetic architecture in hip replacement due to mimicking the bone's stiffness through the use of additively manufactured titanium alloy (Ti6Al4V) [192].

Ghavidelnia *et al*. [193] showed the potential application of 3D re-entrant auxetic structure in femoral hip meta-implant to improve the stress and strain distribution in the implant and surrounding bone tissues, as shown in Figure 2.15. Figure 2.15(a) shows the CAD model, Figure 2.15(b) shows the meshed finite element (FE) model of meta-implant based on 3D re-entrant structure, Figure 2.15(c) shows the meshed assembly of the implant and femur bone model and Figure 2.15(d) shows the applied

load and boundary conditions on the implant and femur bone model The anatomy of the human femur bone was used to design one solid implant and three meta-implants.

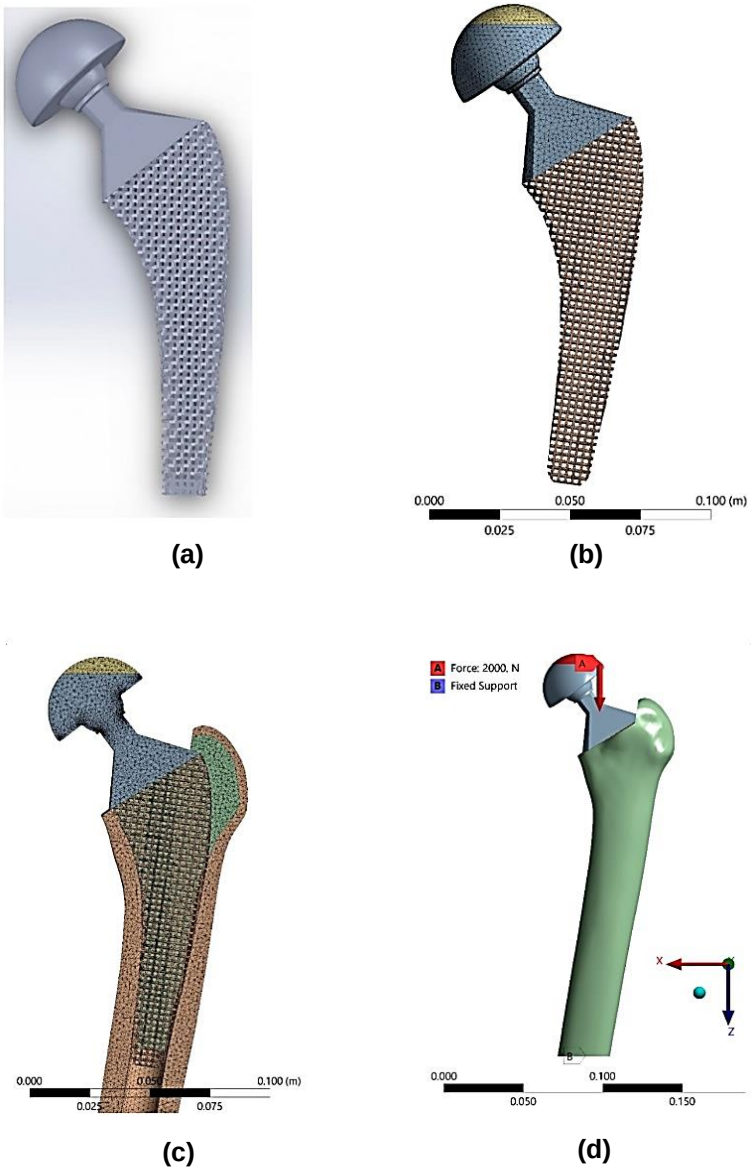

Figure 2.15. Meta-implant (a) CAD model (b) meshed finite element (FE) model of meta-implant based on 3D re-entrant structure (c) Meshed assembly of the implant and femur bone model and (d) Applied load and boundary conditions on the implant and femur bone model [193]

Three meta-implants with positive, negative, and graded Poisson's ratios were created using the novel accurate relationships for mechanical characteristics of 3D re-entrant unit cells. The meta-implants could provide enhanced stress and strain distributions in the implant and its contact areas with the internal bone surface, according to the

numerical results of the implants under compressive loading circumstances. Although all of the meta-implants' micromotion values were within appropriate ranges for bone ingrowth, those with negative and graded Poisson's ratios had a more compatible and uniform distribution of micromotion in significant locations of the bone-implant interface [193].

2.8. Summary and gaps in the literature

This chapter presents a review of the literature on bone, biomaterials, bone scaffolds and their mechanical properties. This is complimented with an extended review of background literature on auxetic materials and types of auxetic cellular structures. Several kinds of auxetic cellular structures both natural and artificial were identified from literature offering different geometries and deformation processes. Previous research shows that superior mechanical performance was observed for indentation resistance, shear modulus, fracture toughness, variable permeability, and energy absorption as a result of negative Poisson's ratio or auxeticity. Despite these superior performances, research focusing on exploring auxetic materials for load-bearing biomedical applications was limited. In any case, only a handful of auxetic studies classified under meta-biomaterials were observed when it comes to metallic materials, largely limited to titanium.

Overall, no studies were found on exploring CoCrMo for the development of auxetic meta-biomaterial bone scaffold for load-bearing bone scaffold applications. This gap in literature can be due to a range of factors, primarily the scaffold should have qualifying characteristics such as mechanical properties similar to host bone. Additionally, the literature suggests the need for porosity greater than 50% for bone

ingrowth which is hard to be achieved through porous titanium when stiffness and strength matching is demanded [11]. The literature review evidence that previous developments in meta-biomaterials failed to match the stiffness of load-bearing bone scaffold with that of the host bone [85,86]. This is primarily the result of the lower young's modulus of the bulk material being used, this is where CoCrMo offers significant potential due to its high strength (200 GPa), an aspect considered in this research.

Even though there is some evidence supporting the development of auxetic bone scaffolds, a comparative analysis considering multiple types of auxetic geometrical designs has not been studied before. As such this thesis presents a comparative analysis of all major auxetic architecture analysis their suitability for bone scaffolds. In addition to the assessment of the biological performance of meta-biomaterials, there are many other aspects regarding their geometrical design and fabrication that require further research as well. The research into novel geometrical designs of meta-biomaterials has just started. Given that the properties achieved through geometrical design are often unusual and even unprecedented, the space of possible applications for such properties is largely unexplored. For example, auxetic meta-biomaterials could be used to create scenario-based performance and targeted Poisson's ratio that are otherwise impossible to achieve. This possibility has, thus far, not been extensively explored which is another aspect covered in this thesis. Finally, this chapter has reviewed and discussed the applications of auxetic structures in bone tissue engineering. So far, no work has been done on CoCrMo auxetic bone scaffolds to reduce the stress shielding effect and improve the mechanical properties on a scenario basis which is revealed in this work.

Chapter 3

Additive manufacturing of biomaterials

3.1. Introduction

This chapter discusses the potential of powder-based Additive Manufacturing (AM) technologies for biomedical applications. AM process types are introduced, followed by materials that are suitable for the respective processes. Subsequent to this, descriptions of the challenges and limitations of the technology are presented. The chapter also summarises the potential use of AM technology for the fabrication of biomaterials suitable for biomedical applications.

3.2. Additive manufacturing (AM)

Additive manufacturing (AM) can be defined as the procedure of binding materials together to create items from 3D model data, typically layer by layer, unlike subtractive production processes like ordinary machining [194]. Additive manufacturing is also called freeform fabrication, rapid prototyping, or 3D printing. This manufacturing process is applied to various industrial sectors like consumer products, tooling, medical, automotive, energy, and the aerospace industry [195,196].

AM technology has been historically applied to create conceptual prototypes in a procedure called Rapid Prototyping (RP). The RP systems combine powder, liquid, or sheet materials to create physical objects. The RP machines fabricate metal, ceramic, wood, and plastic components using thin, horizontal cross-sections of the computer

framework [197]. The prototypes were used to facilitate rapid production of an item and cannot be compared with the final end product. The prototypes were also utilised as inspection and communication models, producing numerous physical tools within a short time, thus shortening the manufacturing process [198]. According to a Wholer's survey, about 23.4% of RP components are utilised as master patterns in direct tooling as well as secondary production processes [197]. Rapid Manufacturing (RM) has emerged through Rapid Prototyping courtesy of technological developments. Rapid Tooling is another sub-category of Rapid Manufacturing and aims at creating consistent models which function as traditional manufacturing processes [199].

Additive manufacturing (AM) represents a set of technologies that create physical items straight from 3D computer-aided design (CAD) data. Additive manufacturing functions by adding powdered, wire, sheet, or liquid materials, layer by layer, to create component sections with no or little additional processes required [200]. This technology offers several advantages, such as unmatched geometric freedom of design, short lead time, and near 100% material usage [201]. Several terminologies have emerged due to technological advancements in the layer-based processing sector.

There are numerous steps that are involved in additive manufacturing, as shown in Figure 3.1. The first step involves the design of a model using any professional CAD software. The model can also be designed using scanning and reverse engineering tools. The second step is converting for AM suitable file type. The typical file type for AM machines is the STL. The CAD software being used allows the CAD model to be saved in STL file type. The STL format transforms the surface of the CAD model into mesh-like triangles. The CAD software enables the user to manage the size and

number of the triangles created. The third step is slicing the file and transferring the STL files to the AM machine. In this step, the file is verified to ascertain that it is of the required orientation and the appropriate size. In the case of several parts, they are placed carefully to ensure that they do not overlap with one another [202].

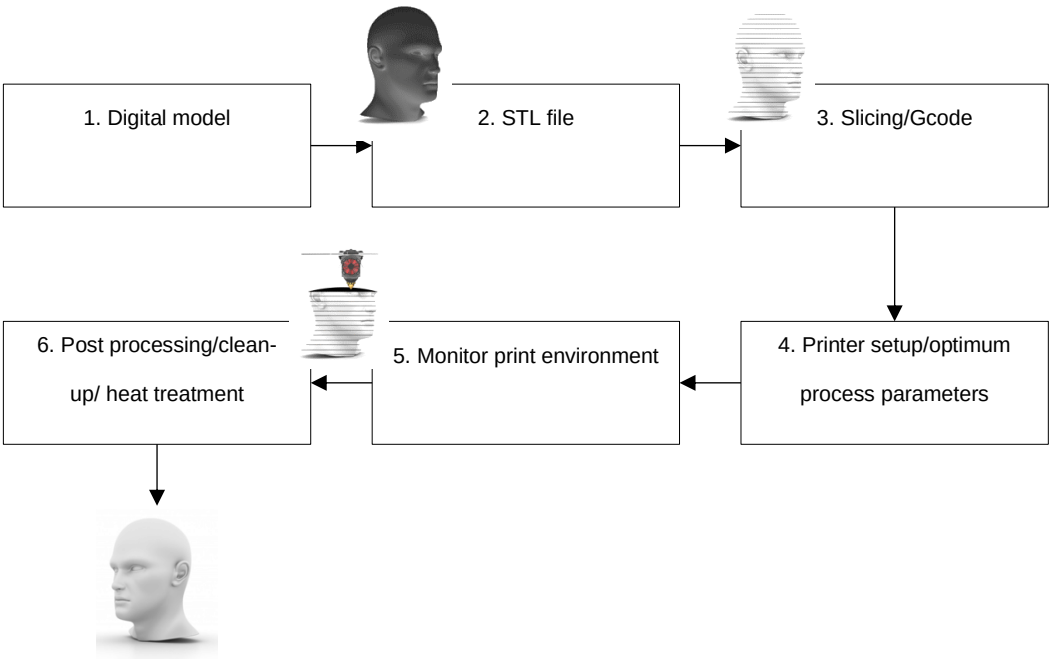

Figure 3.1. Steps leading to additive manufacturing from digital model to the final part

The fourth step is the AM machine setup. The various parameters are set carefully to ensure that the manufactured part has all the required features. Some of the parameters include roller speeds, timing, energy offered, orientation, and layer thickness. The fifth step is the most automatic build phase. The user should partially monitor this process to ensure that there are no errors that occur, and the materials are sufficient. The sixth and final step is the removal phase, where the user takes out the part created. The user observes all safety guidelines and follows the suitable shutdown process to guarantee the safety of the machine and the user. And then is the post-processing of the AM components. This involves additional treatment of the

parts produced, which include cleaning, sintering, and curing [199]. A lot of caution is taken during this process because the parts may be weak and delicate.

3.2.1. Selective Laser Sintering (SLS)

The laser sintering procedure enables the creation of sophisticated 3D items through the selective fusion of successive portions of powdered material. The component being produced is initially in an STL file format after the design process using any CAD software. The STL file is split into discrete layers, where every layer or slice reflects a cross-section of the component. A small film of powder is put on the build platform and computer-aided laser screens over the region, which heats and consolidates the specks of the powder in particular regions, which represent a specific cross-sectional portion of the tool designed. The build plate between the layers is lowered by a little margin of about 0.1 mm, and another powder sheet is laid over the preceding sintered film [203]. This procedure is repeated over all the other films making the component until the whole part has been fabricated. The powder in every layer which is unconsolidated stays intact to reinforce the following sheets. After the building process has been completed, the components, together with the supporting materials surrounding them in the build area, referred to as the “part cake,” are taken away from the building machine. The components are taken from the part cake, and the unattached powder is bead-blasted or blown out. The remaining powder which has not been fused is then sieved and used again for the next builds.

Laser sintering is also known as Selective Laser Sintering and has numerous advantages compared to other polymer additive methods. First, this technique does not utilise reinforcement components that are needed in other additive methods to offer reinforcement to the slim walls and overhangs in part during the building process

[204]. Instead, the part is supported by the unfused powder surrounding it as the build process continues. Besides, laser sintering does not need the use of a binder, which creates a post-processing phase compared to other procedures and may cause toxicity problems, especially for components meant for healthcare applications [205]. Polymer laser sintering processes do not compare to the resolution of the stereolithography additive process, but they produce components that are more stable and tougher, and research has revealed that extra enhancements in resolution are attainable [203]. Nevertheless, the major advantage acknowledged for laser sintering is the remarkable amount of material that is prepared using this process. A wide range of materials can be prepared using laser sintering.

There are various parameters associated with laser processing. One of the parameters is laser power, which refers to the power of the laser applied during the scanning of every layer. The next parameter is the scan count, which refers to the number of times the laser beam crosses a scan vector for each film. The scan speed is another parameter that refers to the speed at which the laser beam crosses over a scan vector. Another parameter is the scan spacing which refers to the distance between parallel laser scans. The manipulation of these parameters influences the capability of a specific material to build effective, and the quality and characteristics of the components prepared. Other parameters include the spot size, layer thickness, delay time and part accuracy [203].

AM through laser sintering has been gaining remarkable interest from various sectors which have recognised the capabilities of this process in terms of the implementation, performance, and design of various parts. Nevertheless, this technology requires a wide variety of materials. Successful production of components may be hindered by

the individual material properties, limits of the latest sintering equipment, and practicalities of manufacturing [206].

3.2.2. Electron Beam Melting (EBM)

Electron beam melting refers to a distinct manufacturing and prototyping technique that can decrease time, weight, and costs simultaneously. It is a quick manufacturing technique whereby entirely dense parts with properties are the same as those of wrought materials created on a layer-by-layer basis. After the procedure of melting and solidifying a single sheet of titanium powder, this procedure is repeated for all the other sheets until the component is successfully completed. For sectors like aerospace, it creates new chances for both prototyping and small-scale development of titanium parts. This technique eliminates the time, cost, and obstacles of investment casting or machining, thus making titanium components more available for installation or functional testing on the aircraft [207]. Moreover, the additive technique creates opportunities for new designs and alternatives for weight reduction.

During this process, high-speed electrons hit the metal powder, converting the kinetic energy into thermal energy. The temperature increases beyond the melting point, making the electron beam quickly liquefy the titanium powder. A tungsten filament located at the electron beam gun boils off a group of electrons. These electrons enter through the gun at a speed almost half that of light. The electrons in high motion are directed and organised by two magnetic fields. One magnetic field function as a magnetic lens where it directs the beam to a suitable diameter. The other magnetic field deflects the directed beam to the target point located on the powder bed. This technique is five times quicker compared to other additive technologies [208].

The EBM components are created in a vacuum to prevent energy loss which might be triggered by the rapid moving electrons making collisions with gas or air molecules. One of the advantages of using the vacuum is that the process is 95% energy efficient, which is more than five times higher compared to laser technology [207]. Another advantage is that the vacuum facilitates the processing of metal, allows it to be considered reactive like titanium. This technique has the ability to build complex designs that may prove impossible or difficult to produce using casting or machining. The freedom of making diverse designs can be used to reduce assembly time, minimise manufacturing costs, and attain exceptional strength-to-weight ratios. EBM is capable of producing true titanium components, thus making it suitable for making parts for military and commercial aircraft. EBM enables the rapid production of flight-ready titanium components [209].

However, the high cost of titanium and challenges associated with its manufacturing slows its adoption even though it is considered the best material for manufacturing particular aircraft parts. In such circumstances, investment or machined cast aluminum is selected to reduce weight. When aluminum proves not to be feasible, steel is then chosen despite its weight. Therefore, EBM provides the combined advantages of steel and aluminum while bypassing the challenges of producing titanium parts [207].

Another advantage of EBM technology is that it provides multi-piece assemblies. When using casting or machining, the designer is forced to develop an assembly which may increase the production costs, but the EBM technology enables the creation of a multi-piece assembly as one part. The combination of two or more parts into one component eliminates the step of assembly, thus reducing the cost of production. Another advantage is that the EBM technique allows the design and production of

aircraft parts with undetermined strength to weight and buy-to-fly ratios. Another advantage offered to buying this technology is that the process can be used to make hollow components with an internal strengthening scaffold. Unlike other processes, the EBM technique can produce the needed mechanical strength with minimal mass [207,210]. The overall weight of the component is reduced as well as the cost of raw materials.

The limitations of EBM include quantity inconsistency, instability in the processes, component defects, and residual roughness of the surface. The surface roughness of the end product may depend on several factors such as the processing parameters like layer thickness, sample geometry, beam diameter, and powder size. Averagely, EBM components tend to have a higher surface roughness than SLM components because of a larger layer thickness, beam diameter, and powder size [208]. Moreover, it is possible to find gas voids and porosities being formed in EBM components. These defects are minimised or reduced by a standardised hot isostatic pressing (HIP), but this process does not remove the defects completely [211].

3.2.3. Selective Laser Melting (SLM)

Selective Laser Melting (SLM) is defined as an AM technique whereby a high-powered laser is used for melting metallic powders in combination to fabricate the part STL data [194]. This technique is also referred to as laser powder bed fusion (LPBF). The process uses a recoater to spread a thin layer of material, as shown in Figure 3.2, which is then fused by an overhead laser following the 2D slice data. This process continues layer-by-layer until the full part has been fabricated. Once the printing step is complete, it is taken for heat treatment and post-processing. The building chamber is usually filled with argon or nitrogen gas, resulting in an inert atmosphere for the SLM

process. An inert atmosphere should also be maintained during heat treatment to prevent oxidation of the metal parts [212].

Table 3.1. SLM Specifications [194]

Parameter	Value
Layer thickness	20-100 µm
Build rate	4-16 mm^3/s
Feedstock reuse	95% of the un-melted powdered material is re-usable
Tolerance	+/- 0.05 µm
Laser power	200-400W
Build size	250x250x300 mm

The laser melting technique is usually applied for low volume production of highly complex components or for prototyping [213]. Table 3.1 lists some parameters associated with the SLM process [194]. The common materials used for metal SLM include Inconel 718 and 625, CoCr, CoCrMo, Ti6Al4V and Ti6Al7Nb, AlSi10Mg, H13 tool steel, and stainless steel [194]. Recently work has also established the potential for SLM in printing highly conductive Cu and Ag as well [214,215].

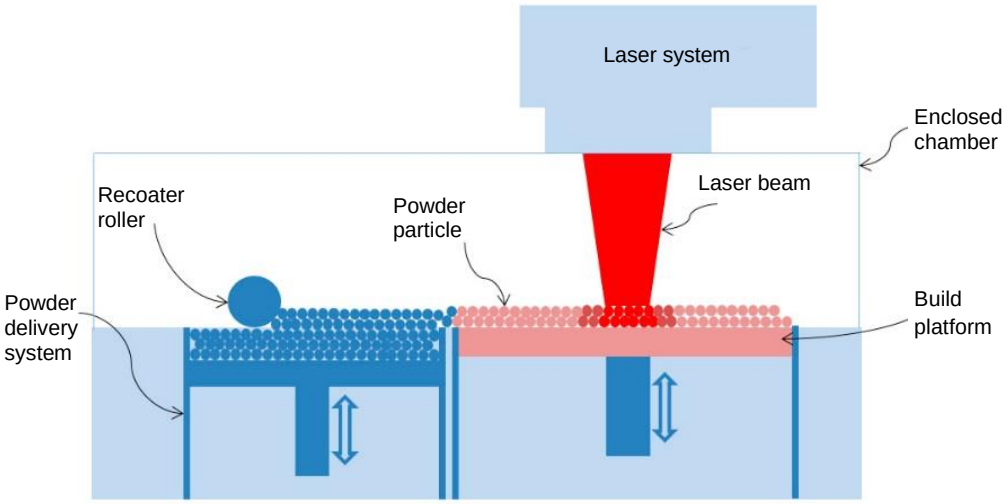

Figure 3.2. Schematic Selective laser melting process (SLM) [216]

When it comes to the modelling and simulation techniques of SLM, they are categorised as macroscopic, microscopic, and mesoscopic models. Macroscopic simulation approaches usually treat the powder stage as a homogenised spectrum leading to effective numerical models having the capacity to stimulate the production of the whole components by SLM [217]. Besides, macroscopic approaches tend to concentrate on identifying spatial distributions of temperature, dimensional warping, and residual stresses within SLM components. Microscopic approaches deal with the advancement of metallurgical microstructure entailing resulting grain sizes, the development of thermodynamically stable and unstable stages, and shapes and orientations. Mesoscopic approaches usually handle single powder grains and melt pool thermo-hydrodynamics to identify component properties like surface quality, adhesion between consecutive layers, and creation strategies of defects like pores and inclusions [217,218].

The SLM process is capable of processing various materials, including metal oxide [219] materials, ceramic, polymers, and engineering plastics, and it has the highest power of the laser for melting powders [220]. SLM is one of the established techniques among all other AM processes, and it is capable of fabricating parts in a large range of materials. SLM utilises an optically guided laser beam to melt selectively and bind together the powder until the desired geometry is attained [170]. The parts are then taken for post-processing, where support structures are removed, and the surface finish is enhanced as desired.

3.2.3.1. Process parameter optimisation

In selective laser melting, a concrete of metal powder is attained by melting and at the same time solidifying some small tracks of materials in a layer-by-layer and track-

by-track design using a high-intensity laser. The laser beam scans over the powder film in a given straight line, and it is able to melt the powder specks under the intense beam; the end process results in the creation of a small molten pool of metals [221]. Thin tracks of solid metals are left behind once the laser beam traverses. The following are some of the factors that will determine the composition of a metal; scan patterns, the kind of atmosphere, and powder-bed temperatures. According to the research conducted on the use of keyhole mode within the conduction mode for selective laser melting deposits, it was observed that the conduction mode gave denser parts with better mechanical characteristics. Dilutions are known to contribute to the general change in the local composition of the melting pool at the same time changing noticeable melting temperatures of the lattice structures in the local single-track vicinity [222].

Several potential impacts influence parameters for selective laser melting (SLM) which is directly involved in the process of additive manufacturing. The arrangement of these parameters is used to evaluate the energy density, which is directly applied to the powder layer during the laser powder bed fusion process [223]. The continuous effects of parameters on the product properties manufactured by laser powder bed fusion are essential in the application of technology. Increasing the powder layer thickness in all involved solidification phases while using the laser will help speed up the whole process; hence the total time covered during manufacturing will be significantly reduced. On the other end, if the powder layer is exceptionally thick, there is a possibility that successive layers may not be created at the end of the process [196]. An extremely thick layer of powder requires a higher laser power and a slower scan speed in order to achieve the same effective melt pool. There will be an effect of

changing the powder layer thickness because as the layer thickness increases, the levels of hardness decrease together with the density. The density of the product is affected by the layer thickness of powder because when the powder layer thickness increases, the product's density is reduced [224].

The effects of changing the powder layer thickness on two different additive manufacturing systems will result in the production of stainless-steel powder. Scan speed is another essential aspect that will determine the overall time spent in the manufacturing process. When the scan time is extremely high, there may be no enough time to melt the powder completely [225]. There are factors when they are adjusted that may lead to improved melting; for instance, increased laser power generally enhances the melting process. On the other hand, reducing the hatch distance will also enhance the melting process and will be able to achieve energy density which will facilitate faster scan speed. When scan speed is increased to extreme rates, they affect the hardness and density of the product. For instance, if the scan speed increases in additive manufacturing, it will decrease both the hardness and density of the steel [226].

3.3. Materials used in AM

The AM procedures utilise four material classifications, which include polymers, metals, ceramics, and composite materials [218]. The table below categorises the AM processes in terms of material form and state.

Table 3.2. AM processes categorisation [227]

Material type	Process	Material class
Liquid	SL	Polymers
	FDM	Polymers
	IJP	Polymers
Powder	3DP	Polymers, metals, and ceramics
	SLS	Polymers, metals, and ceramics
	SLM	Polymers, metals, and ceramics
	EBM	Metals
	DMD	Metals
	CS	Metals
Solid	LOM	Polymers, metals, ceramics, and composites.

Additive manufacturing often utilises all the four material categories, but the rapid tooling process often utilises polymers, ceramics, or generally tools that are in the endoscopy market, and highly strong and precise tools having complex designs which are printed within a very short time. It also uses metals for tooling applications, and rapid prototyping utilises the cheapest material depending on the conditions [227].

AM processes utilise three bulk material states/forms, including liquid, powder, and solid layers. For instance, the liquid is utilised in procedures like light photo-polymerisation, which is also referred to as stereolithography (SL), inkjet printing (IJP), and fused deposition modelling (FDM). The powder is utilised for direct metal deposition (DMD), electron beam melting (EBM), selective laser melting (SLM), and selective laser sintering (SLS). On the other hand, laminated object manufacturing (LOM) utilises solids of any material classification to form an object [227]. Ceramic composites, alloys of titanium, steel, aluminum, and polymers can be printed at a small layer thickness of about 20-100 µm according to the procedure and the physical form of the material being used [226]. Table 3.3 summarises the range of materials and

associated AM techniques that can be used depending on the resolution and scalability requirements.

Table 3.3. Print resolution and scalability can be achieved by various AM techniques [226]

Materials	**AM Technology**	**Resolution (μm)**	**scalability (mm)**
Polymers			
ABS + carbon fibre powders	FDM	50	400
Polylaurylamide and polyether ketone ketone	SLS	80	300
Denture base PMMA	SLA	100	600
Epoxy/clay nanocomposites	DIW	200	800
Metals			
316 L SS	Laser-assisted direct metal deposition	40	10
H13 tool steel	Direct metal deposition	40	60
Ti-Cu alloys	Laser metal deposition		120
Al7075, AL6061	SLM	20	80
Ti-6Al-4V	Shaped metal deposition		275
Ti-6Al-4V	EBM		200
Ti-6Al-4V	EBM	50	47.1
Al-Fe alloys	E-beam deposition		100
Mild steel	Arc additive layer manufacturing		500
Ni-based superalloys	EBM		4.5
Ni-based superalloys	Laser AM		
AlCoCrFeNi HEAs	SLM		10
FeCoCrNi HEAs	SLM		60
CoCrFeNiTi-based HEAs	SEBM		85
CoCrFeNi HEAs	DIW		10
$Zr_{44}Ti_{11}Cu_{10}Ni_{10}Be_{25}$ MG	Fused filament fabrication		

$Zr_{52.5}Ti_5Al_{10}Ni_{14.6}Cu_{17.9}$ MG	Laser foil printing		
$Zr_{55}Cu_{30}Ni_5Al_{10}$ MG	SLM		7.2
Ni	TPL	0.1	0.05
Ceramics			
SiOC matrix nanocomposites	DIW	200	100
SiOC	SLA/SPPW	50	100
SiOC	SLA	25	10
Al_2O_3	TPL and atomic layer deposition	0.9	0.05
Glasses			
Silica glass	Direct heating method	4500	300
Amorphous silica	SLA	50	
Amorphous silica	DIW	500	10
Phase-separating resins	DLP		10
Tetraethyl orthosilicate	DLP	200	10

3.4. Limitations of AM

It is essential to know the limitations of AM technologies to reap their maximum benefits. One of the limitations of AM technologies is part size. When it comes to SLM processes, the part size must be fit within 250x250x250 mm, which is the standard size for bed systems [228]. The part sizes can be larger when it comes to direct energy deposition processes. However, the low powder layers can make it expensive and slow. AM technologies are generally suitable for small or unitary series and not for large-scale manufacturing. However, advancements have been made to improve machine production and hence the manufacturing of bigger series.

SLM processes also require removable support to facilitate overhang angles less than 45° [228]. The choice of materials and the availability of process parameters is another limitation of the AM technologies. Despite the availability of numerous alloys, metal

additive manufacturing cannot be used to process non-weldable metals, and alloys that are difficult to weld need particular techniques. Another limitation is material properties, where components built through AM technologies seem to demonstrate anisotropy along the Z-axis. Additionally, despite the possibility of achieving 99.9% densities, some residual internal porosities may exist [228].

When it comes to the production of metals, the equipment and the cost of materials are very high. Another limitation is that all the components need some post-processing and cannot be installed directly. The maintenance of the machines also requires highly trained personnel, therefore, increasing the maintenance costs [229]. Moreover, the general finish capability of the AM powder is quite rough compared to ordinary powder metal materials. Another limitation of metal additive manufacturing is that it exhibits dimensional challenges like metal injection moulding, especially when processed via binder jetting. For instance, the material may shrink up to around 20% during the sintering process [230]. As a result of the shrinkage, components encounter excess friction during the sintering process. In the manufacture of plastics, it is too slow for mass production, and the deposited layers need perfect calibration; otherwise, they would create weakened components [229].

3.4.1. Overhangs and supports

Care should be taken when creating components layer by layer to avoid having overhangs, as every layer has to be partly reinforced by the preceding layer. When the angle between the build platform and the component is less than 45°, reinforcement systems are required to prevent warping, distortion, and poor surface roughness, which cause build failure [228]. Cooling of the laser melted tracks also causes thermal stresses that curl the material upwards. However, this can be avoided

to a certain extent by strategically placing support structures to act as anchors to hold the components down to the build plate [228].

When it comes to the support structures, they have numerous functions, including providing reinforcement to the component in case of overhangs, strengthening and fixing the component to the building plate, conducting extra heat away, and preventing warping or total build failure [231]. However, optimised support structures have little weight and are easily removed mechanically. Both the orientation and the position of the component on the build plate have a considerable influence on the requirement and type of support systems, thus impacting the post-processing practices and the quality of the complete part [232]. Another demerit of support structures is that they may damage the surface after their removal. Also, the addition of the support structure to the component prolongs the print time as the support system must also be printed [231].

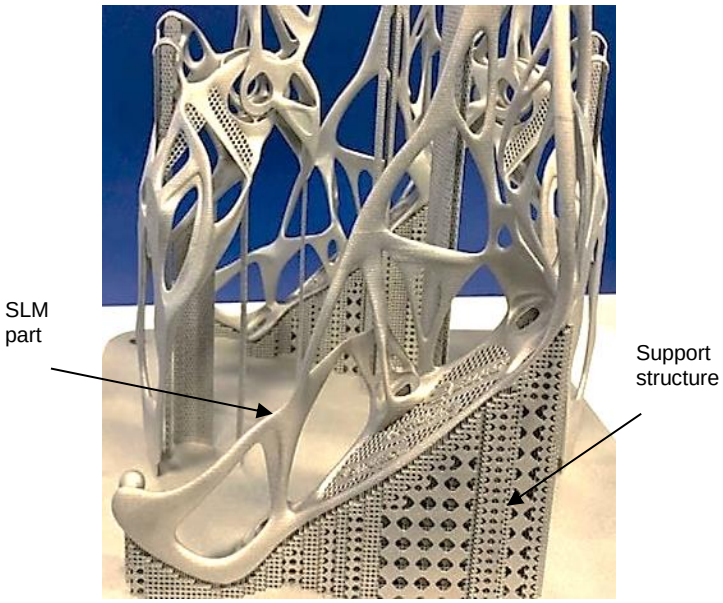

Figure 3.3. Support structures on SLM manufactured part [233]

3.4.2. Thermal stresses and warping

The rapid solidification causes thermal stresses, which are responsible for warping. Warping may distort the component, cause bad junctions between the components and support structures, or cause recoating issues [228]. The formation of residual stress (RS) may cause geometric inaccuracies and compromise performance. In the aspect of geometrical accuracy, the distortions of components happen due to the development of residual stresses. These stresses tend to push or pull the material deflecting the component depending on the direction of the stresses, as often observed in bending, hot rolling, and welding [234]. The residual stresses are considered to exist within the body without the application of any external forces. They are also known as “locked-in” or “internal” stresses, and they may weaken a component or strengthen a material such as toughened glass [234]. They may also be called thermal stresses because they emerge from the steep thermal gradients in the production process.

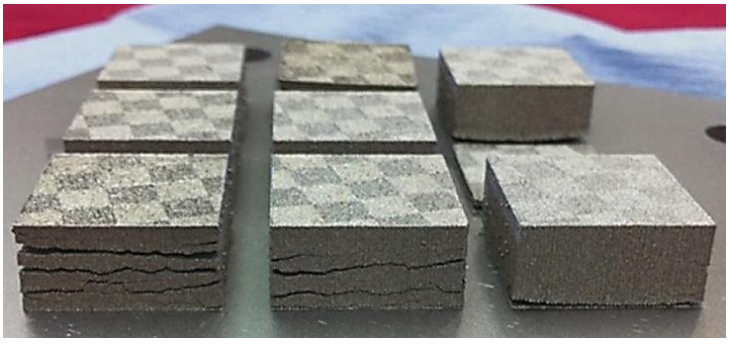

Figure 3.4. Part delamination due to the effect of residual stresses in SLM [235]

The problems caused by thermal stress and warping may cause deformation of printed components and, other times, terminate the printing process. The effects of sheet form and infill line directions (ILDs) on distortion during fused deposition modelling (FDM) were simulated and verified by Chen *et al*. [236]. The findings of the simulation reveal

that ILD has a higher impact on the deformation and the sheet warping worsens after the ILD is aligned with the diagonal of the sheet [236]. To avoid these issues, they proposed to use optimised printing parameters in the FDM process.

Although SLM has several advantages, one of the drawbacks that challenges its wide adoption is the effects of residual stresses. Although heat treatment and other post-processing techniques can considerably reduce the residual stresses that are being generated, they cannot undo the cracking, delamination, and warping deformities that take place throughout the process. However, certain process parameters directly affect the thermal stresses that are being generated. Scanning patterns, scan vector lengths, scan vector angles, rotation angles between layers, component shape, material type, support types, and preheating conditions are a few variables that might affect residual stresses. As such the thermal stresses and their detrimental effects can be reduced by altering one or more of the above factors or by using optimum process parameters. Mugwagwa *et al.* [237] have studied the influence of process parameters on residual stresses and found that increasing laser power and scanning speed gives rise to steep thermal gradients which, in turn, increases the residual stress magnitudes. High porosity in SLM parts can occur due to overheating or insufficient heating. Excessive heat can lead to over-melting, whereas insufficient heat leads to poor interlayer bonding. Increasing the layer thickness results in a decline in residual stresses. The decrease in residual stress magnitude can be attributed to reduced thermal energy input and cooling rate.

The effect of process parameters, such as laser power, layer thickness, scanning speed, and hatch distance, on residual stress in SLM parts, shows that the effect of laser power and scanning speed affects the residual stress. Generally, the residual

stress near the surface decreases with increasing laser power and decreasing scanning speed: larger melt pools promote slower cooling rates and, therefore, lead to reductions in residual stress in metals. Thus, selecting high laser power and low scanning speeds can achieve residual stress reduction while maintaining acceptable part density which is an approach considered in this thesis. In summary, there must be a reasonable compromise between reducing residual stress by increasing/decreasing power, scanning speed or hatch distance, or changing powder layer thickness or spot size to produce fully dense parts with the required accuracy, without cracks and distortions.

3.4.3. Surface Roughness (Stair Step)

For the laser beam melting process, the surface roughness that can be attained is typically between 25 – 40 µm in an as-built state [228]. Much lower values can be achieved through polishing. However, it is critical to note that component design complexity may influence its capability to be polished effectively. Some of the surface defects that need to be avoided include the staircase effect. The staircase effect is visible on curved surfaces and becomes more pronounced following an increase in the surface angle relative to the vertical axis.

The staircase effect deteriorates the surface quality of the AM components, which results from the layered deposition of the material [238]. Another defect is the poor down-skin surface roughness and reduced accuracy dimension, which is mainly associated with the slow evacuation of the heat dissipated by the laser beam on the down-facing surfaces [228].

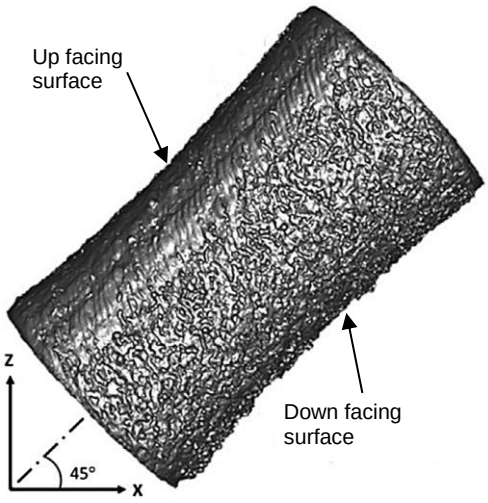

Figure 3.5. X-ray CT image of a 45° orientated additive manufactured part showing a higher surface roughness for the downward-facing side relative to the upward-facing side [239]

3.5 AM for auxetic materials

Additive manufacturing has the ability to aid in the fabrication and development of auxetic structures that have better characteristics and multifunctional capabilities. Unlike traditional methods like braiding, moulding, sintering, and spinning, AM allows for a great deal of flexibility and complexity in the creation of these scaffolds [240]. The majority of experiments involving substantial deformation of auxetic materials and structures used the AM techniques [241].

Because of the increasing precision and ease of manufacture of complicated structures, improvements in the AM of auxetic structures have broadened their scope of use. The use of AM auxetic structures in biomedical and tissue engineering devices aids in the creation of personalised and cost-effective devices. According to Mardling *et al*. [1], auxetic structures could be used in a variety of tissue engineering and biomedical applications. The femoral component for complete hip replacements was

designed and fabricated using auxetic structures created via additive manufacturing [170,192].

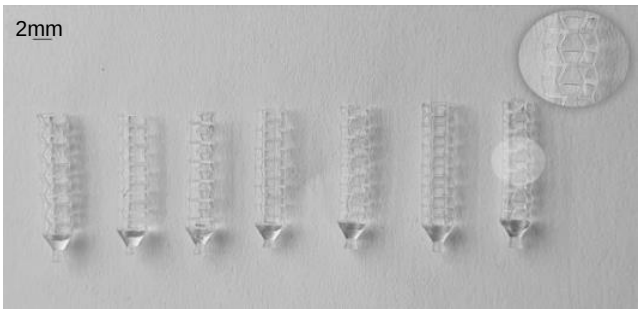

Figure 3.6. Covid-19 sample swab heads [242]

Arjunan *et al*. [242] investigated the additive manufactured biocompatible photopolymer FLSGAM01 auxetic nasopharyngeal swabs for COVID-19 that can possibly reduce patient pain and discomfort as shown in Figure 3.6. It reported that the advances achieved in developing auxetic nasopharyngeal swabs that can shrink when subjected to axial resistance. This reduces the amount of stress on the surrounding tissues as the swab passes through the nasal cavity. This is accomplished using a biocompatible material with carefully designed negative Poisson's ratio $(-\upsilon)$ structures. In this circumstance, AM's quick and diverse manufacturing proved very advantageous for speedy and distributed production.

3.6 AM for bone tissue engineering

AM technology can be applied in various biomedical applications such as bone and dental implants. These implants are made with durable and biocompatible materials such as titanium, cobalt-chrome alloy, bio-ceramics and polymers [194]. Titanium is widely used due to its corrosion-free surface, thus making the implant last for a longer time. The requirements of implants vary from one individual to another, and these design complexities make AM technologies to be the most suitable for the production

of these medical aids [243]. AM enables the production of high-quality biomedical products with complex specifications with quick turnaround in comparison to traditional manufacturing techniques [244,245].

The demand for implants has been on the rise, fueled by the rise in the ageing population and accidents. Hence, it is essential to fabricate patient-specific implants of high quality to improve the quality of life and reduce the risk of non-union fractures [223]. It is also worth noting that personalised implants for bone repair can also offer improved healing and availability in comparison to approaches like distraction osteogenesis and state-of-the-art bone grafts. The ability to fabricate porous geometries in biocompatible materials on-demand makes AM the most suitable approach for patient-specific implants and bone scaffolds [246]

Figure 3.7. Acetabular cup produced by Additive manufacturing [247]

SLM was used by Zhang *et al*. [248] to fabricate a beta-type Ti24Nb4Zr8Sn biomedical titanium alloy acetabular cup, as shown in Figure 3.7. The printing was carried out using a laser power of 200 W at a scan speed range of 300-600 mm/s resulting in near full density components (>99%). It was demonstrated that the part had a low elastic modulus of 53 GPa, a 660 MPa ultimate tensile strength, and a ductility of more than

10%. It was shown that the scan speed has no effect on the strength or modulus of the specimens. However, the ductility was found to be directly related to the scan speed and hence affecting the part density. According to the Wohler's Report 2015 [223], AM techniques have generated over 100,000 acetabular implants, with around 50,000 of these put in patients in recent years. Such information provides a broad picture of how the industrial sector's interest in additive manufacturing has developed, as well as the actual uses of the technology.

Hazlehurst *et al.* [32] used SLM to evaluate the stiffness and strength of square pore CoCrMo cellular structures with a volume based porosity range between 25-95% for possible orthopaedic applications, as shown in Figure 3.8. The porous structures were made from CoCrMo powder supplied by EOS by using an EOISNT M270 Direct metal laser sintering machine. The machine used 200W laser power at a scan speed of 800 mm/s with 100 µm laser diameter and a laser step over a distance of 0.08 mm to selectively melt the powder in an inert nitrogen atmosphere.

Uniaxial compression tests were carried out with build parts and find out that the effective elastic modulus varied between 1.06-28.59 GPa, and the mean compressive yield strength varied between 9.3-327.47 MPa. Compressive elastic modulus and strength values were found for the cortical and cancellous bone from the literature states elastic modulus of 17 GPa for cortical and 2.73 GPa for cancellous bone, with the strength of 193 MPa for cortical and 18 MPa for cancellous bone. This concluded that the manufactured parts have similar stiffness and strength characteristics when compared to host bone [32].

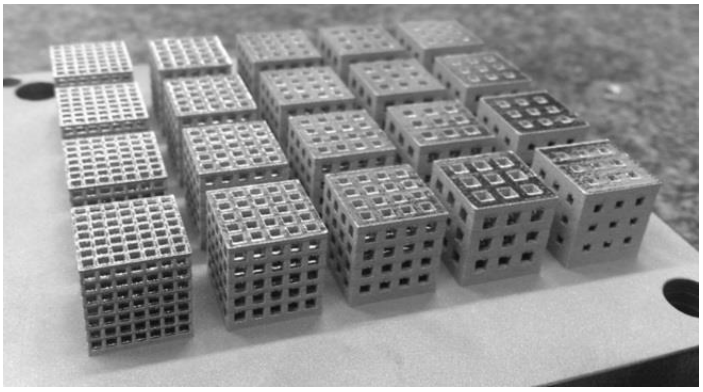

Figure 3.8. Built components with different pore sizes [32]

Ti24Nb4Zr8Sn created an optimal scaffold structure by SLM process with 85% porosity, according to Liu *et al.* [249]. The laser scanning speed and input energy have an impact on relative density. With a scan speed of 750 mm/s and a laser power of 175 W, the highest quality component may be obtained, with 99.3% density. According to the compression testing findings, the strength could reach 51 MPa with the ductility of above 14%. These findings suggest that titanium alloys might be used to make artificial implants.

Functionally Graded Porous Scaffold (FGPS) becomes attractive and promising for bone implant applications due to its combination of improved mechanical and biological requirements with the scaffold gradient to better mimic host tissue [250]. Han *et al.* [128] investigated the strut dimension characterisation, micro topology and mechanical properties of the FGPS with a wide range of graded volume fractions manufactured by the SLM process. Schwartz diamond unit cell design was used to develop the FGPS structures with graded volume fractions from 20% in the distal layer to 5,7.5,10,12.5,15% in the proximal layer, as shown in Figure 3.9. Diamond FGPSs with a wide range of graded volume fractions from 7.97% to 19.99% were produced without any defects, indicating a satisfactory geometric replication of the original designs, according to micro-topology measurements.

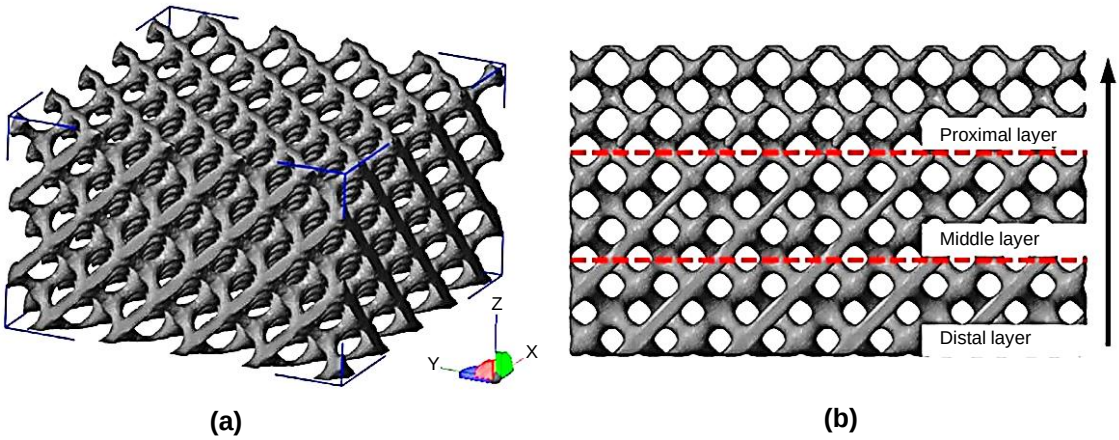

Figure 3.9. (a) Schwartz diamond FGPS model (b) the X-Z plane view. Increase in volume fraction indicated by arrow [128]

The dimensional characterisation shows that SLM is capable of producing titanium diamond FGPSs with strut sizes ranging from 483 to 905 µm. By modifying the graded volume fraction, the elastic modulus and yield strength of titanium diamond FGPSs can be customised in the range of 0.28–0.59 GPa and 3.79–17.75 MPa, respectively which are equivalent to those of cancellous bone. A mathematical relationship is established between a FGPS's graded porosity and compression characteristics. When the volume percentage of the proximal layer is increased to 15%, the deviation between estimated and experimental elastic modulus and yield strength drops to 3.3% and 3.1%, respectively. FGPSs offer a wider range of mutative pore size and porosity than homogeneous diamond porous scaffolds, which may be tailored to optimise the pore space for bone tissue ingrowth [128].

3.7. Mechanical properties of AM lattice materials

Metal additive manufacturing methods of production have been widely used in the production of regular cellular structures characterised by high-energy absorption abilities, which have low relative densities. On top of that, these materials regularly

show other exciting properties that make them more convenient and more preferred construction materials. The low mass of 3D lattice structure has posed more interest to many scientists, and they have conducted many pieces of research. Lattice structures uniformly spread peak force during the process of dynamic loading conditions within a given short period of time [251]. A strong relationship exists between the applied topology of the formed lattice structures and the extent of energy absorption.

When compared to the bulk material properties of the alloys themselves, AM methods can build porous structures with stiffness and strength characteristics that are closer to human bone [252]. The mechanical characteristics of a porous biomaterial made of the titanium alloy Ti6Al4V were investigated by Li *et al.* [253]. The test specimens were made using additive electron beam melting (EBM) technology and put through a static pressure test to determine their mechanical properties. Honeycomb structure, orthogonal structure, and layer structure were all used to make cylindrical samples with a diameter of 10 mm. Pore diameters varied between 500 µm and 600 µm. The porous nature of the material greatly reduced the stress shielding effect, according to the findings. These structures have compressive strengths ranging from 163 MPa to 286 MPa, and elastic modulus values ranging from 14.5 GPa to 38.5 GPa, which are close to cortical bone values [253].

Harrysson *et al*. [254] investigated the mechanical properties of Titanium hip stems manufactured by the EBM process to reduce the stress shielding of the implant. The compressive and flexural characteristics of rhombic dodecahedron cellular structures with cell sizes ranging from 3 and 12 mm were analysed. The volumetric porosity influenced the stiffness and strength of the cellular structures. The compressive

modulus was found to be between 12 and 60 MPa, which is significantly lower than the modulus of Ti6Al4V, which is around 110 GPa.

The compressive characteristics of square pore titanium alloy cellular structures manufactured by EBM and SLM were compared by Sallica-Leva *et al*. [255]. When compared to parts made via EBM, the results indicated that laser-melted components had better mechanical properties. This was attributable to microstructural variances in the two technologies, as well as changes in operating conditions.

Rivera *et al*. [256] investigated the mechanical characteristics of a Selective laser sintered CoCrMo open cellular structure that could help bone develop into an acetabular cup. A structure was proposed with a pore size of 0.50 mm that has mechanical qualities equivalent to commercially available tritanium and tantalum alloys. Yan *et al*. [257] investigated the compressive characteristics of Selective laser melted 316 L stainless steel cellular structures, as illustrated in Figure 3.10. When smaller unit cells were employed, the density of individual struts was found to be greater. When compared to an 8 mm unit cell, the yield strength and elastic modulus of a 2 mm unit cell were 36% and 27% greater, respectively. This meant that when the volumetric porosity increased, the stiffness and strength of the cellular structures decreased, which can be beneficial to reduce the stress shielding.

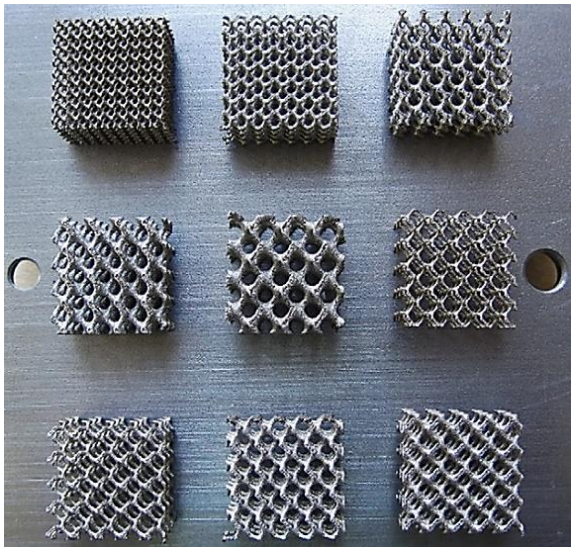

Figure 3.10. Stainless steel cellular structures manufactured by SLM [257]

3.8 AM challenges for biomedical applications

In the current world, additive manufacturing is increasingly being used for biomedical applications due to the advantage of on-demand manufacturing. Biomedical components produced using additive manufacturing includes implants and other special tools used in that field [232]. AM has gained much success due to its capability to produce components with complex geometric shapes. However, some challenges persist in the application of AM for biomedical engineering.

According to Bose *et al*. [258], the focus of fabricating bone tissue lies in optimising the mechanical characteristics of the porous scaffold. This scaffold is usually made of ceramic, which has a high porosity and low mechanical characteristics. Egan *et al*. [259] backed up this argument, claiming that synthetic scaffold tissue is difficult to optimise owing to the difficulty of integrating mechanical characteristics with biological systems. Mechanical qualities, biological performances, and manufacturing restrictions must all be considered in the design. For cellular development to occur, the scaffold structure's mechanical integrity is critical.

Obtaining appropriate mechanical strength and manufacturing feasibility, according to Vasireddi *et al*. [260], are two major challenges. Because these features involve consideration of geometric selection criteria, layer thickness, and the minimum ratio between distribution ratios of pore sizes, the well-perceived need for materials used for fabrication is still insufficient to print different structures. The thickness of the printed layer is also affected by the particle size of the powder. The quality of scaffolds is also affected by the distribution of particle sizes and shapes. The mechanical characteristics of 3D scaffolds are influenced by the lack of pore interconnectivity. Because scaffolds must promote tissue regeneration after implantation, the powder must be biocompatible and biodegradable [261].

Chapter 4

Design and additive manufacture of auxetic scaffolds

4.1. Introduction

Additive manufacturing allows the development of auxetic materials based on repeating unit cells. Currently, there is no literature on the development of CoCrMo auxetic bone scaffolds. As such, this chapter demonstrates the use of digital design tools and SLM additive manufacturing to develop CoCrMo auxetic bone scaffolds. Informed by literature, nine open porous unit cells are investigated for their auxeticity using the finite element method (FEM). In addition, Ashby's criterion was employed to study the mechanical behaviour of the unit cells, namely the elastic modulus and yield strength under uniaxial compression. The results informed the selection of potential unit cell candidates for the design of five auxetic bone scaffolds at a porosity range of 80-87%. Subsequently, these designs were fabricated using SLM along with tensile test coupons using CoCrMo powder feedstock characterised for its suitability for the SLM process. The print quality of all the scaffolds was characterised using scanning electron microscopy (SEM) to identify the deviation of the strut thickness and porosity in comparison to ideal geometry. The chapter found SLM to be suitable for the development of CoCrMo bone scaffolds that offer high porosity. The mechanical performance of the scaffolds will be qualified in upcoming chapters.

4.2. Methodology

4.2.1. Auxetic scaffold design

4.2.1.1. Unit cells considered for initial selection

Cellular architectures, as proposed by Lakes [262], can be considered composites where one phase is solid, and the empty space is filled with fluid. The solid phase consists of a network of struts often referred to as lattices or cells. Cellular solids are typically characterised by unit cells (UCs) with certain symmetry elements [119]. According to Ashby [263], modelling unit cells at milli or micrometre-scale allows the overall solid to be considered both as structures and as materials. As a result, the macroscopic properties of cellular solids, such as the stiffness (elastic modulus E) and strength (compressive yield strength) are governed by both material and structural properties [264–267]. Considering these aspects, 9 different auxetic UCs were conceived for the initial study, as shown in Figure 4.1, that allow for interconnected pores.

The unit cells were designed without overhangs greater than 45° to avoid extensive support requirement differences during the SLM fabrication process [268]. All nine unit cells were designed using the 'Solidworks 2019' CAD software for initial analysis, as shown in Figure 4.1. The designs considered the philosophy of Limmahakhun *et al.* [269], which recommended lattice materials at the millimetre scale to be the best way to reduce the stiffness of the metallic implant. Consequently, each of the unit cells (UC1-UC9) were conceived at a global length, width, and height of 2 mm, resulting in a bulk volume of 8 mm^3. The strut thickness was designed in such a way as to measure 0.3 mm when assembled into a lattice architecture.

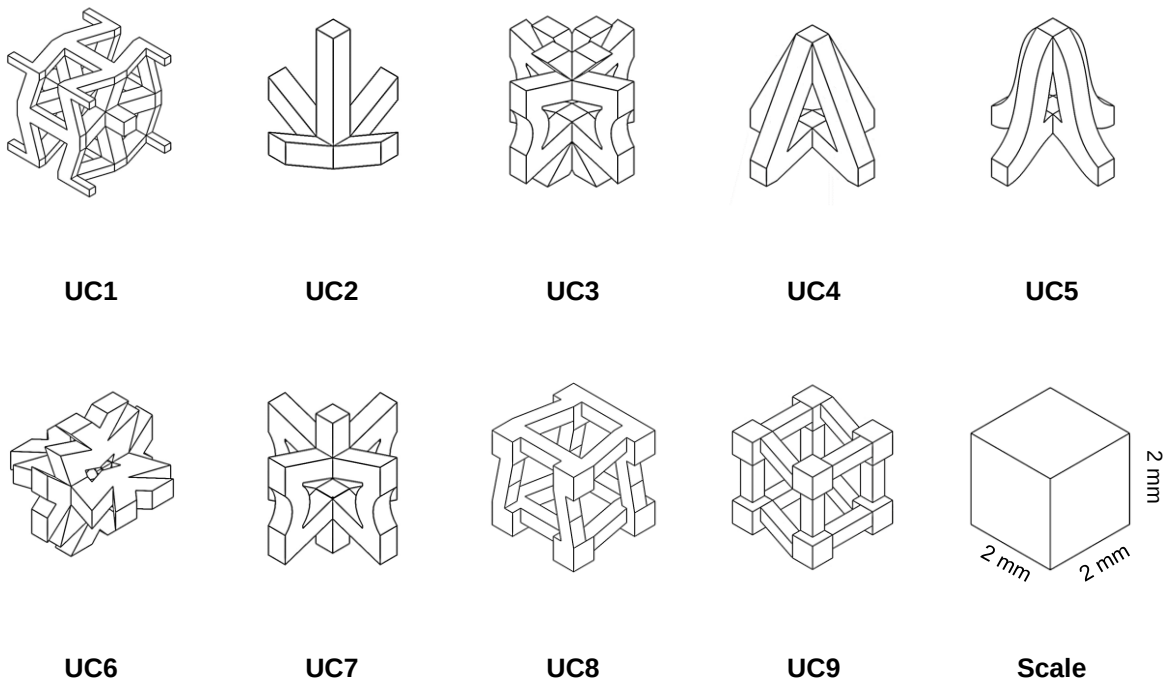

Figure 4.1. All unit cell (UC) variants considered for initial analysis to be qualified for their auxeticity inspired from literature

All the nine unit-cells were claimed in literature [22,270–274] to be auxetic under different dimensions, meaning they demonstrate lateral shrinkage while being axially compressed. However, for meaningful comparison, this thesis conceives all unit cells with one global dimension (2×2×2 mm cube at an 8 mm^3 bulk volume) to make the volume equal. When morphing certain unit cells with different aspect ratios into a cubical architecture the auxeticity was found to be affected. The auxeticity of each unit cell were qualified using finite element analysis (FEA) to identify the best five final set of UCs for scaffold design. To do this, a lattice structure composed of each unit cell arranged in 3x3x3 format, as shown in Figure 4.2, was designed. It should be noted that this is not a scaffold design and is used only as an initial test to select the best design for scaffold development.

However, the auxeticity of each unit cell were qualified using finite element analysis (FEA) to identify the best five final set of UCs for scaffold design. To do this, a lattice structure composed of each unit cell arranged in 3x3x3 format, as shown in Figure 4.2, was designed. It should be noted that this is not scaffold design and is only used as an initial test to select the best design for scaffold development.

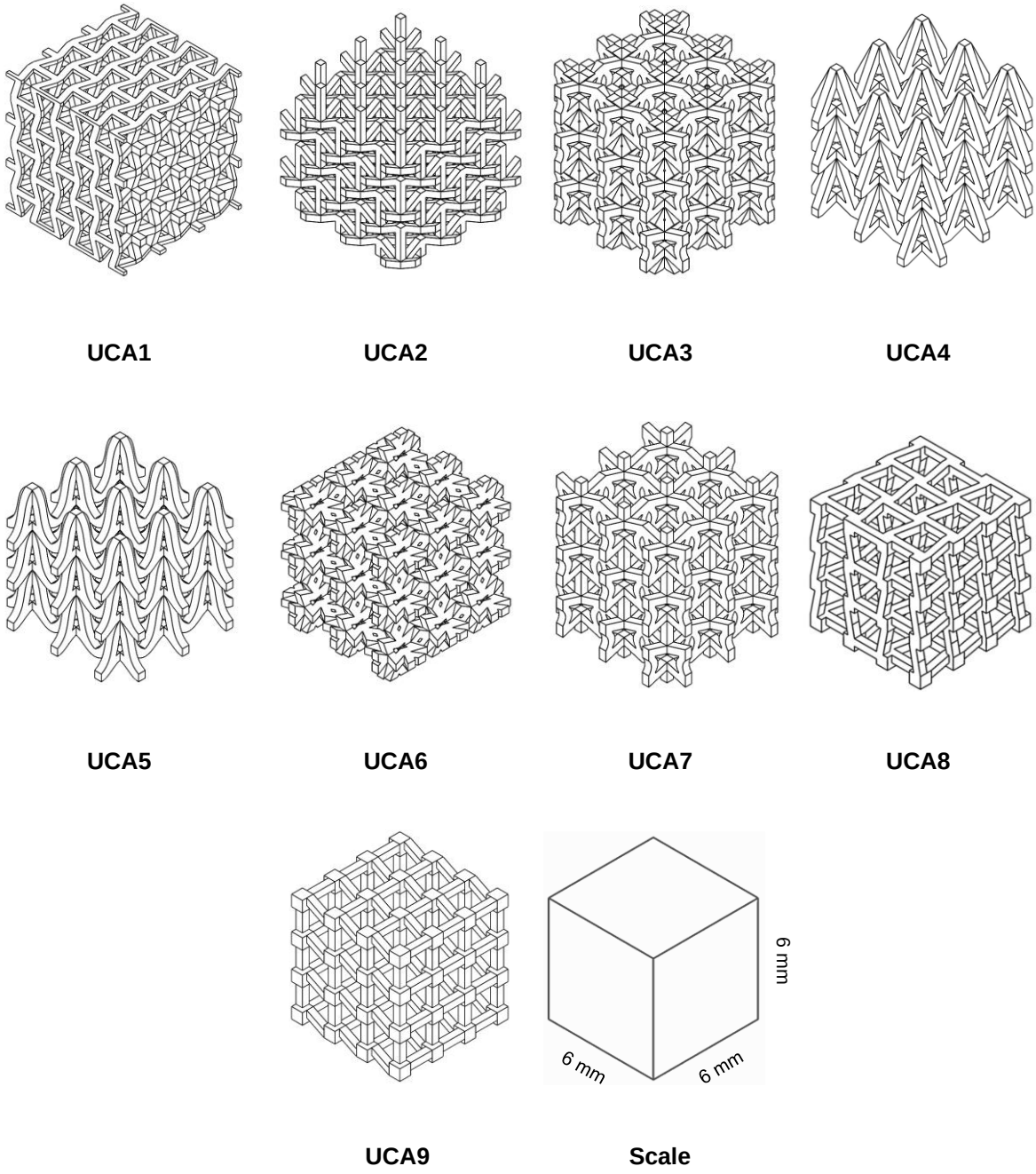

Figure 4.2. Unit cell assemblies (UCA) designed for finite element qualification

4.2.2. Finite element analysis of unit cell assemblies (UCA)

The non-linear elastic-plastic performance of all the nine UCA designs was studied using the finite element method (FEM). The Ansys non-linear mechanical solver was used to simulate the structural behaviour closely following the physical test conditions. Two square platens were modelled with boundary dimensions and thickness of 10 mm and 0.5 mm, respectively, to act as rigid body displacement-controlled actuators, as shown in Figure 4.4.

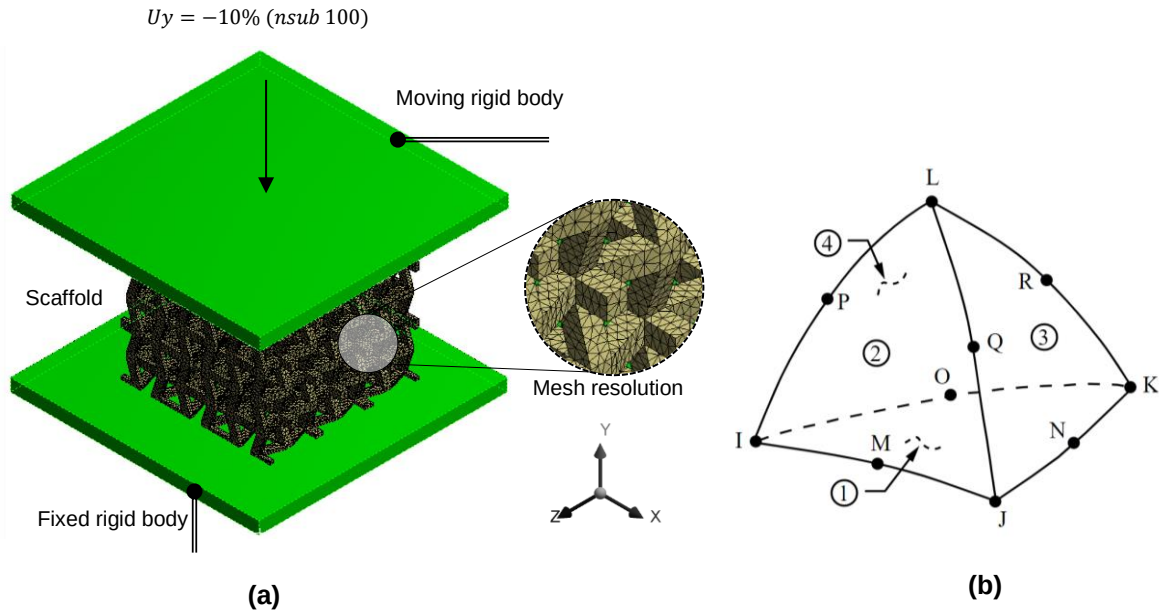

Figure 4.3. Finite element model and associated boundary conditions used to simulate the lateral deformation of unit cell assemblies

The thickness of the square plates is irrelevant as they were assumed to be rigid bodies. Consequently, the 0.5 mm thickness was randomly assumed in comparison with the overall dimensions of the unit cell assembly being simulated. Fixed support was placed for the bottom surface, and a -10% vertical displacement ramped at 100 substeps along the y direction. To avoid any spurious effects, the displacement of the compression plate was constrained in x and z, similar to the physical rig. For

computational efficiency, the contact between the rigid body and scaffold was modelled frictionless. Frictionless support provides support in the normal direction to the selected face or edge. The body cannot move or rotate or deform in the normal direction. But free to move or rotate or rotate in the tangential direction. While this is often not suitable when simulating bulk material with large surfaces in contact. Using frictionless support is a suitable approach when simulating highly porous material with limited contact between the compression plate and material as is the case here. The lower yield point with the lateral shrinkage prevents the material on the top surface from sliding without the need for frictional support while simulating an adequate scenario at significantly reduced solution time and computational efficiency. However, for this approach to work the compression plates to be modelled as rigid bodies justifying a frictionless option to reduce the tangential reaction forces between them.

Table 4.1. Bulk material properties used for the numerical model

Material property	**Value**
Elastic modulus (E_B)	200 (GPa)
Yield strength $\left(\sigma_{y\,(B)}\right)$	1060 (MPa)
Poisson's ratio (ν)	0.29
Density (ρ_B)	8.3 (g/cm^3)

The material model was based on the Bilinear isotropic strain hardening (BISO) to model the unit cell assemblies. Accordingly, the material behaviour is described by a bilinear stress-strain curve where the initial slope is described using E. The curve is assumed to be perfectly plastic post the yield strength. The material parameters used for the numerical analysis were taken from EOS CoCrMo material data sheet [275], as listed in Table 4.1.

Table 4.2. Elemental and nodal distribution associated with the converged structural FE model

Unit cell assemblies	Elements	Nodes
UCA1	209951	416688
UCA2	198209	406814
UCA3	172371	340016
UCA4	110923	229691
UCA5	107618	223237
UCA6	155969	311718
UCA7	150590	311618
UCA8	98608	206012
UCA9	68982	148101

The unit cell assemblies were modelled using 3D, 10 node higher order tetrahedral element SOLID187 as shown in Figure 4.3b resulting in nodal and elemental distribution as listed in Table 4.2. The global elemental matrix was solved using a 6-core i7 10750H CPU at 2.60 GHz assisted by 16 GB RAM, resulting in a solution time of approximately 895.4 seconds.

4.2.3. Additive manufacturing

4.2.3.1. CoCrMo superalloy feedstock

CoCrMo superalloys are famous for their high corrosion resistance and wear resistance [276]. These alloys also present favourable biocompatibility, which makes them be widely utilised as surgical prostheses. This alloy's microstructure and properties, such as hardness, wear resistance, rely primarily on the carbon composition and the nature of heat treatment applied [277]. Experiments have been conducted using various heat treatments to investigate the mechanical characteristics of CoCrMo alloys. Most of these heat treatment studies revealed that M23C6 type carbides precipitated along the grain boundaries of the alloy. Earlier research

regarding laser fabrication of CoCrMo alloy indicated that dense, metallurgically sound parts could be gotten with a fine microstructure upon the optimisation of the process parameters [278,279]. Nevertheless, research on laser-assisted additive production of CoCrMo alloy revealed that high scan speed, low powder feed rate, and high laser power could produce components having perfect electrochemical, tribological, and mechanical characteristics [280].

Cobalt-chrome metal alloys were initially established for aircraft engines and other heat-resistant components. These alloys are considered as having unmatched toughness and strength, alongside high corrosion and wear resistance. This alloy has a better corrosion resistance compared to stainless steel [281]. Generally, the cobalt-chrome alloy is made up of cobalt, chrome and other metal materials, including nickel and molybdenum. Cobalt-chromium or cobalt chrome is typically adopted in complex and demanding applications like dental, medical, gas turbines, rings, and other jewellery, courtesy of its biocompatibility. Cobalt-chrome alloys are mainly utilised for dental casting and artificial joints [281,282].

Table 4.3. Chemical composition of the CoCrMo alloy used

Elements	**Co**	**Cr**	**Mo**	**Si**	**Mn**	**Fe**	**C**	**Ni**
Composition (wt. %)	60-65	26-30	5-7	≤ 1.0	≤ 1.0	≤ 0.75	≤ 0.16	≤ 0.1

CoCrMo alloys are typically utilised for hip replacement and dental restoration because of their biocompatibility, good mechanical characteristics, and high corrosion resistance than titanium alloys [49,277]. When compared to other biomedical alloys such as CoCrMo and stainless steel, titanium alloys are often preferred for orthopaedic applications due to their relatively low stiffness. Nevertheless, the effective

compressive properties of CoCrMo cellular structures with stiffness characteristics that mimic the human femur are of interest. All scaffolds were manufactured using the Cobalt chromium MP1 supplied by EOS, which is a biocompatible CoCrMo superalloy with composition as listed in Table 4.3 suitable for biomedical applications. It has a density of 8.3 g/cm^3, yield strength of 1060 MPa, Poisson's ratio of 0.29 and elastic modulus of 200 GPa as per in material supplier data sheet.

Metallic biomaterials are the preferred choice for engineering industries and orthopaedic applications, such as bone implants, and include cobalt-chromium alloys (CoCrMo) and titanium alloys (Ti6Al4V). Ti6Al4V is the most common material to use in bone scaffold applications due to its biocompatibility, high strength, low weight ratio and outstanding corrosion resistance. In most cases, load-bearing implants were manufactured using Titanium as it has a low bulk stiffness (104GPa) offering lower stiffness when made porous (<50%). Compared to other metallic biomaterials, CoCrMo alloys have superior corrosion resistance in the human body environment, high mechanical strength, and low wear rates together with low coefficients of friction. CoCrMo alloys, however, have a greater Young's modulus of 200 GPa than the characteristics of bone (1-30 GPa). The stress shielding phenomenon, which results in bone resorption around the implant and causes it to loosen, is brought on by the implant's stiffness mismatch with the bone. This necessitates revision operations. As such when considering bulk materials for biomedical applications, using Ti6Al4V offers a higher potential in reducing stress shielding in comparison to CoCrMo due to the comparatively lower E value. However, this advantage does not translate to the development of porous material where mechanical properties can be largely controlled by relative density and pore shape, an aspect that is exploited in this research.

4.2.3.2. CoCrMo Powder characterisation

The CoCrMo powder exhibit a wide range of particle size distribution, where most of its particles are spherical in shape, having a grainy surface, but there are also exist agglomerates that have a smoother surface [283]. The primary properties of powders are particle shape (morphology) and particle size (granulometry). Technological characteristics of powders, such as surface area, flowability, bulk density, among others, and the potential fields of their adoption are determined by these features [284,285]. Therefore, dynamic image analysis was used to confirm the powder quality of CoCrMo superalloy using a Retsch Technology Camsizer X2 particle size analyser.

4.2.3.3. Selective laser melting

The SLM technique was used to fabricate both the scaffold designs and the tensile test coupons. All samples were built by using an EOS M290 direct metal laser sintering machine with a laser spot size of 100 µm and layer thickness of 40 µm. The CoCrMo powder was selectively melted until the needed geometry was fabricated. Optimum process parameters to fabricate a dense part include a laser power of 290 W, a scan speed of 950 mm/s and a hatch distance of 0.11 mm. The process parameters were kept constant for the fabrication of both the tensile test specimen and the scaffolds.

Argon inert gas atmosphere was used inside the chamber with horizontal laser beam scanning to melt the CoCrMo particles together during the process. The process was carried out layer-by-layer, with the build platform being lowered vertically as each layer was completed. Following that, the powder feeder and re-coater spread the powder for the next layer and the process is repeated until a fully dense part is built. A steel base plate with dimensions of 250×250×25 mm fixed on a heating plate at 230˚C was

used as the substrate both for the tensile test and scaffold samples. All samples were heat-treated post-printing at 1150˚C for six hours. Stress relieved scaffolds and tensile test samples were removed from the base plate by using wire Electro discharge machining (EDM).

4.2.4. Scanning Electron Microscopy (SEM)

Microscopes and related technology are used in a wide range of applications, including X-ray microscopy, optical microscopy, scanning probe microscopy, and scanning acoustic microscopy. Scanning Electron microscopy (SEM) is one of the most extensively used techniques among these due to its high magnification [286]. SEM work similarly to optical microscopes, but instead of using light, it employs a focussed stream of electrons to “image” the specimen and obtain information about the microscopic structure and composition [287]. The electronic console and the electron column are the two major components of SEM. Instrument settings such as filament current, accelerating voltage, focus, magnification, brightness, and contrast can all be controlled using the electronic console. The electron column is where an electron beam is produced in a vacuum atmosphere, focussed to a small diameter, and scanned across a specimen’s surface using electromagnetic deflection coils [287,288]. Secondary electrons, backscattered electrons, and distinctive X-rays are produced as the electrons contact the specimen. Then one or more detectors capture these signals to create images, which are then shown on the computer screen [8]. In this work, EVO 50 SEM manufactured by Zeiss is used to characterise the morphology of CoCrMo feedstock and printed samples.

4.3. Results and discussion

4.3.1. Unit cell properties

The focus of the thesis is on developing a bone scaffold that exhibits auxetic behaviour and can be additively manufactured. The first step was to identify a range of suitable unit cells for the scaffold to establish auxetic behaviour from which a suitable variant can be derived for further optimisation. The scope of this unit cell selection was based on auxetic concepts [289–291] that resulted in $-\boldsymbol{\upsilon}$. The Poisson's ratio of a traditional micro-lattices is positive. However, when a material deviates from the norm and gives rise to a negative Poisson's ratio ($-\boldsymbol{\upsilon}$), such structures can be classified auxetic [292–296]. Micro-lattices that exhibit $-\boldsymbol{\upsilon}$ are increasingly being sought due to their peculiar effects, which often cannot be achieved through traditional lattices [297–300]. These effects then translate to their tremendous potential in applications such as the ones explored in this study.

Though there are exceptions, widely studied $-\boldsymbol{\upsilon}$ structures fall under one of the two categories, namely re-entrant [301–306] and chiral [147,162,307–310]. Although additive manufacturing allows conceiving structures that fall under any category, the most studied variant is the re-entrant category. The primary reason for this is the simplicity of the re-entrant architecture allowing it to be used for a wide range of structural applications.

Nine unit cells are considered for initial analysis; the primary criteria for the selection of unit cells to be considered for the scaffold is their auxeticity, which means lateral shrinkage under axial compression. Although this is evaluated through the numerical model presented in a subsequent section, it was deemed appropriate to evaluate the

theoretical mechanical performance of all unit cells to make an informed decision. According to Ashby's criterion [263], cellular structures made up of repeatable unit cells can be theoretically characterised using their relative density. Consequently, the theoretical effective elastic modulus (E_{thr}) and compressive strength ($\sigma_{y\,(thr)}$) can be related to their relative densities (ρ_r) using Equations (4.1) and (4.2) respectively:

$$E_{thr} \approx E_B {\rho_r}^2 \tag{4.1}$$

$$\sigma_{y\,(thr)} \approx \sigma_{y\,(B)} \rho_r^{\left(\frac{3}{2}\right)} \tag{4.2}$$

where E_B and $\sigma_{y\,(B)}$ are Young's modulus and stress at yield of the bulk material, as listed in Table 4.1. The density (ρ_{uc}) of the unit cell can be calculated by the mass (m_{uc}) divide by volume (V_{uc}) on all the UCs.

Table 4.4. Properties of all the nine-unit cell designs where m_{UC}, V_{UC}, ρ_r, E_{thr} and σ_y are mass, volume, relative density, theoretical elastic modulus and yield strength of the unit cells respectively

Scaffold Design	**Properties**				
	$\boldsymbol{m_{UC}}$ **(g)**	$\boldsymbol{V_{UC}}$ **(mm^3)**	$\boldsymbol{\rho_r}$	$\boldsymbol{E_{thr}}$ **(GPa)**	$\boldsymbol{\sigma_y}$ **(MPa)**
UC1	0.0134	8	0.2018	8.144	96.092
UC2	0.0059	8	0.0888	1.577	28.049
UC3	0.0110	8	0.1656	5.484	71.432
UC4	0.0078	8	0.1174	2.756	42.639
UC5	0.0074	8	0.1114	2.481	39.412
UC6	0.0099	8	0.1490	4.440	60.965
UC7	0.0089	8	0.1340	3.591	51.995
UC8	0.0174	8	0.2620	13.728	142.153
UC9	0.0173	8	0.2605	13.572	140.934

Evaluating the theoretical performance of the unit cells based on Ashby's criterion as listed in Table 4.4, UC8 showed the highest effective elastic modulus and compressive strength of 13.728 GPa and 142.153 MPa, respectively which is representative of the

low porosity. The lowest performance was exhibited by UC2 at 1.577 GPa (E_{thr}) and 28.049 MPa ($\sigma_{y\ (thr)}$), which is representative of their high porosity. In summary, the theoretical modulus of all unit cells falls below the elastic modulus of tibial cortical bone at 18 GPa [311–313]. This was expected due to the high porosity of the UC designs considered.

4.3.2. Selection of auxetic unit cells for scaffold design

Using the numerical model, nine unit cell assemblies (UCAs) were evaluated for their potential to be used as the foundation for the auxetic bone scaffold. The properties and associated responses for all the assemblies are summarised in Table 4.5. Auxetic behaviour of cellular lattices are defined by their negative Poisson's ratio (-υ), which indicates a negative lateral strain ($-\varepsilon_{lat}$) signifying lateral shrinkage under axial compression. Traditional materials exhibit a lateral expansion demonstrating a positive lateral strain under axial compression. It can be seen from Table 4.5 that only five of the unit cell assemblies (UCA1-UCA5) exhibit negative lateral strain indicating a -υ.

Table 4.5. Properties of the lattice candidates evaluated for scaffold design

Property	**UCA1**	**UCA 2**	**UCA 3**	**UCA4**	**UCA5**	**UCA6**	**UCA7**	**UCA8**	**UCA9**
$\varepsilon_{axi}(\times 10^{-5})$	4.16	4.65	4.17	4.78	5.38	4.16	4.16	5.06	5.00
$\varepsilon_{lat}(\times 10^{-5})$	-1.31	-0.83	-0.56	-1.19	-1.56	0.34	0.04	0.06	1.24
υ	-0.31	-0.18	-0.13	-0.25	-0.29	0.08	0.12	0.12	0.25

The reason for this can be comprehended from Figure 4.5, which presents the lateral deformation of all the UCAs under axial compression. The lateral deformation exhibited by UCA1 to UCA5 (Figure 4.5a-4.5e) shows auxetic behaviour with lateral walls deforming in opposite directions. The number of unit cells engaged in lateral shrinkage by UCA1 is demonstrates the highest negative Poisson's ratio of -0.31.

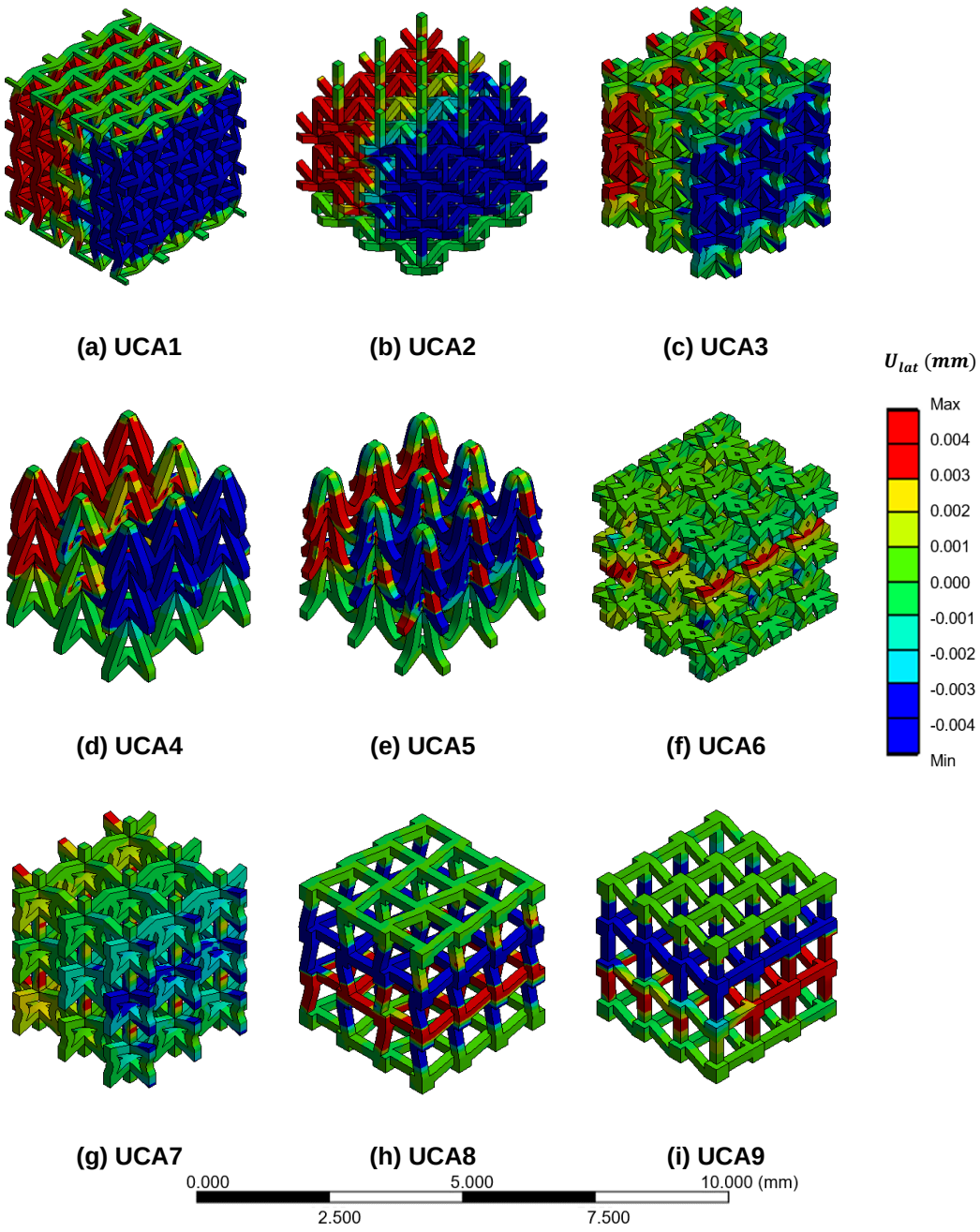

Figure 4.4. Auxeticity of UC assemblies by FEA

Looking at the lateral deformation of UCA6, as shown in Figure 4.5f, shows the lowest expansion, which indicates a Poisson's ratio close to zero at 0.08. A traditional lateral expansion is exhibited by UC7, UC8 and UCA9 (Figure 4.5g-4.5i), indicating a positive Poisson's ratio. Based on the numerical results, only five lattices are suitable for auxetic bone scaffolds, which are UCA1 to UCA5. As such, these designs are

considered for the design of the auxetic bone scaffolds, as explained in subsequent sections.

4.3.3. Design of auxetic bone scaffolds

A structure of an AM porous bone scaffold is informed by the unit cell, which dictates the mechanical properties. A porous scaffold will have a lower elastic modulus (E) and yield strength in comparison to the bulk material properties. In this case of this study, the bulk material of choice is biocompatible CoCrMo superalloy which has significantly larger elastic modulus and yield strength in comparison to tibial bone. As such, the porous design can aid in reducing the stiffness of the scaffold to avoid stress shielding between the scaffold and the host bone.

Following the initial numerical qualification of the different unit cells (UC1-UC9), a total of five unit cells (UC1-UC5) was deemed appropriate for scaffold design. The linear mirroring of UCs in x, y and z coordinates resulted in five respective scaffold designs designated AX1 to AX5, as shown in Figure. 4.5. AX1, AX2, AX3, AX4 and AX5 used unit cells UC1 (re-entrant), UC2 (arrowhead), UC3 (modified re-entrant), UC4 (double arrowhead) and UC5 (bell-shaped) respectively.

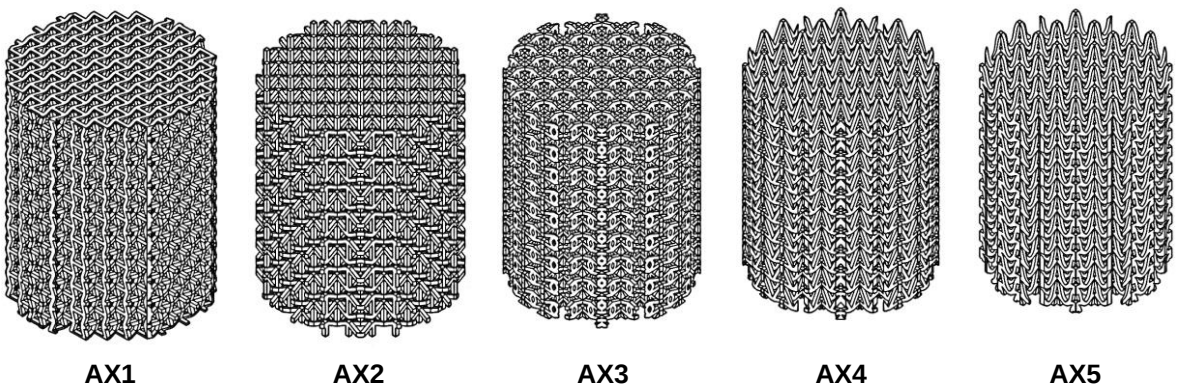

Figure 4.5. Scaffold designs featuring auxetic unit cells UC1 to UC5 considered in this thesis

The global cylindrical dimensions were derived to fit an equivalent tibial segmental horizontal cross-section of 180.024 mm^2. The diameter of an equivalent circle that can fit the tibial cross-section dictated the scaffold's radius of 7.25 mm. Accordingly, the cylindrical scaffolds can substitute an adult tibial section of length 18 mm. In many clinical studies [314–316], a critical size of bone segmental defect falls between 1-3 cm resulting in more than 50% of equivalent circumferential length, where the bone cannot heal unsupported. Accordingly, the length of all the scaffolds developed in this study has 18 mm, qualifying as critical length scaffolds.

Table 4.6. Properties of the auxetic bone scaffold designs

Properties	**Scaffold Designs**				
	AX1	AX2	AX3	AX4	AX5
Relative density (ρ_r)	0.1951	0.1614	0.1662	0.1326	0.1431
Porosity (%)	80.49	83.86	83.38	86.74	85.69

The resulting properties of the five scaffold designs are listed in Table 4.6. It can be seen that the scaffold properties satisfy the porosity requirements of higher than 50% for open porous bone scaffolds. The highest and lowest porosity was exhibited by scaffolds AX4 and AX1 at 86.74% and 80.49%, respectively. Once the designs were fabricated, the porosity data were compared to identify the deviation of the design from the ideal.

4.3.4. Additive manufacturing

4.3.4.1. Powder characteristics

All the five different scaffold designs were additively manufactured using gas atomised CoCrMo with powder morphology, as shown in Figure 4.6. It can be seen that the powdered particles are spherical and have satellite particles attached. Overall, a range

of particle size from 5 to 85 µm was identified. SLM benefits from a variety of particle sizes since it increases the packing density and flowability of the powder, both of which are important in generating a dense part. The particle analysis shows that the feedstock featured a volume and size distribution as shown in Figure 4.7a and 4.7b, respectively.

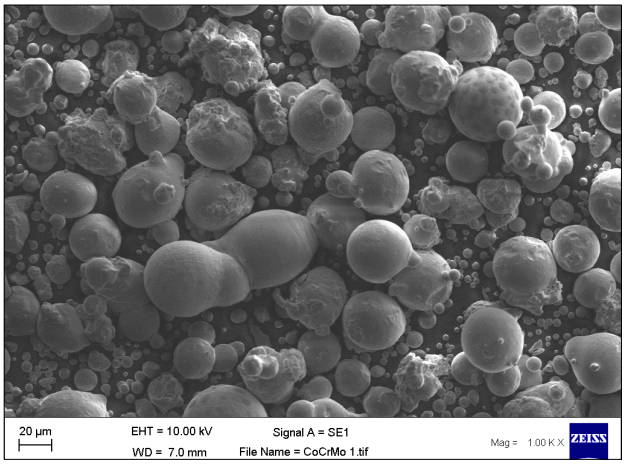

Figure 4.6. SEM micrograph of CoCrMo superalloy used for scaffold fabrication

Particle size distribution shown in Figure 4.7 can affect the flowability and packing of the powder and subsequently, the density, microstructure and mechanical properties of the SLM part [317,318]. For example, a large volume of fine particles can render metallic powder unusable for SLM processing due to strong cohesive forces negatively affecting the powder flowability [317]. The results from the particle analyser were used to distinguish the mode, mean and median values and volume fractions were used (D_{10}, D_{50}, and D_{90}) to identify the Particle Volume Distribution (PVD), as shown in Figure 5a. These values were used to establish excessively high or low particle distribution that can affect the powders' SLM processability.

The PVD analysis concluded a D_{10} of 13.2 µm, D_{50} of 28.8 µm and D_{90} of 46.1 µm. D_{50} represents the median value, and therefore 50% of powder particles were less than

28.8 µm in size. With a D_{10} and D_{90} of 13.2 and 46.1 µm, the results showed that the PVD is relatively evenly spread with only 10% of particles below 18.8 µm. This can be explained by Figure 4.6, where the smaller satellite particles become attached to the larger spherical particles during the atomisation process. Above D_{90} of 10% can result in unusable powder for SLM processing [317]; in comparison, the PSD shown in Figure 4.7b suggest that the atomised CoCrMo powder has a near normal size distribution and is suitable for SLM.

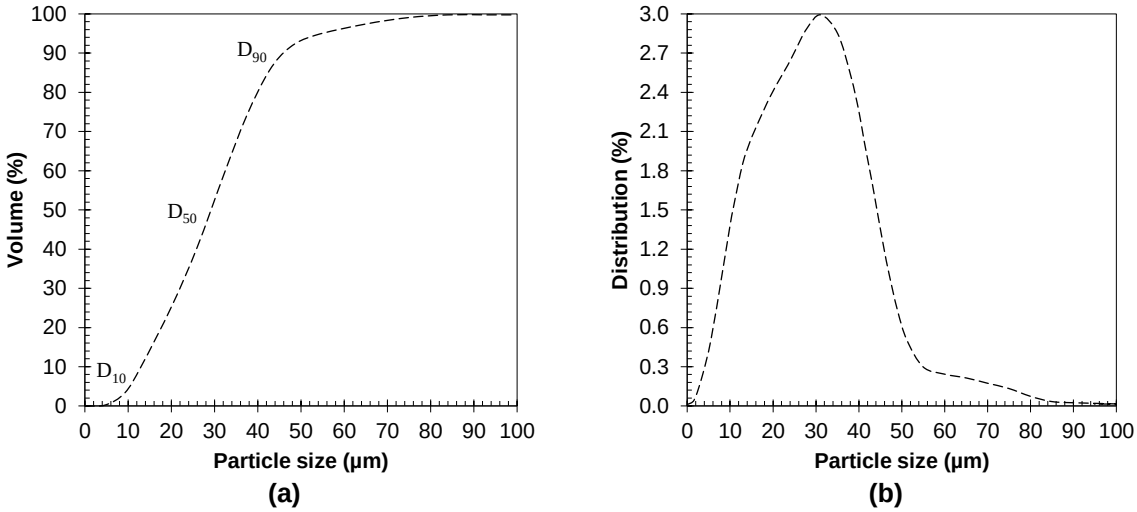

Figure 4.7. Characteristics of the CoCrMo feedstock used for the additive manufacturing of auxetic bone scaffolds showing (a) volume-size distribution and (b) the particle size distribution (PSD)

4.3.4.2. Selective laser melted samples

Selective laser melting was used to additively manufacture the five different scaffold designs (AX1-AX5) along with tensile test coupons, as shown in Figure 4.8. As can be seen from Figure 4.8a and 4.8b, the resulting scaffolds feature an open cellular architecture under varying strut orientation, pore size and porosity [268]. The varying pore size of a unit cell enhances vascularisation, resulting in increased bone ingrowth [319]. Small pores are better for soft tissue growth, and bigger pore sizes increase the permeability, which enhances bone ingrowth [279,280]. Pore sizes between 50 and

650 microns and porosity more than 50% are required for bone ingrowth. Furthermore, the strut thickness of 300 µm accounts for the manufacturing limitation possessed by SLM, allowing the smallest nominal strut thickness of 200 µm [11].

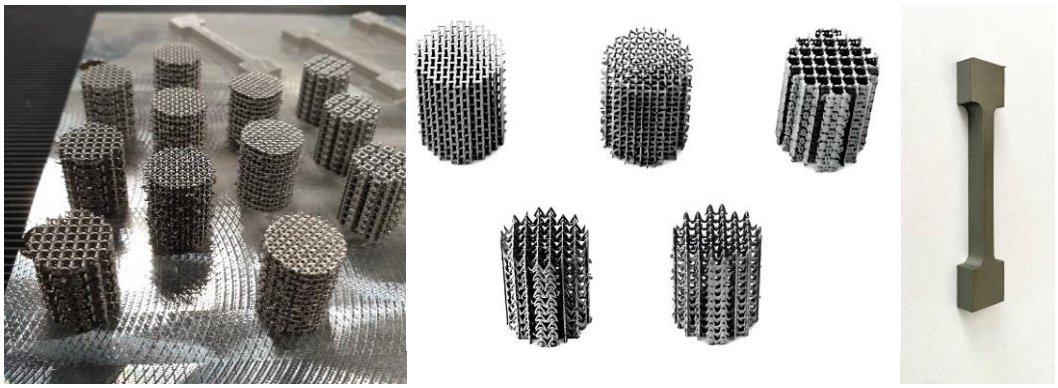

(a) **(b)** **(c)**

Figure 4.8. Selective laser melted CoCrMo samples showing (a) printed samples on the base plate before post-processing, (b) post-processed scaffold samples and (c) tensile test coupon

Three samples were built for each design without the use of support structures owning to the sub-millimetre scale of the unit cell features and the relatively small overhang lengths. Figure 4.8a shows the printed samples on the build plate without post-processing. Subsequently, the samples were removed from the base plate using wire EDM. Shotblasting was used to remove the partially sintered and loose particles revealing a smoother surface as shown in Figure 4.8b and 4.8c.

Table 4.7. Physical parameters and porosity of the additively manufactured scaffolds

Properties	**Additively manufactured scaffolds**				
	AX1	**AX2**	**AX3**	**AX4**	**AX5**
Mass (m_{Ax}) grams	6.4	5.7	5.4	4.4	4.6
Relative density (ρ_r)	0.2695	0.2328	0.2183	0.1802	0.1884
Porosity (%)	73.05	76.72	78.17	81.98	81.16

The resulting porosity of the additively manufactured scaffolds is listed in Table 4.7. It can be seen that the printed scaffolds resulted in a porosity range of 73%-82%, which

is slightly different from ideal geometry at 80-87%. Although the printed scaffolds exhibited a slight lower comparison in comparison to CAD, the trend was similar, as shown in Figure 4.9. SEM analysis of the scaffolds was carried out to characterise the difference in porosity between the printed and ideal scaffolds, which is explained in the next section.

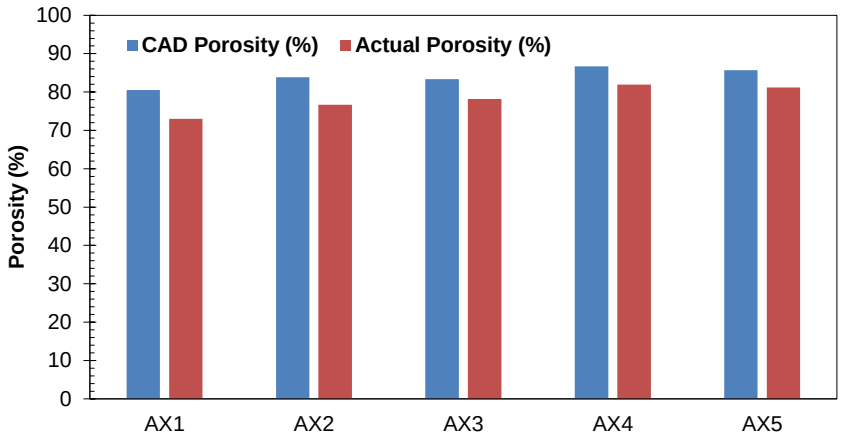

Figure 4.9. Comparison of porosity between ideal and actual scaffolds

4.3.4.3. Morphology of the printed scaffolds

SEM analysis of the printed scaffolds was carried out to analyse the differences in porosity between ideal and printed scaffold samples. Figure 4.10 shows the influence of shot blasting on the printed samples. Comparing the structures before (Figure 4.10a) and after (Figure 4.10b) shot blasting, it is evident that shot blasting removed most of the semi-molten and loose powdered particles from the scaffolds. However, on close inspection of joints, as shown in Figure 4.10c, some semi-molten powders were observed. Although the micron level, considering the number of joints, can contribute to a reduction in porosity which was observed as indicated by Tan *et al.* [11].

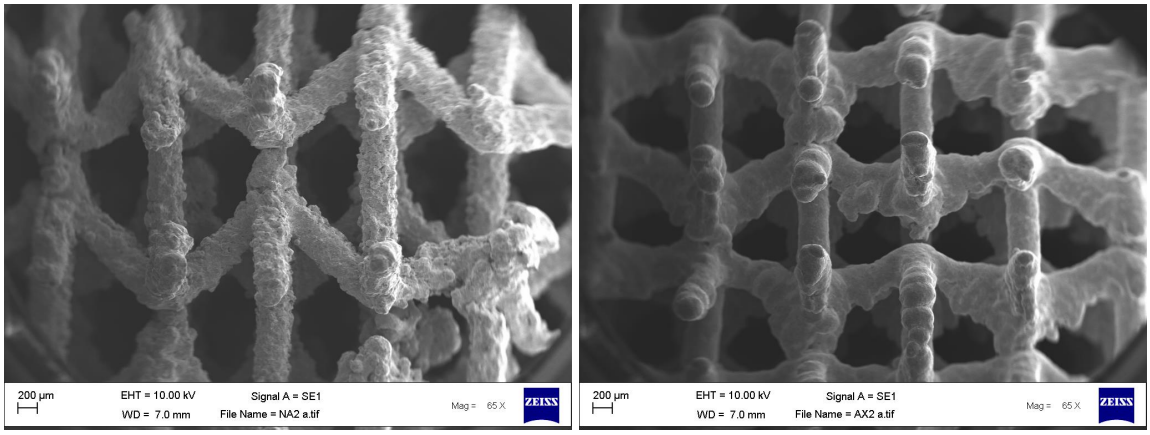

(a) **(b)**

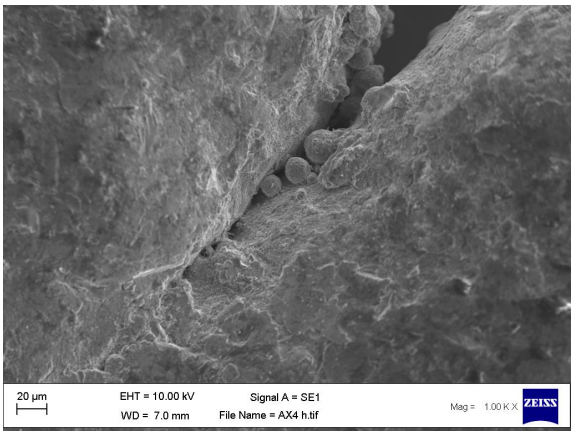

(c)

Figure 4.10. Scanning electron micrograph showing (a) scaffold as manufactured before shot blasting, (b) after shot blasting and (c) variation of joints from ideal after shot blasting

A rough surface finish is also evident in both Figure 4.10 and Figure 4.11, which is representative of the characteristic stair-step effect during SLM. The resulting morphology of all post-processed CoCrMo scaffolds is shown in Figure 4.11. While the interconnected porosity and the representative geometry closely followed the CAD (ideal geometry), the average strut thickness was found to vary by approximately 50 µm. While this is in line with existing literature [318,320–322] on SLM of thin struts (<300 µm), the overall effect was found to contribute to a variation of ~5.8%. This means that the SLM scaffolds showed a porosity of 5.8% lower than their ideal counterparts.

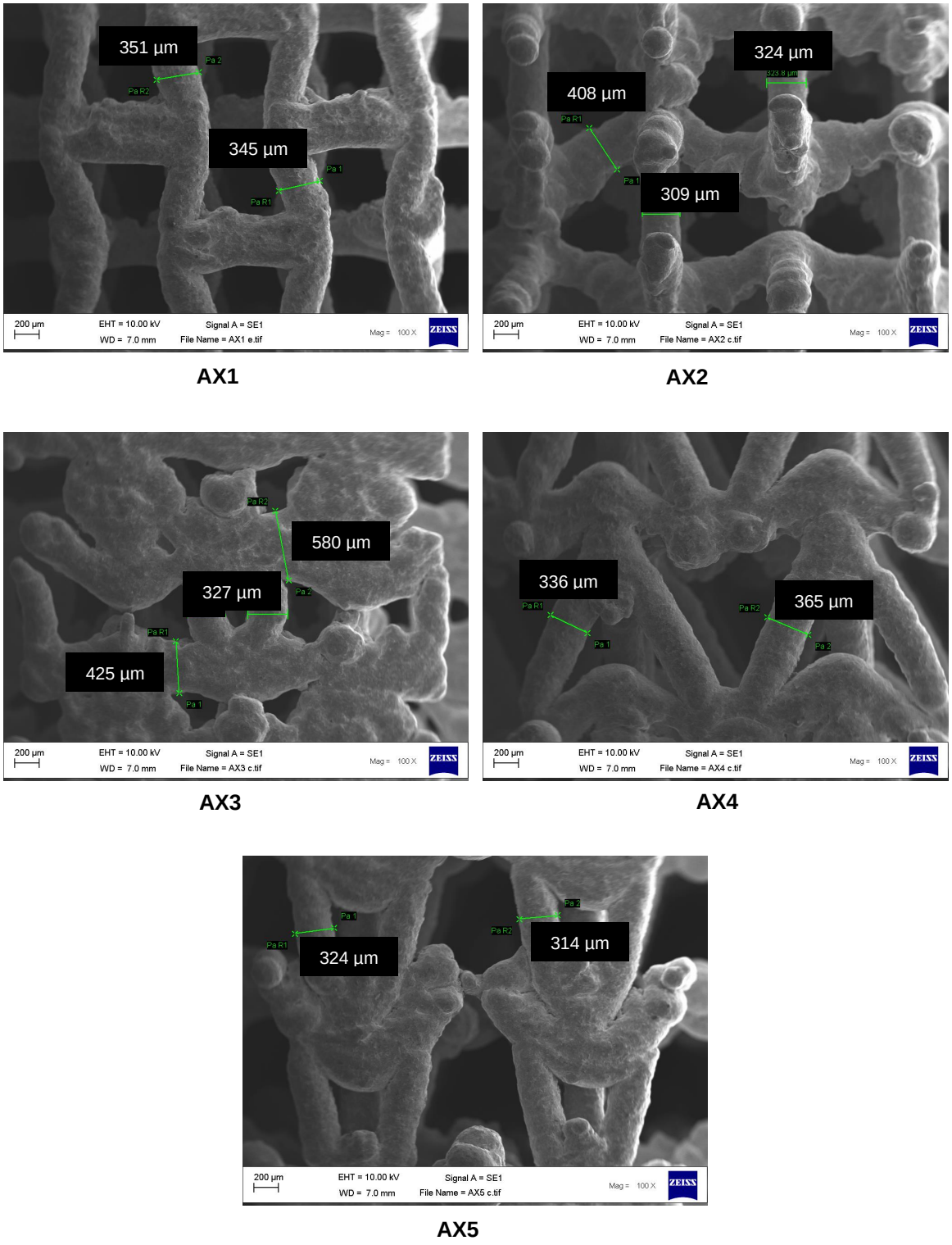

Figure 4.11. SEM data showing the influence of selective laser melting on strut dimension

Comparing the variations in strut thickness observed with that of literature, Benedetti *et al.* [131] reported that the struts parallel to the building direction have an oversizing

tendency largely driven by the laser beam size in comparison to the strut thickness being printed. Furthermore, the existence of un-melted particles bound to the struts can also be a cause of disparity in strut dimension. Although similar observations were found in other studies [11,49], the uneven surface finish in interconnected porosity was highlighted as favourable for tissue ingrowth.

In summary, the observations in Figure 4.11 are consistent with literature with strut thickness deviating from the original design without largely affecting porosity. It can be seen that there is both over and under-sizing of the strut thickness due to the SLM process. However, the variation in strut thickness was largely influenced by strut orientation, with vertically oriented struts under-sized and horizontally oriented struts over-sized [323].

4.4. Conclusion

Auxetic materials are designer biomaterials with unusual and unprecedented properties that originate from their geometrical architecture at micron scales. This concept has been used in the context CoCrMo additively manufactured bone scaffolds with the ultimate aim of offering stiffness matching. In this context, this chapter demonstrates the use of selective laser melting to fabricate porous auxetic CoCrMo bone scaffolds and reports the design, processing parameters and print quality evaluation for the first time.

- Nine open porous unit cell assemblies (UCA1-UCA9) were digitally conceived, and their auxeticity was characterised using the finite element method (FEM). The results identified five potential candidates (UCA1-UCA5) to be suitable for the design of auxetic bone scaffolds exhibiting a υ in the range of -0.13 to -0.31.

- Based on the five auxetic unit cells, open porous cellular bone scaffolds were designed to mimic a tibia critical size bone defect at a porosity range of 80-87%. The theoretical elastic modulus and yield strength of the unit cells were found to be in the range of 1.5-8.1 GPa and 28-96 MPa, respectively.
- A CoCrMo particle volume distribution at D10, D50 and D90 of 13.2 µm, 28.8 µm and 46.1 µm, respectively, was found to be suitable for selective laser melting for all the five porous auxetic bone scaffolds developed.
- SEM analysis has been carried out to identify the dimensional inaccuracies of the lattice structures. The results showed that SLM scaffolds featured an average porosity of 5.8% lower to their ideal design.

Overall, the chapter demonstrated that SLM is suitable to fabricate a range of CoCrMo auxetic bone scaffolds that offer high porosity and quality consistent with the literature on other metallic biomaterials such as titanium. The mechanical performance of the fabricated CoCrMo scaffolds will be characterised through FEM and physical tests in the next chapter.

Chapter 5

Mechanical performance of selective laser melted CoCrMo

5.1. Introduction

This chapter describes the mechanical properties of the SLM processed CoCrMo bulk materials and the compression behaviour of auxetic CoCrMo scaffolds. Tensile test coupons were fabricated using identical SLM process parameters used for the bone scaffolds. These coupons were experimentally tested to derive the bulk material properties of CoCrMo as a result of selective laser melting. The data now only allows to benchmark process with literature as shown in this Chapter but also informs the finite element model in Chapter 6.

The suitability of using Gibson and Ashby models for the mechanical performance of the scaffold were carried out. Compression tests on scaffold prototypes were used to derive the stress-strain curve for each of the scaffolds. The stress-strain curve was subsequently used to evaluate all mechanical parameters such as elastic modulus, yield strength and Poisson's ratio of the scaffolds. The compression test data was also used to evaluate the failure mode of the scaffolds and to evaluate the suitability of the unit cell shape and the SLM process. Overall, the chapter presents the mechanical performance of five different auxetic bone scaffolds informed by re-entrant (AX1), arrowhead (AX2), modified re-entrant (AX3), double-arrowhead (AX4) and bell-shaped (AX5) architecture.

5.2. Methodology

All the test specimens were fabricated as discussed in Chapter 4, Section 4.2.3. The SEM methodology used to analyse the failed scaffold samples were as presented in Chapter 4, Section 4.2.4. To avoid repetition, only new methodologies previously not presented are discussed in this chapter.

5.2.1. Theoretical prediction

According to Gibson and Ashby [263], the mechanical performance of cellular structures can be predicted using their relative density. Density is an important factor that affects the mechanical performance of a cellular structure. Using a digital scale, the masses of the manufactured scaffolds were measured and used to determine the density of each scaffold (ρ_S), which is defined as the ratio of the measured mass to its volume as shown in Equation (5.1).

The density of the porous scaffold can be calculated by the mass (m_S) of the scaffold divided by volume (V_S) of the scaffold. By using the density of bulk material (ρ_B) the relative density ($\rho_{r(S)}$) of the porous scaffolds can be then determined using Equation (5.2). The model was presented by Gibson and Ashby in 1997 and has been used to predict the elastic modulus (E_s), yield strength ($\sigma_{y(s)}$) and density (ρ_S) of the porous scaffold. The elastic modulus of a cellular scaffold can be calculated using Equation (5.3):

$$\rho_S = \frac{m_S}{V_S} \tag{5.1}$$

$$\rho_{r(S)} = \frac{\rho_S}{\rho_B} \tag{5.2}$$

$$\frac{E_S}{E_B} = C\left(\frac{\rho_S}{\rho_B}\right)^2 \tag{5.3}$$

where E_B , ρ_B elastic modulus and density of the fully dense solid material. As such, the theoretical elastic modulus ($E_{thr(S)}$) and yield strength ($\sigma_{thr(S)}$) can be associated with their relative densities ($\rho_{r(S)}$). Therefore, Equations (5.4) and (5.5) can be used to predict the theoretical elastic modulus and yield strength of the scaffold, respectively.

$$E_{thr(S)} \approx E_B {\rho_{r(S)}}^2 \tag{5.4}$$

$$\sigma_{thr(S)} \approx \sigma_{y(B)} {\rho_{r(S)}}^{(\frac{3}{2})} \tag{5.5}$$

5.2.2. Experimental mechanical testing

Zwick Roell 1474 materials testing machine with a maximum load capacity of 100 kN was used to conduct uniaxial tension and compression tests on the bulk material and scaffold, respectively. The test setup featured a mounted camera to capture deformation, as shown in Figure 5.1. The tests were carried out to investigate both the mechanical properties of the bulk material and the compressive performance of five scaffolds following to BSEN ISO 13314 [324] standard. Before commencing the experimental tests, the setup was calibrated according to BSEN ISO 7500-1 [325].

Three samples (n=3) from the same batch have analysed to get the mean value and standard deviation for the elastic modulus and yield strength according to BSEN ISO 6892-1 standards [326]. Crosshead movement at a rate of 0.08 mm/s was used to load the test samples to failure. A maximum load of 80 kN was applied, with a force shutdown threshold of 50% to avoid the platens from crashing if a catastrophic failure occurs.

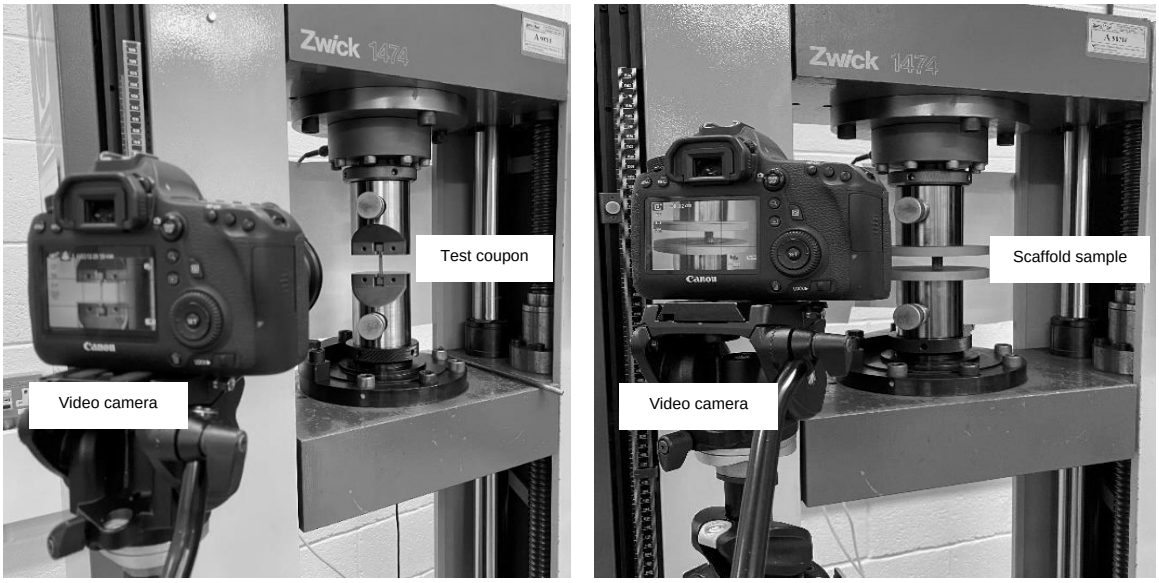

(a) **(b)**

Figure 5.1. Mechanical test setup showing (a) tensile test for the evaluation of CoCrMo bulk material properties and (b) compression test for mechanical properties of the auxetic scaffold

The tensile test coupons were pulled to rupture, and the compressive samples were loaded to deformation of 9 mm (50% of the scaffold height). Three samples from each structure were tested, and mean values of elastic modulus and yield strength were determined by using test data. The video was recorded for every specimen from the beginning of the test to complete failure. The force-displacement data was monitored and used to evaluate the stress-strain ($\sigma - \varepsilon$) curves for all the samples. The curves were subsequently used to calculate the elastic modulus of the bulk material and the scaffold as the slope of the elastic region. The 0.2% offset method was used to determine the yield strength of the specimens from the stress-strain curves.

The lateral strain values for the Poisson's ratio were measured from ImageJ using photographs taken during the elastic deformation of the scaffold. For precision, the transverse strain was computed at each lattice layer, and the average values were used, a method similar to Arjunan *et al.* [242]. Based on the experimental data, Equation (5.6) was used to calculate the Poisson's ratio.

$$v_{yx} = -\left(\frac{\varepsilon_{lat}}{\varepsilon_y}\right) \quad (5.6)$$

5.3. Results and discussion

5.3.1. Mechanical properties of selective laser melted CoCrMo

Mechanical tests were conducted on full dense CoCrMo tensile test coupons manufactured using optimum process parameters presented in Chapter 4, Section 4.2.3.3. Altogether three tensile test coupons (n=3) were axially pulled under quasi-static test conditions. The resulting stress-strain curve and respective failed samples are shown in Figure 5.2a and 5.2b respective.

Analysing the $\sigma - \varepsilon$ curves (Figure 5.2a) reveals consistent elastic and plastic regions for all the tensile coupons tested. However, despite featuring the identical process parameters for all the samples tested, a certain difference in the ultimate tensile strength can be observed between each of the three curves. The mechanical performance derived from average $\sigma - \varepsilon$ is summarised in Table 5.1. Comparing the results observed, it can be seen the parameters describing the strength (σ_y and σ_{ult}) of the material closely follow the datasheet.

Overall, a 2.54% and 8.29% difference was observed for σ_{ult} and σ_y, respectively between the tests carried out and the datasheet from the material supplier. When it comes to Young's modulus, a ~3% difference was found in comparison to the datasheet and others in the literature [327].

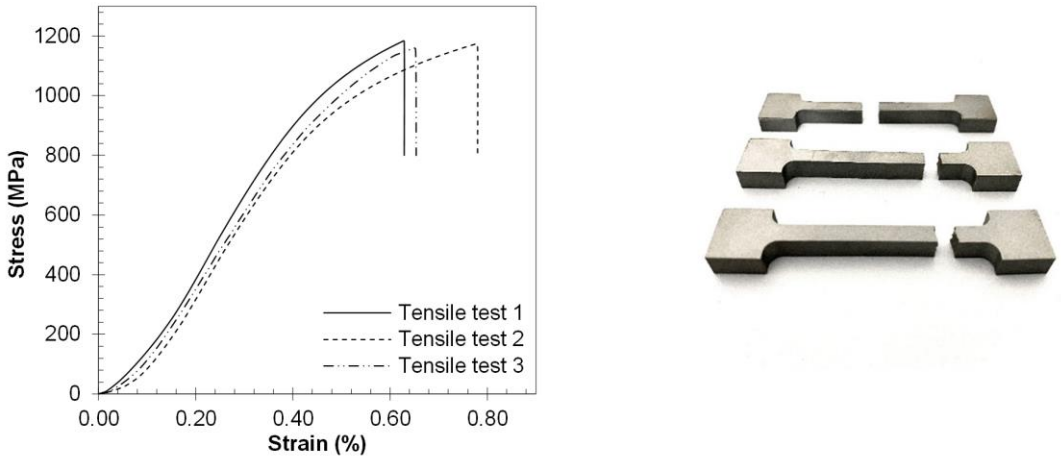

Figure 5.2. Mechanical performance of the selective laser melted CoCrMo material showing (a) the stress-strain relationship and (b) the failed tensile test coupons

Table 5.1. Material properties of CoCrMo obtained from tensile test data showing E, σ_y and σ_{ult} are the Young's modulus, yield strength and ultimate strength, respectively

Identifier	**E (GPa)**	**σ_y (MPa)**	**σ_{ult} (MPa)**	**Ref.**
Tensile test coupon	194.23±1.63	975.6±11	1169.81±10.44	This study
Material Datasheet	200	1060	1200±100	[275]
Dolgov *et al.*	213	720	-	[327]
Cornacchia *et al.*	200	550	975	[328]

However, this was expected due to the process parameters and heat treatment regimens used for the low stiffness variant. To put these observations into perspective, the cumulative parameter, 'laser energy density (e_{ld})' has to be introduced [329–332]. It is widely considered the critical parameter to characterise both the manufacturability [333] and mechanical performance [334] of SLM components and generally represents the energy density in J/mm^3 as shown in Equation (5.7).

$$e_{ld} = \frac{P_l}{v_s \times h_s \times t_l} \tag{5.7}$$

where P_l is the laser power (Watt), t_l is the layer thickness (mm), v_s (mm/s) is the scan speed and h_s (mm) is the hatch distance. Varying the process parameters affects the

thermo-physical properties during laser melting and hence affects the mechanical properties of the manufactured parts. For this study, the optimum process parameter combination and heat treatment regime (1150°C for 6 hrs) to lower the elastic modulus of the material was used. The methodology for this is further explained in the context of other materials in previous studies carried out by Arjunan *et al.* [335]. Reducing the E value of the bulk material is critical to improving the stress shielding and maladapted stress concentration bone scaffolds and allows for a realistic optimisation. Overall, the mechanical performance closely follows both the material test data and literature for SLM CoCrMo.

5.3.2. Ashby's criterion and the performance of CoCrMo auxetic scaffolds

The bending or stretching of cell walls can cause cellular structures to deform. The theoretical elastic modulus and yield strength of each scaffold were predicted using Ashby's criterion, as shown in Figure 5.3.

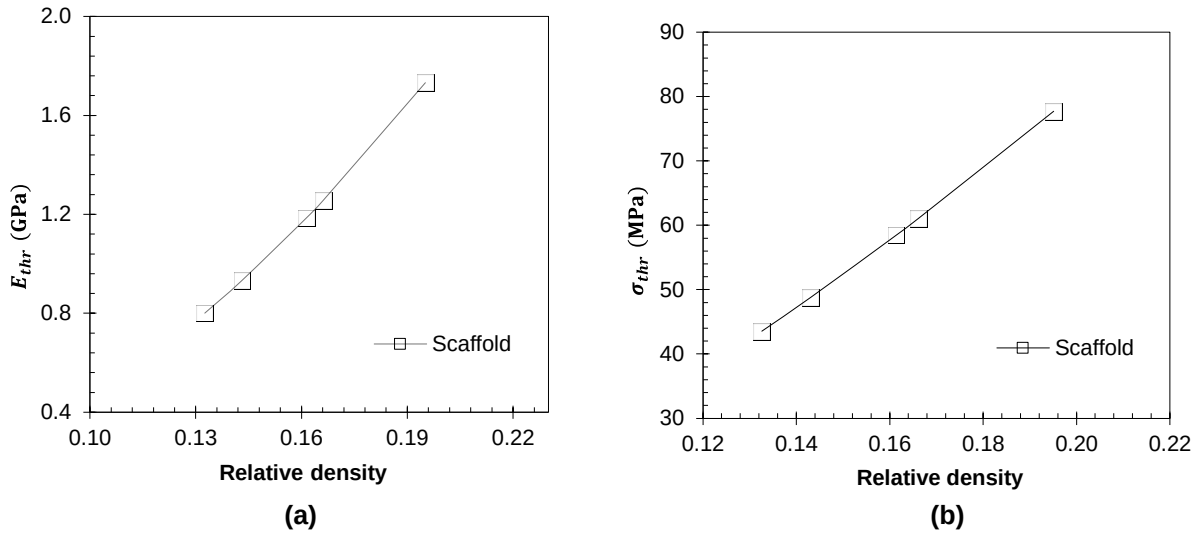

Figure 5.3. Theoretically predicted (a) elastic modulus (E_{thr}) (b) yield strength (σ_{thr}) for respective scaffolds

Using the Gibson and Ashby model, the performance of the scaffold in relation to their relative density was predicted. The scaffold AX1 showed the highest effective elastic modulus and yield strength of 1.73 GPa and 77.73 MPa, respectively. The lowest performance was exhibited by AX4, showing the elastic modulus and yield strength of 0.8 GPa and 43.55 MPa, respectively. As discussed in the literature, the stiffness of the bone depends on age, sex and location within the body. According to that, stiffness of the cortical bone lies between 3-30 GPa. Based on the predicted elastic modulus, some scaffolds fall within this range, making them suitable for further studies [11,86]. However, it is important to note that the aim of the thesis is to fabricate scaffolds that shows both stiffness matching and auxetic performance. Therefore, experimental characterisation of the scaffolds is required to predict the best design for optimisation.

Although Ashby's criterion is a useful tool in to predict the mechanical properties of cellular structures, they do not take into consideration the shape of the unit cell. This is a critical criterion for this research as the unit cell are unconventional, and the behaviour is auxetic. As such, experimental tests on the fabricated scaffolds are carried out to characterise their mechanical performance.

5.3.3. Elastic-plastic performance of CoCrMo auxetic scaffolds

Generally, the $\sigma - \varepsilon$ curve of cellular structures tends to show three characteristic regions, which in its entireness describes the elastic and plastic structural performance, as shown in Figure 5.4 [81]. The first characteristic regions can be speared into linear and non-linear elastic deformation, where a proportional $\sigma - \varepsilon$ relationship is followed by a non-linear region ending in a peak stress value referred to as the ultimate strength (σ_{ult}) [336]. This is usually followed by drop-in stress to the

plateau region, where stress fluctuations or serrations may be observed [337]. Further compression, results in a densification region followed by a plateau where the rises in stress can be primarily attributed to the interaction of the crushed material. However, the occurrence of the densification region depends largely on the type and porosity of the cellular structure and associated boundary conditions [338].

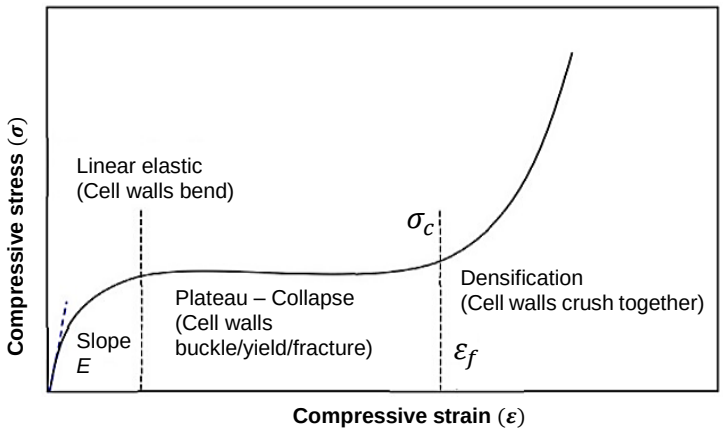

Figure 5.4. Typical compression test stress-strain curve for cellular materials [339]

The compressive $\sigma - \varepsilon$ curve of the SLM manufactured scaffolds are shown in Figure 5.5. Evaluating the results, as shown in Figure 5.5a to 5.5e, all the scaffolds showed both elastic and plastic regions. The scaffolds AX2 showed an initial collapse of around 4.6% of the strain before steadily climbing to peak stress of around 90 MPa before cell wall collapse occurs. This indicates an initial localised failure by the structure without involving the subsequent cellular layers during the initial part of the compression. This is due to the long straight vertical beams that form the primary load-bearing component of the unit-cell (UC2). The vertical beams above the top surface act as isolated load-bearing elements causing localised failure. However, as soon as the vertical beams fail, the cross walls interact with the structure stabilising it allowing it to withstand a higher load. Due to this unique phenomenon, AX2 showed the lowest yield strength of 32 MPa (Table 5.2).

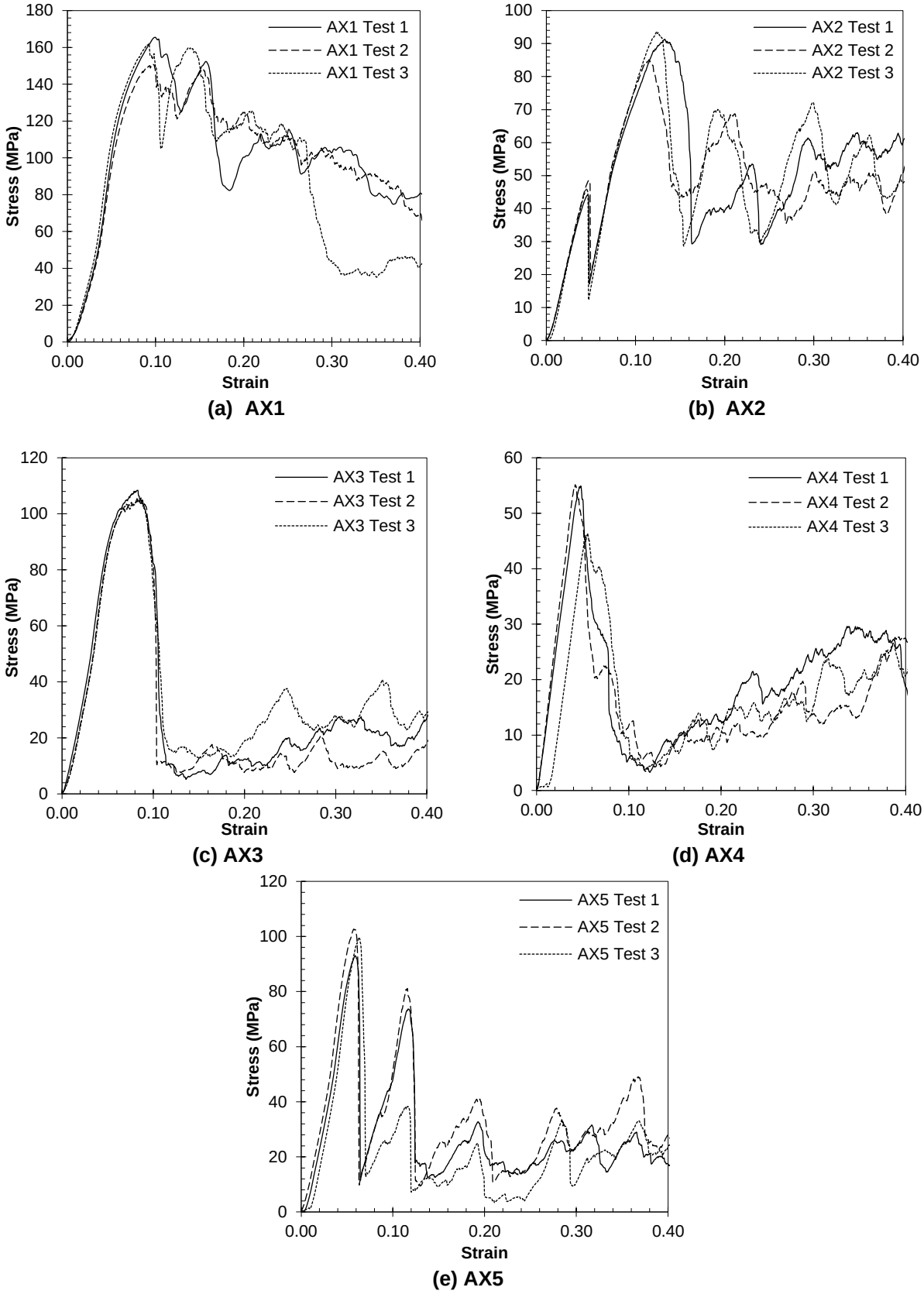

Figure 5.5. The experimental stress-strain relationship for selective laser melted CoCrMo auxetic bone scaffolds showing (a) AX1, (b) AX2, (c) AX3, (d) AX4 and (e) AX5

Comparing the performance of all scaffolds, the AX1 (Figure 5.5a) showed the highest yield strength and elastic modulus of 56 MPa and 1.66 GPa, respectively. The reason for the high performance is evident from the stress-strain curve (Figure 5.5a), where the highest stresses at the elastic range can be observed. This is due to the higher relative density which resulting the lowest porosity among other structures. From the unloaded state, the cell walls compress and bend to reach the plateau stage where plastic hinges form in the cell walls. Due to geometrical instability, they collapse and make self-contact; thus, a strain-hardening effect is initiated until the ultimate failure point.

AX3 showed an elastic modulus of 1.57 GPa and yield strength of 36 MPa, a reduction of 5.5% and 43.5%, respectively, when compared to the highest performing AX1. The large reduction in yield strength can be explained by the Poisson's ratio close to zero (-0.1). This means that the structure is moving vertically down, leading to catastrophic failure of the cell walls signified by the large drop in yield strength, as shown in Figure 5.5c. The post-yield plastic behaviour of AX3 also shows a lower capacity to resist the stress being developed, signified by low plastic peaks.

The catastrophic failure of the AX3 architecture can be observed in Figure 5.7c, confirming these observations. AX4 and AX5 have similar Poisson's ratio (-0.16) and shows classic behaviour of cellular structures with yield initiated by localised failure and post-yield behaviour signified by progressive layer-by-layer failure. Some peeling of boundary cells can also be observed for AX5, causing an initial large drop and subsequent high peak plastic stresses.

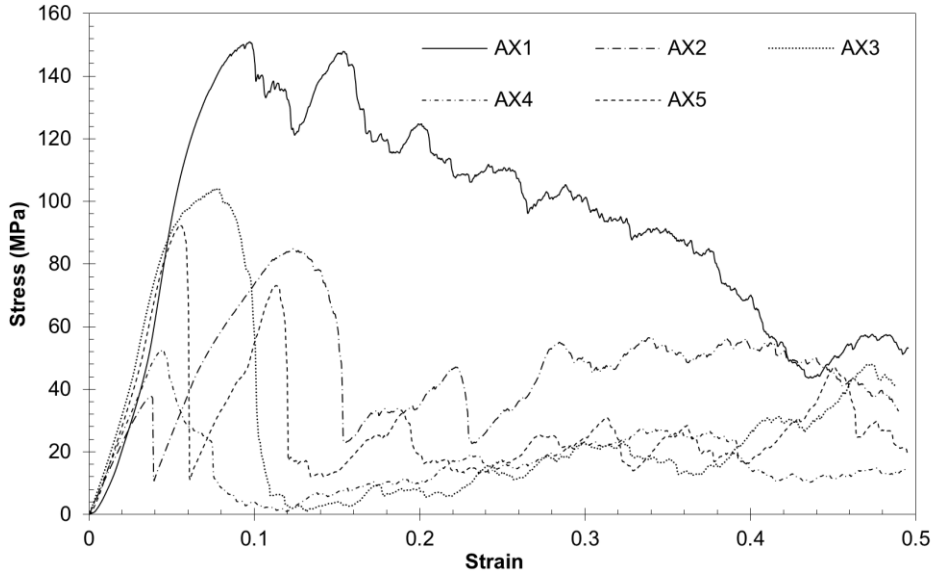

Figure 5.6. Typical compressive stress-strain behaviour for each structure

For the biomedical application of auxetic structures, the stiffness, strength and Poisson's ratio are the key aspects for the design consideration of scaffolds [64,340,341]. Comparing the stress-strain curve for all the five architectures, as shown in Figure 5.6, the overall best performance was observed for AX1 with the highest elastic modulus, yield strength and negative Poisson's ratio. The resulting performance for all the structures is shown in Table 5.2.

Table 5.2. Experimental mechanical properties of scaffolds

Design	**Manufactured sample porosity (%)**	**Mean elastic modulus (GPa)**	**Mean 0.2% Yield strength (MPa)**	**Mean Ultimate stress σ_{ult} (MPa)**	**Poisson's ratio**
AX1	73.05	1.66±0.47	56±1.24	158±6.65	-0.24
AX2	76.72	1.13±0.02	32±0.81	88.87±3.49	-0.13
AX3	78.17	1.57±0.02	36±0.62	104.53±2.40	-0.1
AX4	81.98	1.27±0.03	52±4.71	51.66±4.14	-0.16
AX5	81.16	1.6±0.08	40±0.84	97.9±3.83	-0.16

Overall, the elastic modulus of the structures is varying in between 1.13 GPa and 1.66 GPa, and the yield strength is between 32MPa and 56MPa, with AX2 showing the lowest performance. Previous non-auxetic compressive test studies showed that the stiffness and strength of cellular structures are strongly influenced by the unit cell shape, which is observed in this research as well [49]. Nevertheless, compressive test results showed that there is no significant trend between elastic modulus and the yield strength among the auxetic materials.

5.3.4. Failure mode analysis

Morphology of individual cell structure and associated connections influences the scaffold's structural performance. Figure 5.7 shows the selected still frames from the video recorded during quasi-static compression with a view to characterising the plastic deformation and the collapse of the cellular structure. Chosen frames correspond to the initial, almost not the compressed state; the moment of the first failure followed by 10%, 20% and 30% plastic deformation. From the deformation, it is clear that the shape of the unit cells significantly influences the failure modes (Figure 5.7).

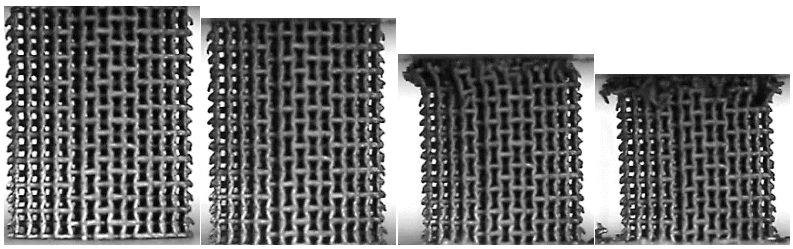

(a) AX1

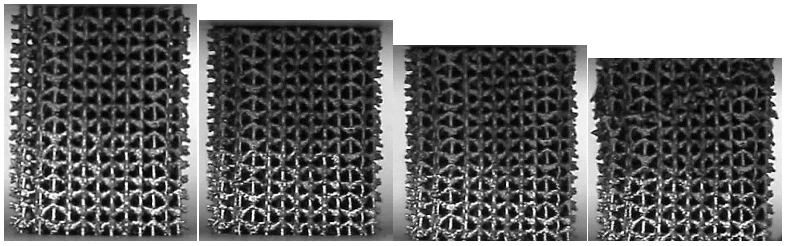

(b) AX2

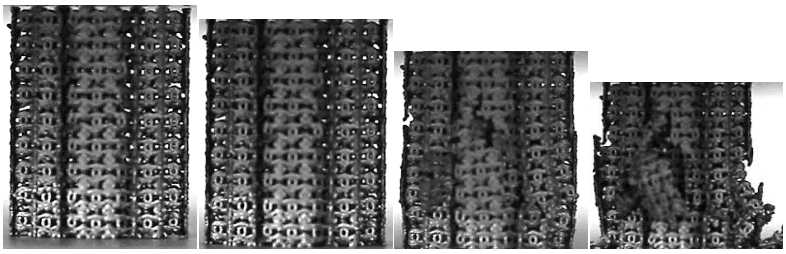

(c) AX3

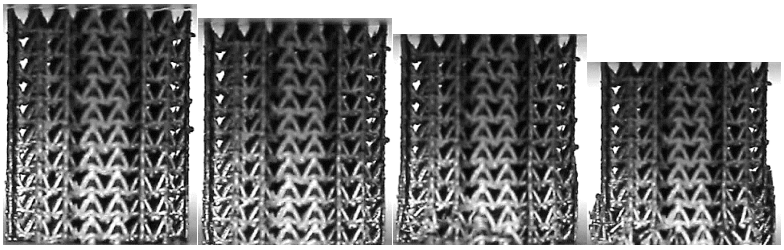

(d) AX4

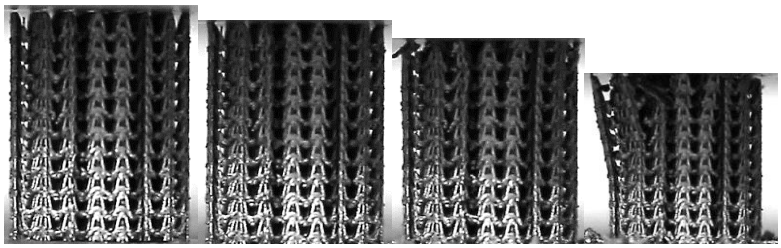

(e) AX5

Figure 5.7. Step by step deformation associated with the five scaffolds (a) AX1, (b) AX2, (c) AX3, (d) AX4 and (e) AX5

The 10% compression of all the scaffolds (Figure 5.7a-5.7e) shown an inward lateral strain under compression, confirming auxetic behaviour. The uniform contraction of the structure demonstrates that the geometry of the unit cell had a significant impact on scaffold behaviour. AX2 (Figure 5.7b) and AX4 (Figure 5.7d) structures showed the highest lateral shrinkage and lowest elastic modulus due to their unit cell geometries.

Both of the structures are based on the arrowhead design featuring different parametric values.

Scaffolds AX1 showed uniform shrinkage at 10%, followed by localised failure starting from the top cellular layer (Figure 5.7a). Although AX5 also showed failure initiating from the top layer, the peeling of boundary beams due to compressive forces resulted in a large drop in stress post-yield. As shown in Figure 5.7c, AX3 did not show crush bands; instead revealed catastrophic failure due to crack propagation through the entire structure. This is a result of the low lateral strain signified by Poisson's ratio close to zero.

To further study the failure behaviour at the micro-scale, the failed samples were investigated under an SEM, as shown in Figure 5.8. For non-auxetic cellular structures of similar thickness and overall dimension, the weak spots created by the SLM process is often cited to drive the failure process [320,342,343]. The reason for this is the localised stress concentrations that appear at the weak spots facilitated by SLM, as observed by Yu *et al.* [344]. In comparison, Figure 5.8a to 5.8e shows that the failure of the structure presented is primarily prescribed by the geometry and the associated lateral joints as opposed to SLM induced discrepancies. A tensile failure of the cross-beam at the centre can be observed in Figure 5.8a. This means that the failure is initiated by the re-entrant beam that stretches to accommodate the negative strain.

For AX2 and AX3, the failure seems to be initiated at the joints, as shown in Figure 5.8b and 5.8c, which can be the reason for the low yield strength observed. This kind of deformation can be a result of progressive folding of the beams at the joints or due to the stress concentration. The abrupt change in geometry of AX2 indicates significant

stress concentration, which can be the contributing factor. Further informing on this can be understood from the finite element analysis, which is carried out in Chapter 6.

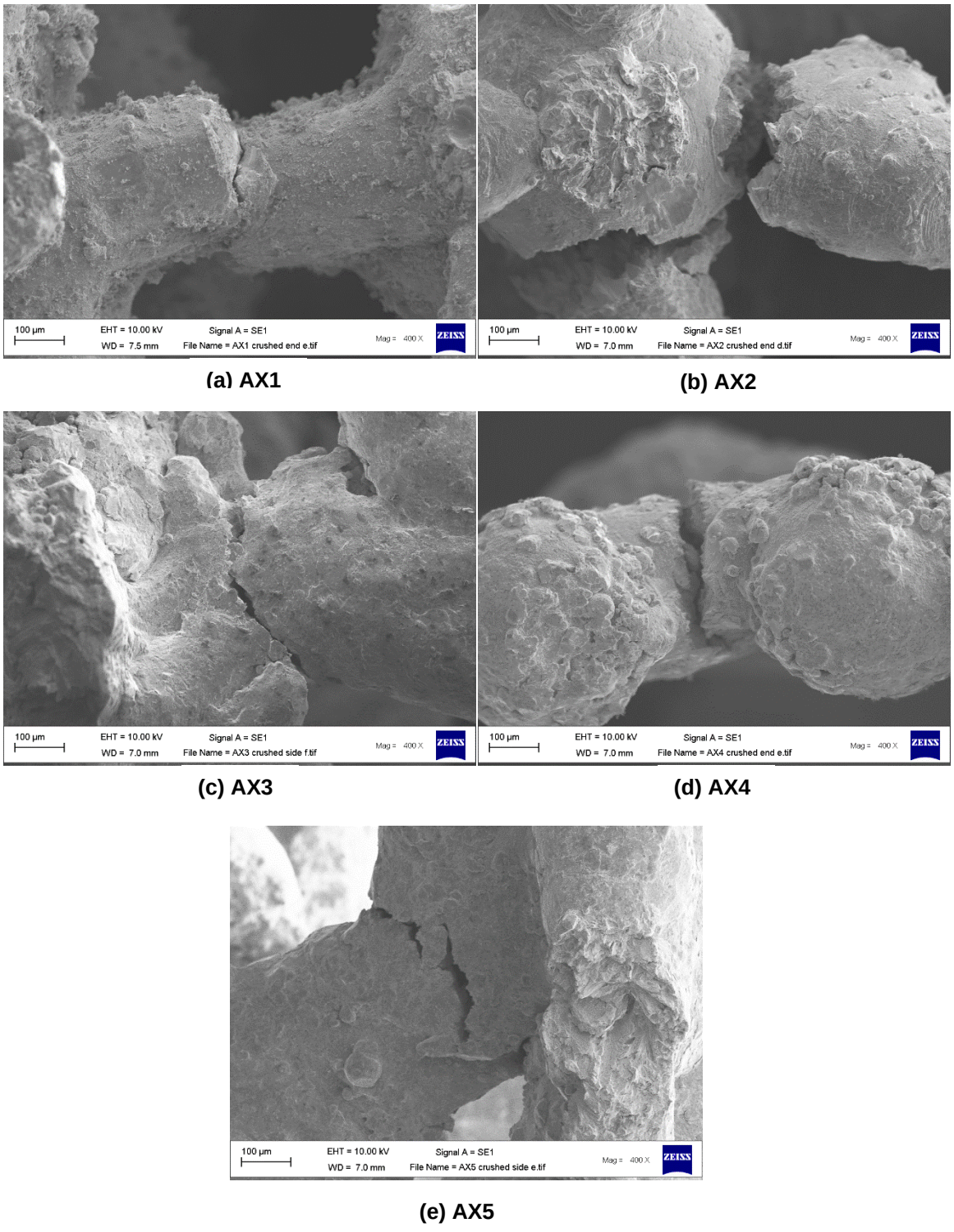

(a) AX1 **(b) AX2**

(c) AX3 **(d) AX4**

(e) AX5

Figure 5.8. SEM data of the failed samples showing (a) AX1, (b) AX2, (d) AX3, (d) AX4 and (e) AX5

A bending induced failure can be observed for AX4 and AX5, as shown in Figure 5.8d and 5.8e, as a result of the progressive folding due to the arrow-head and bell shape unit cell architecture. Overall, no thinning of the beams are visible from Figure 5.8, evidencing a brittle behaviour, which is often observed for SLM processed materials [343,345,346]. Furthermore, the failure is dependent on the collapse of individual unit cells, subsequently leading to layers, a distinction in comparison to traditional cellular structures where a shear plane through the entire structure is often observed [347–349].

5.4. Conclusion

This chapter presents the mechanical properties of the CoCrMo bulk material and auxetic bone scaffolds manufactured by using the SLM process.

- Tensile tests on CoCrMo test coupons revealed that the SLM processed CoCrMo bulk material featured Young's modulus, yield strength and ultimate tensile strength of 194.23 GPa, 975.6 MPa and 1169.81 MPa, respectively. The properties observed were found to be consistent with the literature on additively manufactured CoCrMo.
- The strength and stiffness of the scaffolds were found to be driven by the unit cell shape as opposed to relative density limiting the applicability of the Ashby and Gibson model in characterising the scaffold performance.
- Experimental compressive tests revealed that all the five scaffold designs showed auxetic performance at a Poisson's ratio range of -0.1 to -0.24, with AX1 and AX3 showing the highest and lowest lateral strain, respectively.

- The elastic modulus and compressive strength of the scaffolds were found to be in the range of 1.13-1.66 GPa and 32-56 MPa, respectively. The highest and lowest stiffness was exhibited by AX1 and AX2 receptively.
- The failure modes showed layer-based, localised and catastrophic failures influenced by both the unit cell shape and the SLM process.

Chapter 6

Finite element modelling of CoCrMo auxetic bone scaffolds

6.1. Introduction

The finite element method (FEM) is a numerical procedure that can be used to predict the performance of various geometrical designs, including porous materials. The aim of the thesis is to develop an optimised auxetic scaffold architecture suitable to mimic the stiffness of a tibial bone section. Doing this entirely with the help of prototype testing is unfeasible due to the large number of experiments required. In this regard, a validated finite element model can aid accurate results while significantly reducing the cost of testing. To aid this, the chapter presents the development and validation of a FE model that can be used to predict the mechanical performance of all the five CoCrMo auxetic scaffolds.

The model is built on a bilinear isotropic strain hardening (BISO) material model informed by experimentally tested material properties of selective laser melted bulk CoCrMo. The accuracy of the FE model to characterise the mechanical performance is shown by using to predict the elastic modulus, yield strength and Poisson's ratio of the scaffold designs and comparing it with the experimental test data. The details of meshing strategies and the loading conditions that can yield the best results are presented.

6.2. Finite Element Modelling

6.2.1. Model geometry

The non-linear elastic-plastic performance of all the five scaffold designs was studied using the finite element method (FEM). The Ansys non-linear mechanical solver was used to simulate the structural behaviour closely following the physical test conditions. The digital designs of the scaffolds were carried out as described in Chapter 4. The designs were imported to Ansys numerical modelling package using the Parasolid file format to undertake the finite element analysis. For geometries featuring large data, such as the bone scaffold designs presented in this thesis, the Parasolid format delivers maximum accuracy with minimum data loss.

6.2.2. Material model and boundary conditions

After examining numerous element types, the 10 node higher order tetrahedral element (SOLID187) combined with a Bilinear isotropic strain hardening (BISO) material model was used for the analysis. SOLID187 element exhibits quadratic displacement behaviour, making it ideal for modelling irregular volumetric geometries [350]. It also performs suitability in stress computations in comparison to 4-node tetrahedron elements. A higher-order element was chosen to investigate both the local stress concentration effects at joints and the global deformation of the lattices for the geometries under consideration. The element is delineated by ten nodes, each of which has three degrees of freedom: translations in the nodal $x, y,$ and z directions, as shown in Figure 6.1a. Hyper elasticity, plasticity, stress stiffening, creep, large deflection, and large strain capacities are all features of this element [351].

The BISO material model was found to be the most appropriate for this study as it can simulate both the elastic and plastic behaviour of a material. The BISO model is signified by a bilinear stress-strain curve with the initial slope specified by elastic modulus (E) and the elastic limit represented by the yield strength (σ_y). The post-yield behaviour was modelled perfectly plastic as the aim was to study the behaviour of the scaffolds until failure. For biomaterials and implants, the post-yield behaviour is irrelevant as the scaffold must be designed to not fail during its lifetime.

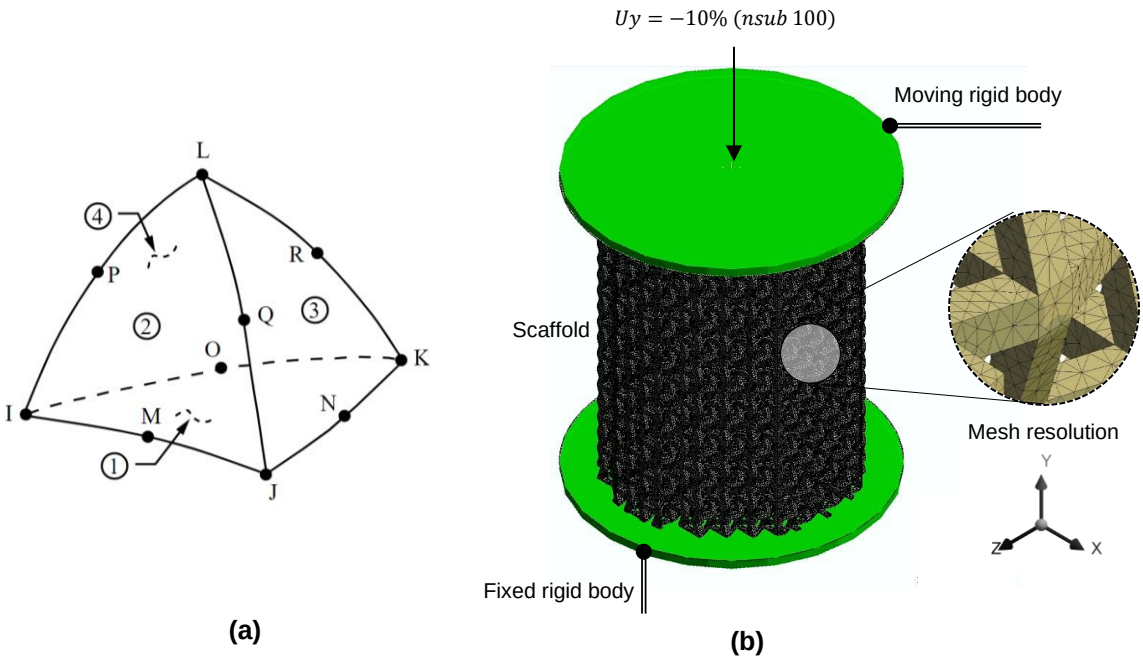

Figure 6.1. Finite element model showing the (a) element type and (b) boundary conditions

Experimentally derived CoCrMo superalloy material properties were used to inform the material model. The material properties were evaluated through tensile test data of fully dense CoCrMo test coupons, as presented in Chapter 5. Young's modulus (E) was specified as 194.23 GPa, yield Strength (σ_y) of 975.6 MPa, Poisson's ratio of 0.29 and the bulk density of 8.3 g/cm^3.

The FEA results indicate how the entire geometry responds to the loads and constraints that are applied. In this study, two cylindrical plates with a 9 mm radius and 0.5 mm thickness were modelled as rigid bodies on the top and bottom surface of the scaffold structure, as shown in Figure 6.1b. The scaffold was not constrained and was free to rotate and deform in all directions. The loading was carried out through 100 sub-steps to avoid spurious effects due to large loading, in addition to monitoring the deformation at a high resolution.

For end plates that were modelled as rigid bodies, the thickness is inconsequential as load transfer through them is not computed. The Bottom plate was fixed in all directions, and the top plate was moved 10% of the height of the scaffold in $-y$ direction (compression) to simulate the crushing behaviour. The connection between the right bodies and the scaffold was treated as frictional with a constant of 0.1 to simulate a realistic behaviour. The large-deflection (NLGEOM, ON) effects were switched on to allow for a realistic simulation of the thin beams within the scaffold. Large-deflection effects are categorised as either large deflection (or large rotation) or large strain. When large deflection effects are included, stress stiffening effects are computed.

6.2.3. Mesh generation and convergence studies

The accuracy of a finite element model is built on the foundation of creating the best discretisation (mesh) possible. In general, a finer mesh provides more precise results as the averaging of a large number of small elements can capture the stress gradients across the element more precisely [352]. Geometric characteristics with high-stress concentrations, such as fillet and chamfers, necessitate a dense mesh to effectively

predict the stress-strain behaviour [353]. However, increasing element density exponentially increase the solution time in addition to the creation of large data. Therefore, a balance between element density and solution time is the requirement for an effective mesh. A mesh convergence study was carried out to analyse the influence of mesh size on outputs of interest. Because changing the mesh size can influence the findings of stress analysis, the convergence study is used to confirm the suitability of the element size. The scaffold designs AX1 to AX5 meshed with a range (0.3 to 0.04 mm) of element sizes, as shown in Figure 6.2. The models were constrained, as shown in Figure 6.1, with the scaffold sandwiched between two endplates. Each design was meshed from 0.300, 0.100, 0.075, 0.060, 0.050 and 0.040 mm using 3D 10 node tetrahedral elements. The simulation was repeated for each element size, and the variation in the force-displacement curve was monitored, as shown in Figure 6.2.

The mesh convergence study was based on the force-displacement curve, as this is the most fundamental data of interest from the simulation. The force-displacement curves were computed from the reaction force and axial deformation for each variation in element size. It can be seen from Figure 6.2 that there is no significant difference between the elastic range of the scaffolds below 0.1 mm element size. As such, a 0.1 mm element size can reasonably predict both the stiffness and strength of the scaffolds. Since the accuracy of post-yield behaviour is not the primary aim of this thesis, a final mesh size of 0.1 mm was considered to model the scaffold designs. The resulting number of elements and nodes, along with the respective solution times, are summarised in Table 6.1. Each of the models was solved using Intel Xeon 8280 CPU

at 2.7 GHz featuring 56 CPUs assisted by 1 TB RAM and 2 NVIDIA Quadro GV100 graphic accelerators.

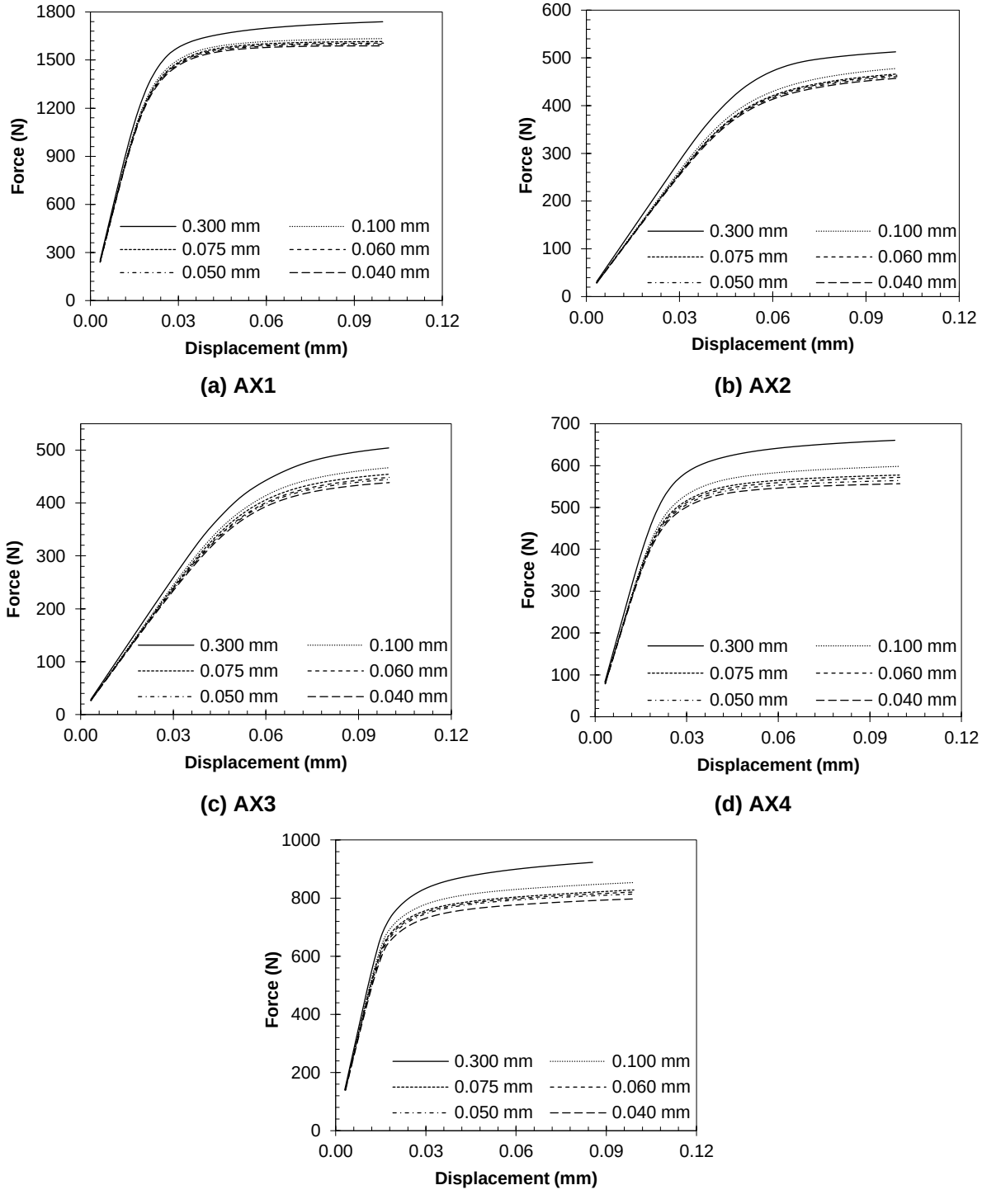

Figure 6.2. Finite element force-displacement curves using different element sizes for (a) AX1, (b) AX2, (c) AX3, (d) AX4 and (e) AX5

Table 6.1. Elements, nodes and solution time associated with the converged finite element model

Parameters	Scaffold Design				
	AX1	**AX2**	**AX3**	**AX4**	**AX5**
Elements	2477887	1715791	2279322	1488321	1574645
Nodes	4635536	3289747	4243063	2862589	2993986
Solution time (Seconds)	10356.7	4725.7	6115.2	3579.2	16038.2

6.2.4. Post-processing for Poisson's ratio evaluation

Poisson's ratio measures the deformation of a material in the direction perpendicular to the direction of the applied force. It is defined as the negative ratio of lateral to axial strain, as shown in Equation (6.1). For conventional materials, the Poisson's ratio is generally positive $(\upsilon > 0)$, implying that the material contracts axially when compressed and expands laterally. Auxetic materials have the opposite behaviour leading to a negative Poisson's ratio. When an auxetic material is subjected to axial compression, its transverse dimensions decrease. The lateral strain (ε_{lat}) to characterise the radial shrinkage was computed from the finite element numerical data as the average elastic strain over the two radial directions, which in this case is ε_x and ε_z as shown in Equation (6.2). The strains were calculated separately for each of the six lattice layers of the scaffold, and the overall shrinkage was represented by their average. Then the negative Poisson's ratio was calculated as the average lateral strain divided by longitudinal strain (ε_y).

$$\upsilon_{yx} = -\left(\frac{\varepsilon_{lat}}{\varepsilon_y}\right) \tag{6.1}$$

$$\varepsilon_{lat} = -\left(\frac{\varepsilon_x + \varepsilon_z}{2}\right) \tag{6.2}$$

6.3. Results and discussion

6.3.1. Finite element model validation

The compressive stress-strain curve of the SLM fabricated scaffolds, and the respective numerical prediction using the FEM is shown in Figure 6.3. The FE predictions were compared with the experimentally recorded stress-strain curve of the scaffold to validate the finite element model. It can be seen from Figure 6.3 that the FEA model is capable of closely mirroring the elastic behaviour of the scaffolds.

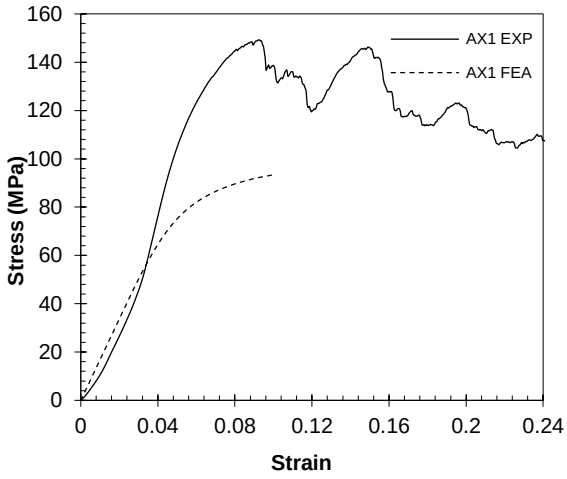

(a) AX1

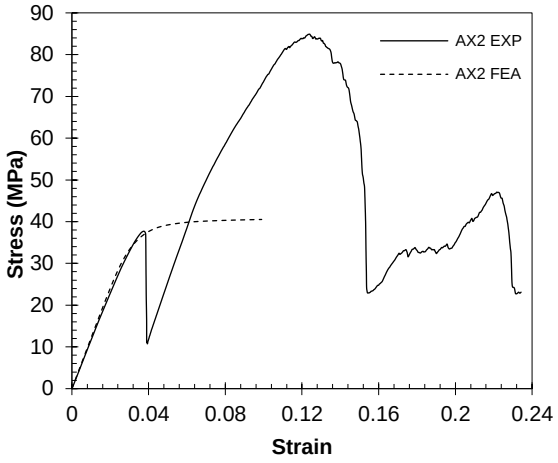

(b) AX2

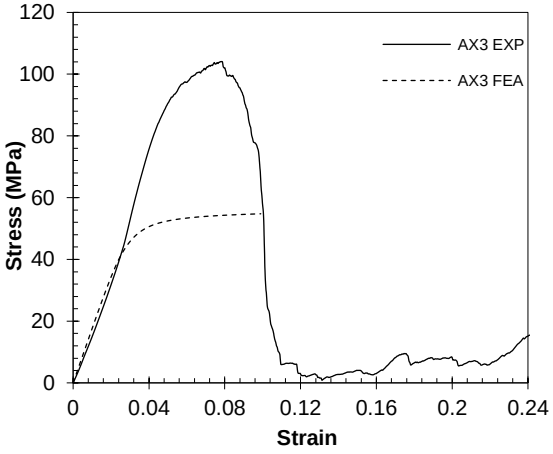

(c) AX3

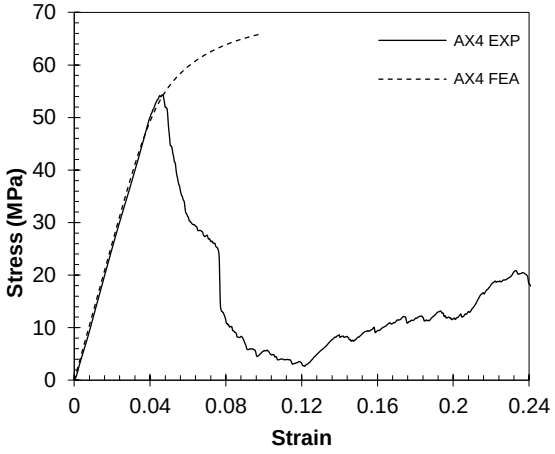

(d) AX4

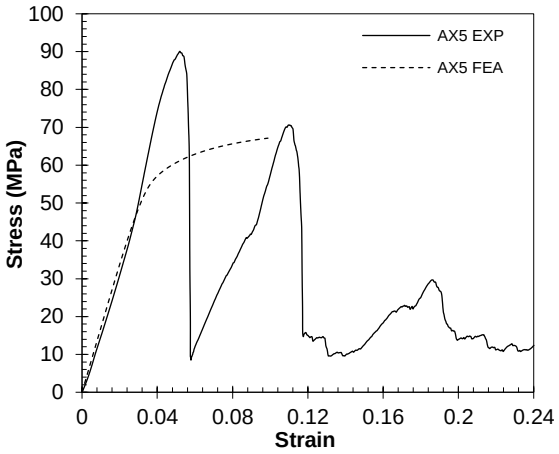

(e) AX5

Figure 6.3. Comparison of stress-strain curves obtained from the finite element model and physical tests for (a) AX1, (b) AX2, (c) AX3, (d)AX4 and (e) AX5

Table 6.2 shows the accuracy of the FE numerical model in predicting the stiffness (E) and strength (σ_y) of the scaffolds. When compared to physical test data under identical conditions similar trend in results can be observed for both cases considered. Nevertheless, the highest difference of 3.41% ineffective elastic modulus was exhibited by AX2 between the two methods. The Poisson's ratio shows a similar trend, with AX2 showing the highest difference of 4.10% in comparison to physical test data. Overall, the Poisson's ratio remained negative for all designs signifying auxetic performance. For yield strength, the least accurate prediction was for AX4, followed by AX1 at a difference of 3.84% and 3.57%, respectively. On the other hand, the closest results between the two methods were found for AX1 followed by AX5 at a difference of 1.19% and 2.50% for E and σ_y, respectively.

Table 6.2. Comparison between the finite element predicted and actual test data on parameters of interest where E referes to the elastic modulus, σ_y yield strength and υ the Poisson's ratio

Scaffold	**AX1**	**AX2**	**AX3**	**AX4**	**AX5**
E **FEA (GPa)**	1.68	1.17	1.59	1.30	1.65
E **EXP (GPa)**	1.66	1.13	1.57	1.27	1.60
E **% Difference**	1.19	3.41	1.25	2.30	3.03
σ_y **FEA (MPa)**	54	31	35	50	39
σ_y **EXP (MPa)**	56	32	36	52	40
σ_y **% Difference**	3.57	3.12	2.77	3.84	2.50
υ **FEA**	-0.26	-0.17	-0.12	-0.19	-0.20
υ **EXP**	-0.24	-0.13	-0.10	-0.16	-0.16
υ **% Difference**	2.12	4.10	2.14	2.51	3.60

While the numerical model identified the trend in mechanical performance with reasonable accuracy, as established in Figure 6.3, further refinements are necessary. The difference between the numerical and experimental data can be primarily attributed to the influence of the SLM additive manufacturing technique. It is well documented that [117,250,354–357] SLM variation in geometry due to the stair-step effect and partly fused powder on the surface, and the effect of this is increasingly significant for porous and geometrically complex thin-walled structures such as the ones presented in this study. While the experimental data accounts for all irregularities, the numerical models assume an idealised structure based on CAD that is homogenous and free from any surface irregularities. Furthermore, the rough surface finish, which is also a salient feature of SLM samples, can significantly influence the mechanical behaviour at the comparable beam and wall thickness. The comparison of the test data showed that all the finite element scaffold models are in reasonable agreement and can be used for further predictions.

6.3.2. Stress distribution within the scaffolds

The theoretical analysis in Chapter 5 showed that the stiffness and strength of the scaffold vary with the square of the relative density. However, both the experimental and FE result revealed deviation from theoretical, with AX1 exhibiting both the highest stiffness and strength despite featuring a porosity of 73% (Table 5.2). Consequently, it is established that the geometry of the unit cell has a higher influence on the mechanical performance of the scaffold and an enhanced understanding of the stress distribution is required to derive design guidelines. Furthermore, when it comes to cellular structures, every aspect of their mechanical performance and failure are dependent on the concentration of stress facilitated by the geometry as opposed to relative density [358].

Table 6.3. Comparison of elastic modulus (E) and yield strength (σ_y) between the different scaffolds evaluated using theoretical, experimental and numerical methods

Scaffold	**AX1**		**AX2**		**AX3**		**AX4**		**AX5**	
Parameters	E (GPa)	σ_y (MPa)	E (GPa)	σ_y (MPa)	E (GPa)	σ_y (MPa)	E (GPa)	σ_y (MPa)	E (GPa)	σ_y (MPa)
Theoretical	1.73	77.73	1.18	58.48	1.25	61.11	0.8	43.55	0.93	48.82
Experimental	1.66	56	1.13	32	1.57	36	1.27	52	1.6	40
FEA	1.68	54	1.17	31	1.59	35	1.3	50	1.65	39

Theoretical calculations were done by using Ashby's criterion, which is designed with the relative density of the cellular structures, but when it comes to the auxetic structures literature showed that there is a higher influence of the geometry than the relative density of the structure on the mechanical properties. This is evident in the present analysis with theoretical performance deviating significantly from both experimental and numerical results as shown in Table 6.3. Comparing theoretical and

experimental results, the lowest deviation in E of 4.13% was observed for AX1, indicating that for this structure the stiffness is primarily driven by the porosity as opposed to geometry. On the contrary, AX5 showed the largest deviation in E of 53% indicating for this structure the pore shape as opposed to relative density driving the stiffness behaviour. Examining the unit cell shapes closely for these two structures, it is evident that the AX1 is primarily composed of straight-line struts which do not bend under uniaxial compression. However, the unique bell-shaped architecture for AX5 features curved beams that offer complex elastic deformation with struts bending within the unit cells reducing the overall load being transferred between unit cell layers. As a result of this phenomenon, the stiffness behaviour is significantly affected by the unit cell shape as opposed to AX1 which explains the difference in the elastic modulus observed.

When it comes to yield strength, the lowest deviation of 17.7% between experimental and theoretical performance was observed for AX4 worsening to 58.5% for AX2. The lower accuracy of Ashby's criterion in predicting the yield strength as opposed to elastic modulus is well documented. However, for the architectures under consideration, the unique unit cell shapes between AX2 and AX4 are responsible for the large deviation between experimental and theoretical results. Despite both AX4 and AX2 being inspired by the arrowhead cellular architectures, the former features straight vertical beams which significantly increase the stress concentration leading to earlier failure which is not captured in the theoretical prediction. On the contrary, the absence of vertical beams within the unit cell for AX4 allows the dissipation of larger loads throughout the structure which is often captured through relative density when using Ashby's criterion.

Following the works of Salimon *et al.* [359], a certain dependence of σ_y was established with ρ_r for cellular structures. Nevertheless, some discrepancies were observed between theoretical and experimental results, which is likely to be contributed by the stress concentration. Overall, it is well established [360–362] that certain designs are more prone to stress concentration and may lead to an early onset of plasticity failure. However, any correlation of this to auxetic structures are still unknown when it comes to the performance of biomedical scaffolds in general. Furthermore, given that scaffolds often require a high porosity (>60%), identifying the location of stress concentration is crucial for the design of functional scaffolds.

Unlike experimental tests, the FE model provides a large set of data, and the close validation allows it to be extended for further analysis. Accordingly, Figure 6.4 shows the stress distribution within the scaffold, which reveals the location of the stress concentration. A constant legend is used to aid visual identification of the best and worst cases for their respective stress profiles. The associated magnitude for σ_{max} can be identified from Figure 6.3 for the respective porosities.

Evaluating the results, depending on the UC, there is a significant disparity in σ_{max} experienced by the scaffolds. The highest stress concentration is exhibited by AX2, followed by AX3 and AX5. The lowest stress concentration with the most uniform stress distribution was exhibited by AX1, followed by AX4. It can be seen that the trend in stress concentration is consistent with the yield strength observed, signifying a reduction in strength due to stress concentration.

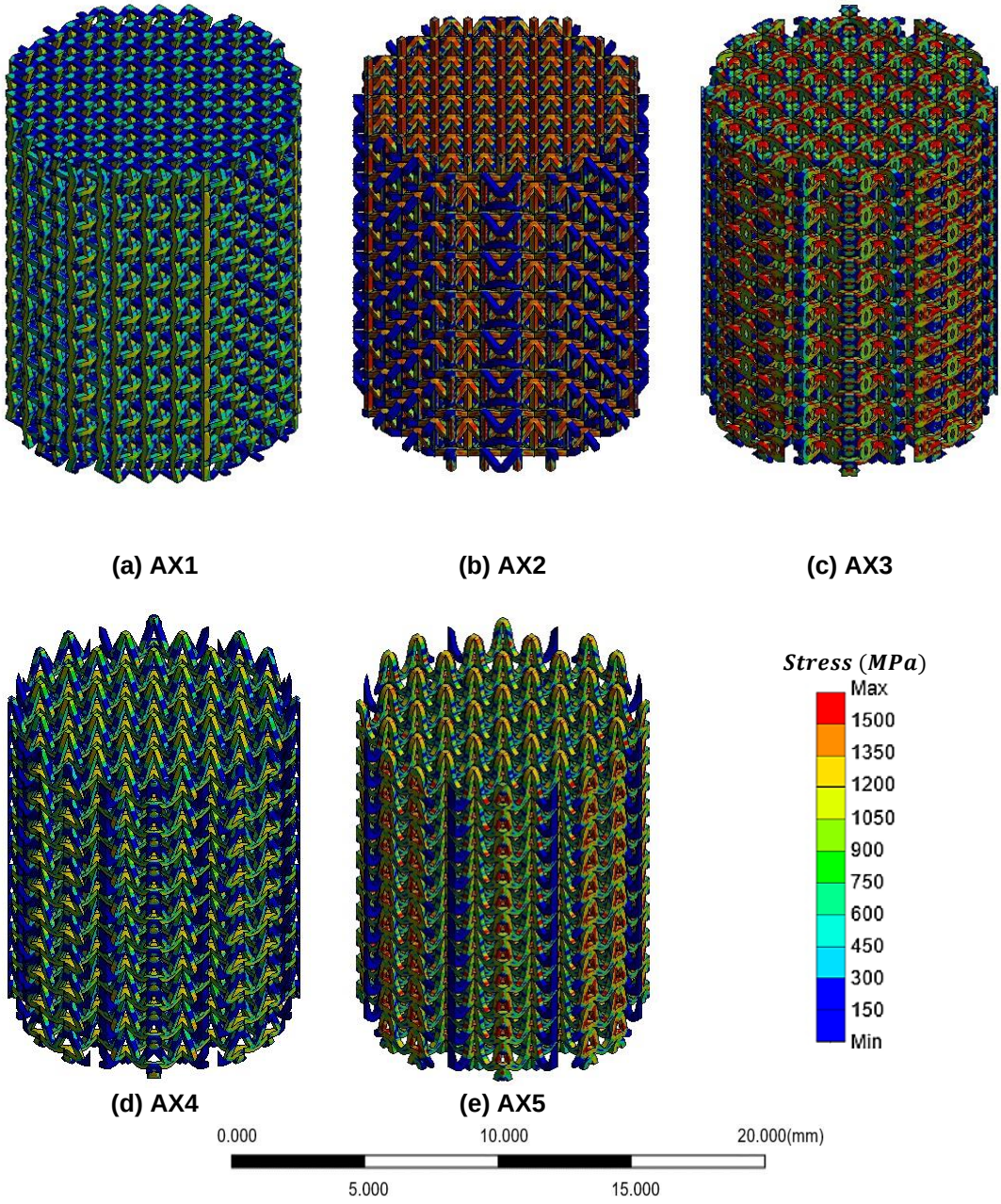

Figure 6.4. Finite element simulation of the stress distribution in the auxetic scaffold showing (a) AX1, (b) AX2, (c) AX3, (d) AX4 and (e) AX5

When the scaffolds are compressed elastically, the macroscopic stresses that are generated within the material is proportional to ε. In chapter 5, we showed the performance of the scaffold is primarily dependent on the unit cell shape and does not follow the power law associated with relative density. It can be seen from the FEA data that this is due to the dependents of the stress concentration on the shape of the UC

and the associated connection to adjacent UCs. Consequently, the design that featured the highest stress showed the lowest E and σ_y. As a result, AX1 shows the highest stiffness and strength due to its lower stress concentration in comparison to other designs analysed. Therefore, it can be concluded that higher stress concentrated auxetic scaffold designs featuring unit cells such as arrowhead (UC2) and modified re-entrant (UC3) should be avoided.

6.4. Conclusion

This chapter presents the develops a finite element model that can be used to predict the mechanical performance of additively manufactured auxetic bone scaffolds.

- The comparison of the finite element and experimental test results showed that the FE model developed in this thesis could predict the mechanical performance of auxetic bone scaffolds at an accuracy of ~96%.
- The results of the mesh convergence study found an element size of 0.1 mm to be suitable for the optimum balance between computational time and accuracy.
- The FE model developed in this study can be used to characterise the Poisson's ratio, elastic modulus and yield strength of CoCrMo bone scaffolds at a difference of 4.10, 3.84 and 3.41%, respectively.
- The finite element model was found to visualise the stress concentration of the scaffolds, which explained the influence of unit cell shape on mechanical performance.

Chapter 7

Identifying best designs using combined TOPSIS and AHP

7.1. Introduction

This chapter presents a potential methodology to identify the best auxetic bone scaffold designs following the multi-criteria decision making procedure. A combination of two techniques, namely the Technique for Order Preference by Similarity to Ideal Solutions (TOPSIS) and Analytic Hierarchy Process (AHP) are considered. The hybrid technique is used to identify the best scaffold design under two scenarios, which can benefit bone scaffold application. The first scenario is to identify a scaffold design that offers a near-zero negative Poisson's ratio $(-\upsilon)$ while satisfying five different criteria required for bone scaffolds. The second scenario was to identify the bone scaffold with the highest $-\upsilon$ while offering suitable performance for other selected parameters. While Scenario 1 can be advantageous for wound healing by limiting the lateral strain, Scenario 2 can offer the highest stimulation for bone growth at the bone-scaffold interface.

This is the first research to bring forward the combined AHP and TOPSIS methodology within the context of auxetic scaffold design to aid decision making. As such, the aim is to reduce the number of designs from five to two to demonstrate parametric analysis and optimisation for targeted auxetic and stiffness matching performance, which are explained in subsequent chapters.

7.2. Multi-criteria decision-making methodology (MCDM)

The TOPSIS approach is used to determine the final ranking, and the AHP is utilised to score and set the share of importance of the relative weights for the decision criterion sets. AHP can effectively handle circumstances in which various individual subjective opinions are considered during the decision-making process. However, dealing with excessive pair-wise comparisons of attributes and options might be challenging [363]. When processing a large number of alternatives, TOPSIS is more effective. The conventional TOPSIS technique, however, makes use of assumed significance weights and lacks an effective way for determining importance weights for different criterions [364]. The AHP model may be used to address the TOPSIS problem with weight elicitation. The TOPSIS and AHP model combines the advantage of AHP (that allows pair-wise comparisons of alternatives while eliciting weights) with those of TOPSIS (that does not have capacity limitations on the numbers of attributes and alternatives considered and involves straightforward computations).

7.2.1. TOPSIS

Most real-life decision-making problems have several conflicting criteria and objectives to be considered simultaneously. Where there are multiple parameters to consider, a multi-criteria decision-making (MCDM) algorithm can be used to identify the best possible solution. MCDM models are used to achieve an optimum decision when encountered with several alternatives featuring non-commensurable and conflicting decision criteria [365]. The MCDM model is renowned for addressing complex real-life issues because of its intrinsic capability of judging diverse alternatives based on numerous decision criteria in order to select the most suitable

choice. While there are numerous MCDM methods, one of the most promising methods in this regard is the Technique for Order of Preference by Similarity to Ideal Solution (TOPSIS) [366].

TOPSIS is one of the most rigid and robust MCDM techniques, and it functions in a multi-dimensional computing area to determine the alternative solution that is near to the ideal and far from the worse case [367]. TOPSIS is widely adopted because of its user-friendliness. The calculation procedures of TOPSIS are similar regardless of how many alternatives are available, thus enabling fast computations. For every alternative, the technique concurrently factors the distance from the worst solution to the best one [368]. The perfect positive solution involves all the good values of every rank, and the perfect negative solution involves all the worst [369].

TOPSIS can be considered as a very reliable technique, despite its failure to consider the relationship of attributes because of its peculiar utilisation of Euclidean distance to determine the distance from the ideal negative and positive solutions. Other similar techniques benchmark the resolution under consideration directly against the most suitable and worst prevailing ones. Because of its robustness and reliability, TOPSIS is applied in numerous fields, including marketing, business, resource management, manufacturing, and engineering [367].

The basic principle of the TOPSIS technique is that the optimal decision is usually closest to the ideal solution and as far away as the worst solution [370]. The perfect solution should possess a rank of one, and the worst alternative must have a rank close to 0 [371]. The TOPSIS method can be broken down into the following six steps.

Step 1: Generally, the process for the TOPSIS algorithm begins with the formulation of the normalise decision matrix r_{ij}, as shown in Equation (7.1) which represents the satisfaction value of every criterion with every alternative. Presume x_{ij} is the decision matrix of alternative j under the evaluation criterion i.

$$r_{ij} = \frac{x_{ij}}{\sqrt{\sum_{j=1}^{m} x_{ij}^2}}, \qquad j = 1,2,\dots,m, \qquad i = 1,2,\dots,n \tag{7.1}$$

Step 2: Normalise the matrix with a required normalising scheme and multiply the values by the criteria weights. W_i is the weights of criteria as given in Equation (7.2).

$$\sum_{i=1}^{n} w_i = 1$$
$$v_{ij} = w_i \times r_{ij}, \qquad j = 1,2,\dots,m, \qquad i = 1,2,\dots,n \tag{7.2}$$

Step 3: The negative ideal and positive ideal solutions are computed for the weighted normalised decision matrix as shown in Equations (7.3) and (7.4):

$$A^* = \{v_1^*, v_2^*, \dots, v_i^*\} = \left\{\left(\underset{j}{Max}\, v_{ij} \middle| i \in I'\right), \quad \left(\underset{j}{Min}\, v_{ij} \middle| i \in I''\right)\right\} \tag{7.3}$$

$$A^- = \{v_1^-, v_2^-, \dots, v_i^-\} = \left\{\left(\underset{j}{Min}\, v_{ij} \middle| i \in I'\right), \quad \left(\underset{j}{Max} v_{ij} \middle| i \in I''\right)\right\} \tag{7.4}$$

where I' is associated with the benefit criteria, and I'' is associated with the cost criteria.

Step 4: Separation measures have been calculated by using the n-dimensional Euclidean distance. Positive ideal solution (D_j^*) and the negative ideal solution (D_j^-) given by Equations (7.5) and (7.6), respectively:

$$D_j^* = \sqrt{\sum_{i=1}^{n} (v_{ij} - v^*)^2}, \qquad j = 1,2,\dots,m \tag{7.5}$$

$$D_j^- = \sqrt{\sum_{i=1}^{n} (v_{ij} - v^-)^2}, \qquad j = 1,2,\dots,m \tag{7.6}$$

Step 5: Calculate the relative closeness to the ideal solution (CC_j^*), where the index value lies between 0 and 1 as shown in Equation (7.7):

$$CC_j^* = \frac{D_j^-}{D_j^* + D_j^-}, \qquad j = 1,2,\dots,m \tag{7.7}$$

Step 6: Rank the alternatives based on their relative proximity based on descending values of CC_j^* to the perfect solution. The larger index value means better performance of the alternatives [372].

The TOPSIS approach can be used to make complex decision making, performing analyses, comparisons and rankings of the identified alternative solutions. The classical TOPSIS technique addresses issues where all decision data are represented by numbers. Other several extensions have been suggested based on the initial TOPSIS technique, offering support for fuzzy or interval criteria, vagueness, lack of information, uncertainty, or fuzzy or interval weights to modelled imprecision [373].

7.2.2. Analytic hierarchy process

The analytical hierarchy process (AHP) refers to the MCDM technique of decision making involving by developing a hierarchy of various levels to disintegrate a complex issue into subproblems [374]. AHP is helpful in carrying out a pairwise comparison of

the criteria on a scale of 1-9 at every level developed by Saaty [375] in 1979s, as listed in Table 7.1.

Table 7.1. Saaty rating scale for analytical hierarchy process (AHP) [371]

Intensity of Importance	**Definition**
1	Equal importance
3	Moderate importance
5	Strong importance
7	Very strong importance
9	Extreme importance
2,4,6,8	Intermediate values
1/3,1/5,1/7,1/9	Values for inverse comparison

AHP is utilised to synthesise data associated with decision-making across all manufacturing areas, starting from the primary sector to the tertiary sector. AHP is widely applied in decision-making processes because of its user-friendliness. Another advantage of this technique is the scalability, which implies that the AHP hierarchical structure can be sized down or upwards, even though this is limited to alternatives achieving the criteria that are assessed with a similar absolute scale [376]. The steps required to perform AHP are as follows:

Step 1: Developing a hierarchical structure with a goal at the top level, criteria at the second level and alternatives at the third level.

Step 2: Determine the relative importance of different criteria with respect to the goal.

Step 3: Calculate the consistency to check the calculated values are correct or not.

Step 4: Get the relative weights.

7.2.3. Scenarios for the selection of auxetic bone scaffolds

As discussed in the literature review presented in Chapter 2, Section 2.5.2, stress shielding, and maladapted stress concentration are major issues when it comes to bone tissue engineering. This is due to the stress mismatching between bone and the implant facilitated by the difference in mechanical properties at the interface. Studies have confirmed that a large mismatch in stiffness between the host bone and the load-bearing implant is the primary cause for both stress shielding and maladapted stress concentration.

Table 7.2. Summary of scenario-based decision-making criterion used for the selection of CoCrMo meta-biomaterial bone scaffold satisfying two different auxetic lateral strain criteria while satisfying the general requirements for load-bearing bone scaffolds

Parameters of interest	**Notation**	**Decision-making criteria**	
		Scenario 1 (S1)	Scenario 2 (S2)
Poisson's ratio	$-\upsilon$	↓	↑
Porosity	φ	↑	
Normalised yield strength	$\overline{\sigma_y}$	↑	
Normalised elastic modulus	$\bar{E}$	↑	
Ease of design	EoD	↑	
Order of influence	-	$-\upsilon > \varphi > \sigma_y > E > EoD$	

Within this context, the thesis aims to develop auxetic bone scaffolds with optimal mechanical properties to reduce the stress shielding effect. Besides that, the regeneration process of the bone is also considered. In porous materials, controlling Poisson's ratio can manipulate the strain stimulus during bone regeneration [185]. Poisson's ratio can be positive, negative or zero values. Previous studies showed that lateral elastic strain of the bone scaffolds during compression influences bone regeneration. Although a high negative lateral strain requires scaffolds with maximum

$-\upsilon$, this might not be ideal under all conditions. As such, to consider multiple eventualities, two scenarios are considered in this study which looks at designs that maximise and minimises Poisson's ratio values for bone scaffold application as summarised in Table 7.2.

7.2.3.1. Scenario 1: Auxetic bone scaffold with near-zero $-\boldsymbol{\upsilon}$

Scaffold with a zero Poisson's ratio (ZPR) may be better at emulating the behaviour of native tissues and accommodating and conveying stresses to the host tissue site during wound healing in tissue engineering applications. The ZPR can be beneficial if the healing process is more important than the faster tissue growth. Soman *et al.* [177] studied single- and double-layer Polyethylene glycol (PEG) scaffolds, which exhibited in-plane ZPR behaviour and stated that ZPR would be beneficial in the engineering of cartilage, corneal and ligament tissues. Considering this recommendation, the first scenario of the scaffold selection looks at achieving a ZPR with a view to optimising the architecture to offer stiffness matching at a suitable porosity.

7.2.3.2. Scenario 2: Auxetic bone scaffold with highest $-\boldsymbol{\upsilon}$

Mechanical stimulation is one of the factors that regulate bone regeneration and healing [377]. Bone regeneration at a tissue-scaffold interface is influenced by the type and magnitude of the mechanical stimulus. Although in the early stages, Kim *et al.* [3] suggest that the auxetic materials that offer mechanical properties tailored to natural tissue show an improved tissue reconstruction ability. According to Velasco *et al.* [378], bone tissue regeneration is influenced by numerous mechano-regulatory phenomenon where high strains can influence faster regeneration in fibrous tissues. As such, a highest $-\upsilon$ may be helpful for tissue reintegration due to the extended

mechanical stimulus it offers [379,380]. To this extent, the second scenario looks at identifying the best scaffold design that offers the highest $-\upsilon$ with a view to optimising for stiffness matching at a suitable porosity.

7.3. Results and discussion

The AHP and TOPSIS methodologies are combined in this study. The TOPSIS approach is utilised to determine the final ranking to identify the best designs, and the AHP is used to score and set the share of the importance of the relative weights for the choice criteria sets. Alternatives in the hierarchy are the five (AX1 to AX5) auxetic scaffolds influenced by five criteria which include the Poisson's ratio (υ), Porosity (φ), yield strength (σ_y), elastic modulus (E) and ease of design (EoD). The yield strength and elastic modulus were normalised with respect to relative density to offer a like for like comparison neutralising the differences in porosity. The ease of design parameter is conceived from a five-point numerical scale, where 5 and 1 are the simplest and most complex designs, respectively (Table 7.2).

Table 7.3. Decisional matrix and the parametric values used for multi-criteria decision making

Design	$\boldsymbol{\upsilon}$	$\boldsymbol{\varphi}$ (%)	$\boldsymbol{\sigma_y}$ $(\boldsymbol{MPa})$	$\boldsymbol{E}$ $(\boldsymbol{GPa})$	$\boldsymbol{EoD}$
AX1	-0.24	73.05	207.78	6.16	4
AX2	-0.13	76.72	137.47	4.85	1
AX3	-0.1	78.17	164.90	7.19	2
AX4	-0.16	81.98	288.50	7.05	5
AX5	-0.16	81.16	212.28	8.49	3

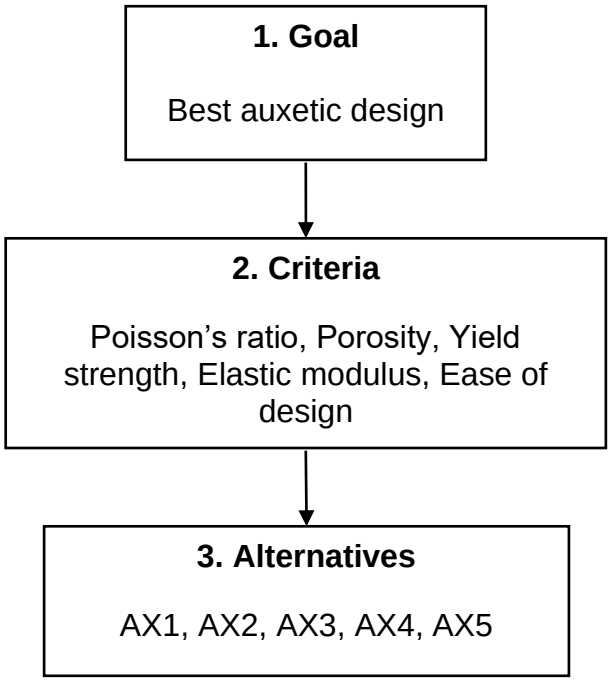

Figure 7.1. Hierarchical model

Using the data shown in Table 7.2, a decision model is created using an analytic hierarchy process (AHP) as shown in Figure 7.1 to derive relative weights for the decision criteria following the Saaty rating scale. The parametric importance of the criteria is in the following form: $\upsilon > \varphi > \sigma_y > E > EoD$.

7.3.1. Scenario 1: Selection of auxetic bone scaffold with near-zero $-\upsilon$

In the analytic hierarchy process, importance values decide the weights of the criteria. Criteria weights were calculated by using step by step procedure discussed in the AHP process. Poisson's ratio has the highest importance than the other alternatives. To achieve scenario one, the lowest value of the $-\upsilon$ is set as the ideal. Therefore, inverse values were used in Poisson's ratio row, as shown in the pairwise comparison matrix in Table 7.3. The pair-wise matrix is normalised by dividing all the values in Table 7.3 by the sum of the column resulting in the normalised pairwise comparison matrix shown in Table 7.4. Finally, the relative weights of each criterion for the selection of

the ideal design are calculated by averaging all the element value in each row (Table 7.4), resulting in Table 7.5.

Table 7.4. Pair-wise comparison matrix to determine the relative importance of the five selected parameters contributing to the selection of a near-zero Poisson's ratio auxetic bone scaffold

	$\boldsymbol{v}$	$\boldsymbol{\varphi}$	$\boldsymbol{\sigma_y}$	$\boldsymbol{E}$	$\boldsymbol{EoD}$
$\boldsymbol{v}$	1	1/3	1/5	1/7	1/9
$\boldsymbol{\varphi}$	3	1	3	5	7
$\boldsymbol{\sigma_y}$	5	1/3	1	3	5
$\boldsymbol{E}$	7	1/5	1/3	1	3
$\boldsymbol{EoD}$	9	1/7	1/5	1/3	1
Sum	25	2.01	4.73	9.48	16.11

Table 7.5. Normalised pair-wise comparison matrix to determine the relative importance of the five selected parameters

	$\boldsymbol{v}$	$\boldsymbol{\varphi}$	$\boldsymbol{\sigma_y}$	$\boldsymbol{E}$	$\boldsymbol{EoD}$
$\boldsymbol{v}$	0.0400	0.1659	0.0423	0.0151	0.0069
$\boldsymbol{\varphi}$	0.1200	0.4976	0.6338	0.5276	0.4345
$\boldsymbol{\sigma_y}$	0.2000	0.1659	0.2113	0.3166	0.3103
$\boldsymbol{E}$	0.2800	0.0995	0.0704	0.1055	0.1862
$\boldsymbol{EoD}$	0.3600	0.0711	0.0423	0.0352	0.0621

Table 7.6. Criteria relative weights showing the importance of the selected parameters in the selection of a near-zero Poisson's ratio auxetic bone scaffold

Criteria	**Criteria weight**
Poisson's ratio	0.0540
Porosity	0.4427
Yield strength	0.2408
Elastic modulus	0.1483
Ease of Design	0.1141

The TOPSIS approach is used in the final stage to fulfil the desired objectives. The main principle of this process is that the best alternative (AX1 to AX5) should be as

close to the most advantageous alternative as possible and as far away from the worst alternative. The best alternative should have a rank of one, while the worst option should be close to zero [371]. The normalised values related to the criteria shown in Table 7.6 was calculated from the decisional matrix in Table 7.2 by using Equation (7.1).

Table 7.7. The normalised values related to the criteria

Design	$\boldsymbol{v}$	$\boldsymbol{\varphi}$	$\boldsymbol{\sigma_y}$	$\boldsymbol{E}$	$\boldsymbol{EoD}$
AX1	0.6515	0.4173	0.4455	0.4018	0.5394
AX2	0.3529	0.4383	0.2947	0.3167	0.1348
AX3	0.2715	0.4466	0.3535	0.4692	0.2697
AX4	0.4343	0.4683	0.6185	0.4597	0.6742
AX5	0.4343	0.4636	0.4551	0.5539	0.4045

The normalised weighted matrix, as shown in Table 7.7, was calculated using Equation (7.2) by multiplying each element of each column of the normalised decision matrix (Table 7.6) by the relative criteria weights (Table 7.5). Subsequently, the negative and positive ideal solutions, as listed in Table 7.8, were calculated for the weighted normalised decision matrix (Table 7.7) by using Equations (7.3) and (7.4).

Table 7.8. Weighted normalised matrix

Design	$\boldsymbol{v}$	$\boldsymbol{\varphi}$	$\boldsymbol{\sigma_y}$	$\boldsymbol{E}$	$\boldsymbol{EoD}$
AX1	0.0352	0.1848	0.1073	0.0596	0.0616
AX2	0.0191	0.1940	0.0710	0.0470	0.0154
AX3	0.0147	0.1977	0.0851	0.0696	0.0308
AX4	0.0235	0.2073	0.1490	0.0682	0.0769
AX5	0.0235	0.2053	0.1096	0.0822	0.0462

Table 7.9. Positive and negative ideal solution

	$\boldsymbol{v}$	$\boldsymbol{\varphi}$	$\boldsymbol{\sigma_y}$	$\boldsymbol{E}$	$\boldsymbol{EoD}$
Positive Solution (A^*)	0.0147	0.2073	0.1490	0.0822	0.0769
Negative Solution (A^-)	0.0352	0.1848	0.0710	0.0470	0.0154

Once the positive and negative ideal solutions are obtained, as shown in Table 7.8, the separation distance of each competitive alternative from the positive (D_j^*) and negative (D_j^-) ideal solutions were calculated using Equations (7.5) and (7.6). In addition, the relative closeness value was calculated using Equation (7.7). Finally, the scaffold alternatives were ranked based on the closeness values to identify the best design, as shown in Table 7.9. It can be seen that the application of the combined AHP and TOPSIS method identified AX4 to be the best scaffold design for offering a near-zero Poisson's ratio (Scenario 1) while meeting all the parametric criteria for further optimisation. The procedure was repeated to identify the best design for Scenario 2.

Table 7.10. Ranking matrix identifying the best auxetic scaffolds meeting all the decision criteria while offering a near zero Poisson's ratio

Design	$\boldsymbol{(D_j^*)}$	$\boldsymbol{(D_j^-)}$	**Relative closeness values** $\boldsymbol{(CC_j^*)}$	**Rank**
AX1	0.0584	0.0601	0.507	3
AX2	0.1063	0.0186	0.149	5
AX3	0.0803	0.0392	0.328	4
AX4	0.0165	0.1047	0.864	1
AX5	0.0508	0.0651	0.562	2

7.3.2. Scenario 2: Auxetic bone scaffold with highest $-\upsilon$

Similar to Scenario 1, importance was assigned given to the alternatives. To achieve scenario two, the highest value of the $-\upsilon$ has to be the ideal. Therefore, inverse values were used in Poisson's ratio column, as shown in the AHP pairwise comparison matrix in Table 7.10. Then the normalised pair-wise comparison matrix listed in Table 7.11 was obtained by dividing the elements of the column by the sum of the column in 7.10. Finally, the criteria weights from the AHP process were calculated by averaging all the element value in each row, as shown in Table 7.12.

Table 7.11. Pair-wise comparison matrix

Design	$\boldsymbol{\upsilon}$	$\boldsymbol{\varphi}$	$\boldsymbol{\sigma_y}$	$\boldsymbol{E}$	$\boldsymbol{EoD}$
$\boldsymbol{\upsilon}$	1	3	5	7	9
$\boldsymbol{\varphi}$	1/3	1	3	5	7
$\boldsymbol{\sigma_y}$	1/5	1/3	1	3	5
$\boldsymbol{E}$	1/7	1/5	1/3	1	3
$\boldsymbol{EoD}$	1/9	1/7	1/5	1/3	1
Sum	1.79	4.68	9.53	16.33	25

Table 7.12. Normalised pair-wise comparison matrix

Design	$\boldsymbol{\upsilon}$	$\boldsymbol{\varphi}$	$\boldsymbol{\sigma_y}$	$\boldsymbol{E}$	$\boldsymbol{EoD}$
$\boldsymbol{\upsilon}$	0.5595	0.6415	0.5245	0.4286	0.3600
$\boldsymbol{\varphi}$	0.1865	0.2138	0.3147	0.3061	0.2800
$\boldsymbol{\sigma_y}$	0.1119	0.0713	0.1049	0.1837	0.2000
$\boldsymbol{E}$	0.0799	0.0428	0.0350	0.0612	0.1200
$\boldsymbol{EoD}$	0.0622	0.0305	0.0210	0.0204	0.0400

TOPSIS method was applied to identify the best design relevant to Scenario 2 using AHP criteria weight results in Table 7.12. The alternative which receives $\boldsymbol{CC_j^*}$ closer to 1 will be the best candidate given the decision-making criteria. The normalised values

related to the criteria in Table 7.6 was used for Scenario 2 with criteria weights listed in Table 7.12.

Table 7.13. Criteria relative weights

Criteria	**Criteria weight**
Poisson's ratio	0.5028
Porosity	0.2602
Yield strength	0.1344
Elastic modulus	0.0678
Ease of Design	0.0348

The Normalised weighted matrix shown in 7.13 was calculated using Equation (7.2) by multiplying each element of each column of the normalised decision matrix (Table 7.6) by the relative criteria weights (Table 7.12).

Table 7.14. Weighted normalised matrix

Design	$\boldsymbol{\upsilon}$	$\boldsymbol{\varphi}$	$\boldsymbol{\sigma_y}$	$\boldsymbol{E}$	$\boldsymbol{EoD}$
AX1	0.3276	0.1086	0.0598	0.0272	0.0188
AX2	0.1774	0.1141	0.0396	0.0215	0.0047
AX3	0.1365	0.1162	0.0475	0.0318	0.0094
AX4	0.2184	0.1219	0.0831	0.0312	0.0235
AX5	0.2184	0.1207	0.0611	0.0375	0.0141

Table 7.15. Positive and negative ideal solutions

	$\boldsymbol{\upsilon}$	$\boldsymbol{\varphi}$	$\boldsymbol{\sigma_y}$	$\boldsymbol{E}$	$\boldsymbol{EoD}$
Positive Solution (A^*)	0.3276	0.1219	0.0831	0.0375	0.0235
Negative Solution (A^-)	0.1365	0.1086	0.0396	0.0215	0.0047

Subsequently, the negative and positive ideal solutions, as shown in Table 7.14, were calculated for the weighted normalised decision matrix by using Equations (7.3) and (7.4). The separation distance for each scaffold designs from the positive (D_j^*) and

negative (D_j^-) ideal solutions were calculated using Equations (7.5) and (7.6). In addition, Equation (7.7) was used to calculate the relative closeness values resulting in the ranking as shown in Table 7.15. The results of the combined AHP and TOPSIS method identified that the most suitable auxetic scaffold design for Scenario 2 is AX1.

Table 7.16. Ranking of alternatives for Scenario 2

Design	$(\boldsymbol{D_j^*})$	$(\boldsymbol{D_j^-})$	**Relative closeness values** $(\boldsymbol{CC_j^*})$	**Rank**
AX1	0.0291	0.1928	0.869	1
AX2	0.1585	0.0413	0.207	4
AX3	0.1951	0.0158	0.075	5
AX4	0.1094	0.0960	0.468	2
AX5	0.1118	0.0875	0.439	3

7.4. Conclusion

This chapter brings forward a hybrid multi-criteria selection model combining AHP and TOPSIS for the selection of bone scaffold designs for the first time. As such, the chapter of the research provides a new way to the selection of auxetic bone scaffolds considering a range of favourable parameters.

- A decision-making procedure for auxetic bone scaffolds featuring five selection criteria in the order Poisson's ratio > Porosity > yield strength > elastic modulus > ease of design applied to two scenarios to identify ideal designs are demonstrated.
- The combined AHP and TOPSIS method identified AX4 as the best scaffold design to offer a near-zero negative Poisson's ratio while satisfying the relative importance of the five selected criteria.

- The combined AHP and TOPSIS method identified AX1 as the best scaffold design to offer the highest negative Poisson's ratio while satisfying the relative importance of the five selected criteria.

These two designs will be used in subsequent chapters for parametric analysis and optimisation for stiffness matching while preserving their auxetic functionalities.

Chapter 8

Parametric analysis of best auxetic design

8.1. Introduction

An optimum auxetic bone scaffold is the one that offers an ideal mechanical response, stiffness matching and targeted porosity and strength. As such, understanding the relationship between these responses and the scaffold design parameters is critical for the generation of optimum designs. However, an optimisation problem requires the design parameters to be linked to the responses first. This can be done through the development of a surrogate model, which uses response surfaces to characterise the influence of geometrical parameters and their interaction on the responses of interest. The surrogate model employs mathematical and statistical techniques that are based on the fit of empirical models to numerical data. This is done by employing polynomial functions to describe the behaviour of the auxetic lattice selected for the bone scaffold and to explore their parametric influence.

This chapter describes the surrogate modelling used to carry out parametric analysis of scaffolds AX1 and AX4 identified by AHP and TOPSIS as the most suitable designs for Scenario 2 (S2) and Scenario 1 (S1), respectively. Response surface methodology (RSM) following Central composite design (CCD) was applied to develop models for the responses of the selected auxetic scaffolds. Variation of design variables on four primary responses are considered, namely the negative Poisson's ratio $(-\upsilon)$, porosity (φ), yield strength (σ_y) and elastic modulus (E).

The analysis carried out on S1 and S2 reveals the influence of design control variables (t and θ) on the performance of near-zero and high strain auxetic bone scaffolds, respectively. The analysis of variance (ANOVA) is used to evaluate the quality of the surrogate model in capturing the influence of φ, $-\upsilon$, σ_y and E for the designs considered. Overall, the chapter presents a response surface model that can adequately capture the influences of varying thickness and angle on the mechanical performance and porosity of auxetic bone scaffolds.

Overall, the chapter shows that the control variables t and θ has a significant influence in varying both the porosity and mechanical performance of both AX1 and AX4 scaffolds. As such, these design parameters can be modulated to achieve targeted performance which will be demonstrated in Chapter 9.

8.2. Response surface methodology

Response surface methodology (RSM) was used to create a surrogate model by using the Central composite design (CCD), which is one of the DoE methods. RSM is a set of statistical and mathematical techniques that can be used to design, improve, and optimise processes. RSM is generally applied when the number of input factors has an impact on the performance of a process or quality characteristic [381,382]. As such, RSM can be used to describe the performance metric or a quality attribute and its relationships to the input variables. The input variables, also known as independent variables, can be selected based on a specific design or process requirements [383].

For the problem under consideration, the design parameters of the scaffolds must be linked to the responses first to obtain the solution for the optimisation problem as conceived in ‘Scenario 1’ and ‘Scenario 2’. The surrogate models were created using

RSM, which use response surfaces to evaluate the effect of geometrical parameters and their interactions on the responses of interest.

It is challenging to identify and control the contribution of all variables and their influence on the scaffold design. As such, the strut thickness (t) and auxetic angle (θ) were chosen as the variables to investigate their significance on both the auxetic behaviour and mechanical performance of the scaffold.

Table 8.1. Design variables selected for the auxetic scaffold to be optimised under Scenario 1

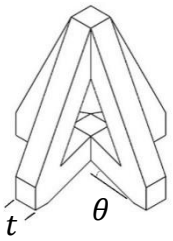

Variable	$\boldsymbol{\theta(deg.)}$	$\boldsymbol{t\ (mm)}$
-1	15	0.38
0	20	0.43
1	25	0.48

Table 8.2. Design variables selected for the auxetic scaffold to be optimised under Scenario 2

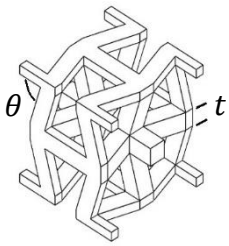

Variable	$\boldsymbol{\theta(deg.)}$	$\boldsymbol{t(mm)}$
-1	65	0.25
0	70	0.30
1	75	0.35

Table 8.1 and 8.2 summarises how these variables correspond to designs selected for 'Scenario 1' and 'Scenario 2', respectively. The thickness (t) ranges chosen for the two scenarios supply a fair balance between the structure's quality and its ability to deform adequately under loading. Angle (θ) was varied between 15° and 25° for scenario one. The upper limit of 25° was the highest angle feasible without penetrating the struts. The lower limit was set to 15° as any further reduction can result in non-auxetic behaviour under compressive loading. Although Chapter 4 showed there exists a slight variation between ideal and additively manufactured samples when it

comes to strut thickness (t) and auxetic angle (θ). The influence of this on $-\upsilon$ was found to be 2.51% (Table 6.2) for AX4 which is the chosen architecture for Scenario 1. At no point, did the slight variation in additively manufactured samples resulted in a positive Poisson's ratio, in this regard, a 2.51% variation cannot change the strain direction of the architecture. As such the approach for optimising near-zero Poisson's ratio architecture guarantees a near zero but negative $-\upsilon$ in real life taking into consideration any variation that may occur during fabrication. Similarly, for Scenario 2, θ below 65° can result in penetration of the struts, and an angle higher than 75° risks non-auxetic behaviour under compression.

Accordingly, four responses are used to represent the model in this study: Poisson's ratio (υ), porosity (φ), yield strength (σ_y) and elastic modulus (E). The response surface model can be used to predict the performance, which can identify the design parameters that has the most influence on the scaffold's performance. The predictions are carried out through fitting the simulation data to suitable polynomial equations from randomised experimental sets.

The use of RSM has the advantage of allowing the responses in a given design space to be identified with a smaller number of experimental sets referred to as the sampling design points. The CCD method employed in this study develops the response surface model following the methodology as summarised in Figure 8.1. CCD is a high-efficiency sampling approach that enables the creation of accurate RS models with fewer experiments.

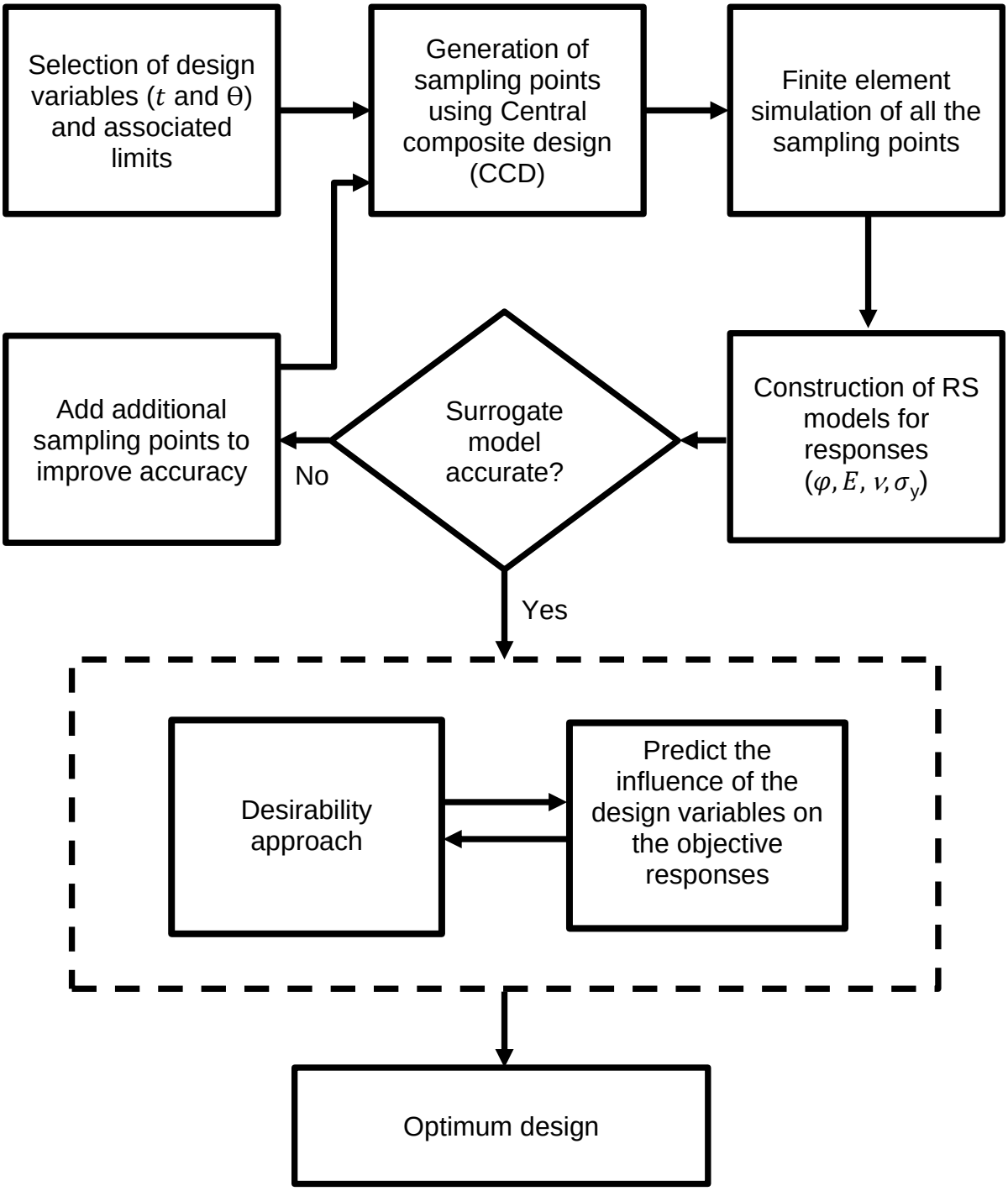

Figure 8.1. Flow chart of the optimisation process using the desirability approach

When it comes to structural mechanics often, a certain relationship exists between output (y) and design variables (x), where a model can be written as shown in Equation (8.1):

$$y = f\ (x_1, x_2, \dots\dots\dots, x_n) + \ \varepsilon \tag{8.1}$$

where, n is the number of independent variables and the error associated with the response y is ε. If a second-order polynomial function is employed to explain the relationship between the responses and the independent variables in RSM, the RS model can be written as shown in Equation (8.2):

$$y = \beta_0 + \sum_{i=1}^{k} \beta_i x_i + \sum_{i=1}^{k} \beta_{ii} {x_i}^2 + \sum_{i} \sum_{j} \beta_{ij} x_i x_j + \varepsilon \tag{8.2}$$

where, $\beta_0, \beta_i, \beta_{ij}\ and\ \beta_{ii}$ are known as regression coefficients of the model. Regression coefficients are estimates describing the relationship between a predictor variable and the response. Once the randomised experimental sets are analysed and the beta values computed, the response surface model can be used to identify what values of x will fulfil a specific set of responses. As such, these models are suited for parametric analysis to conceive specific influences of each of the variables on the responses of interest ($\upsilon, \varphi, \sigma_y, E$). Post-parametric analysis, the response surface model is used in Chapter 9 to identify the optimum values of design variables that satisfy a multi-objective response criterion.

8.3. Results and discussion

Using the methodology discussed in section 8.2, two RS models are generated using RSM, each to satisfy a specific scenario (Scenario 1 and Scenario 2). The combined AHP and TOPSIS analysis presented in Chapter 7 identified AX4 and AX1 as the best scaffold designs to perform optimisation under Scenario 1 and Scenario 2, respectively. As such, a parametric analysis of each of these designs (AX4 and AX1)

are carried out using the CCD method. The accuracy of the RS models is characterised using the analysis of variance (ANOVA) before using it for parametric analysis. Post-validation, the surrogate models are used to create response surfaces (RS) characterising the link between the geometrical parameters (t, θ) and the responses $(\upsilon, \varphi, \sigma_y, E)$ of interest for the auxetic bone scaffold. The subsequent section presents the analysis under respective scenarios starting from Scenario 1.

8.3.1. Scenario 1: Influence of design parameters on the performance of AX4

8.3.1.1. Generation of the response surface model for AX4

The CCD higher-order methodology was used to create the response surface model, which represents the variables of interest as independent factors, as listed in Table 8.3. Design variants of AX4 that met each of the factorial combinations dictated by the sampling points were generated. Each of the design samples was subsequently modelled and analysed using the using finite element method resulting in the responses for υ, φ, σ_y and E, as shown in Table 8.3.

Table 8.3. CCD matrix showing the design variables and responses for AX4 in Scenario 1

Factor 1 **A: t** **(mm)**	**Factor 2** **B: θ** **(Deg.)**	**Response 1** $\boldsymbol{\upsilon}$	**Response 2** $\boldsymbol{\varphi}$ **(%)**	**Response 3** $\boldsymbol{\sigma_y}$ **(MPa)**	**Response 4** $\boldsymbol{E}$ **(GPa)**
0.39	24	-0.08	80.08	47	10.45
0.43	20	-0.05	77.44	52	14.50
0.47	16	-0.02	75.17	63	18.47
0.43	20	-0.05	77.44	52	14.50
0.43	20	-0.05	77.44	52	14.50
0.43	20	-0.05	77.44	52	14.50
0.43	25	-0.06	77.03	54	14.24
0.43	15	-0.04	78.29	50	13.89

0.39	16	-0.05	81.13	46	10.07
0.47	24	-0.03	73.99	64	18.69
0.43	20	-0.05	77.44	52	14.50
0.48	20	-0.02	73.63	64	20.60
0.38	20	-0.07	81.38	41	09.46

The best-fit indicators for the results were calculated and found that the φ, σ_y and E can be characterised by linear models listed in Equations (8.3), (8.4) and (8.5), respectively. However, the υ was found to follow a quadratic trend signifying interaction effects between the design parameters as listed in Equation (8.6):

$$\varphi = 115.35 - 81.35t - 0.14\theta \tag{8.3}$$

$$\sigma_y = -53.55 + 235.21t + 0.27\theta \tag{8.4}$$

$$E = -35.53 + 114.53t + 0.04\theta \tag{8.5}$$

$$\upsilon = 0.59 - 2.42t - 0.02\theta + 0.04t\theta + 2.50t^2 + 5e^{-5}\theta^2 \tag{8.6}$$

The significance of each of the geometrical parameters of AX4 on the resulting mechanical performance was modelled using analysis of variance (ANOVA). Table 8.4 summarises the relevant model terms and adequacy measures evaluating the quality of the response surface model generated. The probability (p-value), coefficient of determination R^2, Adjusted R^2, Predicted R^2, and Adequate precision are the model's accuracy measures.

Table 8.4. Summary of ANOVA for the developed RS model for AX4

Model	F-value	p-value	Statistical measurements			
			R^2	Adj-R^2	Pre-R^2	Adeq-precision
φ	1267.76	< 0.0001	0.9961	0.9953	0.9920	103.2622
E	613.45	< 0.0001	0.9919	0.9903	0.9822	72.873
υ	124.28	< 0.0001	0.9889	0.9809	0.9208	37.6713
σ_y	110.16	< 0.0001	0.9566	0.9479	0.9130	30.6959

Table 8.4 shows that all four models feature large F-values and very low p-values, indicating that all four models are statistically significant. Model terms with p-values less than 0.0001 are considered significant [339]. Furthermore, models with more than four adequate precision ratios show that noise in the model is minimal [242]. And all of the models show high R^2 (>0.9) values, which indicates a good agreement between the anticipated and adjusted R^2. Overall, the analysis of variance reveals that all four models are accurate and can be utilised to carry out a parametric analysis within the range of design variables considered.

After having evaluated the quality of the response surface models using ANOVA, the relationship between the finite element and RS model predictions were compared, as shown in Figure 8.2. For all responses being evaluated $(\varphi, E, \upsilon \; and \; \sigma_y)$, the predictions of the RS model (diagonal dotted line) can be seen to closely follow the numerical results. The comparatively small residuals, as presented in Table 8.5, also confirms that the models are valid. This means that Equations (8.3-8.6) adequately represents the relationship between the geometrical variables and the responses. This demonstrates that the RS models are suitable for predicting both mechanical performance and design parameter interactions for AX4.

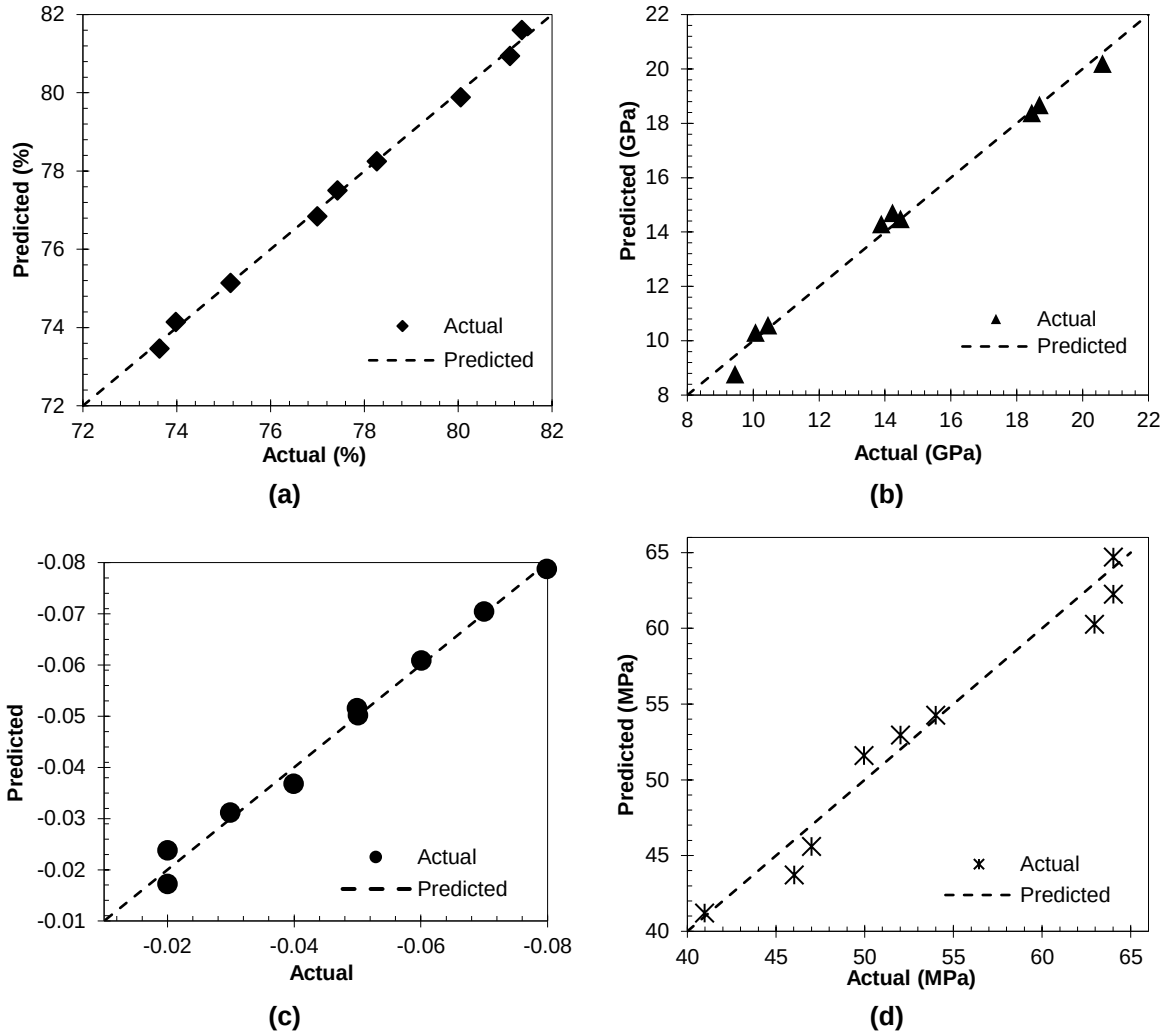

Figure 8.2. Comparison between RS model and finite element predictions for AX4 showing (a) Porosity (φ), (b) elastic modulus (E), (c) Negative Poisson's ratio ($-\upsilon$) and (d) Yield strength (σ_y)

Table 8.5. Residual values for the RS models showing deviation of the sampling point responses with respect to ideal

$\boldsymbol{\varphi}$	$\boldsymbol{E}$	$\boldsymbol{\upsilon}$	$\boldsymbol{\sigma_y}$
0.1745	-0.1276	-0.0014	+1.36
-0.0908	0.0100	0.0000	-1.00
0.0140	0.0676	0.0039	+2.64
-0.0908	0.0100	0.0000	-1.00
-0.0908	0.0100	0.0000	-1.00
-0.0908	0.0100	0.0000	-1.00
0.2084	-0.4436	0.0008	-0.35
0.0500	-0.4064	-0.0033	-1.65

0.2215	-0.2338	0.0016	+2.27
-0.1630	0.0138	0.0009	+1.73
-0.0908	0.0100	0.0000	-1.00
0.1669	0.3834	-0.0029	-0.76
-0.2184	0.6966	0.0004	-0.24

8.3.1.2. Influence of AX4 design parameters on porosity

Figure 8.3 shows that the strut thickness (t) has the largest influence on porosity (Figure 8.3a), followed by the auxetic angle (θ) (Figure 8.3b). As shown in Figure 8.3a, the porosity of the structure increases linearly, consistent with the reduction in strut thickness. Looking at the influence of θ a similar trend could be observed, however, at a significantly lower linear slope.

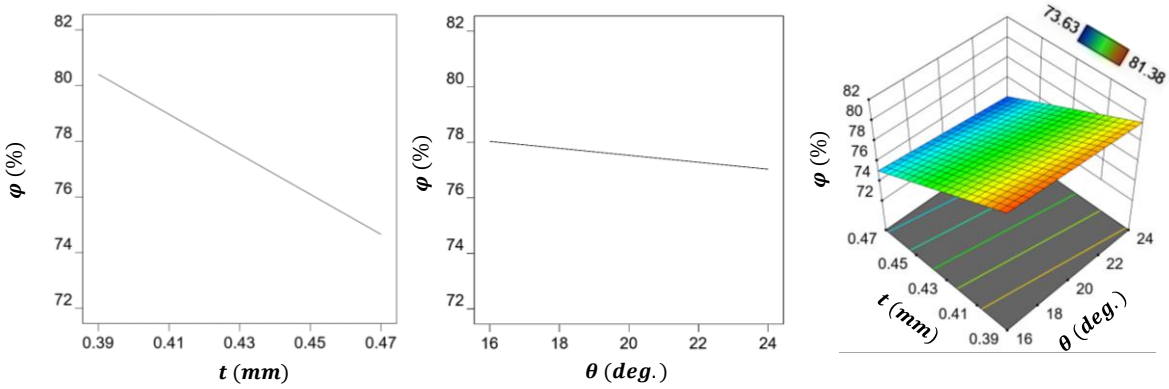

(a) **(b)** **(c)**

Figure 8.3. Influence of the design parameters on AX4 structure showing (a) the influence of strut thickness on porosity, (b) the influence of auxetic angle on porosity and (c) the interdependence of thickness and auxetic angle on porosity

Looking at the interaction effects of the design parameters, as shown in Figure 8.3c, the lowest porosity of 73.63% was observed at the highest values for t and θ. The trend for the interaction effect also continued at the highest porosity of 81.38% at the lowest t and θ. This means that decreasing thickness reduces the relative density of the AX4 architecture, resulting in increased porosity. Decreasing θ reduces the length

of the strut, therefore increasing the relative density, also influencing porosity at a lower rate in comparison to t. Although an interdependence of t and θ on porosity was observed, the cumulative effects are not drastic, as shown in Figure 8.3c. Therefore, for AX4, the porosity of the structure can be changed significantly by varying t. Overall, the first-order effects of t are the most significant parameter on porosity. This indicates that varying porosity by decreasing t will give a higher porosity than decreasing the same amount of θ.

8.3.1.3. Influence of AX4 design parameters on the elastic modulus

It can be seen that the elastic modulus of AX4 primarily depends on t (Figure 8.4a), with the highest (20.6 GPa) and lowest (9.46 GPa) value of E corresponding to the highest and lowest t, respectively. Figure 8.4b shows that the influence of θ on the elastic modulus of AX4 is negligibly signified by an almost straight line across all the angles tested.

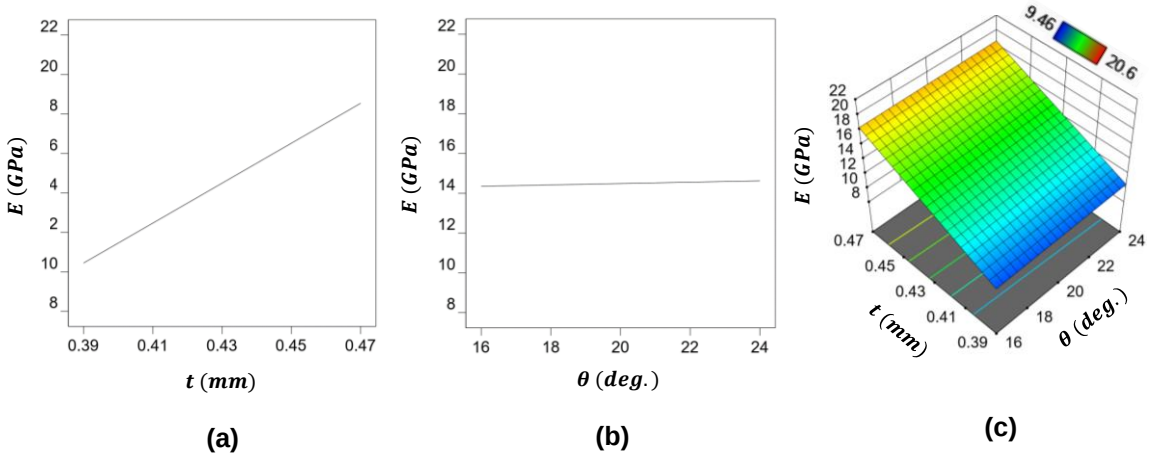

Figure 8.4. Influence of the design parameters on AX4 structure showing (a) the influence of strut thickness on elastic modulus, (b) the influence of auxetic angle on elastic modulus and (c) the interdependence of thickness and auxetic angle on elastic modulus

As such t is the most significant parameter when it comes to modulating the elastic modulus of the AX4 scaffold. This is expected as the thickness was found to have a significant influence on the relative density of the structure, as revealed in section 8.3.1.2. Figure 8.4c shows that the interdependence of the design parameters on E is minimal and has no effect on the performance trend, resulting in a constant performance slope notwithstanding the difference in θ. Therefore, to increase E, increasing t is the only option.

8.3.1.4. Influence of AX4 design parameters on negative Poisson's ratio

Negative Poisson's ratio was found to be significantly affected by both t and θ, as shown in Figure 8.5. A quadratic relationship can be observed in Figure 8.5a, with the absolute value of $-\upsilon$ increasing consistently with thickness. This is due to the lateral shrinkage of the being significantly influenced by the porosity allowing space for elastic deformation. As the thickness increases, the relative density decreases, leading to a higher stiffness lowering elastic deformation. As a result, the lateral shrinkage is reduced, increasing the absolute value $-\upsilon$, as shown in Figure 8.5a.

Although not as significant in comparison to t, θ was also found to significantly affect $-\upsilon$, as shown in Figure 8.5b. The reason for this is due to the influence of the angle on the load transfer of the unit cell; at higher angles, larger loads are being transferred to the lateral connections increasing the lateral strain increasing $-\upsilon$. This means, for AX4, if θ decreases below a certain value, the Poisson's ratio will change from negative to positive. As can be seen, both design variables have a separate function to play in altering the Poisson's ratio, as shown in Figure 8.5c.

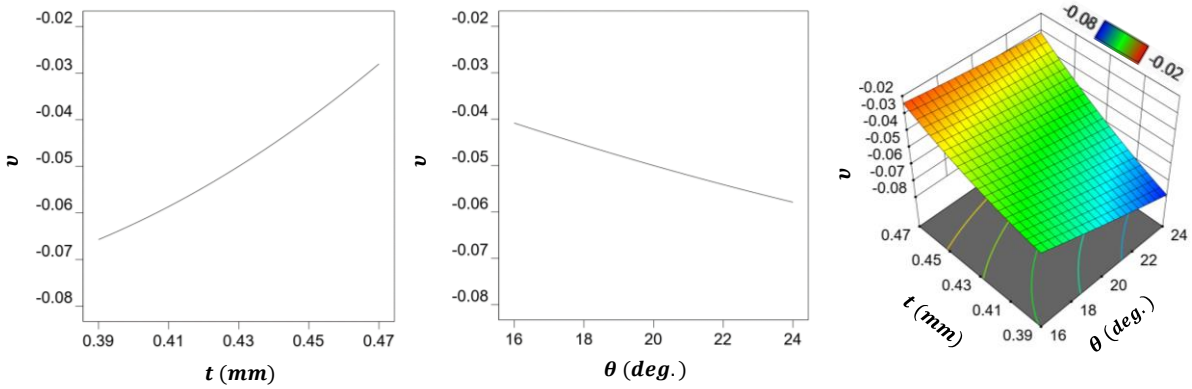

(a) (b) (c)

Figure 8.5. Influence of the design parameters on AX4 structure showing (a) the influence of strut thickness on Poisson's ratio, (b) the influence of auxetic angle on Poisson's ratio and (c) the interdependence of thickness and auxetic angle on Poisson's ratio

Negative Poisson's ratio was found to be increased by decreasing the t and increasing the θ. As a result, the highest value of $-\upsilon$ was found at the highest angle and lowest thickness. It was found that both t has the highest significance on $-\upsilon$, closely followed by θ. Overall, the first-order effect of t is the most significant, followed by θ and finally, the interaction effect of $t\theta$.

8.3.1.5. Influence of AX4 design parameters on yield strength

Figure 8.6a shows that the strut thickness (t) has the largest influence on the yield strength of the scaffold. The yield strength can be seen to increase linearly, consistent with the strut thickness. Looking at the influence of auxetic angle, an increase in θ resulted in an increase in yield strength, as shown in Figure 8.6b. However, the rate of σ_y increase was significantly lower for θ in comparison to t.

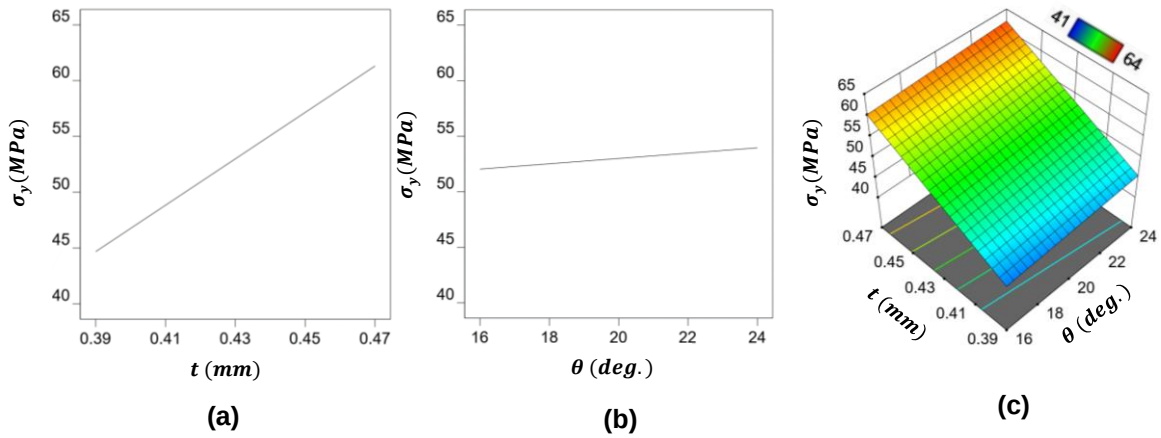

Figure 8.6. Influence of the design parameters on AX4 structure showing (a) the influence of strut thickness on yield strength, (b) the influence of auxetic angle on yield strength and (c) the interdependence of thickness and auxetic angle on yield strength

Figure 8.6c shows the interdependence of the θ and t on the yield strength of the AX4 scaffold. It can be seen that although σ_y is sensitive to both θ and t, the rise in yield strength increases is largely driven by t in a linear fashion with a very small contribution from θ. However, the interaction effects mean that the largest σ_y is obtained with the highest t and θ. Nevertheless, the dependence on σ_y on θ is comparatively minimal and has a limited effect on the performance. As such, the most significant terms on σ_y are the first-order influences of t followed by θ in the order $t > \theta$, where the thickness has a significantly higher influence in comparison to θ. This indicates that increasing t will give a greater σ_y value than increasing the same amount of θ.

8.3.2. Scenario 2: Influence of design parameters on the performance of AX1

8.3.2.1. Generation of the response surface model for AX1

The CCD higher-order methodology was used to create the response surface model, which represents the variables of interest as independent factors, as listed in Table 8.6. Design variants of AX1 that met each of the factorial combinations dictated by the

sampling points were generated. Each of the AX1 design samples was subsequently modelled and analysed using the finite element method resulting in the responses for υ, φ, σ_y and E, as shown in Table 8.6.

Table 8.6. CCD matrix showing the design variables and responses for AX1 in Scenario 2

Factor 1 **A: t** **(mm)**	**Factor 2** **B: θ** **(Deg.)**	**Response 1** υ	**Response 2** φ **(%)**	**Response 3** σ_y **(MPa)**	**Response 4** E **(GPa)**
0.30	70	-0.27	79.75	46	14.89
0.34	66	-0.21	73.95	60	19.08
0.30	70	-0.27	79.75	46	14.89
0.26	66	-0.38	83.77	30	8.60
0.34	74	-0.16	75.50	80	22.58
0.30	65	-0.28	78.93	44	12.91
0.30	75	-0.22	80.43	52	16.79
0.30	70	-0.27	79.75	46	14.89
0.30	70	-0.27	79.75	46	14.89
0.35	70	-0.19	73.46	76	22.6
0.30	70	-0.27	79.75	46	14.89
0.26	74	-0.31	84.71	38	11.48
0.25	70	-0.37	85.36	32	8.94

The best-fit indicators for the results were calculated and found that the φ, υ and E can be characterised by linear models listed in Equations (8.7), (8.8) and (8.9), respectively. However, σ_y was found to follow a quadratic trend signifying interaction effects between the design parameters as listed in Equation (8.10):

$$\varphi = 106.23 - 126.78t + 0.16\theta \quad (8.7)$$

$$\upsilon = -1.38 - 2.03\mathrm{t} + 7.24e^{-3}\theta \quad (8.8)$$

$$E = -57.56 + 144.59t + 0.42\theta \quad (8.9)$$

$$\sigma_y = 1106.34 - 3245.44t - 19.81\theta + 24t\theta + 3400t^2 + 0.1\theta^2 \quad (8.10)$$

The significance of each of the geometrical parameters of AX1 on the resulting mechanical performance was modelled using analysis of variance (ANOVA). Table 8.7 summarises the relevant model terms and adequacy measures evaluating the quality of the response surface model generated. The probability (p-value), coefficient of determination R^2, Adjusted R^2, Predicted R^2, and Adequate precision are the model's accuracy measures.

Table 8.7. Summary of ANOVA for the developed RS model for AX1

Model	**F-value**	**p-value**	**Statistical measurements**			
			R^2	**Adj-R^2**	**Pre-R^2**	**Adeq-precision**
φ	844.03	< 0.0001	0.9941	0.9929	0.9877	84.8287
E	466.58	< 0.0001	0.9894	0.9873	0.9786	61.0712
υ	131.63	< 0.0001	0.9634	0.9561	0.9202	31.8144
σ_y	74.97	< 0.0001	0.9817	0.9686	0.8696	26.4704

Table 8.7 shows that all four models feature large F-values and very low p-values, indicating that they are statistically significant. P-values less than 0.05 indicate that model terms are significant. In comparison, for all the models generated (Equation 8.7-8.10), the p-values are less than 0.0001, signifying a highly accurate model [339]. Furthermore, all the models can be seen to reveal an adequate precision ratio higher than 4, which is the measure showing that the noise in the model is minimal [242]. In addition, all the models were found to feature high R^2 (>0.9), which also indicate that a good agreement can be anticipated for the predicted results. Overall, the analysis of variance reveals that all four models are accurate and can be utilised to carry out a parametric analysis within the range of design variables considered.

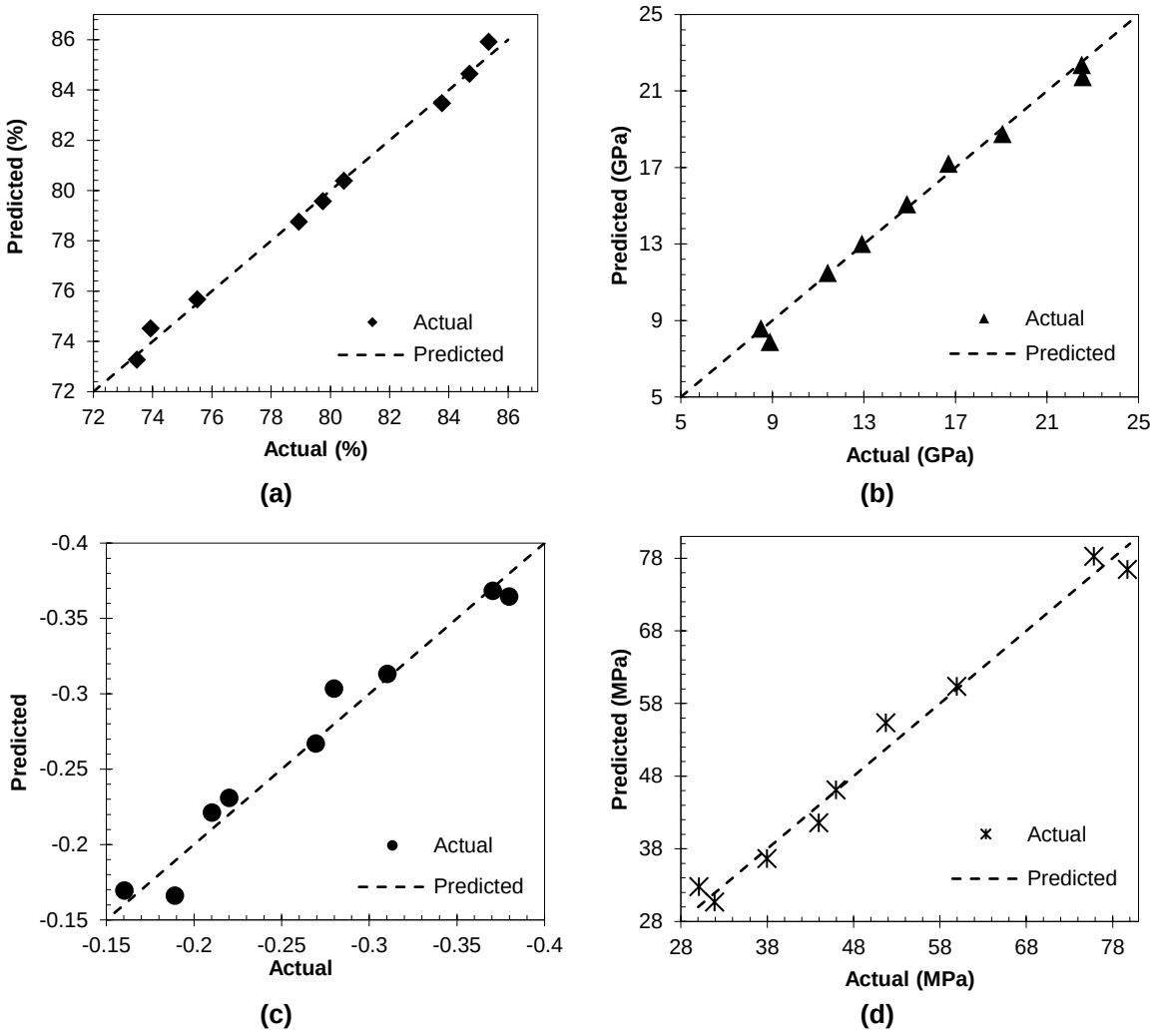

Figure 8.7. Comparison between RS model and finite element predictions for AX1 showing (a) Porosity (φ), (b) elastic modulus (E), (c) Negative Poisson's ratio ($-\upsilon$) and (d) yield strength (σ_y)

After having evaluated the quality of the response surface models using ANOVA, the relationship between the finite element and RS model predictions were compared, as shown in Figure 8.7. For all responses being evaluated ($\varphi, E, \upsilon \; and \; \sigma_y$), the predictions of the RS model (diagonal dotted line) can be seen to closely follow the numerical results. The comparatively small residuals, as presented in Table 8.8, also confirms that the models are valid. This means that Equations (8.7-8.10) adequately represents the relationship between the geometrical variables and the responses of AX1. This

demonstrates that the RS models are suitable for predicting both mechanical performance and design parameter interactions for AX1.

Table 8.8. Residual values for the RS models showing deviation of the sampling point responses with respect to ideal for scaffold AX1

$\boldsymbol{\varphi}$	$\boldsymbol{E}$	$\boldsymbol{\upsilon}$	$\boldsymbol{\sigma_y}$
-0.0031	-0.2969	-0.0031	0.0000
0.0107	0.2642	0.0107	-0.3640
-0.0031	-0.2969	-0.0031	0.0000
-0.0157	0.0087	-0.0157	-2.81
0.0095	0.7974	0.0095	3.81
0.0231	-0.1791	0.0231	2.45
0.0107	-0.4948	0.0107	-3.45
-0.0031	-0.2969	-0.0031	0.0000
-0.0031	-0.2969	-0.0031	0.0000
-0.0246	0.1832	-0.0246	-2.23
-0.0031	-0.2969	-0.0031	0.0000
0.0031	-0.0780	0.0031	1.36
-0.0015	0.9829	-0.0015	1.23

8.3.2.2. Influence of AX1 design parameters on porosity

Figure 8.8 shows that the strut thickness (t) has the largest influence on porosity (Figure 8.8a), followed by the auxetic angle (θ) (Figure 8.8b). As shown in Figure 8.8a, the porosity of the structure increases linearly, consistent with the reduction in strut thickness. Looking at the influence of θ a similar trend could be observed at a lower linear slope.

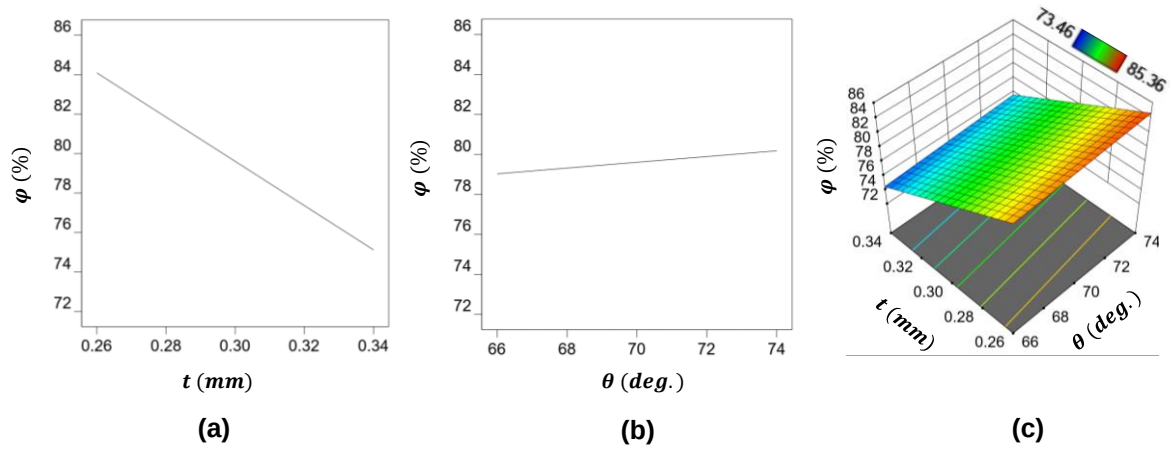

Figure 8.8. Influence of the design parameters on AX1 structure showing (a) the influence of strut thickness on porosity, (b) the influence of auxetic angle on porosity and (c) the interdependence of thickness and auxetic angle on porosity

The porosity of the AX1 scaffold is predominantly determined by the strut thickness (t) and marginally by the auxetic angle (θ) of the re-entrant architecture. The porosity of the structure increases linearly when reducing t and increasing θ, reaching a maximum porosity of 85.36% at lowest t and highest θ. This means that decreasing thickness reduces the relative density of the structure, driving an increase in porosity. Increasing θ, on the other hand, reduces the strut length lowering the relative density while increasing porosity.

Looking at the interaction effects of the design parameters, as shown in Figure 8.8c, the lowest porosity of 73.46% was observed at the highest value of t and lowest θ. The trend for the interaction effect also continued at the highest porosity at the lowest t and highest θ. Although an interdependence of t and θ on porosity was observed, the cumulative effects are not drastic, as shown in Figure 8.8c. Therefore, for AX1, the porosity of the scaffold can be changed significantly by varying t. Overall, the first-order effects of t are the most significant parameter on porosity for AX1. This indicates

that decreasing t will give a higher porosity as opposed to increasing θ by the same amount.

8.3.2.3. Influence of AX1 design parameters on elastic modulus

Figure 8.9 shows that the elastic modulus of the AX1 scaffold is primarily dependent on t (Figure 8.9a) and slightly on θ (Figure 8.9b) linearly. Elastic modulus increases consistently with the rise in t and θ, leading to the highest value of 22.6 GPa at their maximum, as shown in Figure 8.9c.

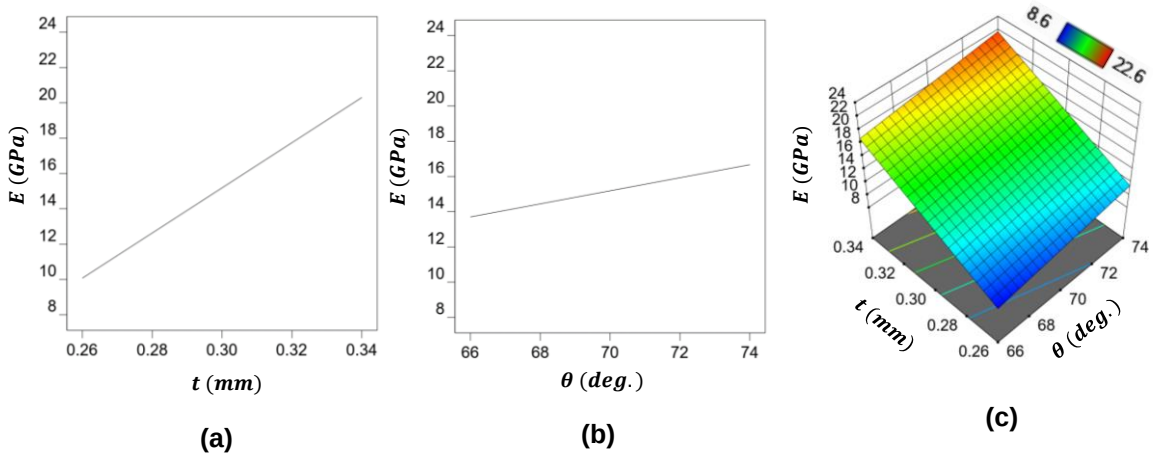

Figure 8.9. Influence of the design parameters on AX1 structure showing (a) the influence of strut thickness on elastic modulus, (b) the influence of auxetic angle on elastic modulus and (c) the interdependence of thickness and auxetic angle on elastic modulus

While t is the most significant design variable driving the stiffness of the AX1 scaffold, θ can also be seen to influence the performance. This means modulating both thickness and angle can influence the elastic modulus at different rates. While increasing thickness raises density and, therefore, higher stiffness, a high auxetic angle helps to push the beams further apart, reducing buckling enhancing E. Figure 8.10c shows that although there is a certain interdependence of the design parameters, E is still largely driven by the thickness. As such, increasing t will yield a

higher E in comparison to increasing the same amount of θ. Overall, the first-order effect of t is the most significant, followed by the θ on the elastic modulus of AX1.

8.3.2.4 Influence of AX1 design parameters on Poisson's ratio

Negative Poisson's ratio $(-\upsilon)$ of AX1 can be seen to be dependent on both t and θ, as shown in Figure 8.10, signifying a change in lateral strain depending upon the parametric values of the design variables. $-\upsilon$ increases linearly consistent with t at a lower rate (Figure 8.10a) in comparison to a reduce in θ (Figure 8.10b) signified by varying slopes of the linear trend. Both design factors have a separate function to play in altering the Poisson's ratio, as shown by the response surface data. As a result, the highest value of $-\upsilon$ was found at the lowest angle and lowest thickness, as shown in Figure 8.10c. As t reduces, the relative density reduces while porosity increases; this leads to a larger lateral strain pushing the $-\upsilon$ values higher.

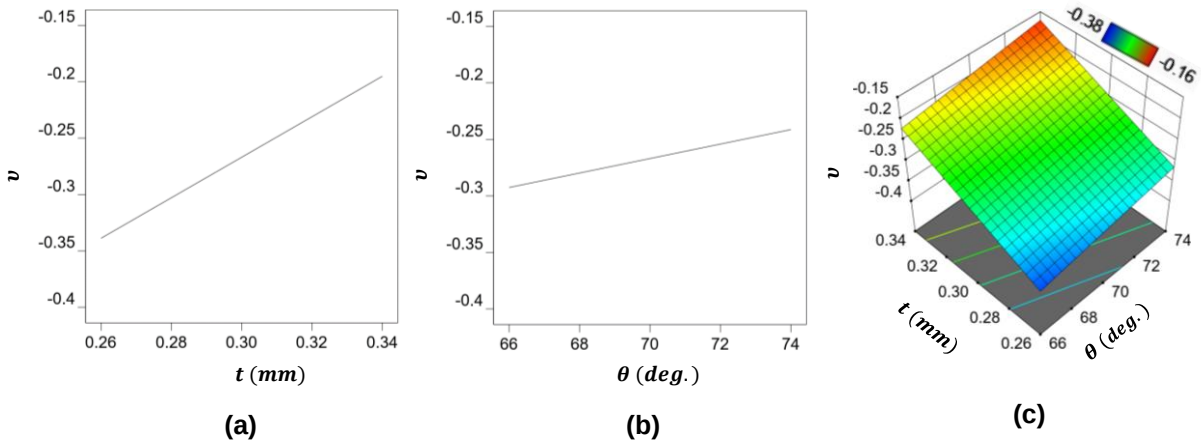

Figure 8.10. Influence of the design parameters on AX1 structure showing (a) the influence of strut thickness on Poisson's ratio, (b) the influence of auxetic angle on Poisson's ratio and (c) the interdependence of thickness and auxetic angle on Poisson's ratio

When it comes to the influence of θ, larger angles lead to more material being influenced by the axial load, which also gives rise to high lateral strain, thus increasing

the $-\upsilon$ albeit at a lower rate in comparison to t. Overall, $-\upsilon$ the most significant factors are the first-order effect of t followed by θ. As such, the $-\upsilon$ for AX1 can be modulated by both adjusting the thickness and angle to obtain the desired performance.

8.3.2.5 Influence of AX1 design parameters on yield strength

The yield strength for AX1 was found to be largely driven t with a small influence from θ, as shown in Figures 8.11a and 8.11b, respectively. This is due to the material deformation being significantly influenced by the porosity. As the thickness increases, the relative density increases leading to a higher strength due to more material resisting plastic deformation. A quadratic relationship can be observed for both the cases with σ_y increasing consistently with both thickness and angle at a higher rate.

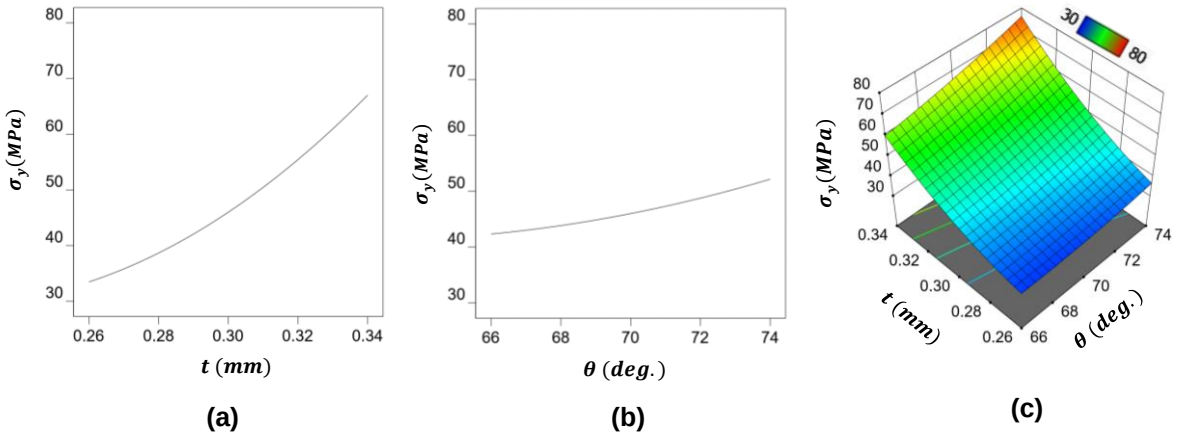

Figure 8.11. Influence of the design parameters on AX1 structure showing (a) the influence of strut thickness on yield strength, (b) the influence of auxetic angle on yield strength and (c) the interdependence of thickness and auxetic angle on yield strength

Figure 8.11c shows a trend in performance which demonstrates a high interaction effect between the design parameters. For example, the highest yield strength was observed when both t and θ peaked. Overall, the order of influence of design parameters on the yield strength of AX1 is of the form $t > \theta > t\theta$.

Overall, looking at both AX1 and AX4, it is evident that the design parameters have a varying influence on both the porosity and mechanical performance. As such, these design parameters can be modulated to achieve targeted performance. This will be demonstrated in Chapter 9 by optimising both the architectures for targeted stiffness (elastic modulus) while preserving high porosity and $-\upsilon$. Both near zero and high $-\upsilon$ materials possess significant potential when it comes to load bearing tissue engineering scaffolds. When such architectures are subjected to axial load, they will shrink locally, when the material is bent, the material exhibits an “arch” shape, which can well resist the bending deformation while offering compatible stiffness with the host bone. Literature shown that this kind of material possesses many advantages compared to conventional counterparts [384]. Furthermore, other physical properties including hardness [385], shear resistance [386] and energy absorption [387] are improved. Although not directly targeting bone scaffolds, increasing number of materials with zero and negative ratio Poisson’s are being investigated for numerous applications. Nevertheless, stiffness matched auxetic materials suitable for bone scaffold application are yet to be explored in literature. As such Chapter 9 shows reveals how meta-biomaterials that can offer near zero and negative Poisson’s ratio can be optimized for targeted performance.

8.4. Conclusion

The chapter presents the parametric analysis of two auxetic bone scaffolds, AX4 and AX1, predicted by the combined AHP and TOPSIS method as being the most suitable for Scenario 1 and Scenario 2, respectively. A methodology for the construction of a Response Surface Model for auxetic bone scaffolds that can adequately predict the trend in Poisson’s ratio (υ), porosity (φ), yield strength (σ_y) and elastic modulus (E)

influenced by design variables strut thickness (t) and auxetic angle (θ) is demonstrated.

- The analysis of variance (ANOVA) found the central composite design (CCD) to adequately capture the influence of all design variables on φ, $-\upsilon$, σ_y and E for both the AX4 and AX1 bone scaffolds.
- The parametric analysis identified a linear dependence of design variables on both porosity and elastic modulus for both AX1 and AX4 scaffolds, with t having a higher influence in comparison to θ.
- When it comes to $-\upsilon$ all parametric combinations demonstrated auxetic performance, with AX1 and AX4 showing a linear and quadratic relationship to design variables, respectively.
- Parametric analysis on yield strength identified AX1 and AX4 to have a quadratic and linear relationship to design variables, respectively.
- In the order of influence on design parameters, all responses were found to be primarily driven by the first-order effects of t and θ in the form $t > \theta$. However, the interaction effects of $t\theta$ were found to be significant for $-\upsilon$ and σ_y for AX4 and AX1, respectively.

Chapter 9

Optimisation and validation of the best auxetic scaffold

9.1. Introduction

The term ‘optimisation’ refers to the process of identifying the best design. Design optimisation is a tool that may be used to speed up the design cycle and improve results by replacing an iterative design process [388]. For the best auxetic bone scaffold, the optimal design is the one that has the ideal characteristics to achieve targeted $-\upsilon$, elastic modulus, strength while exhibiting suitable porosity. Understanding the relationship between these responses and the design parameters will allow for the generation of an optimised result. Based on the scaffold lattice selected for Scenario 1 (AX4) and 2 (AX1), multi-objective optimisation was carried out using a disability criterion that offers stiffness matching while maximising the porosity and yield strength.

This chapter also evaluates the accuracy of the response surface models in deriving optimal solutions under two scenarios. One that offers a near-zero, and the other one maximises negative Poisson’s ratio. The validation of the optimal solutions is carried out by generating suitable finite element models of predicted designs for the two scenarios. Scenario 1 shows an example of an optimised auxetic bone scaffold with a near-zero $-\upsilon$ that can match the modulus of an adult tibial host bone while maximising

porosity yield strength. The difference in Scenario 2 is to maximise the absolute $-\upsilon$ while offering all the same other criteria in Scenario 1.

9.2. Multi-objective optimisation methodology

Multi-objective optimisation methodology can be adopted when a solution to satisfy multiple objective functions are required [389]. The formulation of the optimisation problem will build on the responses surface model developed for Scenario 1 and Scenario 2 presented in Chapter 8. Multi-objective optimisation is part of multiple-criteria decision-making, allows identifying the ideal solution that satisfies an objective desirability criterion. The desirability criteria can be conceived by featuring any number of objectives linked to the design variables and parametric responses [390]. The application of multi-objective optimisation based on the response surface model for auxetic materials was demonstrated by Arjunan *et al*. [242].

The general formulation of the optimisation problem can be represented by using Equation (9.1) which shows the relationship between the objective function and the associated variables [242,391]:

$$\begin{cases} Minimise\ f(x) = [f_1(x), f_2(x), \dots\dots, f_i(x)] \\ \qquad s.t \qquad\qquad x^l \leq x \leq x^u \end{cases} \tag{9.1}$$

where, $x = (x_1, x_2, \dots, x_k)$ is the vector of k design variables, $x^l$and x^u are the lower and upper limits of the design variables, respectively, and $f(x)$ is the objective function [392]. After analysing five potential design candidates (AX1-AX5), the best auxetic architecture to be used for the bone scaffold designs were identified as AX4 and AX1 for Scenario 1 and Scenario 2, respectively. Although the parametric analysis of the

scaffolds in Chapter 8 showed the dependence of design variables on the responses ($\varphi, -\upsilon, E\ and\ \sigma_y$), the optimum values leading to ideal responses are yet to be identified. In order to optimise the scaffold AX4 and AX1, the ideal design variables leading to the desired responses must be identified. The desired responses are the properties of interests (responses) that are thought to be the most beneficial for the problem for which the design is being optimised.

Two optimisation scenarios were considered to identify the ideal scaffold parameters for AX4 and AX1, as summarised in Table 9.1. The suitability of the scaffolds to be applied to two different situations are conceived as Scenario 1 and Scenario 2, presented in Chapter 7. To achieve the first scenario, the optimal auxetic bone scaffold should feature the required design parameters to achieve the lowest lateral strain that can result in a near-zero $-\upsilon$, highest strength and targeted elastic modulus of 18 GPa matching the cortical bone while preserving high porosity. The porosity criteria is used to ensure the effect of design parameters on porosity is minimal. This is critical as a higher than 50% φ is a requirement for bone ingrowth. Furthermore, having a high porosity requirement allows to better characterise the design variables allowing minimal contribution to material mass.

Table 9.1. Summarising optimisation criteria used for the designs to generate optimum auxetic bone scaffold to satisfy multiple scenarios

Optimisation scenario	**S1**	**S2**
Best design identified by AHP and TOPSIS	AX4	AX1
Negative Poisson's ratio ($-\upsilon$)	Near zero	Maximise
Elastic modulus (E)	18 GPa (stiffness matching)	
Yield strength (σ_y)	Maximise	
Porosity (φ)	Maximise	

For the first scenario (S1), the four optimisation criteria conceive a desirability objective that can lead to a scaffold that offers near-zero lateral strain meeting the criteria dictated by Soman *et al.* for near-zero auxetic scaffolds. Generally, micro-strains on the growing bone tissue can lead to an improved tissue ingrowth interface between scaffolds and bone [3]. This can be achieved by conceiving a bone scaffold that features a high $-\upsilon$. As such the study shows the optimisation potential for AX1 in achieving stiffness matching while maximising $-\upsilon$. Therefore, the best auxetic scaffold for the second Scenario (S2) should have the ideal design parameters to achieve the highest $-\upsilon$, σ_y and φ while offering a targeted elastic modulus of 18 GPa to match the cortical bone.

9.3. Results and discussion

9.3.1 Optimum auxetic bone scaffold for Scenario 1

The optimisation problem description is created by combining the design variables, objective function and constraints. As such, the aim is to satisfy the objective function by altering the design variables within their bounds, following the relevant constraints [392,393]. An optimization problem requires design variables to be determined in order to attain the highest quantifiable performance within certain constraints [394]. Therefore, identifying the best design require conceiving a problem statement that focuses on the most significant responses. Where numerous responses are involved, a single objective strategy is ineffective, and a multi-objective description of the optimisation problem is required to find the best solution.

The combined AHP and TOPSIS decision-making criteria identified AX4 as having the best features to be optimised for Scenario 1 (S1). The optimised AX4 structure should

result in a near-zero $-\upsilon$, the elastic modulus of 18 GPa to match the modulus of adult cortical bone to avoid stress shielding and maladapted stress concentration. The yield strength (σ_y) should also be maximised while preserving a high porosity to offer the highest compressive strength while supporting bone reintegration. As such, the multi-objective criteria for S1 can be satisfied by conceiving an optimisation problem as shown in Equation (9.2):

$$\begin{cases} Maximise\ \sigma_y = f_1(\theta, t) \\ Maximise\ \ \varphi = f_2(\theta, t) \\ Maximise - \upsilon = f_3(\theta, t) \\ \quad s.t \quad E = 18\ GPa \\ \\ s.t\ \ 15.0 \leq \theta \leq 25.0 \\ s.t\ \ 0.38 \leq t \leq 0.48 \end{cases} \tag{9.2}$$

where, $-\upsilon, \varphi, \sigma_y$ and E are the responses of interest, θ and t are the design variables, namely the strut thickness and auxetic angle, respectively. Equation (9.2) was solved using the desirability approach to find a single solution that satisfies the optimisation problem. Because of its simplicity, the desirability approach has been widely employed in multi-response optimisation. In this method, multiple objective functions are combined into a single cost objective function, which is a measure of its relative performance [242].

The optimisation solution is converted to a desirability function using the desirability function approach. The approach employs a desirability function, $D(X)$, as an objective function. It shows the acceptable response ranges for each response (di). The desirability ranges from 0 to 1, identifying the least and most optimal solutions, respectively. When a response variable reaches the target value, the desirability function value becomes 1, and when the response variable reduces from the target

value, the desirability function value drops [395]. The geometric mean is used to combine the distinct desirabilities, giving the overall desirability D as shown in Equation (9.3).

$$D = (d_1 \cdot d_2 \cdot \ldots \cdot d_n)^{\frac{1}{n}} = \left(\prod_{i=1}^{n} d_i\right)^{\frac{1}{n}} \tag{9.3}$$

where, n is the number of responses. The overall function becomes 0 if any of the responses or factors fall outside their desirability range.

To carry out simultaneous optimization, each response was assigned a low and high, as shown in Equation (9.2), solved using the desirability approach. Figure 9.1 shows the output of the optimisation as a function of the desirability objective. It was found that the highest desirability of 0.94 can be achieved for design AX4 at an auxetic angle of 23.53° and strut thickness of 0.459 mm, as summarised in Table 9.2.

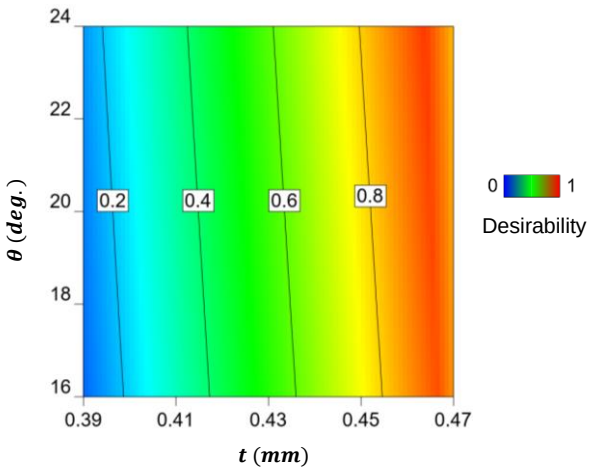

Figure 9.1. The desirability of the optimum solution against design variables for AX4 under Scenario 1

Table 9.2. Predicted optimal solution for AX4 under Scenario 1 criteria

Number	$t(mm)$	$\theta(Deg.)$	**Desirability**
1	0.459	23.53	0.94

Figure 9.1 shows that the highest desirability of 0.94 lies close to the highest auxetic angle and thickness. Scaffold design to satisfy the optimum design parameters was generated and numerically characterised using the finite element method, as shown in Figure 9.2. The von-Mises stress profile shown in Figure 9.2b indicates a stronger scaffold while featuring the optimum characteristics as summarised in Table 9.2. A comparison of the surrogate model and finite element prediction of the optimum AX4 scaffold is shown in Table 9.3.

Comparing the results showed that the response surface prediction underestimated the Poisson's ratio and porosity by 2.7% and 0.39%, respectively. However, the elastic modulus and yield strength were overestimated by 4.39% and 2.27%, respectively. The results showed that the optimal design offers a scaffold with desirable characteristics while offering a near-zero (≤0.037) auxetic performance and stiffness matching behaviour. As such, the optimum AX4 can be used as a bone scaffold where a near-zero $-\upsilon$ is desirable while offering stiffness matching to host bone. Overall, the surrogate model developed in this thesis offers an accuracy of 95.6% for predictions under scenario 1. As such, the response surface modelling presented in this thesis can be adopted for generating auxetic bone scaffold with targeted functionalities.

Table 9.3. Comparison between predicted and FEM values of the optimum AX4 scaffold design

Item	$\boldsymbol{\upsilon}$	$\boldsymbol{\varphi}$	$\boldsymbol{E}$	$\boldsymbol{\sigma_y}$
Predicted	-0.036	74.63	18	60.88
FEM	-0.037	74.93	17.21	59.5
% Difference	2.7	0.39	4.39	2.27

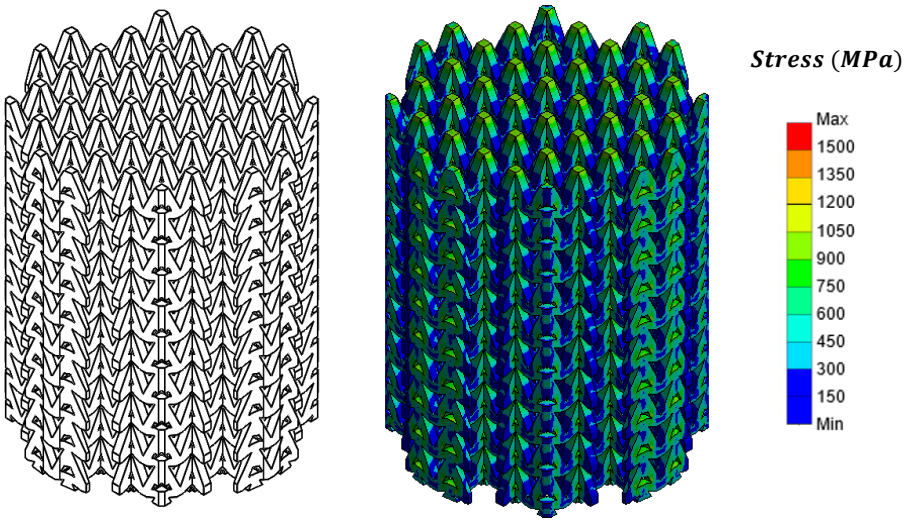

Figure 9.2. Optimised AX4 scaffold satisfying scenario 1 showing (a) optimum design generated and (b) finite element informed von-mises stress distribution

9.3.2 Optimum auxetic bone scaffold for Scenario 2

The combined AHP and TOPSIS decision making criteria identified AX1 as having the best features to be optimised for Scenario 2 (S2). The optimised AX1 scaffold should offer a high $-\upsilon$, E of 18 GPa to match the modulus of adult cortical bone. The scaffold should also maximise σ_y, while preserving a high porosity to offer the highest compressive strength while supporting bone reintegration. As such, the multi-objective criteria for S2 can be satisfied by conceiving an optimisation problem as shown in Equation (9.4):

$$\begin{cases} Maximise\ \sigma_y = f_1(\theta, t) \\ Maximise\ \ \varphi = f_2(\theta, t) \\ Minimise - \upsilon = f_3(\theta, t) \\ \quad s.t \quad E = 18\ GPa \\ \\ s.t \ \ 65.0 \leq \theta \leq 75.0 \\ s.t \ \ 0.25 \leq t \leq 0.35 \end{cases} \tag{9.4}$$

where, $-\upsilon, \varphi, \sigma_y$ and E are the responses of interest, θ and t are the design variables, namely the strut thickness and auxetic angle, respectively, for AX1.

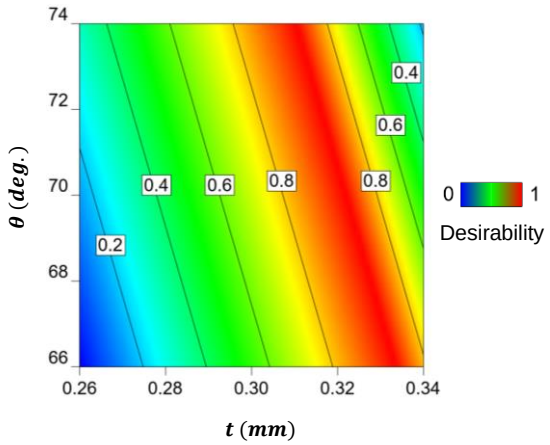

Figure 9.3. The desirability of the optimum solution against design variables for AX1 under Scenario 2

Equation (9.4) was solved using the desirability approach to find a single solution that satisfies the optimisation problem, as shown in Section 9.3.1. Figure 9.3 shows the output of the optimisation as a function of the desirability objective. It was found that the highest desirability of 1 can be achieved for design AX1 at an auxetic angle of 67.93° and strut thickness of 0.325 mm, as summarised in Table 9.4.

Table 9.4. Predicted optimal solution for AX1 under Scenario 2

Number	$\boldsymbol{t}$ $(\boldsymbol{mm})$	$\boldsymbol{\theta}$ $(\boldsymbol{Deg.})$	**Desirability**
1	0.325	67.93	1

Figure 9.3 shows that the highest desirability of 1 lies close to the lowest auxetic angle and the highest thickness. Scaffold design to satisfy the optimum design parameters were generated and numerically characterised using the finite element method, as shown in Figure 9.4. The von-Mises stress profile shown in Figure 9.4b indicates a stronger scaffold while featuring the optimum characteristics as summarised in Table

9.5. A comparison of the surrogate model and finite element prediction of the optimum AX1 scaffold is shown in Table 9.5.

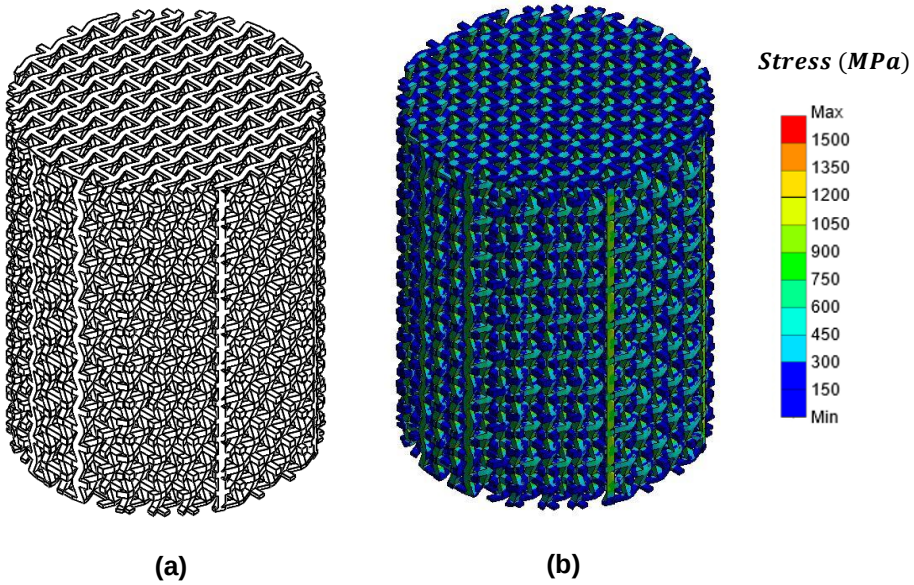

Figure 9.4. Optimised AX1 scaffold satisfying scenario 1 showing (a) optimum design generated and (b) finite element informed von-mises stress distribution

Table 9.5. Comparison between predicted and FEM values of the optimum AX1 scaffold design

Item	υ	φ	E	σ_y
Predicted	-0.230	76.042	18	58.59
FEM	-0.223	76.351	17.53	57.2
% Difference	3.04	0.40	2.61	2.37

The predicted design overestimated the Poisson's ratio, yield strength and elastic modulus by 3.04%, 2.37% and 2.61%, respectively. However, the surrogate underestimated the porosity by 0.4%. The results showed that the optimal design offers a scaffold with desirable characteristics while offering high -υ performance and stiffness matching behaviour. As such, the optimum AX1 can be used as a bone scaffold where a high -υ is desirable while offering stiffness matching to the host bone. In comparison to other works, Arjunan *et al.* [242] used the desirability approach to

optimise 3D printed auxetic nasopharyngeal swabs with predicted strut diameter, auxetic angle and cross-link angle. Here, the results revealed that the predicted surrogate model and the numerical model showed 7.8% and 4.1% in lateral shrinkage and von Mises stress. However, no changes in Poisson's ratio and relative density were observed between the predictions carried out by the surrogate model in comparison to FEM. Overall, the surrogate model developed in that study offered a 92.2% accuracy. In comparison, the surrogate model developed in this thesis offers an accuracy of 97% for predictions under scenario 2 which is higher than previous attempts in literature. As such, the response surface modelling presented in this thesis can be adopted for generating a high -υ bone scaffold featuring targeted strength, stiffness and porosity functionalities.

9.4. Conclusion

The parametric analysis in Chapter 8 revealed that the performance of the selected auxetic design candidates AX4 and AX1 was dependent on the geometrical parameters t and θ. The response surface model showed that the characteristics of the scaffolds could be modulated by varying t followed by θ and $t\theta$ as summarised in Chapter 8. Having captured these relationships using the response surface model, two multi-objective optimisations were carried out to develop the most optimum design to satisfy a near-zero (S1) and high (S2) $-\upsilon$ bone scaffold while offering stiffness matching in addition to high strength and porosity. The results showed that:

- The desirable solution for AX4 can offer a $-\upsilon$ of 0.037 at a t of 0.459 mm and θ of 23.53° while featuring E, σ_y and φ of 17.21 GPa, 59.5 MPa and 74.93%, respectively.

- The desirable solution for AX1 was found to offer a $-\upsilon$ of 0.223 at a t of 0.325 mm and θ of 67.93° while featuring E, σ_y and φ of 17.53 GPa, 57.2 MPa and 76.35%, respectively.
- Validation of the surrogate model developed in this chapter using finite element models showed an accuracy of 96.3% and 97% when applied to Scenario 1 and Scenario 2 of the multi-objective design problem.
- Overall, the study suggests that CoCrMo auxetic bone scaffolds can be developed with targeted Poisson's ratio, mechanical performance and porosity characteristics by selecting t and θ as design parameters using the surrogate model developed in this study.

The chapter, for the first time, presents a methodology for the development of auxetic bone scaffolds that offer targeted $-\upsilon$ and stiffness using re-entrant and double-arrowhead unit cells. The scaffolds developed in this thesis can significantly reduce stress shielding and maladapted stress concentration while offering the advantages of negative and near-zero Poisson's ratios. The validated methodology proposed in this chapter can be used by manufacturers and research institutions to further refine and generate alternate prototypes if necessary.

Chapter 10

Conclusion and future work

Recent literature reveals auxetic properties for a range of biological tissues identified by their negative Poisson's ratio. Researchers continue to develop material architectures that strive to mimic the properties of biological tissue to offer a unique loading environment. A number of early-stage studies have shown the potential of auxetic bone scaffolds in increasing cell proliferation and tissue reintegration. Despite this, research on the development of load-bearing auxetic bone scaffolds is limited. In any case, there is no literature on the adoption of selective laser melting for the on-demand fabrication of auxetic bone scaffolds.

Furthermore, research on the development of stiffness optimised auxetic scaffolds has yet to be reported. Within this context, the thesis presents the first additively manufactured stiffness optimised auxetic bone scaffolds in Cobalt Chromium Molybdenum superalloy. The mechanical behaviour and manufacturability of CoCrMo auxetic bone scaffolds with different unit cells are characteristics using physical and numerical experiments. This chapter describes the main findings of this research and makes recommendations for future work.

10.1. Main findings of the research

This study puts forward an open innovation framework to develop 3D printable CoCrMo bone scaffolds that can perform in an auxetic nature. Auxetic bone scaffolds optimised under two scenarios to reveal their potential to offer near zero and high $-\upsilon$

while offering stiffness matching is demonstrated. The thesis also offers a methodology for developing auxetic bone scaffolds that offer targeted $-\upsilon$ and stiffness matching. The scaffolds developed in this thesis can significantly reduce stress shielding and maladapted stress concentration while offering the advantages of negative and near zero Poisson's ratios. Manufacturers and research institutions can use the validated methodology proposed in this thesis to further refine and generate alternate prototypes if necessary. The results of this thesis go well beyond the development of CoCrMo auxetic bone scaffolds and demonstrate how multiple objectives such as stiffness matching and high strength and porosity can be achieved in a single additively manufactured architecture.

The main findings of this research are chapter-specific and have been summarised in the respective chapters throughout this thesis. However, the section below aims to synthesise the main findings of this research in relation to the aim and objectives presented in the introduction of this thesis. As such, the following conclusions can be drawn from the results presented in this thesis:

- Nine open porous unit cell assemblies (UCA1-UCA9) were digitally conceived, and their auxeticity was characterised using the finite element method (FEM). The results identified five potential candidates (UCA1-UCA5) to be suitable for the design of auxetic bone scaffolds exhibiting a $-\upsilon$ in the range of -0.13 to -0.31.
- Informed by the five identified unit cells, open porous auxetic bone scaffolds (AX1-AX5) to mimic a tibia critical size bone defect at a porosity of 80-87% were demonstrated. The theoretical elastic modulus and yield strength were revealed to be in the range of 1.5-8.1 GPa and 28-96 MPa, respectively.

- A CoCrMo particle volume distribution at D10, D50 and D90 of 13.2 µm, 28.8 µm and 46.1 µm, respectively was found to be suitable for selective laser melting for all the auxetic bone scaffolds developed. However, SEM investigation revealed slight dimensional inaccuracies leading to a porosity variation of 5.8% between digital and physical scaffolds.
- SLM processed CoCrMo bulk material offered Young's modulus, yield strength and ultimate tensile strength of 194.23 GPa, 975.6 MPa and 1169.81 MPa, respectively consistent with the literature.
- Experimental tests on physical scaffold prototypes found that the strength and stiffness of the scaffolds were primarily driven by the unit cell shape as opposed to relative density. Comparing the tests data with theoretical predictions found the applicability of the Ashby and Gibson model was limited in characterising the performance of auxetic materials.
- Experimental compressive tests demonstrated auxetic performance for all the scaffolds at a Poisson's ratio of -0.1 to -0.24, with AX1 and AX3 showing the highest and lowest lateral strain, respectively. In addition, the elastic modulus and compressive strength of the scaffolds were found to be in the range of 1.13-1.66 GPa and 32-56 MPa, respectively. The highest and lowest stiffness was exhibited by scaffolds AX1 and AX2 receptively.
- The failure mode analysis on the printed scaffolds identified layer-based, localised and catastrophic failures beyond the yield strength influenced by the unit cell shape and the SLM process.
- The comparison of the finite element and experimental test results showed that the FE model developed in this thesis could be used to predict the mechanical

performance of CoCrMo auxetic bone scaffolds at an accuracy of ~96% using a 0.1 mm element size.

- For the first time, the thesis demonstrates the combined use of AHP and TOPSIS for the scenario-based selection of the best auxetic bone scaffolds. This is carried out considering five favourable parameters in the relative importance of $-\upsilon > \varphi > \sigma_y > E > EoD$ applicable to specific scenarios.
- The multi-criteria decision-making algorithms revealed AX4 and AX1 as the ideal scaffold designs to be optimised for a near zero and high $-\upsilon$ behaviour respectively, while satisfying the relative importance of the five selected criteria.
- The analysis of variance found the surrogate model developed in this thesis for both Scenario 1 (Equations 8.3 to 8.6) and Scenario 2 (Equations 8.7 to 8.10) to adequately capture the influence design variables (t and θ) on φ, $-\upsilon$, σ_y and E for both the AX4 and AX1 bone scaffolds.
- The parametric analysis identified a linear dependence of design variables on both porosity and elastic modulus for both AX1 and AX4 scaffolds, with t having a higher influence in comparison to θ. However, a quadratic relationship was observed when it comes to σ_y and $-\upsilon$ for AX1 and AX4, respectively.
- The response surface model revealed that the order of influence of design parameters on the scaffold characteristics was primarily dictated by the first-order effects of t and θ in the form $t > \theta$. However, the interaction effects of $t\theta$ were found to be significant for $-\upsilon$ and σ_y for AX4 and AX1 respectively.
- The parametric optimisation of AX4 auxetic bone scaffold revealed an optimum $-\upsilon$ of 0.037 at a t of 0.459 mm and θ of 23.53° while featuring E, σ_y and φ of 17.21 GPa, 59.5 MPa and 74.93%, respectively. For AX1, the optimum solution

was at a t of 0.325 mm and θ of 67.93° leading to a $-\upsilon$, E, σ_y and φ of 0.223, 17.53 GPa, 57.2 MPa and 76.35%, respectively.

- Overall, the study suggests that CoCrMo auxetic bone scaffolds can be additively manufactured with targeted Poisson's ratio, mechanical performance and porosity characteristics by selecting t and θ as design parameters using the surrogate model developed in this study. The surrogate model can be used for user-defined scenarios at an accuracy of 96.3% and 97% when applied to optimise scaffolds for near zero and high $-\upsilon$, respectively, while offering stiffness matching to host bone.

10.2. Implications of the research

As summarised in the literature review, numerous studies report the potential for the development of auxetic materials for tissue engineering. As a response, this study puts forward an open innovation framework to develop CoCrMo auxetic bone scaffolds that can be fabricated on demand using selective laser melting. Developing meaningful interventions bringing in new functionalities such as $-\upsilon$ also requires addressing existing challenges in the development of load-bearing bone scaffolds. Stress shielding has been described as one of the major problems that lead to bone loss and revision surgery in the load-bearing bone scaffold. For regulating stress concentration and lowering stress shielding, a scaffold's stiffness and strength must be carefully constructed.

Previous research has revealed that titanium alloy bone scaffolds made by additive manufacturing have the potential to improve load transfer to the bone scaffold [86,268]. Furthermore, Hazlehurst [49] has demonstrated the feasibility of using SLM

to create a surface topography that can increase the stability of CoCrMo cellular structures. This means SLM has the potential to produce porous cellular structures with enhanced stiffness while retaining bone-implant contact stability.

Titanium alloys are frequently employed in the development of porous bone scaffolds; however, Cobalt-chromium-molybdenum (CoCrMo) superalloy has been chosen as the biomaterial of choice in this study as a result of its high Young's modulus and density, leading to superior stiffness performance. This, in turn, allows for a significant opportunity to develop highly porous structures that can reduce stress-shielding effects associated with highly stiff implants.

Auxetic structures are unusual architectures that show unconventional strain behaviour resulting in a negative Poisson's ratio. In doing so, these structures exhibit deformation modes and mechanical characteristics different from traditional porous architecture. It can lead to favourable outcomes for load-bearing tissue engineering applications, which this research is aimed to exploit. In doing so, the thesis, for the first time, explored the possibilities of developing the CoCrMo bone scaffolds that show both targeted auxetic and stiffness matching behaviour to alleviate concerns regarding stress shielding and maladapted stress concentrations. Careful attention was also placed on incorporating all necessary design parameters such as porosity and strength that are required for an effective bone scaffold.

This work has shown the potential of manufacturing CoCrMo auxetic bone scaffolds using SLM under multiple user-specified scenarios. The scaffolds developed in this thesis can significantly reduce stress shielding and maladapted stress concentration while offering the advantages of negative and near zero Poisson's ratios. The

validated methodology proposed in this thesis can be used by manufacturers and research institutions to further refine and generate alternate prototypes as necessary.

10.3. Limitations of the research

The research presented in this thesis combined three topical areas of research; they are auxetic materials, numerical modelling, and selective laser melting. Assumptions were made when developing the numerical model using the finite element method. In Chapter 6, the material properties of the auxetic scaffolds were modelled using a bilinear isotropic strain hardening (BISO) model derived from experimentally tested bulk material. The BISO model simplifies the stress-strain relationship into a linear and perfectly plastic behaviour which is often suitable for simulating materials where the accuracy of post-plastic behaviour is not of significant concern. For the analysis carried out in this thesis, the use of BISO is justified as the numerical models are used only to predict mechanical performance up to failure, and the post-plastic behaviour is not of interest. The BISO material model is widely used by researchers when simulating the mechanical performance of implants, bone and bone scaffolds [86,268]. Furthermore, the validation of the parameters of interest predicted by the numerical model showed good agreement.

The mechanical testing, performed in Chapter 5, utilised quasi-static loading conditions. Generally, bone scaffolds post-implantation can experience both static and dynamic loading. It may be perceived that the effects of cyclic loading should have been investigated. However, before cyclic loading can be considered, it is thought that the mechanical behaviour and stiffness matching of the auxetic bone scaffolds stems when subjected to monotonic loads needed to be understood first.

10.4. Recommendations for future work

In order to further the understanding and develop the research presented in this thesis, the following areas of research are proposed for future work:

- Dynamic loading of auxetic bone scaffolds

The thesis primarily examined the characterisation of the CoCrMo bone scaffolds under quasi-static loading conditions. At the same time, this is adequate to characterise the mechanical performance of the scaffolds under static conditions. The loading does not take into consideration the effects on the scaffold under a cyclic loading environment. The SLM process is notorious for its fatigue properties, as such design refinements may be necessary for the scaffolds. As such, investigations on the dynamic properties of CoCrMo auxetic bone scaffolds will aid in improving the understanding of adopting laser melting technology for their on-demand fabrication.

- Influence of fixing mechanism

This work has investigated the compressive behaviour of auxetic bone scaffolds manufactured using selective laser melting. From reviewing the literature, this is the first study to investigate the design, manufacture and performance of such a scaffold. The design, optimisation and manufacturing approach employed in this work demonstrates auxetic scaffolds that exhibit stiffness matching the characteristics of the host bone. However, the length of the scaffold considered was arbitrary; it is anticipated that a ‘limited contact locking compression plate’ fixing mechanism resembling the ones reported by Wieding *et al*. [396] and Reichert *et al*. [397] may be adopted as the fixing mechanism of choice. However, further studies on the whole

assembly are required to evaluate the impact of such a fixing mechanism on the auxetic scaffold.

- *In vitro* and *In vivo* bone regeneration

The thesis only looked at the structural and materials engineering aspect relating to the development of auxetic bone scaffolds. As such, future research should look at the influence of auxetic behaviour on cell proliferation, migration, alignment, differentiation, and target tissue regeneration. The bone growth analysis should be carried out both *in vitro* and *in vivo* in large animal models before clinical evaluation can begin. Auxetic structures and their unique deformation characteristics have been explored in several biomedical devices, including implants, stents, and surgical screws. Although still in the early stages, the auxetic structure, which can create mechanical properties tailored to natural tissue by changing the internal architecture of the structure, is expected to show an improved tissue reconstruction ability. In addition, continuous research at the cellular level using the auxetic macro and microarchitectures could provide a breakthrough for tissue reconstruction.

- Functionally graded auxetic architecture

One of the great promises of additive manufacturing is the ability to build parts with volumetrically graded parameters that would be difficult or impossible with traditional manufacturing. This thesis looked at developing an auxetic bone scaffold that features uniform strut thickness and pore size. However, to effectively mimic human bone requires a functionally graded architecture that offers both porosity and stiffness grading that effectively mimics both the cancellous and cortical sections. As such,

further studies on functional grading can open new possibilities for auxetic bone scaffolds to mimic both the porosity and stiffness of natural tissue.

References

[1] P. Mardling, A. Alderson, N. Jordan-Mahy, C.L. Le Maitre, The use of auxetic materials in tissue engineering, Biomater. Sci. 8 (2020) 2074–2083. https://doi.org/10.1039/c9bm01928f.

[2] J.L. Williams, J.L. Lewis, Properties and an anisotropic model of cancellous bone from the proximal tibial epiphysis, J. Biomech. Eng. 104 (1982) 50–56. https://doi.org/10.1115/1.3138303.

[3] Y. Kim, K.H. Son, J.W. Lee, Auxetic Structures for Tissue Engineering Scaffolds and Biomedical Devices, Materials (Basel). 14 (2021). https://doi.org/10.3390/ma14226821.

[4] J.J. Warner, A.R. Gillies, H.H. Hwang, H. Zhang, R.L. Lieber, S. Chen, 3D-printed biomaterials with regional auxetic properties, J. Mech. Behav. Biomed. Mater. 76 (2017) 145–152. https://doi.org/10.1016/j.jmbbm.2017.05.016.

[5] Y. Jin, C. Xie, Q. Gao, X. Zhou, G. Li, J. Du, Y. He, Fabrication of multi-scale and tunable auxetic scaffolds for tissue engineering, Mater. Des. 197 (2021) 109277. https://doi.org/10.1016/j.matdes.2020.109277.

[6] C.E. Baker, Auxetic Spinal Implants: Consideration of Negative Poisson's Ratio in the Design of an Artificial Intervertebral Disc, J. Chem. Inf. Model. 53 (2013) 1689–1699. https://doi.org/10.1017/CBO9781107415324.004.

[7] H.J. Choi, J.J. Lee, Y.J. Park, J.-W.J.W.J.W. Shin, H.-J.J. Sung, J.-W.J.W.J.W. Shin, Y. Wu, J.K. Kim, MG-63 osteoblast-like cell proliferation on auxetic PLGA scaffold with mechanical stimulation for bone tissue regeneration, Biomater. Res. 20 (2016) 1–8. https://doi.org/10.1186/s40824-016-0080-4.

[8] M.M. Kareem, Composite Bone Tissue Engineering Scaffolds Produced by Coaxial Electrospinning, 2018. http://theses.gla.ac.uk/30822/1/2018KareemPhD.pdf.

[9] L. Vidal, C. Kampleitner, M. Brennan, A. Hoornaert, P. Layrolle, Reconstruction

of Large Skeletal Defects: Current Clinical Therapeutic Strategies and Future Directions Using 3D Printing, Front. Bioeng. Biotechnol. 8 (2020). https://doi.org/10.3389/fbioe.2020.00061.

[10] A. Nauth, E. Schemitsch, B. Norris, Z. Nollin, J.T. Watson, Critical-Size Bone Defects: Is There a Consensus for Diagnosis and Treatment?, J. Orthop. Trauma. 32 (2018) S7–S11. https://doi.org/10.1097/BOT.0000000000001115.

[11] K. Bari, A. Arjunan, Extra low interstitial titanium based fully porous morphological bone scaffolds manufactured using selective laser melting, J. Mech. Behav. Biomed. Mater. 95 (2019) 1–12. https://doi.org/10.1016/j.jmbbm.2019.03.025.

[12] E.F. Morgan, G.U. Unnikrisnan, A.I. Hussein, Bone Mechanical Properties in Healthy and Diseased States, Physiol. Behav. 176 (2011) 139–148. https://doi.org/10.1146/annurev-bioeng-062117-121139.Bone.

[13] D. Barati, Biodegradable Hybrid Tissue Engineering Scaffolds For Reconstruction Of Large Bone Defects, University of South carolina, 2016. https://scholarcommons.sc.edu/cgi/viewcontent.cgi?article=4831&context=etd.

[14] T. Winkler, F.A. Sass, G.N. Duda, K. Schmidt-Bleek, A review of biomaterials in bone defect healing, remaining shortcomings and future opportunities for bone tissue engineering: The unsolved challenge, Bone Jt. Res. 7 (2018) 232–243. https://doi.org/10.1302/2046-3758.73.BJR-2017-0270.R1.

[15] B. Jahani, X. Wang, A. Brooks, Additive Manufacturing Techniques for Fabrication of Bone Scaffolds for Tissue Engineering Applications, Recent Prog. Mater. 2 (2020) 1–41. https://doi.org/10.21926/rpm.2003021.

[16] M. Kheirallah, H. Almeshaly, Present Strategies for Critical Bone Defects Regeneration, Oral Heal. Case Reports. 02 (2016). https://doi.org/10.4172/2471-8726.1000127.

[17] M. Mir, M.N. Ali, J. Sami, U. Ansari, Review of mechanics and applications of auxetic structures, Adv. Mater. Sci. Eng. 2014 (2014).

https://doi.org/10.1155/2014/753496.

[18] K.W. Wojciechowski, J.N. Grima, K.L. Alderson, J. Rybicki, Auxetic Materials and Related Systems, Phys. Status Solidi Basic Res. 250 (2013) 1313–1314. https://doi.org/10.1002/pssb.201240925.

[19] K.E. Evans, K.L. Alderson, Auxetic materials: the positive side of being negative, Eng. Sci. Educ. J. 9 (2000) 148–154. https://doi.org/10.1049/esej:20000402.

[20] A. Alomarah, Mechanical properties of novel auxetic structures, Swinburne University of Technology, 2021. https://doi.org/10.1057/978-1-349-96042-2_7974.

[21] K. Qiu, R. Wang, J. Zhu, W. Zhang, Optimization design of chiral hexagonal honeycombs with prescribed elastic properties under large deformation, Chinese J. Aeronaut. (2019). https://doi.org/10.1016/j.cja.2019.09.025.

[22] Q. Gao, C. Ge, W. Zhuang, L. Wang, Z. Ma, Crashworthiness analysis of double-arrowed auxetic structure under axial impact loading, Mater. Des. 161 (2019) 22–34. https://doi.org/10.1016/j.matdes.2018.11.013.

[23] D.R. Veronda, R.A. Westmann, Mechanical characterization of skin-Finite deformations, J. Biomech. 3 (1970) 111–124. https://doi.org/10.1016/0021-9290(70)90055-2.

[24] C. Lees, J.F.V. Vincent, J.E. Hillerton, Poisson's ratio in skin, Biomed. Mater. Eng. 1 (1991) 19–23. https://doi.org/10.3233/BME-1991-1104.

[25] C. Wiebe, G.W. Brodland, Tensile properties of embryonic epithelia measured using a novel instrument, J. Biomech. 38 (2005) 2087–2094. https://doi.org/10.1016/j.jbiomech.2004.09.005.

[26] L.H. Timmins, Q. Wu, A.T. Yeh, J.E. Moore, S.E. Greenwald, Structural inhomogeneity and fiber orientation in the inner arterial media, Am. J. Physiol. - Hear. Circ. Physiol. 298 (2010) 1537–1545. https://doi.org/10.1152/ajpheart.00891.2009.

[27] R. Gatt, M. Vella Wood, A. Gatt, F. Zarb, C. Formosa, K.M. Azzopardi, A. Casha, T.P. Agius, P. Schembri-Wismayer, L. Attard, N. Chockalingam, J.N. Grima, Negative Poisson's ratios in tendons: An unexpected mechanical response, Acta Biomater. 24 (2015) 201–208. https://doi.org/10.1016/j.actbio.2015.06.018.

[28] A. Derrouiche, F. Zaïri, F. Zaïri, A chemo-mechanical model for osmo-inelastic effects in the annulus fibrosus, Biomech. Model. Mechanobiol. 18 (2019) 1773–1790. https://doi.org/10.1007/s10237-019-01176-8.

[29] G. Dusfour, S. LeFloc'h, P. Cañadas, D. Ambard, Heterogeneous mechanical hyperelastic behavior in the porcine annulus fibrosus explained by fiber orientation: An experimental and numerical approach, J. Mech. Behav. Biomed. Mater. 104 (2020). https://doi.org/10.1016/j.jmbbm.2020.103672.

[30] C. Lira, F. Scarpa, R. Rajasekaran, A gradient cellular core for aeroengine fan blades based on auxetic configurations, J. Intell. Mater. Syst. Struct. 22 (2011) 907–917. https://doi.org/10.1177/1045389X11414226.

[31] S.H. Choi, H.H. Cheung, A multi-material virtual prototyping system, CAD Comput. Aided Des. 37 (2005) 123–136. https://doi.org/10.1016/j.cad.2004.06.002.

[32] K. Hazlehurst, C.J. Wang, M. Stanford, Evaluation of the stiffness characteristics of square pore CoCrMo cellular structures manufactured using laser melting technology for potential orthopaedic applications, Mater. Des. 51 (2013) 949–955. https://doi.org/10.1016/j.matdes.2013.05.009.

[33] O. López-Costas, Ó. Lantes-Suárez, A. Martínez Cortizas, Chemical compositional changes in archaeological human bones due to diagenesis: Type of bone vs soil environment, J. Archaeol. Sci. 67 (2016) 43–51. https://doi.org/10.1016/j.jas.2016.02.001.

[34] J. Fisher, A. Reddi, Functional tissue engineering of bone: signals and scaffolds, Top. Tissue Eng. (2003) ch5. http://www.oulu.fi/spareparts/ebook_topics_in_t_e/abstracts/fisher_1.pdf.

[35] C. Licini, C. Vitale-Brovarone, M. Mattioli-Belmonte, Collagen and non-collagenous proteins molecular crosstalk in the pathophysiology of osteoporosis, Cytokine Growth Factor Rev. 49 (2019) 59–69. https://doi.org/10.1016/j.cytogfr.2019.09.001.

[36] P. Cardiff, Development of the Finite Volume Method for Hip Joint Stress Analysis, University College Dublin, 2012. https://www.researchgate.net/publication/262772501_Development_of_the_Finite_Volume_Method_for_Hip_Joint_Stress_Analysis.

[37] J.A. Gasser, M. Kneissel, Chapter 2 Bone physiology and biology, 2017. https://doi.org/10.1007/978-3-319-56192-9.

[38] J. Turner, P. Lymbery, Brittle Bones : Osteoporosis and the Battery Cage, A Rep. Compassion World Farming. 44 (1999) 1–26. https://www.ciwf.org.uk/media/3818832/brittle-bones.pdf.

[39] W. Qiao, Q. Liu, Z. Li, H. Zhang, Z. Chen, Changes in physicochemical and biological properties of porcine bone derived hydroxyapatite induced by the incorporation of fluoride, Sci. Technol. Adv. Mater. 18 (2017) 110–121. https://doi.org/10.1080/14686996.2016.1263140.

[40] H.Q. Woodard, The elementary composition of human cortical bone, Health Phys. 8 (1962) 513–517. https://doi.org/10.1097/00004032-196210000-00005.

[41] B. Jonsson, N. Jonsson, Bone Development and Growth, Ecol. Atl. Salmon Brown Trout. (2011) 137–209. https://doi.org/10.1007/978-94-007-1189-1_4.

[42] A.R. Amini, C.T. Laurencin, S.P. Nukavarapu, Bone tissue engineering: Recent advances and challenges, Crit. Rev. Biomed. Eng. 40 (2012) 363–408. https://doi.org/10.1615/CritRevBiomedEng.v40.i5.10.

[43] Y. Liu, D. Luo, T. Wang, Hierarchical Structures of Bone and Bioinspired Bone Tissue Engineering, Small. 12 (2016) 4611–4632. https://doi.org/10.1002/smll.201600626.

[44] N. Eliaz, N. Metoki, Calcium phosphate bioceramics: A review of their history,

structure, properties, coating technologies and biomedical applications, Materials (Basel). 10 (2017) 334. https://doi.org/10.3390/ma10040334.

[45] G.J. Tortora, B.H. Derrickson, Principles of Anatomy and Physiology, 15th ed., wiley, 2018. https://www.vitalsource.com/en-uk/products/principles-of-anatomy-and-physiology-gerard-j-tortora-bryan-h-v9781119320647.

[46] U.G.K. Wegst, H. Bai, E. Saiz, A.P. Tomsia, R.O. Ritchie, Bioinspired structural materials, Nat. Mater. 14 (2015) 23–36. https://doi.org/10.1038/nmat4089.

[47] Mohammad Sanami, Auxetic materials for biomedical applications, University of Bolton, 2015. http://ubir.bolton.ac.uk/785/1/M Sanami- Revised PhD thesis-Sep 2015.pdf.

[48] E.B.W. Giesen, M. Ding, M. Dalstra, T.M.G.J. Van Eijden, Mechanical properties of cancellous bone in the human mandibular condyle are anisotropic, J. Biomech. 34 (2001) 799–803. https://doi.org/10.1016/S0021-9290(01)00030-6.

[49] K.B. Hazlehurst, The adoption of laser melting technology for the manufacture of functionally graded cobalt chrome alloy femoral stems, University of Wolverhampton, 2014. https://doi.org/https://citeseerx.ist.psu.edu/viewdoc/download?doi=10.1.1.858.8982&rep=rep1&type=pdf.

[50] J.S. Kenkre, J.H.D. Bassett, The bone remodelling cycle, Ann. Clin. Biochem. 55 (2018) 308–327. https://doi.org/10.1177/0004563218759371.

[51] P. Katsimbri, The biology of normal bone remodelling, Eur. J. Cancer Care (Engl). 26 (2017) 1–5. https://doi.org/10.1111/ecc.12740.

[52] B. Clarke, Normal Bone Anatomy and Physiology The Skeleton, Clin J Am Soc Nephrol. 3 (2008) 131–139. https://doi.org/10.2215/CJN.04151206.

[53] J. Hemza, Controversies in the Management of Open Fractures of the Skull Base, Skull Base. 19 (2009) 178–184. https://doi.org/10.1055/s-2009-1222362.

[54] A. Chitnis, B. Ray, C. Sparks, Y. Grebenyuk, M. Vanderkarr, C.E. Holy, Long

bone fractures: treatment patterns and factors contributing to use of intramedullary nailing, Expert Rev. Med. Devices. 17 (2020) 731–738. https://doi.org/10.1080/17434440.2020.1779055.

[55] A. Oryan, S. Monazzah, A. Bigham-Sadegh, Bone injury and fracture healing biology, Biomed. Environ. Sci. 28 (2015) 57–71. https://doi.org/10.3967/bes2015.006.

[56] V. Sathyendra, M. Darowish, Basic science of bone healing, Hand Clin. 29 (2013) 473–481. https://doi.org/10.1016/j.hcl.2013.08.002.

[57] M. Rahmati, J.J. Blaker, S.P. Lyngstadaas, J.F. Mano, H.J. Haugen, Designing multigradient biomaterials for skin regeneration, Mater. Today Adv. 5 (2020) 100051. https://doi.org/10.1016/j.mtadv.2019.100051.

[58] Y. Zeng, J. Hoque, S. Varghese, Biomaterial-assisted local and systemic delivery of bioactive agents for bone repair, Acta Biomater. 93 (2019) 152–168. https://doi.org/10.1016/j.actbio.2019.01.060.

[59] J.L. Dziki, S.F. Badylak, Immunomodulatory biomaterials, Curr. Opin. Biomed. Eng. 6 (2018) 51–57. https://doi.org/10.1016/j.cobme.2018.02.005.

[60] V. Migonney, Biomaterials, John Wiley & Sons, Inc., Hoboken, NJ, USA, 2014. https://doi.org/10.1002/9781119043553.

[61] Q. Chen, G. Houas, Biomaterials: A Basic Introduction, Taylor and Francis, 2014. https://doi.org/10.1201/b17553.

[62] D.F. Williams, Biomaterials and biocompatibility, Med. Prog. Technol. 4 (1976) 31–42. https://doi.org/10.1177/039139889601900904.

[63] R.J. Narayan, Monitoring and Evaluation of Biomaterials and their Performance In Vivo, Elsevier Inc., 2016. https://doi.org/10.1016/c2014-0-04050-6.

[64] N. Soro, H. Attar, X. Wu, M.S. Dargusch, Investigation of the structure and mechanical properties of additively manufactured Ti-6Al-4V biomedical scaffolds designed with a Schwartz primitive unit-cell, Mater. Sci. Eng. A. 745

(2019) 195–202. https://doi.org/10.1016/j.msea.2018.12.104.

[65] Y.S. Chang, H.O. Gu, M. Kobayashi, M. Oka, Influence of various structure treatments on histological fixation of titanium implants, J. Arthroplasty. 13 (1998) 816–825. https://doi.org/10.1016/S0883-5403(98)90037-7.

[66] A. Arjunan, A. Baroutaji, A.S. Praveen, J. Robinson, C. Wang, Classification of Biomaterial Functionality, in: Ref. Modul. Mater. Sci. Mater. Eng., Elsevier, 2020. https://doi.org/https://doi.org/10.1016/B978-0-12-815732-9.00027-9.

[67] B. Wysocki, J. Idaszek, K. Szlązak, K. Strzelczyk, T. Brynk, K. Kurzydłowski, W. Święszkowski, Post Processing and Biological Evaluation of the Titanium Scaffolds for Bone Tissue Engineering, Materials (Basel). 9 (2016) 197. https://doi.org/10.3390/ma9030197.

[68] H.M.A. Kolken, S. Janbaz, S.M.A. Leeflang, K. Lietaert, H.H. Weinans, A.A. Zadpoor, Rationally designed meta-implants: a combination of auxetic and conventional meta-biomaterials, Mater. Horizons. 5 (2018) 28–35. https://doi.org/10.1039/C7MH00699C.

[69] J. Wua, Q. Ding, A. Dutta, Y. Wang, Y.H. Huang, H. Wenga, L. Tang, Y. Hong, An injectable extracellular matrix derived hydrogel for meniscus repair and regeneration, Acta Biomater. 16 (2015) 49–59. https://doi.org/10.1016/j.actbio.2015.01.027.

[70] M. Prakasam, J. Locs, K. Salma-Ancane, D. Loca, A. Largeteau, L. Berzina-Cimdina, Biodegradable materials and metallic implants-A review, J. Funct. Biomater. 8 (2017) 1–15. https://doi.org/10.3390/jfb8040044.

[71] S.B. Baig, N. Arshid, J. Iqbal, Conducting Polymer Composites in Electrochemical Sensors, (2019). https://www.researchgate.net/publication/332766769_Conducting_Polymer_Composites_in_Electrochemical_Sensors.

[72] P. Ghosh, Polymer science: Fundamentals of polymer science, Kolkata Polym. Study Cent. (2006) 34.

http://nsdl.niscair.res.in/jspui/bitstream/123456789/404/2/Basic concepts.pdf.

[73] M.H. Gil, J.F.J. Coelho, P. Ferreira, P. Alves, Polymers for biomedical applications: Chemical modification and biofunctionalization, Nanocomposite Part. Bio-Applications Mater. Bio-Interfaces. (2011) 21–44. https://doi.org/10.4032/9789814267816.

[74] Meheta Datta, Kazi Madina Maraz, Naziza Rahman, Ruhul A. Khan, Application of polymer in biomedical implication, GSC Biol. Pharm. Sci. 14 (2021) 098–114. https://doi.org/10.30574/gscbps.2021.14.2.0038.

[75] R. Song, M. Murphy, C. Li, K. Ting, C. Soo, Z. Zheng, Current development of biodegradable polymeric materials for biomedical applications, Drug Des. Devel. Ther. 12 (2018) 3117–3145. https://doi.org/10.2147/DDDT.S165440.

[76] S. Anju, N. Prajitha, V.S. Sukanya, P. V. Mohanan, Complicity of degradable polymers in health-care applications, Mater. Today Chem. 16 (2020) 100236. https://doi.org/10.1016/j.mtchem.2019.100236.

[77] J. Ma, B.X. Huang, X.C. Zhao, C.Z. Wang, H.M. Zhang, Effect of zinc substitution for calcium on the structure, dissolution behavior and apatite formation of CaO–ZnO–SiO2–P2O5 bioceramics, Mater. Lett. 206 (2017) 154–157. https://doi.org/10.1016/j.matlet.2017.07.010.

[78] M. Ali, M.A. Hussein, N. Al-Aqeeli, Magnesium-based composites and alloys for medical applications: A review of mechanical and corrosion properties, J. Alloys Compd. 792 (2019) 1162–1190. https://doi.org/10.1016/j.jallcom.2019.04.080.

[79] K. Prasad, O. Bazaka, M. Chua, M. Rochford, L. Fedrick, J. Spoor, R. Symes, M. Tieppo, C. Collins, A. Cao, D. Markwell, K. Ostrikov, K. Bazaka, Metallic biomaterials: Current challenges and opportunities, Materials (Basel). 10 (2017). https://doi.org/10.3390/ma10080884.

[80] K. Schindhelm, B.K. Milthorpe, An overview of biomaterials., Australas. Phys. Eng. Sci. Med. 9 (2003) 29–32. http://www.pubmedcentral.nih.gov/articlerender.fcgi?artid=3975359&tool=pmc

entrez&rendertype=abstract.

[81] M. Kaur, K. Singh, Review on titanium and titanium based alloys as biomaterials for orthopaedic applications, Mater. Sci. Eng. C. 102 (2019) 844–862. https://doi.org/10.1016/j.msec.2019.04.064.

[82] S. Ur Rahman, M. Nagrath, S. Ponnusamy, P.R. Arany, Nanoscale and macroscale scaffolds with controlled-release polymeric systems for dental craniomaxillofacial tissue engineering, Materials (Basel). 11 (2018). https://doi.org/10.3390/ma11081478.

[83] I. Khodarahmi, A. Isaac, E.K. Fishman, D. Dalili, J. Fritz, Metal about the Hip and Artifact Reduction Techniques: From Basic Concepts to Advanced Imaging, Semin. Musculoskelet. Radiol. 23 (2019) E68–E81. https://doi.org/10.1055/s-0039-1687898.

[84] D.W. Hutmacher, Scaffolds in tissue engineering bone and cartilage, Biomater. Silver Jubil. Compend. 21 (2000) 175–189. https://doi.org/10.1016/B978-008045154-1.50021-6.

[85] A. Ataee, Y. Li, M. Brandt, C. Wen, Ultrahigh-strength titanium gyroid scaffolds manufactured by selective laser melting (SLM) for bone implant applications, Acta Mater. 158 (2018) 354–368. https://doi.org/10.1016/j.actamat.2018.08.005.

[86] A. Vance, K. Bari, A. Arjunan, Compressive performance of an arbitrary stiffness matched anatomical Ti64 implant manufactured using Direct Metal Laser Sintering, Mater. Des. 160 (2018) 1281–1294. https://doi.org/10.1016/j.matdes.2018.11.005.

[87] A. Wardhana, M. Valeria, Tissue engineering and regenerative medicine: A review, J. Plast. Rekonstruksi. 7 (2020) 10–17. https://doi.org/10.14228/jpr.v7i1.278.

[88] H. Qu, H. Fu, Z. Han, Y. Sun, Biomaterials for bone tissue engineering scaffolds: A review, RSC Adv. 9 (2019) 26252–26262.

https://doi.org/10.1039/c9ra05214c.

[89] A.J. Salgado, O.P. Coutinho, R.L. Reis, Bone tissue engineering: State of the art and future trends, Macromol. Biosci. 4 (2004) 743–765. https://doi.org/10.1002/mabi.200400026.

[90] H. Kaul, Y. Ventikos, On the genealogy of tissue engineering and regenerative medicine, Tissue Eng. - Part B Rev. 21 (2015) 203–217. https://doi.org/10.1089/ten.teb.2014.0285.

[91] A.I. Caplan, Tissue Engineering: Then, Now, and the Future, Tissue Eng. - Part A. 25 (2019) 515–517. https://doi.org/10.1089/ten.tea.2019.0011.

[92] T. Ghassemi, A. Shahroodi, M.H. Ebrahimzadeh, A. Mousavian, J. Movaffagh, A. Moradi, Current concepts in scaffolding for bone tissue engineering, Arch. Bone Jt. Surg. 6 (2018) 90–99. https://doi.org/10.22038/abjs.2018.26340.1713.

[93] M. Lipowiecki, D. Brabazon, Design of bone scaffolds structures for rapid prototyping with increased strength and osteoconductivity, Adv. Mater. Res. 83–86 (2010) 914–922. https://doi.org/10.4028/www.scientific.net/AMR.83-86.914.

[94] S. Gómez, M.D. Vlad, J. López, E. Fernández, Design and properties of 3D scaffolds for bone tissue engineering, Acta Biomater. 42 (2016) 341–350. https://doi.org/10.1016/j.actbio.2016.06.032.

[95] M. Navarro, A. Michiardi, O. Castaño, J.A. Planell, Biomaterials in orthopaedics, J. R. Soc. Interface. 5 (2008) 1137–1158. https://doi.org/10.1098/rsif.2008.0151.

[96] P. Netti, Biomedical foams for tissue engineering applications, Woodhead Publishing, 2014. https://www.sciencedirect.com/book/9780857096968/biomedical-foams-for-tissue-engineering-applications#book-info.

[97] J. Robinson, M. Stanford, A. Arjunan, Correlation between selective laser melting parameters, pore defects and tensile properties of 99.9 % silver, Mater. Today Commun. 25 (2020) 101550.

https://doi.org/10.1016/j.mtcomm.2020.101550.

[98] P. Sepulveda, J.R. Jones, L.L. Hench, Bioactive sol-gel foams for tissue repair, J. Biomed. Mater. Res. 59 (2002) 340–348. https://doi.org/10.1002/jbm.1250.

[99] G. Turnbull, J. Clarke, F. Picard, P. Riches, L. Jia, F. Han, B. Li, W. Shu, 3D bioactive composite scaffolds for bone tissue engineering, Bioact. Mater. 3 (2018) 278–314. https://doi.org/10.1016/j.bioactmat.2017.10.001.

[100] E. Cichoń, K. Haraźna, S. Skibiński, T. Witko, A. Zima, A. Ślósarczyk, M. Zimowska, M. Witko, B. Leszczyński, A. Wróbel, M. Guzik, Novel bioresorbable tricalcium phosphate/polyhydroxyoctanoate (TCP/PHO) composites as scaffolds for bone tissue engineering applications, J. Mech. Behav. Biomed. Mater. 98 (2019) 235–245. https://doi.org/10.1016/j.jmbbm.2019.06.028.

[101] F. Baino, G. Novajra, C. Vitale-Brovarone, Bioceramics and Scaffolds: A Winning Combination for Tissue Engineering., Front. Bioeng. Biotechnol. 3 (2015) 202. https://doi.org/10.3389/fbioe.2015.00202.

[102] X. Wang, G. Wang, L. Liu, D. Zhang, The mechanism of a chitosan-collagen composite film used as biomaterial support for MC3T3-E1 cell differentiation, Sci. Rep. 6 (2016). https://doi.org/10.1038/srep39322.

[103] K. Mallick, Bone substitute biomaterials, Woodhead Publishing, 2014. https://doi.org/https://doi.org/10.1016/C2013-0-16287-3.

[104] E.M. Engelhardt, L.A. Micol, S. Houis, F.M. Wurm, J. Hilborn, J.A. Hubbell, P. Frey, A collagen-poly(lactic acid-co-e{open}-caprolactone) hybrid scaffold for bladder tissue regeneration, Biomaterials. 32 (2011) 3969–3976. https://doi.org/10.1016/j.biomaterials.2011.02.012.

[105] J.O. Hollinger, Y. Hu, D.W. Grainger, S.R. Winn, Fabrication of poly(α-hydroxy acid) foam scaffolds using multiple solvent systems, J. Biomed. Mater. Res. 59 (2002) 563–572. https://doi.org/10.1002/jbm.1269.

[106] L. Zhang, G. Jia, M. Tang, C. Chen, J. Niu, H. Huang, B. Kang, J. Pei, H. Zeng, G. Yuan, Simultaneous enhancement of anti-corrosion, biocompatibility, and

antimicrobial activities by hierarchically-structured brushite/Ag3PO4-coated Mg-based scaffolds, Mater. Sci. Eng. C. 111 (2020). https://doi.org/10.1016/j.msec.2020.110779.

[107] A.S.P. Lin, T.H. Barrows, S.H. Cartmell, R.E. Guldberg, Microarchitectural and mechanical characterization of oriented porous polymer scaffolds, Biomaterials. 24 (2003) 481–489. https://doi.org/10.1016/S0142-9612(02)00361-7.

[108] S. Wu, X. Liu, K.W.K. Yeung, C. Liu, X. Yang, Biomimetic porous scaffolds for bone tissue engineering, Mater. Sci. Eng. R Reports. 80 (2014) 1–36. https://doi.org/10.1016/j.mser.2014.04.001.

[109] Y. Li, P. Pavanram, J. Zhou, K. Lietaert, F.S.L. Bobbert, Y. Kubo, M.A. Leeflang, H. Jahr, A.A. Zadpoor, Additively manufactured functionally graded biodegradable porous zinc, Biomater. Sci. 8 (2020) 2404–2419. https://doi.org/10.1039/c9bm01904a.

[110] C. Torres-Sanchez, F.R.A. Al Mushref, M. Norrito, K. Yendall, Y. Liu, P.P. Conway, The effect of pore size and porosity on mechanical properties and biological response of porous titanium scaffolds, Mater. Sci. Eng. C. 77 (2017) 219–228. https://doi.org/10.1016/j.msec.2017.03.249.

[111] R. Sivakumar, On the relevance and requirements of biomaterials, Bull. Mater. Sci. 22 (1999) 647–655. https://doi.org/10.1007/BF02749981.

[112] G. Schmalz, K.M. Galler, Biocompatibility of biomaterials – Lessons learned and considerations for the design of novel materials, Dent. Mater. 33 (2017) 382–393. https://doi.org/10.1016/j.dental.2017.01.011.

[113] Y. Arteshi, A. Aghanejad, S. Davaran, Y. Omidi, Biocompatible and electroconductive polyaniline-based biomaterials for electrical stimulation, Eur. Polym. J. 108 (2018) 150–170. https://doi.org/10.1016/j.eurpolymj.2018.08.036.

[114] S. Yousaf, S.H. Keshel, G.A. Farzi, M. Momeni-Moghadam, E.D. Ahmadi, M. Mozafari, F. Sefat, Scaffolds for intraocular lens, in: Handb. Tissue Eng. Scaffolds Vol. Two, Elsevier, 2019: pp. 693–709. https://doi.org/10.1016/B978-

0-08-102561-1.00028-2.

[115] S. Ramakrishna, M. Ramalingam, T.. S.S. Kumar, W.O. Soboyejo, Biomaterials : a nano approach, CRC Press, 2010.

[116] L. Ghasemi-Mobarakeh, D. Kolahreez, S. Ramakrishna, D. Williams, Key terminology in biomaterials and biocompatibility, Curr. Opin. Biomed. Eng. 10 (2019) 45–50. https://doi.org/10.1016/j.cobme.2019.02.004.

[117] L. Wang, J. Kang, C. Sun, D. Li, Y. Cao, Z. Jin, Mapping porous microstructures to yield desired mechanical properties for application in 3D printed bone scaffolds and orthopaedic implants, Mater. Des. 133 (2017) 62–68. https://doi.org/10.1016/j.matdes.2017.07.021.

[118] Z. Jia, P. Xiu, P. Xiong, W. Zhou, Y. Cheng, S. Wei, Y. Zheng, T. Xi, H. Cai, Z. Liu, C. Wang, W. Zhang, Z. Li, Additively Manufactured Macroporous Titanium with Silver-Releasing Micro-/Nanoporous Surface for Multipurpose Infection Control and Bone Repair - A Proof of Concept, ACS Appl. Mater. Interfaces. 8 (2016) 28495–28510. https://doi.org/10.1021/acsami.6b10473.

[119] A. Baroutaji, A. Arjunan, A. Niknejad, T. Tran, A.-G. Olabi, Application of Cellular Material in Crashworthiness Applications: An Overview, in: Ref. Modul. Mater. Sci. Mater. Eng., Elsevier, 2019. https://doi.org/10.1016/B978-0-12-803581-8.09268-7.

[120] K.M. Pawelec, A.A. White, S.M. Best, Properties and characterization of bone repair materials, in: Bone Repair Biomater., Elsevier, 2019: pp. 65–102. https://doi.org/10.1016/b978-0-08-102451-5.00004-4.

[121] T.T. Li, L. Ling, M.C. Lin, Q. Jiang, Q. Lin, J.H. Lin, C.W. Lou, Properties and mechanism of hydroxyapatite coating prepared by electrodeposition on a braid for biodegradable bone scaffolds, Nanomaterials. 9 (2019). https://doi.org/10.3390/nano9050679.

[122] L. Zhang, E.M. Haddouti, K. Welle, C. Burger, D.C. Wirtz, F.A. Schildberg, K. Kabir, The Effects of Biomaterial Implant Wear Debris on Osteoblasts, Front.

Cell Dev. Biol. 8 (2020) 1–17. https://doi.org/10.3389/fcell.2020.00352.

[123] D.R. Sumner, J.O. Galante, Determinants of stress shielding: Design versus materials versus interface, Clin. Orthop. Relat. Res. (1992) 202–212. https://doi.org/10.1097/00003086-199201000-00020.

[124] M.I.Z. Ridzwan, S. Shuib, A.Y. Hassan, A.A. Shokri, M.N. Mohammad Ibrahim, Problem of stress shielding and improvement to the hip implant designs: A review, J. Med. Sci. 7 (2007) 460–467. https://doi.org/10.3923/jms.2007.460.467.

[125] L. Chao, C. Jiao, H. Liang, D. Xie, L. Shen, Z. Liu, Analysis of Mechanical Properties and Permeability of Trabecular-Like Porous Scaffold by Additive Manufacturing, Front. Bioeng. Biotechnol. 9 (2021) 1–13. https://doi.org/10.3389/fbioe.2021.779854.

[126] L. Li, J. Shi, K. Zhang, L. Yang, F. Yu, L. Zhu, H. Liang, X. Wang, Q. Jiang, Early osteointegration evaluation of porous Ti6Al4V scaffolds designed based on triply periodic minimal surface models, J. Orthop. Transl. 19 (2019) 94–105. https://doi.org/10.1016/j.jot.2019.03.003.

[127] L. Zhang, B. Song, S.K. Choi, Y. Shi, A topology strategy to reduce stress shielding of additively manufactured porous metallic biomaterials, Int. J. Mech. Sci. 197 (2021) 106331. https://doi.org/10.1016/j.ijmecsci.2021.106331.

[128] C. Han, Y. Li, Q. Wang, S. Wen, Q. Wei, C. Yan, L. Hao, J. Liu, Y. Shi, Continuous functionally graded porous titanium scaffolds manufactured by selective laser melting for bone implants, J. Mech. Behav. Biomed. Mater. 80 (2018) 119–127. https://doi.org/10.1016/j.jmbbm.2018.01.013.

[129] E. Hernández-Nava, C.J. Smith, F. Derguti, S. Tammas-Williams, F. Léonard, P.J. Withers, I. Todd, R. Goodall, The effect of density and feature size on mechanical properties of isostructural metallic foams produced by additive manufacturing, Acta Mater. 85 (2015) 387–395. https://doi.org/10.1016/j.actamat.2014.10.058.

[130] P. Koudelka, O. Jiroušek, J. Valach, Determination of mechanical properties of materials with complex inner structure using microstructural models, (2011) 4–7. https://www.academia.edu/63417042/Determination_of_mechanical_properties_of_materials_with_complex_inner_structure_using_microstructural_models.

[131] M. Benedetti, J. Klarin, F. Johansson, V. Fontanari, V. Luchin, G. Zappini, A. Molinari, Study of the compression behaviour of Ti6Al4V trabecular structures produced by additive laser manufacturing, Materials (Basel). 12 (2019). https://doi.org/10.3390/ma12091471.

[132] Z. Wang, H. hu, Auxetic materials and their potential applications in textiles, Text. Res. J. 84 (2014) 1600–1611. https://doi.org/10.1177/0040517512449051.

[133] C.W. Smith, J.N. Grima, K.E. Evans, Novel mechanism for generating auxetic behaviour in reticulated foams: Missing rib foam model, Acta Mater. 48 (2000) 4349–4356. https://doi.org/10.1016/S1359-6454(00)00269-X.

[134] M. Ashjari, Auxetic Materials with Negative Poisson's Ratio, Mater. Sci. Eng. Int. J. 1 (2017) 11–13. https://doi.org/10.15406/mseij.2017.01.00011.

[135] A. Alomarah, J. Zhang, D. Ruan, S. Masood, G. Lu, Mechanical Properties of the 2D Re-entrant Honeycomb Made via Direct Metal Printing, IOP Conf. Ser. Mater. Sci. Eng. 229 (2017). https://doi.org/10.1088/1757-899X/229/1/012038.

[136] A.D. Lantada, A. Muslija, J.P. Garcia-Ruiz, Auxetic tissue engineering scaffolds with nanometric features and resonances in the megahertz range, Smart Mater. Struct. 24 (2015). https://doi.org/10.1088/0964-1726/24/5/055013.

[137] H.W.I. and D.C. L. Yang, O. Harrysson, Design and characterization of orthotropic re-entrant structures made via EBM using Ti6Al4V and pure copper, (2011) 1–38. https://www.researchgate.net/publication/287602309_Design_and_characterization_of_orthotropic_re-entrant_auxetic_structures_made_via_EBM_using_Ti6Al4V_and_pure_copper

.

[138] K. Wang, C.C. Ho, C. Zhang, B. Wang, A Review on the 3D Printing of Functional Structures for Medical Phantoms and Regenerated Tissue and Organ Applications, Engineering. 3 (2017) 653–662. https://doi.org/10.1016/J.ENG.2017.05.013.

[139] L. Mirante, Auxetic Structures: toward bending-active architectural applications, Polytechnic University of Milan, 2015. https://www.politesi.polimi.it/bitstream/10589/116372/1/2015_12_Mirante.pdf.

[140] Y. Liu, H. Hu, A review on auxetic structures and polymeric materials, Sci. Res. Essays. 5 (2010) 1052–1063. https://www.researchgate.net/publication/273889759%0AA.

[141] A. Alderson, K.L. Alderson, Auxetic materials, Proc. Inst. Mech. Eng. Part G J. Aerosp. Eng. 221 (2007) 565–575. https://doi.org/10.1243/09544100JAERO185.

[142] Y. Prawoto, Seeing auxetic materials from the mechanics point of view: A structural review on the negative Poisson's ratio, Comput. Mater. Sci. 58 (2012) 140–153. https://doi.org/10.1016/j.commatsci.2012.02.012.

[143] F. Auricchio, A. Bacigalupo, L. Gambarotta, M. Lepidi, S. Morganti, F. Vadalà, A novel layered topology of auxetic materials based on the tetrachiral honeycomb microstructure, Mater. Des. 179 (2019) 1–34. https://doi.org/10.1016/j.matdes.2019.107883.

[144] M. Fu, F. Liu, L. Hu, A novel category of 3D chiral material with negative Poisson's ratio, Compos. Sci. Technol. 160 (2018) 111–118. https://doi.org/10.1016/j.compscitech.2018.03.017.

[145] Q. Wang, Z. Yang, Z. Lu, X. Li, Mechanical responses of 3D cross-chiral auxetic materials under uniaxial compression, Mater. Des. 186 (2020) 108226. https://doi.org/10.1016/j.matdes.2019.108226.

[146] A. Bacigalupo, M. Lepidi, G. Gnecco, L. Gambarotta, Optimal design of auxetic

hexachiral metamaterials with local resonators, Smart Mater. Struct. 25 (2016) 1–41. https://doi.org/10.1088/0964-1726/25/5/054009.

[147] Y. Jiang, Y. Li, 3D Printed Auxetic Mechanical Metamaterial with Chiral Cells and Re-entrant Cores, Sci. Rep. 8 (2018) 1–11. https://doi.org/10.1038/s41598-018-20795-2.

[148] D. Prall, R.S. Lakes, Properties of chiral honeycombe with Poisson's ratio of -1, Int. J. Mech. Sci. 39 (1997). https://doi.org/10.1016/S0020-7403(96)00025-2.

[149] Y. Chen, G. Lanzara, Auxetic Films with a Miniaturized Cellular Structure, Proceedings. 2 (2018) 486. https://doi.org/10.3390/icem18-05390.

[150] P.D. Dubrovski, N. Novak, M. Borovinšek, M. Vesenjak, Z. Ren, In-plane behavior of auxetic non-woven fabric based on rotating square unit geometry under tensile load, Polymers (Basel). 11 (2019). https://doi.org/10.3390/polym11061040.

[151] P.S. Farrugia, R. Gatt, E. Zammit Lonardelli, J.N. Grima, K.E. Evans, Different Deformation Mechanisms Leading to Auxetic Behavior Exhibited by Missing Rib Square Grid Structures, Phys. Status Solidi Basic Res. 256 (2019) 1–7. https://doi.org/10.1002/pssb.201800186.

[152] J.N. Grima, K.E. Evans, Auxetic behavior from rotating triangles, J. Mater. Sci. 41 (2006) 3193–3196. https://doi.org/10.1007/s10853-006-6339-8.

[153] J. Dagdelen, J. Montoya, M. De Jong, K. Persson, Computational prediction of new auxetic materials, Nat. Commun. 8 (2017) 1–8. https://doi.org/10.1038/s41467-017-00399-6.

[154] J.N. Grima, E. Manicaro, D. Attard, Auxetic behaviour from connected different-sized squares and rectangles, Proc. R. Soc. A Math. Phys. Eng. Sci. 467 (2011) 439–458. https://doi.org/10.1098/rspa.2010.0171.

[155] B.D. Caddock, K.E. Evans, Microporous materials with negative Poisson's ratios. I. Microstructure and mechanical properties, J. Phys. D. Appl. Phys. 22 (1989) 1877. https://doi.org/10.1088/0022-3727/22/12/012.

[156] P. Ma, Y. Chang, A. Boakye, G. Jiang, Review on the knitted structures with auxetic effect, J. Text. Inst. 108 (2017) 947–961. https://doi.org/10.1080/00405000.2016.1204901.

[157] P. Ma, A Review on Auxetic Textile Structures, Their Mechanism and Properties, J. Text. Sci. Fash. Technol. 2 (2019) 1–10. https://doi.org/10.33552/jtsft.2019.02.000526.

[158] S. Li, K. Al-Badani, Y. Gu, M. Lake, L. Li, G. Rothwell, J. Ren, The Effects of Poisson's Ratio on the Indentation Behavior of Materials With Embedded System in an Elastic Matrix, Phys. Status Solidi Basic Res. 254 (2017) 1–8. https://doi.org/10.1002/pssb.201600832.

[159] P.U. Kelkar, H.S. Kim, K.H. Cho, J.Y. Kwak, C.Y. Kang, H.C. Song, Cellular auxetic structures for mechanical metamaterials: A review, Sensors (Switzerland). 20 (2020) 1–26. https://doi.org/10.3390/s20113132.

[160] X. Yu, J. Zhou, H. Liang, Z. Jiang, L. Wu, Mechanical metamaterials associated with stiffness, rigidity and compressibility: A brief review, Prog. Mater. Sci. 94 (2018) 114–173. https://doi.org/10.1016/j.pmatsci.2017.12.003.

[161] W. Yang, Z.M. Li, W. Shi, B.H. Xie, M.B. Yang, Review on auxetic materials, J. Mater. Sci. 39 (2004) 3269–3279. https://doi.org/10.1023/B:JMSC.0000026928.93231.e0.

[162] H.M.A.M.A. Kolken, A.A. Zadpoor, Auxetic mechanical metamaterials, Royal Society of Chemistry, 2017. https://doi.org/10.1039/c6ra27333e.

[163] J.E. Li, B.L. Wang, Effect of negative Poisson's ratio on the fracture mechanics parameters due to mechanical and thermal loads, Int. J. Eng. Sci. 150 (2020) 1–11. https://doi.org/10.1016/j.ijengsci.2020.103256.

[164] C.K.A. Chidire Anurag, A Sri Harsha, Auxetic Materials, Int. J. Trends Eng. Technol. 5 (2015) 156–160. https://www.academia.edu/16730448/Auxetic_Materials.

[165] T. Li, F. Liu, L. Wang, Enhancing indentation and impact resistance in auxetic

composite materials, Compos. Part B Eng. 198 (2020) 108229. https://doi.org/10.1016/j.compositesb.2020.108229.

[166] H.M.A. Kolken, K. Lietaert, T. van der Sloten, B. Pouran, A. Meynen, G. Van Loock, H. Weinans, L. Scheys, A.A. Zadpoor, Mechanical performance of auxetic meta-biomaterials, J. Mech. Behav. Biomed. Mater. 104 (2020) 103658. https://doi.org/10.1016/j.jmbbm.2020.103658.

[167] R. Naboni, L. Mirante, Metamaterial computation and fabrication of auxetic patterns for architecture, (2010) 129–136. https://www.researchgate.net/publication/301454028_Metamaterial_computation_and_fabrication_of_auxetic_patterns_for_architecture.

[168] C. Moroney, A. Alderson, T. Allen, M. Sanami, P. Venkatraman, The Application of Auxetic Material for Protective Sports Apparel, Proceedings. 2 (2018) 251. https://doi.org/10.3390/proceedings2060251.

[169] U. Aksu, M. Seha Tatlıer, An investigation on auxetic feature and its applications, Int. Adv. Res. Eng. J. 02 (2018) 167–176. https://dergipark.org.tr/en/download/article-file/522675.

[170] K.B. Hazlehurst, C.J. Wang, M. Stanford, An investigation into the flexural characteristics of functionally graded cobalt chrome femoral stems manufactured using selective laser melting, Mater. Des. 60 (2014) 177–183. https://doi.org/10.1016/j.matdes.2014.03.068.

[171] A. Alderson, J. Rasburn, K.E.E. Evans, J.N.N. Grima, Auxetic polymeric filters display enhanced de-fouling and pressure- compensation properties, Membr. Technol. 2001 (2001) 6–8. https://doi.org/10.1016/S0958-2118(01)80299-8.

[172] X. Ren, Studies on three-dimensional metamaterials and tubular structures with negative Poisson’s ratio, (2017). https://researchbank.rmit.edu.au/view/rmit:162197.

[173] V.H. Carneiro, H. Puga, V.H. Carneiro, J. Meireles, H. Puga, Auxetic materials-A review, Mater. Sci. 31 (2013) 561–571. https://doi.org/10.2478/s13536-013-

0140-6.

[174] O. Duncan, T. Shepherd, C. Moroney, L. Foster, P.D. Venkatraman, K. Winwood, T. Allen, A. Alderson, Review of auxetic materials for sports applications: Expanding options in comfort and protection, Appl. Sci. 8 (2018). https://doi.org/10.3390/app8060941.

[175] J.U. Surjadi, L. Gao, H. Du, X. Li, X. Xiong, N.X. Fang, Y. Lu, Mechanical Metamaterials and Their Engineering Applications, Adv. Eng. Mater. 21 (2019) 1–37. https://doi.org/10.1002/adem.201800864.

[176] P. Soman, J.W. Lee, A. Phadke, S. Varghese, S. Chen, Spatial tuning of negative and positive Poisson's ratio in a multi-layer scaffold, Acta Biomater. 8 (2012) 2587–2594. https://doi.org/10.1016/j.actbio.2012.03.035.

[177] P. Soman, D.Y. Fozdar, J.W. Lee, A. Phadke, S. Varghese, S. Chen, A three-dimensional polymer scaffolding material exhibiting a zero Poisson's ratio, Soft Matter. 8 (2012) 4946–4951. https://doi.org/10.1039/c2sm07354d.

[178] W. Zhang, P. Soman, K. Meggs, Tuning the Poisson's Ratio of Biomaterials for Investigating Cellular Response, Bone. 23 (2013) 1–7. https://doi.org/10.1002/adfm.201202666.Tuning.

[179] J.W. Lee, P. Soman, J.H. Park, S. Chen, D.W. Cho, A tubular biomaterial construct exhibiting a negative poisson's ratio, PLoS One. 11 (2016) 1–14. https://doi.org/10.1371/journal.pone.0155681.

[180] C.B. Ahn, K.H. Son, Y.S. Yu, T.H. Kim, J.I. Lee, J.W. Lee, Development of a flexible 3D printed scaffold with a cell-adhesive surface for artificial trachea, Biomed. Mater. 14 (2019). https://doi.org/10.1088/1748-605X/AB2A6C.

[181] C.B. Ahn, J.H. Kim, J.H. Lee, K.Y. Park, K.H. Son, J.W. Lee, Development of Multi-layer Tubular Vascular Scaffold to Enhance Compliance by Exhibiting a Negative Poisson's Ratio, Int. J. Precis. Eng. Manuf. Technol. 2021 83. 8 (2021) 841–853. https://doi.org/10.1007/S40684-021-00332-9.

[182] Y.S. Yu, C.B. Ahn, K.H. Son, J.W. Lee, Motility improvement of biomimetic

trachea scaffold via hybrid 3d-bioprinting technology, Polymers (Basel). 13 (2021) 1–15. https://doi.org/10.3390/polym13060971.

[183] A. Muslija, A. Díaz Lantada, Deep reactive ion etching of auxetic structures: present capabilities and challenges, Smart Mater. Struct. 23 (2014) 087001. https://doi.org/10.1088/0964-1726/23/8/087001.

[184] M. Kapnisi, C. Mansfield, C. Marijon, A.G. Guex, F. Perbellini, I. Bardi, E.J. Humphrey, J.L. Puetzer, D. Mawad, D.C. Koutsogeorgis, D.J. Stuckey, C.M. Terracciano, S.E. Harding, M.M. Stevens, Auxetic Cardiac Patches with Tunable Mechanical and Conductive Properties toward Treating Myocardial Infarction, Adv. Funct. Mater. 28 (2018). https://doi.org/10.1002/ADFM.201800618.

[185] Y.J. Park, J.K. Kim, The effect of negative Poisson's ratio polyurethane scaffolds for articular cartilage tissue engineering applications, Adv. Mater. Sci. Eng. 2013 (2013). https://doi.org/10.1155/2013/853289.

[186] H.J. Choi, J.J. Lee, J.B. Lee, H.J. Sung, J.W. Shin, J.W. Shin, Y. Wu, J.K. Kim, MG-63 cells proliferation following various types of mechanical stimulation on cells by auxetic hybrid scaffolds, Biomater. Res. 20 (2016). https://doi.org/10.1186/S40824-016-0079-X.

[187] L. Song, M.F. Ahmed, Y. Li, C. Zeng, Y. Li, Vascular differentiation from pluripotent stem cells in 3-D auxetic scaffolds, J. Tissue Eng. Regen. Med. 12 (2018) 1679–1689. https://doi.org/10.1002/TERM.2695.

[188] Y. Yan, Y. Li, L. Song, C. Zeng, Y. Li, Pluripotent stem cell expansion and neural differentiation in 3-D scaffolds of tunable Poisson's ratio, Acta Biomater. 49 (2017) 192–203. https://doi.org/10.1016/j.actbio.2016.11.025.

[189] M. V Deshpande, A.J. West, S.H. Bernacki, K. Luan, M.W. King, Poly(ε-Caprolactone) Resorbable Auxetic Designed Knitted Scaffolds for Craniofacial Skeletal Muscle Regeneration., Bioeng. (Basel, Switzerland). 7 (2020) 1–15. https://doi.org/10.3390/bioengineering7040134.

[190] F. Scarpa, Auxetic materials for bioprostheses, IEEE Signal Process. Mag. 25 (2008). https://doi.org/10.1109/MSP.2008.926663.

[191] M.S. Salit, M. Jawaid, N. Bin Yusoff, M.E. Hoque, Manufacturing of natural fibre reinforced polymer composites, Manuf. Nat. Fibre Reinf. Polym. Compos. (2015) 1–383. https://doi.org/10.1007/978-3-319-07944-8.

[192] O. Abdelaal, S. Darwish, Analysis, Fabrication and a Biomedical Application of Auxetic Cellular Structures, Int. J. Eng. Innov. Technol. 2 (2012) 218–223. http://ijeit.com/vol 2/Issue 3/IJEIT1412201209_40.pdf.

[193] N. Ghavidelnia, M. Bodaghi, Reza Hedayati, Femur Auxetic Meta-Implants with Tuned Micromotion Distribution, Materials (Basel). (2021) 1–29. https://www.researchgate.net/publication/348073571_Femur_Auxetic_Meta-Implants_with_Tuned_Micromotion_Distribution.

[194] Mina Aliakbari, Additive Manufacturing: State - of - the - Art, Capabilities, and Sample Applications with Cost Analysis, (2012) 91. http://www.diva-portal.org/smash/get/diva2:560827/FULLTEXT02.pdf.

[195] S. Dufera, K. Reddy, Additive Manufacturing Technologies, (2019) 19–39. https://doi.org/10.1007/978-981-13-8281-9_2.

[196] Ferdinando Auricchio, Alessandro Greco, Gianluca Alaimo, Valentina Giacometti, Stefania Marconi, Valeria Mauri, 3D Printing Technology for Buildings' Accessibility: The Tactile Map for MTE Museum in Pavia, J. Civ. Eng. Archit. 11 (2017) 736–747. https://doi.org/10.17265/1934-7359/2017.08.002.

[197] T. Wohlers, Rapid Prototyping & Tooling State of the Industry: 1998 Worldwide Progress Report, Mater. Technol. 13 (1998) 174–176. https://doi.org/10.1080/10667857.1998.11752797.

[198] S. Mellor, L. Hao, D. Zhang, Additive Manufacturing: A Framework for Implementation *Title page including author details Click here to download Title page including author details: Title page.docx, 149 (2014) 194–201. https://ore.exeter.ac.uk/repository/bitstream/handle/10871/22191/Additive

Manufacturing A Framework for Implementation.pdf?sequence=1&isAllowed=y.

[199] Y. Zhang, H. Liu, Application of Rapid Prototyping Technology in Die Making of Diesel Engine, Tsinghua Sci. Technol. 14 (2009) 127–131. https://doi.org/10.1016/S1007-0214(09)70079-3.

[200] D. Kokotsaki, V. Menzies, A. Wiggins, Implications of lattice structures on economics and productivity of metal powder bed fusion, Crit. Stud. Secur. 2 (2014) 210–222. https://doi.org/10.1016/j.addma.2019.100947.

[201] M. Jiménez, L. Romero, I.A. Domínguez, M.D.M. Espinosa, M. Domínguez, Additive Manufacturing Technologies: An Overview about 3D Printing Methods and Future Prospects, Complexity. 2019 (2019). https://doi.org/10.1155/2019/9656938.

[202] I. Gibson, D.W.R. L, B. Stucke, Additive Manufacturing Technologies, 2019. https://doi.org/10.1007/978-3-642-35950-7_16866-1.

[203] R.D. Goodridge, C.J. Tuck, R.J.M. Hague, Laser sintering of polyamides and other polymers, Prog. Mater. Sci. 57 (2012) 229–267. https://doi.org/10.1016/j.pmatsci.2011.04.001.

[204] S. Berretta, K. Evans, O. Ghita, Additive manufacture of PEEK cranial implants: Manufacturing considerations versus accuracy and mechanical performance, Mater. Des. 139 (2018) 141–152. https://doi.org/10.1016/j.matdes.2017.10.078.

[205] Ż.A. Mierzejewska, W. Markowicz, Selective Laser Sintering – Binding Mechanism And Assistance In Medical Applications, Adv. Mater. Sci. 15 (2015) 5–16. https://doi.org/10.1515/adms-2015-0011.

[206] S. Kumar, Selective laser sintering: A qualitative and objective approach, J. Miner. 55(10) (2003) 43–47. https://www.researchgate.net/publication/225597064_Selective_Laser_Sintering_A_Qualitative_and_Objective_Approach.

[207] J. Hiemenz, Electron Beam Melting, Compr. Mater. Process. 10 (2014) 135–161. https://doi.org/10.1016/B978-0-08-096532-1.01004-9.

[208] A. Nouri, A. Sola, Electron beam melting in biomedical manufacturing, 2020. https://doi.org/10.1016/b978-0-08-102965-7.00008-4.

[209] S. Liu, Y.C. Shin, Additive manufacturing of Ti6Al4V alloy: A review, Mater. Des. 164 (2019) 107552. https://doi.org/10.1016/j.matdes.2018.107552.

[210] M. Markl, M. Lodes, M. Franke, C. Körner, Additive manufacturing using selective electron beam melting, Weld. Cut. 16 (2017) 177–184. https://www.researchgate.net/publication/317955281_Additive_manufacturing_using_selective_electron_beam_melting.

[211] O.H. Ulf Lindhe, Rapid Manufacturing with Electron Beam Melting (EBM) – A manufacturing revolution?, 2006 (2003) 433–438. http://www.arcam.com/Downloads/PDF/SME_aug_18/Arcam_SME presentation_Dearborn_0818.pdf.

[212] C.Y. Yap, H.K. Tan, Z. Du, C.K. Chua, Z. Dong, Selective laser melting of nickel powder, Rapid Prototyp. J. 23 (2017) 750–757. https://doi.org/10.1108/RPJ-01-2016-0006.

[213] K.G. Prashanth, Selective laser melting: Materials and applications, J. Manuf. Mater. Process. 4 (2020) 19–22. https://doi.org/10.3390/jmmp4010013.

[214] J. Robinson, A. Arjunan, M. Stanford, I. Lyall, C. Williams, Effect of silver addition in copper-silver alloys fabricated by laser powder bed fusion in situ alloying, J. Alloys Compd. 857 (2021) 157561. https://doi.org/https://doi.org/10.1016/j.jallcom.2020.157561.

[215] J. Robinson, A. Arjunan, A. Baroutaji, M. Martí, A. Tuñón Molina, Á. Serrano-Aroca, A. Pollard, Additive manufacturing of anti-SARS-CoV-2 Copper-Tungsten-Silver alloy, Rapid Prototyp. J. ahead-of-p (2021). https://doi.org/10.1108/RPJ-06-2021-0131.

[216] S.H. Ahmed, A. Mian, Influence of material property variation on computationally calculated melt pool temperature during laser melting process, Metals (Basel). 9 (2019). https://doi.org/10.3390/met9040456.

[217] C. Meier, R.W. Penny, Y. Zou, J.S. Gibbs, A.J. Hart, Thermophysical Phenomena in Metal Additive Manufacturing By Selective Laser Melting: Fundamentals, Modeling, Simulation, and Experimentation, Annu. Rev. Heat Transf. 20 (2018) 241–316. https://doi.org/10.1615/annualrevheattransfer.2018019042.

[218] C.Y. Yap, C.K. Chua, Z.L. Dong, Z.H. Liu, D.Q. Zhang, L.E. Loh, S.L. Sing, Review of selective laser melting: Materials and applications, Appl. Phys. Rev. 2 (2015). https://doi.org/10.1063/1.4935926.

[219] S. Pfeiffer, M. Makowska, K. Florio, D.F. Sanchez, F. Marone, X. Zhang, C.G. Aneziris, H. Van Swygenhoven, K. Wegener, T. Graule, Selective laser melting of thermal pre-treated metal oxide doped aluminum oxide granules, Open Ceram. 2 (2020) 100007. https://doi.org/10.1016/j.oceram.2020.100007.

[220] A. Dehghanghadikolaei, N. Namdari, B. Mohammadian, Additive Manufacturing Methods: A Brief Overview, J. Sci. Eng. Res. 5(8) (2018) 123–131. https://www.researchgate.net/publication/327701079_Additive_Manufacturing_Methods_A_Brief_Overview.

[221] N.E. Putra, M.J. Mirzaali, I. Apachitei, J. Zhou, A.A. Zadpoor, Multi-material additive manufacturing technologies for Ti-, Mg-, and Fe-based biomaterials for bone substitution, Acta Biomater. 109 (2020) 1–20. https://doi.org/10.1016/j.actbio.2020.03.037.

[222] J.J.S. Dilip, S. Zhang, C. Teng, K. Zeng, C. Robinson, D. Pal, B. Stucker, Influence of processing parameters on the evolution of melt pool, porosity, and microstructures in Ti-6Al-4V alloy parts fabricated by selective laser melting, Prog. Addit. Manuf. 2 (2017) 157–167. https://doi.org/10.1007/s40964-017-0030-2.

[223] F. Trevisan, F. Calignano, A. Aversa, G. Marchese, M. Lombardi, S. Biamino, D. Ugues, D. Manfredi, Additive manufacturing of titanium alloys in the biomedical field: processes, properties and applications, J. Appl. Biomater. Funct. Mater. 16 (2018) 57–67. https://doi.org/10.5301/jabfm.5000371.

[224] S.H. Choi, S. Samavedam, Modelling and optimisation of rapid prototyping, Comput. Ind. 47 (2002) 39–53. https://doi.org/10.1016/S0166-3615(01)00140-3.

[225] A. Saboori, A. Abdi, S.A. Fatemi, G. Marchese, S. Biamino, H. Mirzadeh, Hot deformation behavior and flow stress modeling of Ti–6Al–4V alloy produced via electron beam melting additive manufacturing technology in single β-phase field, Mater. Sci. Eng. A. 792 (2020) 139822. https://doi.org/10.1016/j.msea.2020.139822.

[226] G. Liu, X. Zhang, X. Chen, Y. He, L. Cheng, M. Huo, J. Yin, F. Hao, S. Chen, P. Wang, S. Yi, L. Wan, Z. Mao, Z. Chen, X. Wang, Z. Cao, J. Lu, Additive manufacturing of structural materials, Mater. Sci. Eng. R Reports. 145 (2021) 100596. https://doi.org/10.1016/j.mser.2020.100596.

[227] R.M. Chandima Ratnayake, Enabling RDM in challenging environments via additive layer manufacturing: enhancing offshore petroleum asset operations, Prod. Plan. Control. 30 (2019) 522–539. https://doi.org/10.1080/09537287.2018.1540054.

[228] Ralf Carlström, C. Aumund-Kopp, A. Riou, O. Coube, K. Murray, Introduction to Additive Manufacturing Technology, 2015. http://s550682939.onlinehome.fr/CommissionsThematiques/DocComThematiques/EPMA_Additive_Manufacturing.pdf.

[229] B. Durakovic, Design for additive manufacturing: Benefits, trends and challenges, Period. Eng. Nat. Sci. 6 (2018) 179–191. https://doi.org/10.21533/pen.v6i2.224.

[230] D. Thomas, Costs, benefits, and adoption of additive manufacturing: a supply chain perspective, Int. J. Adv. Manuf. Technol. 85 (2016) 1857–1876. https://doi.org/10.1007/s00170-015-7973-6.

[231] J. Jiang, X. Xu, J. Stringer, Support Structures for Additive Manufacturing: A Review, J. Manuf. Mater. Process. 2 (2018) 64. https://doi.org/10.3390/jmmp2040064.

[232] A. Mohammed, A. Elshaer, P. Sareh, M. Elsayed, H. Hassanin, Additive Manufacturing Technologies for Drug Delivery Applications, Int. J. Pharm. 580 (2020) 119245. https://doi.org/10.1016/j.ijpharm.2020.119245.

[233] P.R. Maina, A Study on the Effect of Varying Selective Laser Melting Process Parameters by Build Process Simulation Proses Simülasyonu ile Lazerle Metal Toz Ergitme Proses Parametrelerinin Etkisi Üzerine Bir Çalışma Y ÜKSEK LİSANS TEZİ Havacılık Bilimi ve Teknolojile, (2021). https://doi.org/10.13140/RG.2.2.14173.13286.

[234] K. Carpenter, A. Tabei, On residual stress development, prevention, and compensation in metal additive manufacturing, Materials (Basel). 13 (2020). https://doi.org/10.3390/ma13020255.

[235] M. Garibaldi, Laser Additive Manufacturing of Soft Magnetic Cores for Rotating Electrical Machinery : Materials Development and Part Design, 2019. https://www.researchgate.net/publication/329610071%0ALaser.

[236] G. Chen, D. Wang, W. Hua, W. Wu, W. Zhou, Y. Jin, W. Zheng, Simulating and Predicting the Part Warping in Fused Deposition Modeling by Thermal–Structural Coupling Analysis, 3D Print. Addit. Manuf. 00 (2021) 1–13. https://doi.org/10.1089/3dp.2021.0119.

[237] L. Mugwagwa, I. Yadroitsev, S. Matope, Effect of Process Parameters on Residual Stresses , Distortions , and Porosity in Selective Laser Melting of Maraging Steel 300 Effect of Process Parameters on Residual Stresses , Distortions , and Porosity in Selective Laser Melting of Maraging Steel 300, (2019). https://doi.org/10.3390/met9101042.

[238] F. Kaji, A. Barari, Evaluation of the surface roughness of additive manufacturing parts based on the modelling of cusp geometry, IFAC-PapersOnLine. 28 (2015) 658–663. https://doi.org/10.1016/j.ifacol.2015.06.157.

[239] A. Yadollahi, N. Shamsaei, Additive manufacturing of fatigue resistant materials: Challenges and opportunities, Int. J. Fatigue. 98 (2017) 14–31. https://doi.org/10.1016/j.ijfatigue.2017.01.001.

[240] A. Joseph, V. Mahesh, D. Harursampath, On the application of additive manufacturing methods for auxetic structures: a review, Adv. Manuf. 9 (2021) 342–368. https://doi.org/10.1007/s40436-021-00357-y.

[241] J. Zhang, G. Lu, Z. You, Large deformation and energy absorption of additively manufactured auxetic materials and structures: A review, Compos. Part B Eng. 201 (2020) 108340. https://doi.org/10.1016/j.compositesb.2020.108340.

[242] A. Arjunan, S. Zahid, A. Baroutaji, J. Robinson, 3D printed auxetic nasopharyngeal swabs for COVID-19 sample collection, J. Mech. Behav. Biomed. Mater. 114 (2021) 104175. https://doi.org/10.1016/j.jmbbm.2020.104175.

[243] D.D. Lima, S.A. Mantri, C. V. Mikler, R. Contieri, C.J. Yannetta, K.N. Campo, E.S. Lopes, M.J. Styles, T. Borkar, R. Caram, R. Banerjee, Laser additive processing of a functionally graded internal fracture fixation plate, Mater. Des. 130 (2017) 8–15. https://doi.org/10.1016/j.matdes.2017.05.034.

[244] S.H. Saheb, V.K. Durgam, A. Chandrashekhar, A review on metal powders in additive manufacturing, AIP Conf. Proc. 2281 (2020). https://doi.org/10.1063/5.0026203.

[245] M. Zanardini, A. Bacchetti, M.A. Pour, S. Zanoni, Benefits and costs of additive manufacturing applications: An evaluation guideline, Proc. Summer Sch. Fr. Turco. (2015) 43–48. https://www.researchgate.net/publication/306100171_Benefits_and_Costs_of_Additive_Manufacturing_Applications_An_Evaluation_Guideline.

[246] Y. Liu, W. Wang, L.C. Zhang, Additive manufacturing techniques and their biomedical applications, Fam. Med. Community Heal. 5 (2017) 286–298. https://doi.org/10.15212/FMCH.2017.0110.

[247] S. Lou, L. Pagani, W. Zeng, M.U. Ghori, X. Jiang, P.J. Scott, Surface texture evaluation of additively manufactured metallic cellular scaffolds for acetabular implants using X-ray computed tomography, Bio-Design Manuf. 2 (2019) 55–64. https://doi.org/10.1007/s42242-019-00042-x.

[248] L.C. Zhang, D. Klemm, J. Eckert, Y.L. Hao, T.B. Sercombe, Manufacture by selective laser melting and mechanical behavior of a biomedical Ti-24Nb-4Zr-8Sn alloy, Scr. Mater. 65 (2011) 21–24. https://doi.org/10.1016/j.scriptamat.2011.03.024.

[249] Y.J. Liu, X.P. Li, L.C. Zhang, T.B. Sercombe, Processing and properties of topologically optimised biomedical Ti-24Nb-4Zr-8Sn scaffolds manufactured by selective laser melting, Mater. Sci. Eng. A. 642 (2015) 268–278. https://doi.org/10.1016/j.msea.2015.06.088.

[250] F. Liu, Z. Mao, P. Zhang, D.Z. Zhang, J. Jiang, Z. Ma, Functionally graded porous scaffolds in multiple patterns: New design method, physical and mechanical properties, Mater. Des. 160 (2018) 849–860. https://doi.org/10.1016/j.matdes.2018.09.053.

[251] S. Kumar, A.K.S. Choudhary, A.K. Singh, A.K. Gupta, A Comparison of Additive Manufacturing Technologies, Int. J. Innov. Res. Sci. Technol. 3 (2016) 147–152. http://www.ijirst.org/articles/IJIRSTV3I1093.pdf.

[252] L.E. Murr, S.M. Gaytan, F. Medina, H. Lopez, E. Martinez, B.I. MacHado, D.H. Hernandez, L. Martinez, M.I. Lopez, R.B. Wicker, J. Bracke, Next-generation biomedical implants using additive manufacturing of complex cellular and functional mesh arrays, Philos. Trans. R. Soc. A Math. Phys. Eng. Sci. 368 (2010) 1999–2032. https://doi.org/10.1098/RSTA.2010.0010.

[253] X. Li, Y.F. Feng, C.T. Wang, G.C. Li, W. Lei, Z.Y. Zhang, L. Wang, Evaluation of Biological Properties of Electron Beam Melted Ti6Al4V Implant with Biomimetic Coating In Vitro and In Vivo, PLoS One. 7 (2012) 1–12. https://doi.org/10.1371/journal.pone.0052049.

[254] O.L.A. Harrysson, O. Cansizoglu, D.J. Marcellin-Little, D.R. Cormier, H.A. West, Direct metal fabrication of titanium implants with tailored materials and mechanical properties using electron beam melting technology, Mater. Sci. Eng. C. 28 (2008) 366–373. https://doi.org/10.1016/j.msec.2007.04.022.

[255] E. Sallica-Leva, A.L. Jardini, J.B. Fogagnolo, Microstructure and mechanical

behavior of porous Ti-6Al-4V parts obtained by selective laser melting, J. Mech. Behav. Biomed. Mater. 26 (2013) 98–108. https://doi.org/10.1016/J.JMBBM.2013.05.011.

[256] S. Rivera, M. Panera, D. Miranda, F.J. Belzunce Varela, Development of dense and cellular solids in CrCoMo alloy for orthopaedic applications, Procedia Eng. 10 (2011) 2979–2987. https://doi.org/10.1016/j.proeng.2011.04.494.

[257] C. Yan, L. Hao, A. Hussein, D. Raymont, Evaluations of cellular lattice structures manufactured using selective laser melting, Int. J. Mach. Tools Manuf. 62 (2012) 32–38. https://doi.org/10.1016/j.ijmachtools.2012.06.002.

[258] S. Bose, S. Vahabzadeh, A. Bandyopadhyay, Bone tissue engineering using 3D printing, Mater. Today. 16 (2013) 496–504. https://doi.org/10.1016/J.MATTOD.2013.11.017.

[259] P. Egan, S.J. Ferguson, Design and 3D printing of hierarchical tissue engineering scaffolds based on mechanics and biology perspectives, (2016) 1–10. https://www.researchgate.net/publication/311457591_Design_and_3D_Printing_of_Hierarchical_Tissue_Engineering_Scaffolds_Based_on_Mechanics_and_Biology_Perspectives.

[260] R. Vasireddi, B. Basu, Conceptual design of three-dimensional scaffolds of powder-based materials for bone tissue engineering applications, Rapid Prototyp. J. 21 (2015) 716–724. https://doi.org/10.1108/RPJ-12-2013-0123.

[261] N. Shahrubudin, P. Koshy, J. Alipal, M.H.A. Kadir, T.C. Lee, Challenges of 3D printing technology for manufacturing biomedical products: A case study of Malaysian manufacturing firms, Heliyon. 6 (2020) e03734. https://doi.org/10.1016/j.heliyon.2020.e03734.

[262] R. Lakes, Materials with structural hierarchy, Nature. 361 (1993) 511–515. https://doi.org/10.1038/361511a0.

[263] M.F. Ashby, The properties of foams and lattices, Philos. Trans. R. Soc. A Math.

Phys. Eng. Sci. 364 (2006) 15–30. https://doi.org/10.1098/rsta.2005.1678.

[264] J. Bauer, S. Hengsbach, I. Tesari, R. Schwaiger, O. Kraft, High-strength cellular ceramic composites with 3D microarchitecture, Proc. Natl. Acad. Sci. U. S. A. 111 (2014) 2453–2458. https://doi.org/10.1073/pnas.1315147111.

[265] S. Yang, K.-F. Leong, Z. Du, C.-K. Chua, The design of scaffolds for use in tissue engineering. Part II. Rapid prototyping techniques, Tissue Eng. 8 (2002) 1–11. https://doi.org/10.1089/107632702753503009.

[266] N.K. Tolochko, V.V. Savich, T. Laoui, L. Froyen, G. Onofrio, E. Signorelli, V.I. Titov, Dental root implants produced by the combined selective laser sintering/melting of titanium powders, Proc. Inst. Mech. Eng. Part L J. Mater. Des. Appl. 216 (2002) 267–270. https://doi.org/10.1243/146442002760387952.

[267] A. Barbas, A.-S.S. Bonnet, P. Lipinski, R. Pesci, G. Dubois, Development and mechanical characterization of porous titanium bone substitutes, J. Mech. Behav. Biomed. Mater. 9 (2012) 34–44. https://doi.org/10.1016/j.jmbbm.2012.01.008.

[268] A. Arjunan, M. Demetriou, A. Baroutaji, C. Wang, Mechanical performance of highly permeable laser melted Ti6Al4V bone scaffolds, J. Mech. Behav. Biomed. Mater. 102 (2020) 103517. https://doi.org/10.1016/j.jmbbm.2019.103517.

[269] S. Limmahakhun, A. Oloyede, K. Sitthiseripratip, Y. Xiao, C. Yan, Stiffness and strength tailoring of cobalt chromium graded cellular structures for stress-shielding reduction, Mater. Des. 114 (2017) 633–641. https://doi.org/10.1016/j.matdes.2016.11.090.

[270] M.S. Rad, Z. Ahmad, A. Alias, Computational approach in formulating mechanical characteristics of 3D star honeycomb auxetic structure, Adv. Mater. Sci. Eng. 2015 (2015). https://doi.org/10.1155/2015/650769.

[271] S. Krödel, T. Delpero, A. Bergamini, P. Ermanni, D.M. Kochmann, 3D auxetic microlattices with independently controllable acoustic band gaps and quasi-static elastic moduli, Adv. Eng. Mater. 16 (2014) 357–363.

https://doi.org/10.1002/adem.201300264.

[272] W. Wu, D. Qi, H. Liao, G. Qian, L. Geng, Y. Niu, J. Liang, Deformation mechanism of innovative 3D chiral metamaterials, Sci. Rep. 8 (2018) 3–12. https://doi.org/10.1038/s41598-018-30737-7.

[273] M. Bruggi, A. Corigliano, Optimal 2D auxetic micro-structures with band gap, Mecc. 2019 5413. 54 (2019) 2001–2027. https://doi.org/10.1007/S11012-019-00981-W.

[274] X. Fei, L. Jin, X. Zhang, X. Li, M. Lu, Three-dimensional anti-chiral auxetic metamaterial with tunable phononic bandgap, Appl. Phys. Lett. 116 (2020) 021902. https://doi.org/10.1063/1.5132589.

[275] E. optical Systems, Material data sheet EOS CobaltChrome MP1 Material data sheet Technical data, (2011) 1–6. http://www.e-manufacturing.it/downloads/EOS_CobaltChrome_MP1.pdf.

[276] L.A. Dobrzański, Ł. Reimann, Influence of Cr and Co on hardness and corrosion resistance CoCrMo alloys used on dentures, J. Achiev. Mater. Manufaturing Eng. 49 (2011) 193–199. https://www.researchgate.net/publication/239522994%0AInfluence.

[277] K. Monroy, J. Delgado, J. Ciurana, Study of the pore formation on CoCrMo alloys by selective laser melting manufacturing process, Procedia Eng. 63 (2013) 361–369. https://doi.org/10.1016/j.proeng.2013.08.227.

[278] K.M. Mantrala, M. Das, V.K. Balla, C.S. Rao, V.V.S. Kesava Rao, Additive Manufacturing of Co-Cr-Mo Alloy: Influence of Heat Treatment on Microstructure, Tribological, and Electrochemical Properties, Front. Mech. Eng. 1 (2015). https://doi.org/10.3389/fmech.2015.00002.

[279] A. Bordin, A. Ghiotti, S. Bruschi, L. Facchini, F. Bucciotti, Machinability characteristics of wrought and EBM CoCrMo alloys, Procedia CIRP. 14 (2014) 89–94. https://doi.org/10.1016/j.procir.2014.03.082.

[280] S.R. Mohamed, S.A.C. Ghani, W. Sawangsri, Mechanical properties of additive

manufactured cocrmo meta-biomaterials for load bearing implants, J. Tribol. 21 (2019) 93–107. https://jurnaltribologi.mytribos.org/v21/JT-21-93-107.pdf.

[281] C. dos Santos, A.F. Habibe, B.G. Simba, J.F.C. Lins, B.X. de Freitas, C.A. Nunes, CoCrMo-base alloys for dental applications obtained by selective laser melting (slm) and cad/cam milling, Mater. Res. 23 (2020) 1–6. https://doi.org/10.1590/1980-5373-MR-2019-0599.

[282] B. Behl, I. Papageorgiou, C. Brown, R. Hall, J.L. Tipper, J. Fisher, E. Ingham, Biological effects of cobalt-chromium nanoparticles and ions on dural fibroblasts and dural epithelial cells, Biomaterials. 34 (2013) 3547–3558. https://doi.org/10.1016/j.biomaterials.2013.01.023.

[283] Ada Steponavičiūtė, A. Šlivinskas, G. Mordas, G. Račiukaitis, Characterization and performance of CoCrMo powder for additive manufacturing, (n.d.) 1.

[284] V. Mikli, H. Kaerdi, P. Kulu, M. Besterci, Characterization of powder particle morphology, Proc. Est. Acad. Sci. Eng. 7 (2001) 22–34. http://vana.kirj.ee/public/va_te/t50-1-2.pdf.

[285] W.C. Rodrigues, L.R. Broilo, L. Schaeffer, G. Knörnschild, F.R.M. Espinoza, Powder metallurgical processing of Co-28%Cr-6%Mo for dental implants: Physical, mechanical and electrochemical properties, Powder Technol. 206 (2011) 233–238. https://doi.org/10.1016/j.powtec.2010.09.024.

[286] C. Scheu, W.D. Kaplan, Introduction to Scanning Electron Microscopy, In-Situ Electron Microsc. Appl. Physics, Chem. Mater. Sci. (2012) 1–37. https://doi.org/10.1002/9783527652167.ch1.

[287] M. Sapti, A Textbook on Fundamentals and Applications of Nanotechnology, Kemamp. Koneksi Mat. (Tinjauan Terhadap Pendekatan Pembelajaran Savi). 53 (2019) 1689–1699.

[288] A. Kaech, An Introduction To Electron Microscopy Instrumentation, Imaging and Preparation, Cent. Microsc. Image Anal. (2013) 1–26. http://www.zmb.uzh.ch/static/bio407/assets/Script_AK_2014.pdf.

[289] K. Bertoldi, V. Vitelli, J. Christensen, M. Van Hecke, Flexible mechanical metamaterials, Nat. Rev. Mater. 2 (2017). https://doi.org/10.1038/natrevmats.2017.66.

[290] D. Zhang, J. Xiao, W. Yu, Q. Guo, J. Yang, Hierarchical metal/polymer metamaterials of tunable negative Poisson's ratio fabricated by initiator-integrated 3D printing (i3DP), Nanotechnology. 29 (2018) 505704. https://doi.org/10.1088/1361-6528/aae283.

[291] H. Yang, B. Wang, L. Ma, Mechanical properties of 3D double-U auxetic structures, Int. J. Solids Struct. 180–181 (2019) 13–29. https://www.researchgate.net/publication/334332076_Mechanical_properties_of_3D_double-U_auxetic_structures.

[292] K.E. Evans, Auxetic polymers: a new range of materials, Endeavour. 15 (1991) 170–174. https://doi.org/10.1016/0160-9327(91)90123-S.

[293] M.-J. Choi, S.-H. Kang, M.-H. Oh, S. Cho, Controllable optimal design of auxetic structures for extremal Poisson's ratio of −2, Compos. Struct. 226 (2019) 111215. https://doi.org/10.1016/J.COMPSTRUCT.2019.111215.

[294] M.J. Mirzaali, A. Caracciolo, H. Pahlavani, S. Janbaz, L. Vergani, A.A. Zadpoor, Multi-material 3D printed mechanical metamaterials: Rational design of elastic properties through spatial distribution of hard and soft phases, Appl. Phys. Lett. 113 (2018) 241903. https://doi.org/10.1063/1.5064864.

[295] M.J. Mirzaali, H. Pahlavani, A.A. Zadpoor, Auxeticity and stiffness of random networks: Lessons for the rational design of 3D printed mechanical metamaterials, Appl. Phys. Lett. 115 (2019) 021901. https://doi.org/10.1063/1.5096590.

[296] K.W. Wojciechowski, Remarks on "Poisson ratio beyond the limits of the elasticity theory," J. Phys. Soc. Japan. 72 (2003) 1819–1820. https://doi.org/10.1143/JPSJ.72.1819.

[297] S. Jin, Y.P. Korkolis, Y. Li, Shear resistance of an auxetic chiral mechanical

metamaterial, Int. J. Solids Struct. 174–175 (2019) 28–37. https://doi.org/10.1016/J.IJSOLSTR.2019.06.005.

[298] A.R. El Dhaba, M. Shaat, Modeling deformation of auxetic and non-auxetic polymer gels, Appl. Math. Model. 74 (2019) 320–336. https://doi.org/10.1016/J.APM.2019.04.050.

[299] I. Shufrin, E. Pasternak, A. V. Dyskin, Effective properties of layered auxetic hybrids, Compos. Struct. 209 (2019) 391–400. https://doi.org/10.1016/J.COMPSTRUCT.2018.10.072.

[300] S. Jeong, H.H. Yoo, Shape optimization of bowtie-shaped auxetic structures using beam theory, Compos. Struct. 224 (2019) 111020. https://doi.org/10.1016/j.compstruct.2019.111020.

[301] A. Spagnoli, R. Brighenti, M. Lanfranchi, F. Soncini, On the Auxetic Behaviour of Metamaterials with Re-entrant Cell Structures, Procedia Eng. 109 (2015) 410–417. https://doi.org/10.1016/j.proeng.2015.06.252.

[302] H. Lekesiz, S.K. Bhullar, A.A. Karaca, M.B.G. Jun, Mechanical characterization of auxetic stainless steel thin sheets with reentrant structure, Smart Mater. Struct. 26 (2017) 085022. https://doi.org/10.1088/1361-665X/aa73a4.

[303] A. Alomarah, D. Ruan, S. Masood, Tensile properties of an auxetic structure with re-entrant and chiral features—a finite element study, Int. J. Adv. Manuf. Technol. 99 (2018) 2425–2440. https://doi.org/10.1007/s00170-018-2637-y.

[304] Y. Jiang, B. Rudra, J. Shim, Y. Li, Limiting strain for auxeticity under large compressive Deformation: Chiral vs. re-entrant cellular solids, Int. J. Solids Struct. 162 (2019) 87–95. https://doi.org/10.1016/J.IJSOLSTR.2018.11.035.

[305] T. Wang, L. Wang, Z. Ma, G.M. Hulbert, Elastic analysis of auxetic cellular structure consisting of re-entrant hexagonal cells using a strain-based expansion homogenization method, Mater. Des. 160 (2018) 284–293. https://doi.org/10.1016/J.MATDES.2018.09.013.

[306] B. Nečemer, J. Kramberger, T. Vuherer, S. Glodež, Fatigue crack initiation and

propagation in re-entrant auxetic cellular structures, Int. J. Fatigue. 126 (2019) 241–247. https://doi.org/10.1016/J.IJFATIGUE.2019.05.010.

[307] S.C. Han, D.S. Kang, K. Kang, Two nature-mimicking auxetic materials with potential for high energy absorption, Mater. Today. 26 (2019) 30–39. https://doi.org/10.1016/j.mattod.2018.11.004.

[308] K.W. Wojciechowski, Two-dimensional isotropic system with a negative poisson ratio, Phys. Lett. A. 137 (1989) 60–64. https://doi.org/10.1016/0375-9601(89)90971-7.

[309] K.W. Wojciechowski, Constant thermodynamic tension Monte Carlo studies of elastic properties of a two-dimensional system of hard cyclic hexamers, Mol. Phys. 61 (1987) 1247–1258. https://doi.org/10.1080/00268978700101761.

[310] L. Mizzi, D. Attard, R. Gatt, A.A. Pozniak, K.W. Wojciechowski, J.N. Grima, Influence of translational disorder on the mechanical properties of hexachiral honeycomb systems, (2015). https://doi.org/10.1016/j.compositesb.2015.04.057.

[311] B.K. Hoffmeister, S.R. Smith, S.M. Handley, J.Y. Rho, Anisotropy of Young's modulus of human tibial cortical bone., Med. Biol. Eng. Comput. 38 (2000) 333–8. https://doi.org/https://doi.org/10.1007/bf02347055.

[312] J. Rho, R. Ashman, C. Turner, Young's modulus of trabecular and cortical bone material: Ultrasonic and microtensile measurements, J. Biomech. 26 (1993) 111–119. https://doi.org/10.1016/0021-9290(93)90042-D.

[313] P.K. Zysset, X. Edward Guo, C. Edward Hoffler, K.E. Moore, S.A. Goldstein, Elastic modulus and hardness of cortical and trabecular bone lamellae measured by nanoindentation in the human femur, J. Biomech. 32 (1999) 1005–1012. https://doi.org/10.1016/S0021-9290(99)00111-6.

[314] E.H. Schemitsch, Size Matters: Defining Critical in Bone Defect Size!, J. Orthop. Trauma. 31 (2017) S20–S22. https://doi.org/10.1097/BOT.0000000000000978.

[315] D.N. Utomo, K.D. Hernugrahanto, M. Edward, L. Widhiyanto, F. Mahyudin,

Combination of Bone Marrow Aspirate, Cancellous Bone Allograft, and Platelet-rich Plasma as an Alternative Solution to Critical-sized Diaphyseal Bone Defect: A Case Series, Int. J. Surg. Case Rep. 58 (2019) 178–185. https://doi.org/10.1016/j.ijscr.2019.04.028.

[316] C. Christou, R.A. Oliver, M.H. Pelletier, W.R. Walsh, Ovine model for critical-size tibial segmental defects., Comp. Med. 64 (2014) 377–85. https://www.ncbi.nlm.nih.gov/pmc/articles/PMC4236786/pdf/cm2014000377.pdf.

[317] C. Pleass, S. Jothi, Influence of powder characteristics and additive manufacturing process parameters on the microstructure and mechanical behaviour of Inconel 625 fabricated by Selective Laser Melting, Addit. Manuf. 24 (2018) 419–431. https://doi.org/10.1016/j.addma.2018.09.023.

[318] J.H. Tan, W.L.E. Wong, K.W. Dalgarno, An overview of powder granulometry on feedstock and part performance in the selective laser melting process, Addit. Manuf. 18 (2017) 228–255. https://doi.org/10.1016/j.addma.2017.10.011.

[319] Y. Kang, J. Chang, Channels in a porous scaffold: A new player for vascularization, Regen. Med. 13 (2018) 705–715. https://doi.org/10.2217/rme-2018-0022.

[320] A. Ahmed, A. Majeed, Z. Atta, G. Guozhu, Dimensional Quality and Distortion Analysis of Thin-Walled Alloy Parts of AlSi10Mg Manufactured by Selective Laser Melting, J. Manuf. Mater. Process. 3 (2019) 51. https://doi.org/10.3390/jmmp3020051.

[321] A.A.A.A. Zadpoor, Mechanics of additively manufactured biomaterials, Elsevier Ltd, 2017. https://doi.org/10.1016/j.jmbbm.2017.03.018.

[322] V. Weißmann, P. Drescher, R. Bader, H. Seitz, H. Hansmann, N. Laufer, Comparison of Single Ti 6 Al 4 V Struts Made Using Selective Laser Melting and Electron Beam Melting Subject to Part Orientation, Metals (Basel). (2017). https://doi.org/10.3390/met7030091.

[323] I. Echeta, X. Feng, B. Dutton, R. Leach, S. Piano, Review of defects in lattice structures manufactured by powder bed fusion, Int. J. Adv. Manuf. Technol. 106 (2020) 2649–2668. https://doi.org/10.1007/s00170-019-04753-4.

[324] International Organization for Standardization, Mechanical testing of metals – Ductility testing – Compression test for porous and cellular metals, Int. Organ. Stand. 2011 (2011) 1–7. https://www.iso.org/standard/53669.html.

[325] International Organization for Standardization, Metallic materials — Calibration and verification of static uniaxial testing machines, 2018 (2018). https://www.iso.org/standard/72572.html.

[326] The British Standards Institution, ISO 6892-1:2016 - Tensile testing Part 1 : Method of test at room temperature, Bsi. (2016). https://www.iso.org/standard/61856.html.

[327] A. Dolgov, N, T. Dikova, D. Dzhendov, D. Pavlova, M. Simov, Mechanical properties of dental Co-Cr alloys fabricated via casting and selective laser melting, Sci. Proc. Ii Int. Sci. Conf. "Innovations Eng. 2016. 33 (2016) 29–33. https://www.researchgate.net/publication/304332094_Mechanical_Properties_of_Dental_Co-Cr_Alloys_Fabricated_via_Casting_and_Selective_Laser_Melting.

[328] G. Cornacchia, S. Cecchel, D. Battini, C. Petrogalli, A. Avanzini, Microstructural, Mechanical, and Tribological Characterization of Selective Laser Melted CoCrMo Alloy under Different Heat Treatment Conditions and Hot Isostatic Pressing, Adv. Eng. Mater. 2100928 (2021). https://doi.org/10.1002/adem.202100928.

[329] M. Yakout, M.A. Elbestawi, S.C. Veldhuis, Density and mechanical properties in selective laser melting of Invar 36 and stainless steel 316L, J. Mater. Process. Technol. 266 (2019) 397–420. https://doi.org/10.1016/J.JMATPROTEC.2018.11.006.

[330] A.H. Maamoun, Y.F. Xue, M.A. Elbestawi, S.C. Veldhuis, A.H. Maamoun, Y.F. Xue, M.A. Elbestawi, S.C. Veldhuis, Effect of Selective Laser Melting Process

Parameters on the Quality of Al Alloy Parts: Powder Characterization, Density, Surface Roughness, and Dimensional Accuracy, Materials (Basel). 11 (2018) 2343. https://doi.org/10.3390/ma11122343.

[331] J. Ciurana, L. Hernandez, J. Delgado, Energy density analysis on single tracks formed by selective laser melting with CoCrMo powder material, Int. J. Adv. Manuf. Technol. 68 (2013) 1103–1110. https://doi.org/10.1007/s00170-013-4902-4.

[332] N. Read, W. Wang, K. Essa, M.M. Attallah, Selective laser melting of AlSi10Mg alloy: Process optimisation and mechanical properties development, 65 (2015) 417–424. https://doi.org/10.1016/j.matdes.2014.09.044.

[333] T. de Terris, O. Andreau, P. Peyre, F. Adamski, I. Koutiri, C. Gorny, C. Dupuy, Optimization and comparison of porosity rate measurement methods of Selective Laser Melted metallic parts, Addit. Manuf. 28 (2019) 802–813. https://doi.org/10.1016/j.addma.2019.05.035.

[334] N. Li, S. Huang, G. Zhang, R. Qin, W. Liu, H. Xiong, G. Shi, J. Blackburn, Progress in additive manufacturing on new materials: A review, J. Mater. Sci. Technol. 35 (2019) 242–269. https://doi.org/10.1016/J.JMST.2018.09.002.

[335] A. Arjunan, J. Robinson, E. Al Ani, W. Heaselgrave, A. Baroutaji, C. Wang, Mechanical performance of additively manufactured pure silver antibacterial bone scaffolds, J. Mech. Behav. Biomed. Mater. 112 (2020) 104090. https://doi.org/10.1016/j.jmbbm.2020.104090.

[336] M. Mahbod, M. Asgari, Elastic and plastic characterization of a new developed additively manufactured functionally graded porous lattice structure: Analytical and numerical models, Int. J. Mech. Sci. 155 (2019) 248–266. https://doi.org/10.1016/J.IJMECSCI.2019.02.041.

[337] N.H. Pham, R.S. Voronov, S.B. Vangordon, V.I. Sikavitsas, D. V Papavassiliou, Predicting the stress distribution within scaffolds with ordered architecture., Biorheology. 49 (2012) 235–47. https://doi.org/10.3233/BIR-2012-0613.

[338] S. Campanelli, N. Contuzzi, A. Ludovico, F. Caiazzo, F. Cardaropoli, V. Sergi, Manufacturing and Characterization of Ti6Al4V Lattice Components Manufactured by Selective Laser Melting, Materials (Basel). 7 (2014) 4803–4822. https://doi.org/10.3390/ma7064803.

[339] A. Arjunan, M. Singh, A. Baroutaji, C. Wang, Additively manufactured AlSi10Mg inherently stable thin and thick-walled lattice with negative Poisson's ratio, Compos. Struct. 247 (2020) 112469. https://doi.org/10.1016/j.compstruct.2020.112469.

[340] R. Singh, P.D. Lee, T.C. Lindley, C. Kohlhauser, C. Hellmich, M. Bram, T. Imwinkelried, R.J. Dashwood, Characterization of the deformation behavior of intermediate porosity interconnected Ti foams using micro-computed tomography and direct finite element modeling, Acta Biomater. 6 (2010) 2342–2351. https://doi.org/10.1016/j.actbio.2009.11.032.

[341] W.J. Hendrikson, C.A. van Blitterswijk, J. Rouwkema, L. Moroni, The Use of Finite Element Analyses to Design and Fabricate Three-Dimensional Scaffolds for Skeletal Tissue Engineering, Front. Bioeng. Biotechnol. 5 (2017) 30. https://doi.org/10.3389/fbioe.2017.00030.

[342] K. Genovese, S. Leeflang, A.A. Zadpoor, Microscopic full-field three-dimensional strain measurement during the mechanical testing of additively manufactured porous biomaterials, J. Mech. Behav. Biomed. Mater. 69 (2017) 327–341. https://doi.org/10.1016/j.jmbbm.2017.01.010.

[343] Z. Dong, X. Zhang, W. Shi, H. Zhou, H. Lei, J. Liang, Study of Size Effect on Microstructure and Mechanical Properties of AlSi10Mg Samples Made by Selective Laser Melting., Mater. (Basel, Switzerland). 11 (2018). https://doi.org/10.3390/ma11122463.

[344] T. Yu, H. Hyer, Y. Sohn, Y. Bai, D. Wu, Structure-property relationship in high strength and lightweight AlSi10Mg microlattices fabricated by selective laser melting, Mater. Des. 182 (2019) 108062. https://doi.org/10.1016/J.MATDES.2019.108062.

[345] W.H. Kan, Y. Nadot, M. Foley, L. Ridosz, G. Proust, J.M. Cairney, Factors that affect the properties of additively-manufactured AlSi10Mg: Porosity versus microstructure, Addit. Manuf. 29 (2019) 100805. https://doi.org/10.1016/J.ADDMA.2019.100805.

[346] A. Hadadzadeh, B. Shalchi Amirkhiz, A. Odeshi, J. Li, M. Mohammadi, Role of hierarchical microstructure of additively manufactured AlSi10Mg on dynamic loading behavior, Addit. Manuf. 28 (2019) 1–13. https://doi.org/10.1016/J.ADDMA.2019.04.012.

[347] J. Chen, W. Hou, X. Wang, S. Chu, Z. Yang, Microstructure, porosity and mechanical properties of selective laser melted AlSi10Mg, Chinese J. Aeronaut. (2019). https://doi.org/10.1016/j.cja.2019.08.017.

[348] C. Yan, L. Hao, A. Hussein, S.L. Bubb, P. Young, D. Raymont, Evaluation of light-weight AlSi10Mg periodic cellular lattice structures fabricated via direct metal laser sintering, J. Mater. Process. Technol. 214 (2014) 856–864. https://doi.org/10.1016/J.JMATPROTEC.2013.12.004.

[349] M. Liu, N. Takata, A. Suzuki, M. Kobashi, Development of gradient microstructure in the lattice structure of AlSi10Mg alloy fabricated by selective laser melting, J. Mater. Sci. Technol. (2019). https://doi.org/10.1016/J.JMST.2019.06.015.

[350] M.N. Oza, D.S. Shah, Theoretical and experimental modal analysis of centrifugal pump radial flow impeller, IOP Conf. Ser. Mater. Sci. Eng. 992 (2020). https://doi.org/10.1088/1757-899X/992/1/012003.

[351] K.L. Gowtham, S.R. Srivatsa, Study of Convergence of Results in Finite Element Analysis of a Plane Stress Bracket, J. Eng. Res. Appl. (2018) 7–12. https://www.ijera.com/special_issue/(NAME) 2018/Volume 1/02. 07-12.pdf.

[352] E.M. Alawadhi, Meshing guide, Finite Elem. Simulations Using ANSYS. 15317 (2020) 407–424. https://doi.org/10.1201/b18949-12.

[353] N.S. Ghokale, Practical finite element analysis, Finite to infinite, Pune, India,

2008.

[354] S.L. Sing, W.Y. Yeong, F.E. Wiria, B.Y. Tay, Characterization of Titanium Lattice Structures Fabricated by Selective Laser Melting Using an Adapted Compressive Test Method, Exp. Mech. 56 (2016) 735–748. https://doi.org/10.1007/s11340-015-0117-y.

[355] M. De Wild, R. Schumacher, K. Mayer, E. Schkommodau, D. Thoma, M. Bredell, A. Kruse Gujer, K.W. Grätz, F.E. Weber, Bone regeneration by the osteoconductivity of porous titanium implants manufactured by selective laser melting: A histological and micro computed tomography study in the rabbit, Tissue Eng. - Part A. 19 (2013) 2645–2654. https://doi.org/10.1089/ten.tea.2012.0753.

[356] M. Speirs, B. Van Hooreweder, J. Van Humbeeck, J.-P. Kruth, Fatigue behaviour of NiTi shape memory alloy scaffolds produced by SLM, a unit cell design comparison, J. Mech. Behav. Biomed. Mater. 70 (2017) 53–59. https://doi.org/10.1016/j.jmbbm.2017.01.016.

[357] N. Taniguchi, S. Fujibayashi, M. Takemoto, K. Sasaki, B. Otsuki, T. Nakamura, T. Matsushita, T. Kokubo, S. Matsuda, Effect of pore size on bone ingrowth into porous titanium implants fabricated by additive manufacturing: An in vivo experiment, Mater. Sci. Eng. C. 59 (2016) 690–701. https://doi.org/10.1016/j.msec.2015.10.069.

[358] Z. Wahid, M.K.A.M. Ariffin, B.T.H.T. Baharudin, M.I.S. Ismail, F. Mustapha, Abaqus Simulation of Different Critical Porosities Cubical Scaffold Model, IOP Conf. Ser. Mater. Sci. Eng. 530 (2019) 012018. https://doi.org/10.1088/1757-899X/530/1/012018.

[359] A. Salimon, Y. Bréchet, M.F. Ashby, A.L. Greer, Potential applications for steel and titanium metal foams, J. Mater. Sci. 40 (2005) 5793–5799. https://doi.org/10.1007/s10853-005-4993-x.

[360] J. Favre, P. Lohmuller, B. Piotrowski, S. Kenzari, P. Laheurte, F. Meraghni, A continuous crystallographic approach to generate cubic lattices and its effect on

relative stiffness of architectured materials, Addit. Manuf. 21 (2018) 359–368. https://doi.org/10.1016/j.addma.2018.02.020.

[361] L.D. Bobbio, S. Qin, A. Dunbar, P. Michaleris, A.M. Beese, Characterization of the strength of support structures used in powder bed fusion additive manufacturing of Ti-6Al-4V, Addit. Manuf. 14 (2017) 60–68. https://doi.org/10.1016/J.ADDMA.2017.01.002.

[362] G. Savio, S. Rosso, A. Curtarello, R. Meneghello, G. Concheri, Implications of modeling approaches on the fatigue behavior of cellular solids, Addit. Manuf. 25 (2019) 50–58. https://doi.org/10.1016/j.addma.2018.10.047.

[363] Venkata Rao, Evaluating flexible manufacturing systems using a combined multiple attribute decision making method, Int. J. Prod. Res. (n.d.). https://doi.org/http://dx.doi.org/10.1080/00207540601011519.

[364] Yan Zhang, Consumer Choice Modeling: Comparing and Contrasting the MAAM, AHP, TOPSIS and AHP-TOPSIS Methodologies, 2014. https://doi.org/https://mspace.lib.umanitoba.ca/bitstream/handle/1993/23888/Zhang_Yan.pdf?sequence=3&isAllowed=y.

[365] J. Raigar, V.S. Sharma, S. Srivastava, R. Chand, J. Singh, A decision support system for the selection of an additive manufacturing process using a new hybrid MCDM technique, Sadhana - Acad. Proc. Eng. Sci. 45 (2020). https://doi.org/10.1007/s12046-020-01338-w.

[366] I. Emovon, O.S. Oghenenyerovwho, Application of MCDM method in material selection for optimal design: A review, Results Mater. 7 (2020) 100115. https://doi.org/10.1016/j.rinma.2020.100115.

[367] M. Bertolini, G. Esposito, G. Romagnoli, A TOPSIS-based approach for the best match between manufacturing technologies and product specifications, Expert Syst. Appl. 159 (2020) 113610. https://doi.org/10.1016/j.eswa.2020.113610.

[368] M. Sabaghi, C. Mascle, P. Baptiste, Application of DOE-TOPSIS technique in decision-making problems, IFAC-PapersOnLine. 28 (2015) 773–777.

https://doi.org/10.1016/j.ifacol.2015.06.176.

[369] R. Rahim, S. Supiyandi, A.P.U. Siahaan, T. Listyorini, A.P. Utomo, W.A. Triyanto, Y. Irawan, S. Aisyah, M. Khairani, S. Sundari, K. Khairunnisa, TOPSIS Method Application for Decision Support System in Internal Control for Selecting Best Employees, J. Phys. Conf. Ser. 1028 (2018). https://doi.org/10.1088/1742-6596/1028/1/012052.

[370] H. Nikkhah, A. Baroutaji, A.G. Olabi, Crashworthiness design and optimisation of windowed tubes under axial impact loading, Thin-Walled Struct. 142 (2019) 132–148. https://doi.org/10.1016/j.tws.2019.04.052.

[371] A.D. Berdie, M. Osaci, I. Muscalagiu, C. Barz, A combined approach of AHP and TOPSIS methods applied in the field of integrated software systems, IOP Conf. Ser. Mater. Sci. Eng. 200 (2017). https://doi.org/10.1088/1757-899X/200/1/012041.

[372] M. Yazdani, A.F. Payam, A comparative study on material selection of microelectromechanical systems electrostatic actuators using Ashby, VIKOR and TOPSIS, Mater. Des. 65 (2015) 328–334. https://doi.org/10.1016/j.matdes.2014.09.004.

[373] E. Roszkowska, Multi-Criteria Decision Making Models By Applying the Topsis Method To Crisp and Interval Data, Int. Sci. J. 6 (2011) 200–230. https://mcdm.ue.katowice.pl/files/papers/mcdm11(6)_11.pdf.

[374] V. Dohale, M. Akarte, S. Gupta, V. Verma, Additive Manufacturing Process Selection Using MCDM, Lect. Notes Mech. Eng. (2021) 601–609. https://doi.org/10.1007/978-981-15-3639-7_72.

[375] A.A. Vithalani, C.H. Vithalani, Application of combined TOPSIS and AHP method for Spectrum Selection in Cognitive Radio by Channel Characteristic Evaluation, Int. J. Electron. Commun. Eng. 10 (2017) 71–79. http://www.irphouse.com.

[376] A. Jozaghi, B. Alizadeh, M. Hatami, I. Flood, M. Khorrami, N. Khodaei, E.G.

Tousi, A comparative study of the AHP and TOPSIS techniques for dam site selection using GIS: A case study of Sistan and Baluchestan Province, Iran, Geosci. 8 (2018) 1–23. https://doi.org/10.3390/geosciences8120494.

[377] M. Ngiam, S. Liao, T. Ong Jun Jie, Xiaodi Sui, Yixiang Dong, S. Ramakrishna, C.K. Chan, Effects of mechanical stimulation in osteogenic differentiation of bone marrow-derived mesenchymal stem cells on aligned nanofibrous scaffolds:, Http://Dx.Doi.Org/10.1177/0883911510393162. 26 (2010) 56–70. https://doi.org/10.1177/0883911510393162.

[378] M.A. Velasco, C.A. Narváez-Tovar, D.A. Garzón-Alvarado, Design, materials, and mechanobiology of biodegradable scaffolds for bone tissue engineering, Biomed Res. Int. 2015 (2015). https://doi.org/10.1155/2015/729076.

[379] C. Perier-Metz, G.N. Duda, S. Checa, Mechano-Biological Computer Model of Scaffold-Supported Bone Regeneration: Effect of Bone Graft and Scaffold Structure on Large Bone Defect Tissue Patterning, Front. Bioeng. Biotechnol. 8 (2020) 1–15. https://doi.org/10.3389/fbioe.2020.585799.

[380] J.L. Milan, J.A. Planell, D. Lacroix, Simulation of bone tissue formation within a porous scaffold under dynamic compression, Biomech. Model. Mechanobiol. 9 (2010) 583–596. https://doi.org/10.1007/s10237-010-0199-5.

[381] R. V. Lenth, Response-surface methods in R, using RSM, J. Stat. Softw. 32 (2009) 1–17. https://doi.org/10.18637/jss.v032.i07.

[382] R.L. Lorza, M.Á.M. Calvo, C.B. Labari, P.J.R. Fuente, Using the multi-response method with desirability functions to optimize the Zinc electroplating of steel screws, Metals (Basel). 8 (2018) 1–20. https://doi.org/10.3390/met8090711.

[383] A.I. Khuri, S. Mukhopadhyay, Response surface methodology, Wiley Interdiscip. Rev. Comput. Stat. 2 (2010) 128–149. https://doi.org/10.1002/wics.73.

[384] J. Fan, L. Zhang, S. Wei, Z. Zhang, S.-K. Choi, B. Song, Y. Shi, A review of additive manufacturing of metamaterials and developing trends, Mater. Today. 50 (2021) 303–328.

https://doi.org/https://doi.org/10.1016/j.mattod.2021.04.019.

[385] L.L. Hu, M.Z. Zhou, H. Deng, Dynamic indentation of auxetic and non-auxetic honeycombs under large deformation, Compos. Struct. 207 (2019) 323–330. https://doi.org/10.1016/J.COMPSTRUCT.2018.09.066.

[386] J. Ju, J.D. Summers, Compliant hexagonal periodic lattice structures having both high shear strength and high shear strain, Mater. Des. 32 (2011) 512–524. https://doi.org/https://doi.org/10.1016/j.matdes.2010.08.029.

[387] J. Xiang, J. Du, Energy absorption characteristics of bio-inspired honeycomb structure under axial impact loading, Mater. Sci. Eng. A. 696 (2017) 283–289. https://doi.org/https://doi.org/10.1016/j.msea.2017.04.044.

[388] J.S. Arora, Introduction to Design Optimization, Introd. to Optim. Des. (2012) 1–15. https://doi.org/10.1016/b978-0-12-381375-6.00001-2.

[389] N. Gunantara, A review of multi-objective optimization: Methods and its applications, Cogent Eng. 5 (2018) 1–16. https://doi.org/10.1080/23311916.2018.1502242.

[390] P. Cortez, Multi-Objective Optimization, (2014) 99–117. https://doi.org/10.1007/978-3-319-08263-9_6.

[391] S. Nayak, C. Tammer, P. Weidner, Multiobjective Optimization, Fundam. Optim. Tech. with Algorithms. (2020) 285–354. https://doi.org/10.1007/978-3-030-44723-6_7.

[392] A. Ning, J.R.R.A. Martins, Engineering design optimization, 2020. https://mdobook.github.io.

[393] A.A. Javadi, A. Faramarzi, R. Farmani, Design and optimization of microstructure of auxetic materials, Eng. Comput. (Swansea, Wales). 29 (2012) 260–276. https://doi.org/10.1108/02644401211212398.

[394] G.N. Vanderplaats, Design optimization - A powerful tool for the competitive edge, 1st AIAA, Aircraft, Technol. Integr. Oper. Forum. (2001).

https://doi.org/10.2514/6.2001-5214.

[395] D.H. Lee, I.J. Jeong, K.J. Kim, A desirability function method for optimizing mean and variability of multiple responses using a posterior preference articulation approach, Qual. Reliab. Eng. Int. 34 (2018) 360–376. https://doi.org/10.1002/qre.2258.

[396] J. Wieding, A. Wolf, R. Bader, Numerical optimization of open-porous bone scaffold structures to match the elastic properties of human cortical bone, J. Mech. Behav. Biomed. Mater. 37 (2014) 56–68. https://doi.org/10.1016/j.jmbbm.2014.05.002.

[397] J.C. Reichert, M.E. Wullschleger, A. Cipitria, J. Lienau, T.K. Cheng, M.A. Schütz, G.N. Duda, U. Nöth, J. Eulert, D.W. Hutmacher, Custom-made composite scaffolds for segmental defect repair in long bones, Int. Orthop. 2010 358. 35 (2010) 1229–1236. https://doi.org/10.1007/S00264-010-1146-X.